Velocity Resolved - Scalar Modeled Simulations of High Schmidt Number Turbulent Transport

Thesis by

Siddhartha Verma

In Partial Fulfillment of the Requirements

for the Degree of

Doctor of Philosophy

California Institute of Technology

Pasadena, California

2014

(Defended May 22, 2014)

For माँ, पापा, और प्यारी बच्ची

Acknowledgements

I am grateful to Professor Ravichandran, and to the Keck Institute for Space Studies, for having given me the opportunity to come to Caltech. Throughout my time here, I have relied on guidance from a great many faculty members. They have always been warm and welcoming, more so than I have ever experienced at any other institution. I am especially indebted to Professors Dan Meiron and Tony Leonard, for being replete with encouraging and thought-provoking discussions; their enthusiasm and love for science is infectious. I am in debt to my advisor, Professor Blanquart, for always having allowed me unrestricted creative leeway, and for being a staunch supporter when the going got rough. Professor Colonius has my deepest gratitude, for always believing in me, when few others in the western hemisphere did. And finally, I am grateful to my thesis committee for teaching me the most crucial lesson I learned at Caltech: Always think before you speak.

Abstract

The objective of this thesis is to develop a framework to conduct velocity resolved - scalar modeled (VR-SM) simulations, which will enable accurate simulations at higher Reynolds and Schmidt (Sc) numbers than are currently feasible. The framework established will serve as a first step to enable future simulation studies for practical applications. To achieve this goal, in-depth analyses of the physical, numerical, and modeling aspects related to $Sc \gg 1$ are presented, specifically when modeling in the viscous-convective subrange. Transport characteristics are scrutinized by examining scalar-velocity Fourier mode interactions in Direct Numerical Simulation (DNS) datasets and suggest that scalar modes in the viscous-convective subrange do not directly affect large-scale transport for high Sc. Further observations confirm that discretization errors inherent in numerical schemes can be sufficiently large to wipe out any meaningful contribution from subfilter models. This provides strong incentive to develop more effective numerical schemes to support high Sc simulations. To lower numerical dissipation while maintaining physically and mathematically appropriate scalar bounds during the convection step, a novel method of enforcing bounds is formulated, specifically for use with cubic Hermite polynomials. Boundedness of the scalar being transported is effected by applying derivative limiting techniques, and physically plausible single sub-cell extrema are allowed to exist to help minimize numerical dissipation. The proposed bounding algorithm results in significant performance gain in DNS of turbulent mixing layers and of homogeneous isotropic turbulence. Next, the combined physical/mathematical behavior of the subfilter scalar-flux vector is analyzed in homogeneous isotropic turbulence, by examining vector orientation in the strain-rate eigenframe. The results indicate no discernible dependence on the modeled scalar field, and lead to the identification of the tensor-diffusivity model as a good representation of the subfilter flux. Velocity resolved

- scalar modeled simulations of homogeneous isotropic turbulence are conducted to confirm the behavior theorized in these *a priori* analyses, and suggest that the tensor-diffusivity model is ideal for use in the viscous-convective subrange. Simulations of a turbulent mixing layer are also discussed, with the partial objective of analyzing Schmidt number dependence of a variety of scalar statistics. Large-scale statistics are confirmed to be relatively independent of the Schmidt number for $Sc \gg 1$, which is explained by the dominance of subfilter dissipation over resolved molecular dissipation in the simulations. Overall, the VR-SM framework presented is quite effective in predicting large-scale transport characteristics of high Schmidt number scalars, however, it is determined that prediction of subfilter quantities would entail additional modeling intended specifically for this purpose. The VR-SM simulations presented in this thesis provide us with the opportunity to overlap with experimental studies, while at the same time creating an assortment of baseline datasets for future validation of LES models, thereby satisfying the objectives outlined for this work.

Contents

List of Figures

List of Tables

Chapter 1

Introduction

1.1 Motivation

The study of turbulent scalar transport in fluids finds use in a variety of important environmental, industrial, and engineering applications. Turbulence greatly enhances the process of molecular mixing, a fact that we exploit routinely to our advantage in the optimal operation of machinery and industrial processes. The critical dimensionless parameter that governs turbulent flow behavior is the Reynolds number ($Re = ul/\nu$), which represents the ratio of inertial to viscous forces. u and l are characteristic velocity and length scales associated with the problem of interest, and ν is the kinematic viscosity of the fluid. At sufficiently large values of Re, viscous forces become too weak to damp minor perturbations effectively. These perturbations quickly develop into flow instabilities, leading to seemingly chaotic flow behavior.

One of the ubiquitous examples where turbulent mixing plays a crucial role, is in the design of aircraft and internal combustion engines where achieving efficient and thorough mixing of fuel and oxidizer is one of the critical goals. Enhanced mixing in turbulent flows comes about due to the tendency of turbulent fluctuations to twist and stretch scalar material elements. This distortion leads to an increase in the scalar gradient and interface surface area available for molecular diffusion (Fig. 1.1). The key dimensionless parameter that governs the ensuing mixing process is the Schmidt number [36, 13, 14, 43], which is defined as the ratio of the fluid viscosity to the molecular diffusivity of the scalar ($Sc = \nu/\mathcal{D}$).

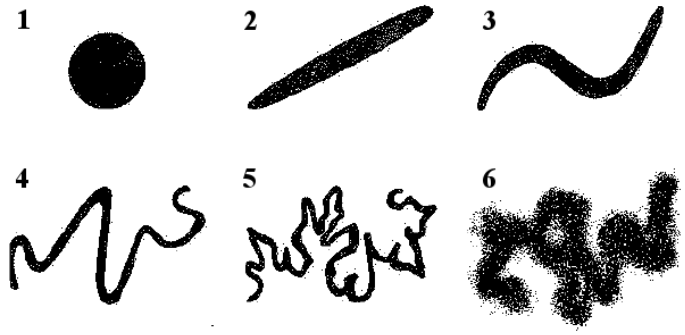

Figure 1.1: Evolution of scalar material element under straining by a turbulent velocity field. Figure adapted from Ref [122].

For extremely low-diffusivity scalars (i.e., $Sc \gg 1$), the transport characteristics at the small length scales are distinctly different from those evident for scalars with $Sc \lesssim 1$ [13]. These differences become important when considering high Schmidt number scalar transport in a natural setting, for instance, in the dispersal of pollutants in the atmosphere and oceans, and in turbulent mixing of a variety of solutes in liquids (e.g., gases and nutrients dissolved in water) [72, 43, 95]. The dispersal of soot particles in air involves Schmidt numbers on the order of 10^5 to 10^6, on account of the particles being heavy, unwieldy agglomerates of unburnt hydrocarbon molecules. The massive inertia of the particles results in very limited Brownian motion, which leads to extremely small molecular diffusivity, and hence, to high Sc. Similarly, the low molecular diffusivity of dissolved gases (e.g., O_2, CO_2) and ions (nitrates, phosphates, etc.) in water yields $Sc = O(10^2)$ [22, 23, 95].

Advances in our understanding of the transport physics of such low-diffusivity scalars, and a reliable means of conducting accurate simulations at high Reynolds and Schmidt numbers, can prove to be invaluable in addressing critical matters of socio-economic import. For instance, the joint effects of household and ambient air pollution (which consists of a large quantity of high Sc particulate matter) caused close to 7 million deaths in 2002 [1], a number which accounted for approximately 1 in 8 deaths worldwide. About half of these deaths were the result of ambient pollution, which is directly correlated with the alarming levels of air pollution in metropolitan cities (e.g., Los Angeles, Paris, and Beijing). Naturally occurring events, such as smoke issuing from wildfires and erupting volcanoes, also highlight a pressing need for improved understanding

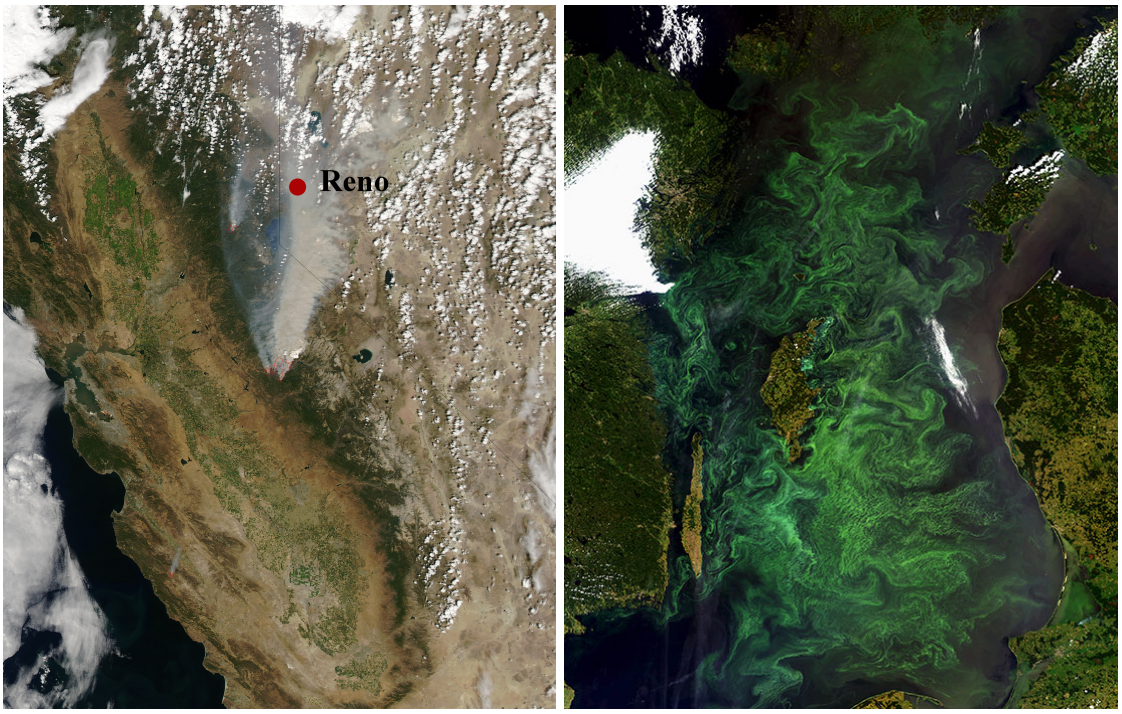

(a) Smoke from the Yosemite Rim Fire: August 2013 [66] (b) Algal bloom in the Baltic sea: July 2005 [65]

Figure 1.2: Two examples of high Sc flows in nature.

of $Sc \gg 1$ flows. The Yosemite Rim Fire in the summer of 2013 (Fig. 1.2(a)) [66] raised serious concerns about pollutants threatening air quality in cities as far away as Reno, and tainting San Francisco's primary water reservoir. Advancing currently available simulation capability can help us tackle these issues, for instance by guiding informed evacuation of areas under threat of toxic levels of particulate matter, or by taking preemptive measures to minimize collateral damage. An example of preventative action could involve arranging for alternate drinking water supply in case simulations indicate a high probability of the primary reservoir getting tainted.

Another important example of high Sc transport involves the continually increasing occurrence of 'dead zones' in coastal waters throughout the world. Excessive fertilizer runoff (comprised of nitrate, sulphate, and phosphate ions, among other things) has been known to give rise to rapid growth of algae, referred to as 'algal bloom' (Fig. 1.2(b)) [65]. The subsequent decomposition of algae by bacteria leads to severe hypoxia (depletion of dissolved oxygen) in coastal waters, which has a debilitating impact on marine life and the surrounding communities. Improved simulation capability, and a comprehensive physical understanding of high Sc transport, can help implement

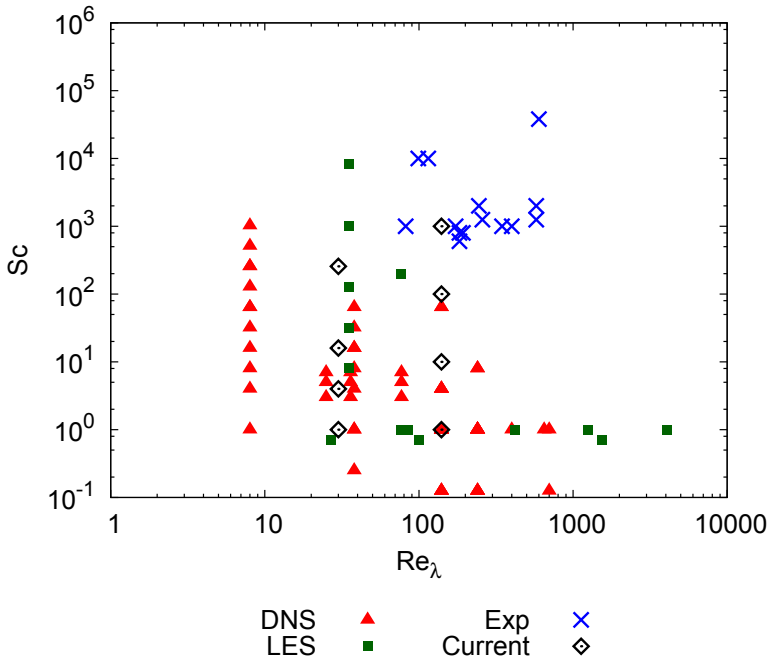

Figure 1.3: High Schmidt number experiments and simulations available in the literature [15, 37, 96, 102, 71, 48, 89, 91, 19, 29, 42, 131, 144, 143, 142, 87, 49, 105, 26, 47]. DNS—Direct numerical simulation, LES—Large eddy simulation, Exp—Experiments, Current—DNS/LES established for present work. Reynolds numbers have been approximated from data available in the references.

effective measures to minimize the hazardous impact on human health and the environment. For instance, acceptable levels of runoff emanating from point sources, that result in reduced severity of the occurrence of dead zones, can be determined using simulations. In areas blighted with low dissolved oxygen content, simulations could even assist in predicting recovery of the high Sc dissolved O_2 to normal levels.

In addition to the scenarios discussed, the study of high Schmidt number transport also finds use in a variety of non-environmental situations. One such example involves mixing related studies of organic dyes in water ($Sc = O(10^3)$) in laboratory settings [15, 37, 96, 102, 71, 89, 91, 68, 42, 49]. A non-inclusive compilation of several relevant turbulence experiments and simulation-based studies available in the literature is depicted in Fig. 1.3. The Taylor-scale Reynolds number ($Re_\lambda = \lambda u'/\nu$, where λ is the Taylor-microscale, and u' is the r.m.s. velocity) used in the studies is plotted on the horizontal axis, and the corresponding Schmidt number is plotted on the vertical axis. We note that the atmospheric and oceanic flows discussed earlier involve Re_λ values much larger than

either experiments or simulations can attain. Nevertheless, these studies, even at comparatively low Reynolds numbers, provide vital physical insight that can aid practical applications in the future. Thus, the primary goal of this thesis is to analyze and develop approaches that will enable accurate simulations at higher Reynolds and Schmidt numbers than are currently feasible. This will serve as a first step to enable future simulation studies for practical applications. We restrict our effort to investigating high Schmidt number transport involving passive scalars, which allows us to address a number of important issues necessary to attain the objectives of the thesis (outlined in Sec. 1.3), without being encumbered by the additional physical and numerical complications that accompany reacting scalars. It is hoped that the tools developed, and analytical and numerical examination presented, will serve as stepping-stones towards augmenting studies of reacting flow in the future.

1.2 Background

Passive scalar turbulence has attracted considerable research interest in the past, and comprehensive reviews are available on various aspects. Warhaft [134] and Shraiman et al. [117] provide a diverse and well-rounded survey of progress made in the previous century. A detailed examination of the statistical behavior of passive scalars in high-resolution simulations is undertaken by Watanabe & Gotoh [135]. Antonia & Orlandi [3] present a thorough review regarding Schmidt number effects on the transport process, albeit for restricted values of Reynolds numbers. We note that the term 'passive' in these works refers to the inability of the transported scalar to alter the flow velocity. Some typical examples of such scalars include: tracers used in fluid visualization; minor fluctuations in fluid temperature that, under carefully controlled conditions, are too weak to give rise to buoyancy effects; and moisture transport in air, which is a critical component of weather and climate simulations.

One of the curious properties of 'scalar turbulence' is that even though the passive scalar is supposedly under direct control of the velocity field, the statistical properties of scalar fluctuations behave somewhat independently of those of the turbulent velocity fluctuations [75, 117, 134]. For instance, in grid turbulence experiments, a -5/3 slope is evident in the scalar spectrum even at low Reynolds numbers, when no asymptotic slope may have developed in the velocity spectrum [119, 134].

This is a remarkable fact, given that the scalar transport equation itself is linear in nature, and is one of the many reasons why scalar turbulence has merited extensive attention from researchers.

1.2.1 Batchelor's theory

A survey of the literature reveals that the bulk of scalar transport studies focus almost exclusively on turbulent scalar transport with $Sc = O(1)$. The dominant cause of this scarcity of high Sc studies is the difficulty posed by the spatial resolution necessary to resolve the Batchelor scale (η_B). For $Sc \gg 1$, turbulent scalar fluctuations can persist at length scales much smaller than the Kolmogorov scale, η ($\eta = (\nu^3/\epsilon)^{1/4}$, where ϵ is the mean kinetic energy dissipation rate). The Kolmogorov scale is associated with the smallest dynamically important length scales; the majority of the turbulent kinetic energy cascading down from the large scales is dissipated by viscous effects at this length scale. Batchelor [13] deduced that the analogous length scale for scalars obeys the relation $\eta_B = \left(\mathcal{D}^2\nu/\epsilon\right)^{1/4} = \eta/\sqrt{Sc}$. By the time the turbulent cascade reaches this level η_B, the majority of the scalar variance (a term used interchangeably with 'scalar energy' throughout this thesis) is lost to molecular diffusion. As can be deduced from the dependence of η_B on Sc, the scalar material element shown in Fig. 1.1 tends to get stretched into progressively thinner 'filaments' with increasing Schmidt number, before molecular diffusion becomes sufficiently strong to take over.

Using arguments based on linear straining of scalar material elements, Batchelor predicted that at extremely high Schmidt numbers, there must exist an intermediate range of wavenumbers (κ), where the scalar spectrum exhibits a κ^{-1} scaling. This particular region of the spectrum is referred to as the 'viscous-convective subrange'. The fluid viscosity heavily influences scalar transport in this subrange, but the scalar diffusivity does not yet play an appreciable role. Figure 1.4 provides a lucid overview of the Schmidt number dependent classification of various subranges in the scalar variance spectrum.

Several attempts have been made to verify Batchelor's predicted κ^{-1} power law in the viscous-convective subrange, but experimental evidence of its validity remains scant [52, 71, 90, 89, 91]. Some early experiments claim to observe the existence of a κ^{-1} scaling law [54, 56], although for

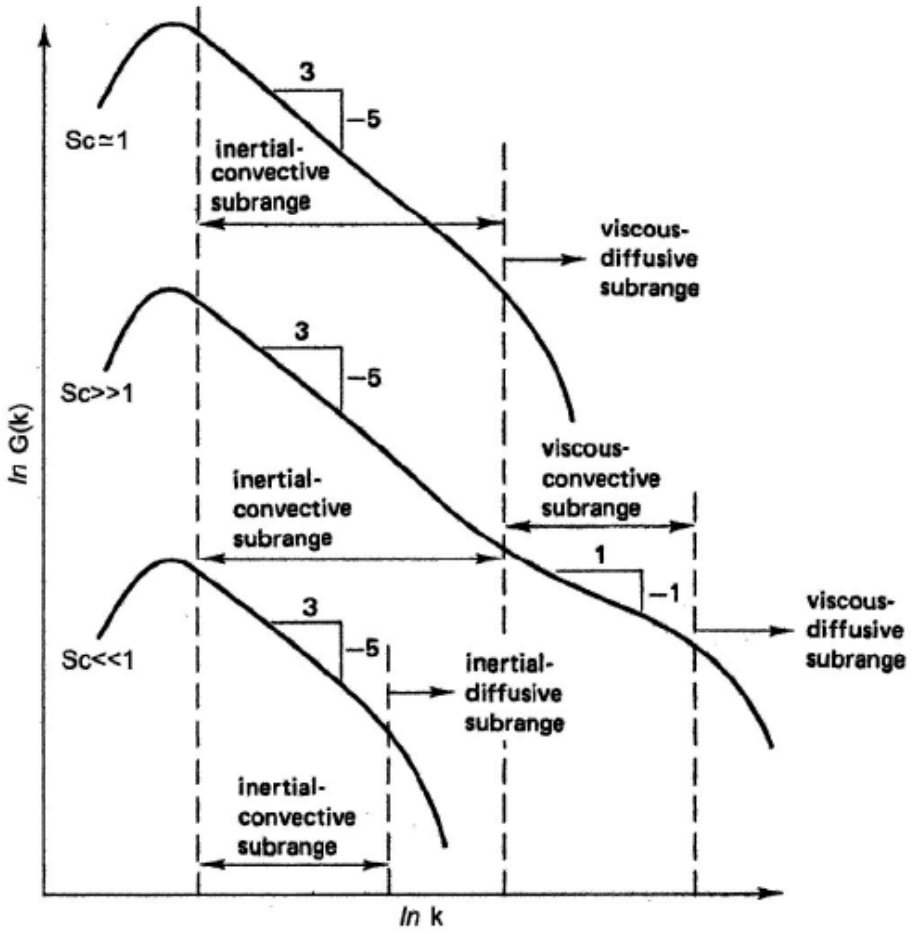

Figure 1.4: Various subranges depending on the Schmidt number. Figure adapted from Ref. [57]. $G(k)$ (also referred to as $E(\kappa)$ in this thesis) is the scalar variance spectrum, and k is the wavenumber.

temperature fluctuations in water with $Sc = O(10)$. Most simulations of homogeneous isotropic turbulence for $Sc \gg 1$, with an artificially imposed mean scalar gradient to act as a source of turbulent scalar fluctuations, support the power-law [68, 143, 26, 47]. To complicate matters further, Direct numerical simulations with unforced scalars, i.e., scalar fluctuations decaying naturally under the combined action of the velocity field and molecular diffusion, have failed to yield any semblance of a κ^{-1} scaling [3, 31]. There even exist theoretical objections to the κ^{-1} scaling, based on the requirement of boundedness of the scalar variance [44]. More specifically, it was shown that the scalar variance tends to diverge with a -1 power law as $Sc \to \infty$, which is inconsistent with the fact that the scalar being transported must obey physical bounds. The contradicting evidence suggests that reconciliation between experiments, simulations, and theory is difficult at present, and the validity of κ^{-1} scaling remains an open question [3]. In light of the prevailing dissonance, any extensive dependence on putative scaling laws has been avoided in the analyses presented and methodologies developed throughout this thesis.

1.2.2 Direct numerical simulation

The scale separation between η and η_B in high Sc flows can be several orders of magnitude, which is a major obstacle in both experimental and numerical work due to resolution limitations of experimental visualization hardware [91, 3], as well as processing power and memory constraints associated with computational hardware [114]. In spite of computational limitations, high resolution Direct numerical simulation (DNS) has proven to be an invaluable tool for studying the underlying physics of high Sc transport, albeit at relatively low Reynolds numbers. A vast majority of the relevant studies [144, 143, 142, 47] draw on concepts that can be traced back to Batchelor's seminal work [13]. In general, simulations provide a distinct advantage over experimental studies, on account of the complete flow history being available over the entire flow domain. This is useful for examining interactions between the small scale scalar and velocity fluctuations, for instance, by computing the scalar variance transfer spectrum. Scalar transfer-spectra [141, 139] explicitly depict energy exchange resulting from convective transport. Scrutinizing these scalar-velocity interactions can lead to better

parameterization of the small scale characteristics peculiar to high Schmidt number cases, which is essential for guiding development [127, 120, 134] of subfilter models for Large eddy simulations (LES). Calculating similar quantities from experiments is challenging, especially due to the need for detailed three-dimensional (3D) measurements.

Nevertheless, simulations suffer from being limited in scope to either very low Reynolds numbers, or relatively modest Schmidt numbers. This shortcoming is evident from Fig. 1.3, from which it is clear that simulations struggle to attain the $Re_\lambda - Sc$ combinations that experiments are capable of. For example, some of the best available combinations of Reynolds and Schmidt numbers used in Direct numerical simulations are $Re_\lambda = 8, Sc = 1024$ by Yeung et al. [143], and $Re_\lambda = 140, Sc = 64$ by Donzis et al. [47]. Experiments, on the other hand, routinely operate with $Re_\lambda = O(10^2)$ and $Sc = O(10^3)$. The reason for this disparity is the stringent requirement that the Batchelor scale imposes on grid resolution in simulations, which in turn is constrained by computational hardware capability, as mentioned earlier.

1.2.3 Large eddy simulation

While DNS is a useful research tool with immense value for scrutinizing scalar transport physics, it is not optimal for large scale practical applications, such as the scenarios described in Sec. 1.1. To achieve the Reynolds and Schmidt numbers relevant for such applications, it is necessary to resort to Large eddy simulation (LES), which alleviates the severe cost of DNS to a great extent. LES relies on applying a spatial filter on the various transport equations and as such does not resolve the smallest physical scales, which results in a significantly relaxed grid resolution requirement. The drawback of using LES though, is that the effect of the unresolved scales (i.e., the subfilter scales) on the resolved scales (or 'superfilter scales') dynamics must be modeled through an additional term in the Navier-Stokes/scalar transport equations. A variety of models are available in the literature for this purpose, namely, variants of the Smagorinsky model [118, 53, 83], the stretched vortex model [92, 110, 131], the similarity model [11, 12], and the tensor-diffusivity model [79, 35, 16]. Classical LES using these models generally entails filtering both the momentum and scalar transport equations. Thus, two

models are required to work in tandem, with the scalar model usually being inherently dependent on the quality of the velocity model. This introduces additional complications in modeling of scalar transport.

The formulation of accurate LES models relies heavily on results from theoretical analysis, and on observed, or hypothesized, behavior of the subfilter scalar-flux vector in filtered experimental or numerical simulation data. The mathematical term to be modeled is obtained by applying a homogeneous spatial filtering operation ($\widetilde{\cdot}$) to the passive scalar transport equation:

$$\frac{\partial \phi}{\partial t} + \nabla \cdot (\boldsymbol{u}\phi) \quad = \quad \mathcal{D}\nabla^2 \phi \tag{1.1}$$

which leads to:

$$\frac{\partial \widetilde{\phi}}{\partial t} + \nabla \cdot \left(\widetilde{\boldsymbol{u}}\widetilde{\phi}\right) \quad = \quad \mathcal{D}\nabla^2 \widetilde{\phi} - \nabla \cdot \boldsymbol{\tau}_\phi \tag{1.2}$$

$$\boldsymbol{\tau}_\phi \quad = \quad \widetilde{\boldsymbol{u}\phi} - \widetilde{\boldsymbol{u}}\widetilde{\phi} \tag{1.3}$$

Here, $\boldsymbol{\tau}_\phi$ is the subfilter scalar-flux (SFF) vector, and encapsulates the effects of non-linear interactions among the resolved and unresolved length scales. The filter-width associated with the filtering operation is generally represented by Δ, and the corresponding cutoff wavenumber for the filter is denoted κ_c ($\kappa_c = \pi/\Delta$). Information at wavenumbers larger than κ_c corresponds to 'subfilter' scales. Parameterization of these subfilter scales, with regard to their effect on the resolved scales (i.e., on Fourier modes with wavenumber magnitude smaller than κ_c), is one of the principal goals of modeling approaches used in Large eddy simulations. We make a distinction between subfilter scales and 'subgrid' scales (which is the more prevalent term used in the literature), depending on whether the simulation grid in a LES resolves physical scales smaller than the effective filter-width Δ. If $\Delta > \Delta x$ the physical scales being modeled will be referred to as 'subfilter' scales, whereas if $\Delta = \Delta x$, the term used will be 'subgrid' scales.

All of the facets involved in scrutinizing the SFF term, namely theoretical, numerical, and experimental means, present significant challenges at large Schmidt numbers. As a result, limited amount

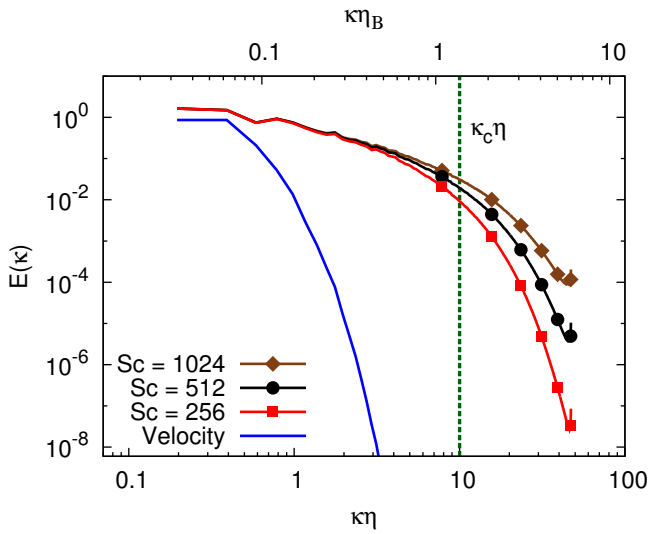

Figure 1.5: 3D spectra for velocity and three different scalars. Data taken from DNS by Yeung et al. [143]. $\kappa\eta_B$ axis shown is for Sc=256 ($\eta = 0.1958$).

of work relating to high Sc scalar transport has been conducted to date using LES. For instance, Calmet et al. [28, 29] and Magnaudet et al. [87] adapted the Dynamic Mixed Model proposed by Zang et al. [146], to investigate high Sc mass transfer through turbulent interfaces, by filtering at relatively low values of κ_c. We remark that the eddy-diffusivity approximation for the subfilter scalar-flux, which forms an integral part of the Dynamic Mixed Model, is known to suffer from excessive dissipation at the smallest resolved scales [9].

1.3 Velocity resolved - scalar modeled simulation

A promising framework to reduce the cost of numerical simulations for $Sc \gg 1$, and still retain most of the relevant non-linear interactions, is to place the LES filter-width in the viscous-convective subrange [26, 130]. The central idea is to exploit the wide scale separation between η_B and η, by using an LES-type filter of width Δ such that $\eta_B \ll \Delta \ll \eta$ ($\eta_B \ll \Delta$ being a desirable rather than a necessary condition, for minimizing simulation cost). One such filter placement, corresponding to the vertical line $\kappa_c\eta = 10$, is depicted in Fig. 1.5 which shows 3D energy spectra for velocity and high Sc passive scalars. Under these conditions, the velocity field is fully resolved and only the scalar field is modeled.

Outlining a framework to use this 'velocity resolved - scalar modeled' (VR-SM) approach for accurate simulation of high Schmidt number scalar transport is the main objective of this thesis. This approach provides a number of advantages over conventional LES where the filter-width is placed in the inertial subrange. For example: 1) we can focus on evaluating the capability of subfilter models to depict scalar transport accurately, without being concerned with possible detrimental impact from the quality of velocity models (which are necessary to use when modeling in the inertial subrange); 2) the grid size does not limit the Schmidt numbers that can be simulated, if the aim is to focus on large-scale behavior; and 3) results from VR-SM simulations can be used for model validation of 'true' LES (i.e., scalar modeling in the inertial subrange), when generating DNS datasets at the desired physical parameters (i.e., large Re_λ and Sc) becomes unfeasible. Given the promising outlook of this approach, we focus our attention in this thesis onto developing and testing VR-SM simulations for high Sc turbulent flows, using a multifaceted combination of physics, numerics, and modeling.

A few studies available in the literature that are similar in spirit to the VR-SM approach are discussed now. One such study by Burton [26, 25] used LES by placing the filter-width in the viscous-convective subrange for validating the performance of the 'non-linear LES' (n-LES) model in homogeneous turbulence, and in a round turbulent jet. The formulation of the n-LES model, unfortunately, depends on *a priori* knowledge of the scalar spectrum at the subfilter scales; several model coefficients assume a κ^{-1} scalar spectrum. As a result, the n-LES model is not very general, since it may not be able to recreate scenarios where a κ^{-1} power law is not observed, e.g., in high Sc simulations with decaying fluctuations [3, 31]. Other large scale numerical simulations of soot formation, growth, and transport in homogeneous isotropic turbulence [18], turbulent mixing layers, and in jets [7] have also made use of the scale separation between η and η_B. In these simulations, the numerical grid was selected such that the velocity field as well as all close-to-unity Schmidt number scalars were fully resolved. A fully Lagrangian scheme [5] was used in place of an Eulerian scheme for the number density of soot particles (high Schmidt scalar) to circumvent resolution issues. A tri-linear interpolation of the velocity field at the particle location was used to mimic the locally

constant velocity gradient at small scales predicted by Batchelor [13]. Analogous simulations were performed to analyze the evolution of an aerosol in turbulent mixing layers [147]. While offering a promising approach, the mathematical formalism behind these simulations was not laid out clearly and the effects of unresolved-subfilter scale physics was not addressed.

Most of the subfilter models mentioned in Sec. 1.2.3 were designed primarily for filtering in the inertial subrange, and remain largely untested in the viscous-convective subrange. This leaves a sizable knowledge gap in terms of expected performance of these models, when they are combined with filter-width placement in the viscous-convective subrange. Thus, one of the goals of this thesis is to establish the behavior of the subfilter scalar-flux term ($\boldsymbol{\tau}_\phi$) in this subrange, and to assess how well the aforementioned models perform in predicting expected transport behavior. As will be shown later, when filtering in the viscous-convective subrange, the magnitude of the SFF term is very small and is prone to becoming overwhelmed by numerical errors. Therefore, a second goal of this work is to ensure minimal detrimental impact of numerical discretization errors inherent in scalar transport schemes. The third and final goal is to evaluate the accuracy of the framework for velocity-resolved scalar modeled simulations in homogeneous isotropic turbulence, and to apply it in simulations of turbulent mixing layers. All of these separate pieces contribute in a combined manner to advancing currently available simulation capability, which can eventually help support full-scale simulations of atmospheric and oceanic studies in the future.

1.4 Outline of the thesis

We now provide a brief description of the structure of the thesis. Chapter 2 presents a thorough examination of non-linear scalar-velocity interactions relevant to the convective transfer of scalar variance in the viscous-convective subrange. The analysis is done specifically with regard to understanding the impact of filtering in this subrange, on the scalar transport process pertinent to Large eddy simulations. The results bring to light important realizations concerning the nature of non-linear interactions originating in the far-dissipation range [74, 32, 143] ($\kappa\eta \gg 1$). These results also highlight the need for improved numerical schemes for scalar transport.

In Chapter 3, we develop a novel semi-Lagrangian scheme, targeted specifically for turbulent transport of passive scalars. The scheme introduces an improved method of ensuring scalar boundedness which attains the critical goal of minimizing numerical dissipation inherent in the scheme. A variety of laminar and turbulent tests are used to assess performance gains that the new technique offers, over comparable algorithms available in the literature. High spatial accuracy, as well as the capability to take relatively large timesteps, result in *at least* an order of magnitude reduction in computational cost over Eulerian schemes of comparable accuracy. The cost effectiveness of the proposed algorithm, combined with the compact stencil it uses (which is conducive to fine-grain parallelism), make it especially suitable for use in massively parallel simulations.

In Chapter 4, we take a critical look at the behavior of the subfilter scalar-flux vector in the viscous-convective subrange. Specifically, the filter-width, filter-shape, and Schmidt number dependence of the subfilter flux vector orientation is examined, using the local strain-rate eigenvectors to define the appropriate reference frame. The analysis indicates that the orientation is largely independent of the filtered scalar field, and instead, is determined by velocity dependent quantities. This dependence is explained via detailed mathematical analysis of the tensor-diffusivity model [79, 35, 80, 16]. The results enable us to identify this model as a good representation of subfilter terms, when filtering in the viscous-convective subrange using either a box or Gaussian kernel.

Chapter 5 details *a posteriori* validation of the tensor-diffusivity model in high Sc velocity resolved - scalar filtered simulations of homogeneous isotropic turbulence. Comparison of VR-SM results with filtered DNS data in the homogeneous simulations suggests that the model is capable of producing extremely accurate results, when used in combination with explicit filtering. Filtering with extremely large filter-widths results in solution instability, which is addressed by limiting backscatter via model-regularization. Further examination of filtered DNS indicates that close to 95% of the total dissipation is accounted for up until $\kappa = 2\kappa_c$, which provides strong incentive to use grids with truncation wavenumbers no larger than $2\kappa_c$. As an added advantage, the presence of numerical diffusion in the scalar transport schemes used on such truncated grids does not have

a detrimental impact on the resolved scales. This is beneficial since increased numerical diffusion associated with coarse grids, if present in substantial amounts, would severely limit our capability to perform such simulations accurately with reasonable computational expense.

Finally, Chapter 6 discusses results from velocity resolved - scalar filtered simulations of a turbulent mixing layer, with the tensor-diffusivity model implemented as the subfilter term. Scalars differing in the Schmidt number by three orders of magnitude are transported simultaneously, and mixing characteristics are examined before and after entering the self-similar mixing regime. The regularized form of the model is used to avoid excessive breach of physical scalar bounds. The Schmidt number dependence of a variety of scalar statistics (namely, the scalar-variance, scalar autocorrelation functions, and 1D scalar-energy spectra) tends to saturate with increasing Sc, which is explained by the subfilter dissipation becoming increasingly dominant over molecular dissipation, thereby leading to identical behavior at very large Schmidt numbers. One limitation that manifests in the VR-SM approach is the inability to predict subfilter scalar quantities, which may be overcome by incorporating additional modeling for the subfilter quantities in the framework outlined.

Overall, simulations run with the numerical and modeling framework presented in this thesis ('current' simulations on Fig. 1.3) provide us with the opportunity to attain an overlap with experimental studies, while at the same time creating an assortment of baseline datasets for future validation of LES models that may benefit high Sc transport by filtering in the inertial subrange.

Chapter 2

On Filtering in the Viscous-Convective Subrange for Turbulent Mixing of High Schmidt Number Passive Scalars[1]

The work presented in this chapter is a first step towards establishing a more complete picture of scalar transport in the viscous-convective subrange. The consequence of filtering in the viscous-convective subrange and related discussion in terms of Batchelor's theory, are presented in Section 2.1. The behavior of the subfilter scalar-flux magnitude (computed by filtering DNS data) with regard to its dependence on the filter width, the Reynolds number, and the Schmidt number is discussed in Section 2.2. The limited range of influence of the subfilter terms on the superfilter scales, which can be attributed to the distinctive behavior of scalar spectral transfer in the viscous-convective subrange, is examined in Section 2.3. Finally, Section 2.4 presents direct comparison of velocity resolved - scalar modeled (VR-SM) runs, with no subfilter model implemented, to DNS data.

[1]The work in this chapter has been published in large part in Verma, S., Blanquart, G., On filtering in the viscous-convective sub-range for turbulent mixing of high Schmidt number passive scalars, Physics of Fluids (2013), doi:10.1063/1.4807061

2.1 Consequence of filtering in the viscous-convective subrange

2.1.1 Filtered transport equation

To observe the effect of filtering out the large wavenumbers, we start with the most general convection-diffusion equation, which is the conservation law governing the transport of a passive scalar. We use the symbol $\boldsymbol{u}$ to represent the velocity vector, and ϕ to represent any general passive scalar.

$$\frac{\partial \phi}{\partial t} + \nabla \cdot (\boldsymbol{u}\phi) \quad = \quad \mathcal{D}\nabla^2 \phi \tag{2.1}$$

This transport equation may be filtered using a homogeneous spatial filter (i.e., a filter that preserves a constant, obeys linearity, and commutes with derivatives) of any general type. The most commonly used filtering kernels are the Sharp-Spectral filter, the Gaussian filter, and the Box filter. We use variables with an overtilde $\widetilde{(\cdot)}$ to represent filtered quantities.

$$\frac{\partial \widetilde{\phi}}{\partial t} + \nabla \cdot \left(\widetilde{\boldsymbol{u}\phi}\right) \quad = \quad \mathcal{D}\nabla^2 \widetilde{\phi} \tag{2.2}$$

The main drawback of the filtering operation is that Eq. 2.2 does not contain the flux term $\nabla \cdot \left(\widetilde{\boldsymbol{u}}\widetilde{\phi}\right)$ that the passive scalar transport equations actually solve for. This leaves a residual term in the filtered equation, which is referred to as the subfilter scalar flux (SFF) term.

$$\frac{\partial \widetilde{\phi}}{\partial t} + \nabla \cdot \left(\widetilde{\boldsymbol{u}}\widetilde{\phi}\right) = \mathcal{D}\nabla^2 \widetilde{\phi} - \nabla \cdot \left(\widetilde{\boldsymbol{u}\phi} - \widetilde{\boldsymbol{u}}\widetilde{\phi}\right) \tag{2.3a}$$

$$SFF = \widetilde{\boldsymbol{u}\phi} - \widetilde{\boldsymbol{u}}\widetilde{\phi} \tag{2.3b}$$

An algebraic model (e.g., any variant of the Smagorinsky model [118, 53, 83], the stretched vortex model [92, 110, 131], the similarity model [11, 12], and the tensor-diffusivity model [79, 35, 16]) is often used to represent the SFF term shown in Eq. 2.3. The modeled scalar transport equation then

takes the following form:

$$\frac{\partial \bar{\phi}}{\partial t} + \nabla \cdot \left(\boldsymbol{u}\bar{\phi}\right) \quad = \quad \mathcal{D}\nabla^2 \bar{\phi} - \nabla \cdot \boldsymbol{\tau}_\phi \tag{2.4}$$

$\boldsymbol{\tau}_\phi$ here is the algebraic model that tries to emulate the SFF term, and it is expressed entirely in terms of the resolved quantities (i.e., $\boldsymbol{u}$ and $\bar{\phi}$). The distinction between $\bar{\phi}$ used in the equation above, and $\widetilde{\phi}$ used in Eq. 2.3 is that $\bar{\phi}$ represents the resolved scalar field obtained as the solution of the modeled equation (Eq. 2.4), whereas $\widetilde{\phi}$ represents the solution obtained by filtering a DNS dataset with a particular filtering kernel. The objective of the model term in Eq. 2.4 ($\boldsymbol{\tau}_\phi$) is to ensure that $\bar{\phi}$ resembles $\widetilde{\phi}$ as closely as possible. We clarify that if is a solution of the original scalar transport equation is desired instead (i.e., ϕ in Eq. 2.1), additional subfilter modeling may be required, which is out of the scope of the work presented in this thesis.

2.1.2 The SFF in the viscous-convective subrange

To assess the effect of filtering with a Sharp-Spectral filter, we write out the velocity in terms of its Fourier modes.

$$\boldsymbol{u}(\boldsymbol{x}) = \sum_{|\boldsymbol{\kappa}|=0}^{N/2} \widehat{\boldsymbol{u}}(\boldsymbol{\kappa}) e^{i\boldsymbol{\kappa}\cdot\boldsymbol{x}} \tag{2.5}$$

Given that the cutoff wavenumber κ_c is set to a sufficiently large value ($\kappa_c\eta \gg 1$), the subfilter velocity fluctuation amplitude (i.e., the subfilter velocity Fourier coefficients) can be approximated to be zero. This is in accordance with the extremely low kinetic energy content at high wavenumbers. Thus, the filtered velocity resembles very closely the unfiltered velocity ($\widetilde{\boldsymbol{u}} \approx \boldsymbol{u} : \forall\ \kappa_c\eta \gg 1$), and can be expressed as follows in terms of the Fourier modes

$$\boldsymbol{u}(\boldsymbol{x}) \quad \approx \quad \sum_{|\boldsymbol{\kappa}|\leq\kappa_c} \widehat{\boldsymbol{u}}(\boldsymbol{\kappa}) e^{i\boldsymbol{\kappa}\cdot\boldsymbol{x}} \tag{2.6}$$

We can further argue that since the majority of the kinetic energy is concentrated at the lower

wavenumbers, it can be assumed that the velocity field is spatially uniform, *within the filter width* (Fig. 2.1), for very high cutoff wavenumbers. The same argument does not apply to the scalar quantity ϕ or the flux $u\phi$ since the scalar spectrum may retain a considerable amount of energy at high wavenumbers (Fig. 1.5).

Using these assumptions, combined with the fact that we are using a homogeneous filter, the two terms in the SFF can be approximated as

$$\widetilde{\boldsymbol{u}\phi} \approx \boldsymbol{u}\widetilde{\phi} \quad \& \quad \widetilde{\boldsymbol{u}}\widetilde{\phi} \approx \boldsymbol{u}\widetilde{\phi} \tag{2.7}$$

which in turn leads to

$$SFF = \widetilde{\boldsymbol{u}\phi} - \widetilde{\boldsymbol{u}}\widetilde{\phi} \approx 0 \tag{2.8}$$

Eq. 2.8 is a simplification, and suggests that neglecting subfilter information would have limited adverse effect on superfilter scale dynamics, assuming that we place the filter cutoff κ_c at a sufficiently large wavenumber. The result in Eq. 2.8, although obtained independently, was pointed out earlier by Calmet and Magnaudet [28].

We remark that Eq. 2.8 is not identically zero, as can be confirmed by decomposing the velocity and scalar quantities into their filtered $\widetilde{(\cdot)}$ and subfilter $(\cdot')$ contributions:

$$\boldsymbol{u} = \widetilde{\boldsymbol{u}} + \boldsymbol{u}' \tag{2.9a}$$

$$\phi = \widetilde{\phi} + \phi', \tag{2.9b}$$

where $\boldsymbol{u}' = 0$ for $\kappa_c \eta \gg 1$. Using Eq. 2.9, we get:

$$\widetilde{\boldsymbol{u}\phi} = \widetilde{\widetilde{\boldsymbol{u}}\widetilde{\phi}} + \widetilde{\widetilde{\boldsymbol{u}}\phi'} \tag{2.10}$$

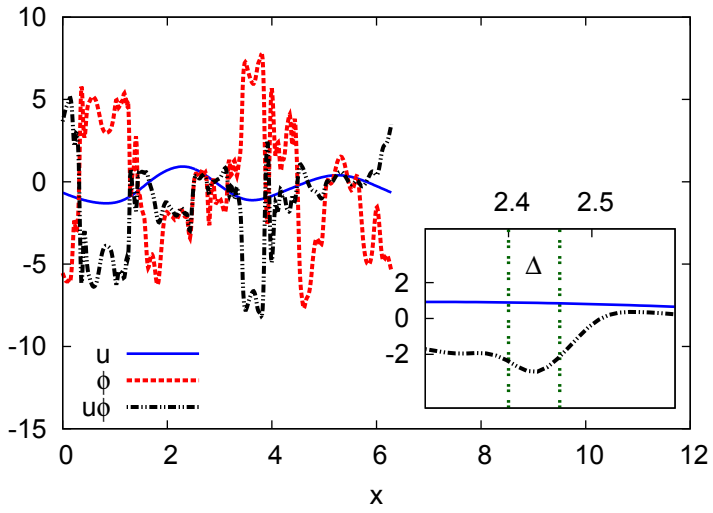

Figure 2.1: Plot of the velocity, scalar, and the scalar flux along a line across the DNS field for Case 5. Inset shows magnified view, with effective filter width Δ corresponding to $\kappa_c\eta = 10$.

Substituting this expression in the original definition of the SFF, we get multiple terms as follows:

$$SFF = \widetilde{\boldsymbol{u}\phi} - \widetilde{\boldsymbol{u}}\widetilde{\phi} \tag{2.11}$$

$$= \widetilde{\widetilde{\boldsymbol{u}}\widetilde{\phi}} + \widetilde{\widetilde{\boldsymbol{u}}\phi'} - \widetilde{\boldsymbol{u}}\widetilde{\phi} \tag{2.12}$$

which is not strictly zero, although the terms involved may be small. This will be confirmed by analyzing Joint Probability Density Functions (JPDFs) in Fig. 2.2 (Sec. 2.2.2), which indicate that the difference between $\widetilde{\boldsymbol{u}\phi}$ and $\widetilde{\boldsymbol{u}}\widetilde{\phi}$ becomes larger with increasing filter-width, even for $\kappa_c\eta > 1$.

2.1.3 Assumption of locally uniform velocity

The principal assumption made in Eq. 2.7 is that the velocity field can be treated to be uniform in space, with respect to the filtering operation. We plot in Fig. 2.1 a single component of the velocity vector and the corresponding scalar flux from one of the DNS datasets used for *a priori* analysis. The inset shows a magnified region of the plot along with the characteristic filter width ($\Delta = \pi/\kappa_c$) in physical space, corresponding to a filter cutoff wavenumber of $\kappa_c\eta = 10$. Within the confines of the filter width, the low wavenumber dominated velocity signal (u) appears to be virtually a flat line, whereas the flux signal ($u\phi$) retains considerable curvature. We can therefore justify treating

the velocity signal to be locally uniform in space, over the width of the filtering kernel, on condition that the cutoff wavenumber is sufficiently large (i.e., $\kappa_c\eta \gg 1$).

This view of locality is certainly not robust, since the Gaussian and Sharp-Spectral filtering kernels are non-local in physical space. However, the rapid attenuation of the filtering kernels in physical space, away from the filtering location makes this a reasonable assumption. The approximation used in Eq. 2.7 becomes more accurate at higher κ_c, owing to a decrease in the filter width Δ and the corresponding faster attenuation of the filtering kernels.

Although the assumption of a locally uniform velocity is useful for exploratory purposes, we note that in the derivation of the κ^{-1} scaling [13], Batchelor assumed that at sufficiently small scales, material 'blobs' of the scalar are acted upon by essentially constant strain rates ($\gamma \sim (\epsilon/\nu)^{1/2}$) that are inversely proportional to the Kolmogorov time scale ($\tau_\eta = (\nu/\epsilon)^{1/2}$). This suggests that the majority of the deformation of scalar blobs (which may be much smaller in size than the Kolmogorov length scale) is caused by linearly varying velocity fields associated with Kolmogorov sized eddies. With a filter width located in the viscous-convective subrange ($\kappa_c\eta \gg 1$), these Kolmogorov sized eddies, along with the accompanying constant straining motion, are fully resolved in the proposed VR-SM simulations.

2.2 *A priori* testing

The behavior of the SFF magnitude, in particular its dependence on the Reynolds and the Schmidt numbers, is analyzed by filtering DNS data obtained from homogeneous isotropic turbulent simulations ('baseline data'). The simulation parameters, along with the source of the data are listed in Table 2.1. The range of Re_λ used in the simulations was 8—140, and the range for Sc was 64—1024. In these simulations, it was necessary to restrict Re_λ to relatively low values for the largest Schmidt numbers used, since resolving the Batchelor scale at high Sc incurs considerable computational cost. Nonetheless, scalar scalar transport in the viscous-convective subrange is governed largely by the velocity scales in the dissipative range [13], which show universal behavior to some extent even at low Reynolds numbers [143]. The results of the analysis were found to be independent of the nu-

Table 2.1: Baseline DNS datasets used for *a priori* analysis. Data source: Cases 1, 2, and 6—present work with Finite Difference solver [41]; Cases 3, 4, and 5—Ref. [143]; Case 7—Ref. [47].

Case	N	Re_λ	Sc	ν	η	$\kappa_{max}\eta$	$\kappa_{max}\eta_B$
1	192	8	64	0.1590	0.1285	12	1.5
2	384	8	256	0.1590	0.1285	24	1.5
3	512	8	256	0.1590	0.1958	48	3
4	512	8	512	0.1590	0.1958	48	2.1
5	512	8	1024	0.1590	0.1958	48	1.5
6	512	30	64	0.0200	0.0460	12	1.5
7	2048	140	64	0.0028	0.0114	11	1.4

merical solver used to perform the simulation. The baseline datasets have been filtered using the Sharp-Spectral filter.

2.2.1 Filtering methodology

Since the SFF requires us to take the product of two terms, it is necessary to take additional precaution to ensure that aliasing from wavenumbers greater than κ_{max} does not impact the calculations. The SFF terms are dealiased in accordance with Orszag's 'two-thirds truncation rule' [100]. More specifically, the Fourier components corresponding to the upper third of the wavenumbers are discarded prior to performing any calculations. This operation is equivalent to filtering with the sharp spectral filter at a low-pass cutoff wavenumber of $\frac{2}{3}\kappa_{max}$. We shall refer to the resulting output as 'truncated data'. We clarify here that the aliasing error in question arises during the post-processing of the data, and is not associated with the DNS dataset itself. Eq. 2.13 shows a schematic presentation of the steps followed, with 'FFT' denoting the Fast Fourier Transform, and 'IFFT' denoting the Inverse Fast Fourier Transform. The terms with the overhat $\widehat{(\cdot)}$ represent Fourier coefficients, and the subscript 'd' indicates truncated data.

$$\begin{aligned} \boldsymbol{u} &\xrightarrow{FFT} \widehat{\boldsymbol{u}} \xrightarrow{Truncation} \widehat{\boldsymbol{u}}_d \xrightarrow{IFFT} \boldsymbol{u}_d \\ \phi &\xrightarrow{FFT} \widehat{\phi} \xrightarrow{Truncation} \widehat{\phi}_d \xrightarrow{IFFT} \phi_d \end{aligned} \tag{2.13}$$

To obtain the first term in the SFF ($\widetilde{\boldsymbol{u}\phi}$), the two truncated quantities are multiplied, followed

by the operations shown below

$$\boldsymbol{u}_d\phi_d \xrightarrow{FFT} \widehat{\boldsymbol{u}_d\phi_d} \xrightarrow{Filter} \widehat{\widetilde{\boldsymbol{u}_d\phi_d}} \xrightarrow{IFFT} \widetilde{\boldsymbol{u}_d\phi_d} \tag{2.14}$$

To obtain the second term in the SFF ($\widetilde{\boldsymbol{u}}\widetilde{\phi}$), the following operations are first performed on the truncated data

$$\begin{aligned} \boldsymbol{u}_d &\xrightarrow{FFT} \widehat{\boldsymbol{u}}_d \xrightarrow{Filter} \widehat{\widetilde{\boldsymbol{u}}}_d \xrightarrow{IFFT} \widetilde{\boldsymbol{u}}_d \\ \phi_d &\xrightarrow{FFT} \widehat{\phi}_d \xrightarrow{Filter} \widehat{\widetilde{\phi}}_d \xrightarrow{IFFT} \widetilde{\phi}_d \end{aligned} \tag{2.15}$$

and then the filtered quantities are multiplied to get $\widetilde{\boldsymbol{u}}_d\widetilde{\phi}_d$. From this point forward, we shall drop the subscript 'd' for convenience, and assume that truncated and dealiased data is used, unless otherwise stated.

2.2.2 Qualitative analysis

To observe the degree of correlation between $\widetilde{\boldsymbol{u}\phi}$ and $\widetilde{\boldsymbol{u}}\widetilde{\phi}$, Fig. 2.2 shows Joint Probability Density Functions (*JPDF*) computed using various filter cutoffs, with the corresponding color map shown to the right of each frame. The homogeneous isotropic turbulence data used corresponds to baseline Case 5 in Table 2.1, at $Re_\lambda = 30$ and $Sc = 256$. Any scatter in the direction perpendicular to the 45-degree diagonal is indicative of the differences introduced by filtering, between $\widetilde{\boldsymbol{u}\phi}$ and $\widetilde{\boldsymbol{u}}\widetilde{\phi}$, which should be accounted for by subfilter models.

Fig. 2.2(a) with $\kappa_c\eta = 33 = \frac{2}{3}\kappa_{max}\eta$ serves as the baseline case, since dealiasing reduces the largest wavenumber available in the data. We can clearly identify that $\widetilde{\boldsymbol{u}\phi}$ and $\widetilde{\boldsymbol{u}}\widetilde{\phi}$ are identical in this case, based on the perfect correlation between the two quantities. Fig. 2.2 suggests that the relative differences between $\widetilde{\boldsymbol{u}\phi}$ and $\widetilde{\boldsymbol{u}}\widetilde{\phi}$ increase as $\kappa_c\eta$ is moved to lower values, since a wider JPDF is indicative of increasing disparity between the two terms. Nevertheless, the shape of the joint PDF remains fundamentally the same throughout the viscous-convective subrange (Figs. 2.2(b) and 2.2(c)) and the increase in the width is relatively modest. In the limit when $\kappa_c\eta = 1$, the JPDF

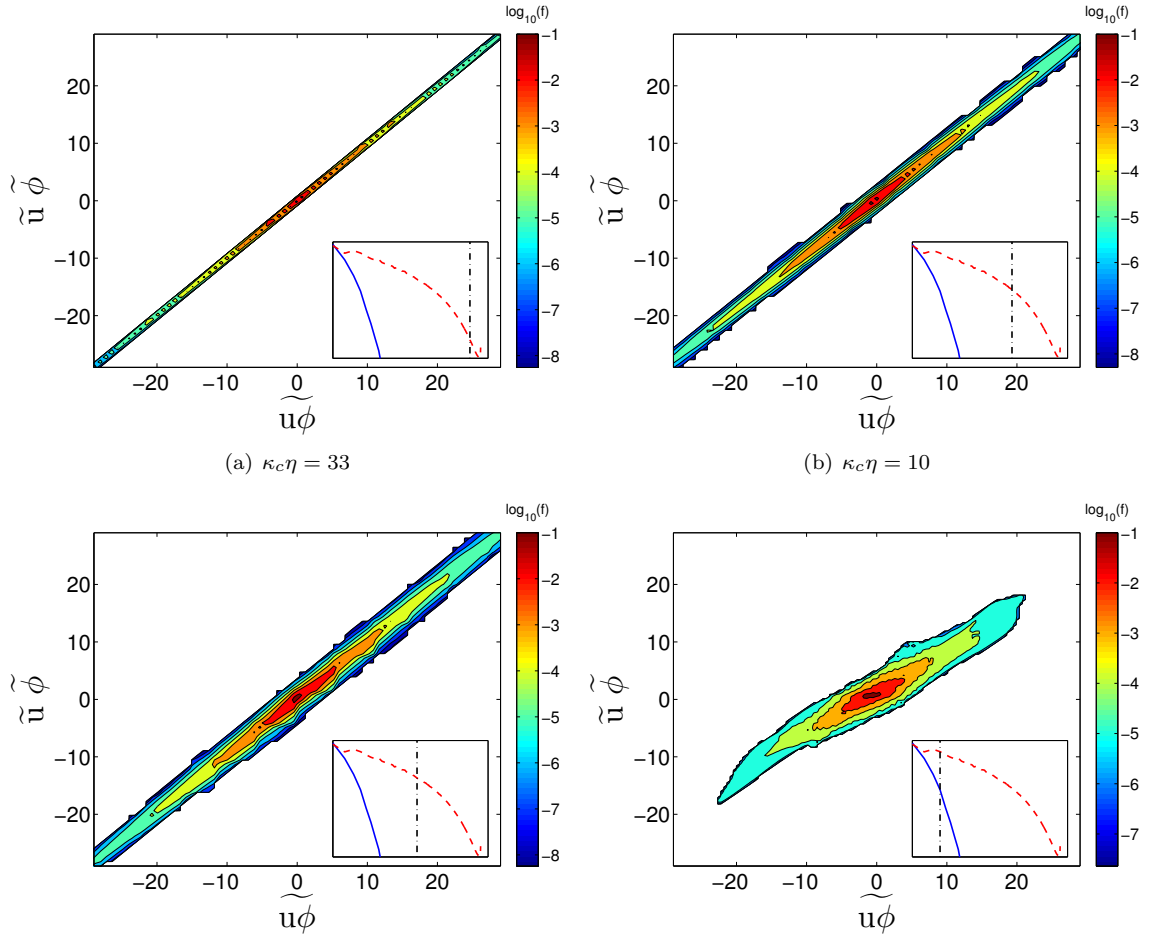

(a) $\kappa_c\eta = 33$

(b) $\kappa_c\eta = 10$

(c) $\kappa_c\eta = 6$

(d) $\kappa_c\eta = 1$

Figure 2.2: Joint Probability Density Function for the two terms in the SFF at various sharp filter cutoff wavenumbers. Whitespace indicates absence of data points. The inset figures show the corresponding location of the cutoff with respect to the velocity and scalar spectra. Data taken from baseline Case 5 (Table 2.1). Only the y and z components of the scalar flux have been used (Appendix A).

no longer adheres to the 45-degrees diagonal, which suggests that the magnitude of the subfilter term is substantial.

2.2.3 Magnitude of the SFF term

Following the qualitative analysis in the previous subsection, we now analyze quantitatively the effects of filter width, Reynolds number, and Schmidt number on the magnitude of the SFF term.

2.2.3.1 Definitions

Using the symbol $SFF_{i,j,k}$ to represent the calculated value of the SFF at a particular grid location ($i, j, k \, \epsilon \, [1, N]$, where N is the number of grid points in each direction), Eq. 1.3 gives:

$$SFF_{i,j,k} \quad = \quad \widetilde{\boldsymbol{u}\phi}_{i,j,k} - \widetilde{\boldsymbol{u}}_{i,j,k}\widetilde{\phi}_{i,j,k} \tag{2.16}$$

Then, the L_2 norm ($|SFF|$) can be written as

$$|SFF| \quad = \quad \left(\frac{1}{N^3} \sum_{i,j,k=1}^{N} \left(SFF_{i,j,k}\right)^2 \right)^{\frac{1}{2}} \tag{2.17}$$

Normalizing this L_2 norm using the standard deviations for the truncated velocity (σ_u) and scalar (σ_ϕ) fields, we arrive at a suitable definition for the non-dimensional relative magnitude 'm'

$$m = \frac{|SFF|}{\sigma_u \cdot \sigma_\phi} \tag{2.18}$$

Given that the SFF defined in Eq. 2.16 is a vector quantity, we calculate m as follows

$$m = \frac{1}{\sigma_\phi \sqrt{2}} \cdot \sqrt{\left(\frac{|SFF|_v}{\sigma_v} \right)^2 + \left(\frac{|SFF|_w}{\sigma_w} \right)^2}, \tag{2.19}$$

where σ_v and σ_w are standard deviations of the v and w components of the velocity, respectively. The u component of the SFF has been excluded in this definition, since the flux component in the

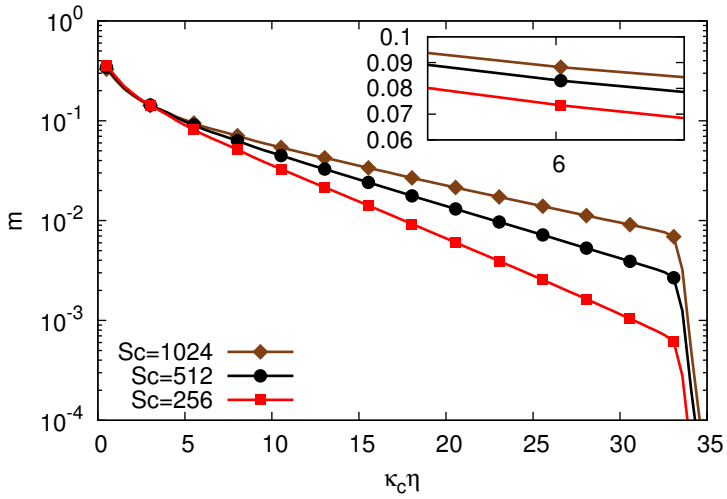

Figure 2.3: Relative magnitude *vs.* sharp filter cutoff wavenumber. Data taken from baseline Cases 3, 4, and 5, averaged over 4 stationary snapshots (t/τ_{eddy}= 5.7, 10, 11.6, and 13.8).

direction of the imposed mean scalar gradient differs systematically from the other two components (Appendix A).

2.2.3.2 Dependence on $\kappa_c\eta$ and Sc

Figure 2.3 shows the variation of m with $\kappa_c\eta$ when a Sharp-Spectral filter was used for filtering the baseline datasets. We can identify two regions of distinct behavior with respect to $\kappa_c\eta$. For $\kappa_c\eta < 3$, the magnitude grows very rapidly with decreasing κ_c, and is independent of the Schmidt number. This distinctive change in SFF behavior happens since we are neglecting useful velocity information close to the Kolmogorov length scale. As was discussed in Section 2.1.3, these velocity modes play a crucial role during scalar transport even in the viscous-convective subrange. The non-ideal shape of the joint PDF shown in Fig. 2.2(d) is consistent with these results, however, we must be mindful of the fact that few Fourier modes remain for the case shown at $\kappa_c\eta = 1$.

For $\kappa_c\eta > 5$, we observe a slower, exponential drop in relative magnitude of the SFF term with the selected cutoff wavenumber. The decay rate in this region is dependent on the Schmidt number; higher Schmidt numbers result in a smaller slope. This behavior is expected since, for the same $\kappa_c\eta$, we ignore a larger proportion of the useful information available at higher Schmidt numbers. We can infer this from Fig. 1.5, where the spectrum for a smaller Schmidt number scalar decays faster

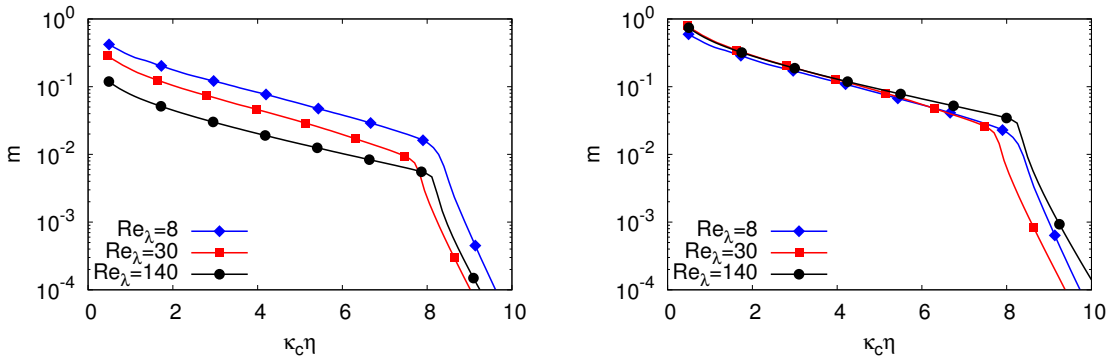

(a) m as defined in Eq. 2.19

(b) Rescaled m as defined in Eq. 2.20.

Figure 2.4: Comparison of m *vs.* $\kappa_c\eta$ plots for Sc=64 and three different Reynolds numbers. Baseline Cases 1, 6, and 7.

than that for a larger Schmidt number scalar.

An important trend to note from Fig. 2.3, is that the magnitude increase, quantifiable by the vertical shift of the SFF magnitude curve, slows down with increasing Schmidt number. For instance, at approximately $\kappa_c\eta = 6$, the relative magnitude increases by 1% going from Sc=256 to Sc=512, but only by another 0.5% when going from Sc=512 to Sc=1024. One would thus hope that the SFF magnitude curve tends towards an asymptotic shape at very high Schmidt numbers, thereby making the computed magnitude of the SFF term independent of the Schmidt number for $Sc \gg 1$.

Finally, the rapid decrease in the SFF magnitude for filtering beyond $\kappa_c\eta = 33$, which is the value for $\kappa_{max}\eta$ after dealiasing for the case shown, serves as a check for the *a priori* analysis. Filtering beyond the dealiasing limit merely removes noise from the data and the two terms that constitute the SFF are now exactly equal.

2.2.3.3 Dependence on Re_λ

To determine the effect of changing the Reynolds number, we compare the normalized magnitude of the SFF term in Fig. 2.4 at a fixed Schmidt number ($Sc = 64$) and at three different Reynolds numbers. With the current normalization of the magnitude of the SFF term introduced in Eq. 2.19, the results are dependent on the Reynolds number; a higher Reynolds number results in lower magnitude. However, when the definition of m is altered to rescale with the Kolmogorov velocity

scale ($u_\eta \sim (\epsilon\eta)^{(1/3)}$) instead of σ_u, the curves collapse almost perfectly (Fig. 2.4(b)).

$$m = \frac{1}{u_\eta \sigma_\phi \sqrt{2}} \cdot \sqrt{|SFF|_v^{\,2} + |SFF|_w^{\,2}} \tag{2.20}$$

This collapse is not unexpected and confirms that it is indeed the small velocity scales that are important for determining m. Furthermore, we can conclude from the collapse that the magnitude of the SFF, when appropriately normalized, behaves independently of the Reynolds number for high Schmidt number mixing. We stress that the observations made in this section are specific to the homogeneous isotropic turbulent cases tested. Extension to more general cases would require additional testing, for instance by analyzing DNS datasets of high Sc turbulent mixing layers, before a definitive conclusion can be reached.

2.3 Scalar energy transfer

Filtering the scalar transport equation alters the transfer of scalar energy from the large scales to the small scales. This transfer is fundamentally different in the viscous-convective subrange when compared to the inertial subrange. Inspecting the transfer spectrum can provide insight into how triadic interactions among velocity and scalar modes in certain wavenumber ranges influence transport at all other wavenumbers. This is central in understanding the role of the SFF term in the viscous-convective subrange.

2.3.1 The scalar transfer spectrum

The relevant term corresponding to spectral transfer in the scalar energy equation is obtained by first taking the Fourier transform of the transport equation. This is followed by multiplication with the conjugate of the scalar Fourier coefficient ($\widehat{\phi}^*(\boldsymbol{\kappa})$). Finally, the scalar transfer spectrum $T(k)$ is

computed by averaging the convective term over spherical wave-shells:

$$\begin{aligned} T(\kappa) &= \left\langle -2Re\left(\widehat{\phi}^*(\boldsymbol{\kappa})\ \widehat{\boldsymbol{u}\cdot\nabla\phi}(\boldsymbol{\kappa})\right)\right\rangle \\ &= \left\langle 2\boldsymbol{\kappa}\cdot Im\left(\widehat{\phi}^*(\boldsymbol{\kappa})\int_{\boldsymbol{\kappa}=\boldsymbol{p}+\boldsymbol{q}}\widehat{\boldsymbol{u}}(\boldsymbol{p})\widehat{\phi}(\boldsymbol{q})d\boldsymbol{p}\right)\right\rangle \end{aligned} \tag{2.21}$$

The averaging operation is denoted by angled brackets. All products involved are dealiased as discussed in Section 2.2.1. The expression obtained involves triadic interactions between scalar and velocity modes ($\widehat{\boldsymbol{u}}$ and $\widehat{\phi}$, respectively) which contribute to the scalar flux mode ($\widehat{\boldsymbol{u}\cdot\nabla\phi}$) associated with wavenumber vector $\boldsymbol{\kappa}$. We would like to point out that during scalar transport, each velocity mode (wavenumber vector $\boldsymbol{p}$) interacts with each scalar mode (wavenumber vector $\boldsymbol{q}$), and the resultant corresponds to a new mode with wavenumber vector $\boldsymbol{p}+\boldsymbol{q}=\boldsymbol{\kappa}$. Analytically, these vectors span all possible combinations such that components of $\boldsymbol{p}$, $\boldsymbol{q}$, $\boldsymbol{\kappa}$ lie in the range $[-\infty,\infty]$. However, they are restricted to the range $[-N/2, N/2]$ in the discretized simulations.

It is instructive to decompose the transfer spectrum $T(\kappa)$ into contributions from various velocity ($V(\kappa|p)$) and scalar ($S(\kappa|q)$) modes [141, 139] as follows:

$$V(\kappa|p_A) = \left\langle 2\boldsymbol{\kappa}\cdot Im\left(\widehat{\phi}^*(\boldsymbol{\kappa})\int_{|\boldsymbol{p}|\epsilon A}\widehat{\boldsymbol{u}}(\boldsymbol{p})\widehat{\phi}(\boldsymbol{\kappa}-\boldsymbol{p})d\boldsymbol{p}\right)\right\rangle \tag{2.22}$$

$$S(\kappa|q_A) = \left\langle 2\boldsymbol{\kappa}\cdot Im\left(\widehat{\phi}^*(\boldsymbol{\kappa})\int_{|\boldsymbol{q}|\epsilon A}\widehat{\boldsymbol{u}}(\boldsymbol{\kappa}-\boldsymbol{q})\widehat{\phi}(\boldsymbol{q})d\boldsymbol{q}\right)\right\rangle \tag{2.23}$$

'A' in these equations represents all wavenumbers contained within a bandpass filtered region of interest. The decomposed contributions, $V(\kappa|p)$ and $S(\kappa|q)$, must sum up individually to give back the transfer spectrum.

$$T(\kappa) = \sum_p V(\kappa|p) = \sum_q S(\kappa|q) \tag{2.24}$$

$V(\kappa|p)$ and $S(\kappa|q)$ are plotted in Fig. 2.5 and 2.6, respectively, using logarithmically spaced ranges

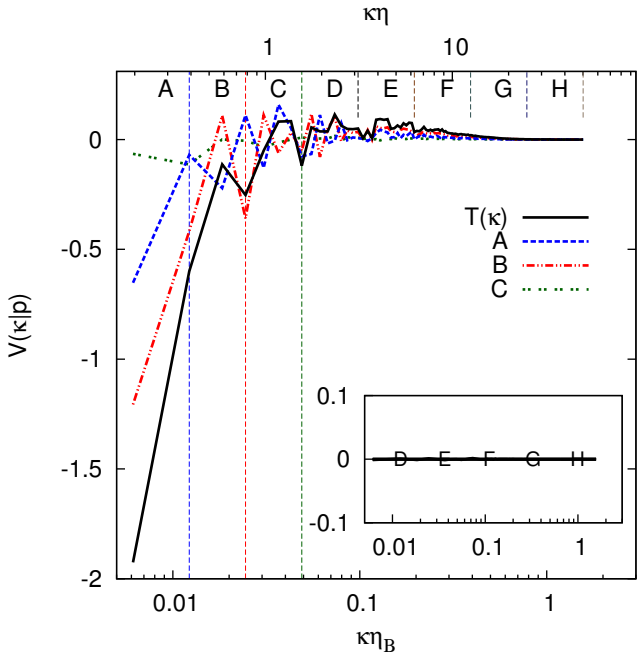

Figure 2.5: Contribution of velocity modes $V(\kappa|p)$ (lines A through H) to the scalar transfer spectrum $T(\kappa)$ (Eq. 2.22). Inset shows velocity modes for wavenumber ranges D and higher.

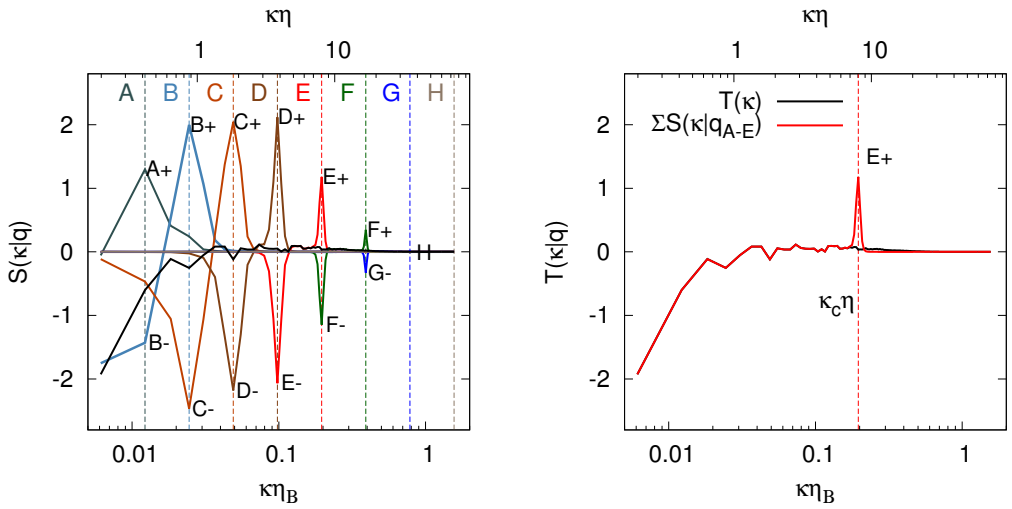

(a) Decomposition of $T(\kappa)$ (solid black line) into $S(\kappa|q)$.

(b) Comparison of full transfer spectrum $T(\kappa)$, and that obtained after filtering scalar modes beyond $\kappa_c\eta \approx 6$.

Figure 2.6: Contribution of scalar modes $S(\kappa|q)$ to the scalar transfer spectrum $T(\kappa)$ (Eq. 2.23). $S(\kappa|q)$ from wavenumber ranges A through E are summed up in (b) to emulate the effect of filtering with a Sharp-Spectral filter (at $\kappa_c\eta \approx 6$).

for the contributing modes. The data shown was taken from baseline Case 5 (Table 2.1), averaged over 4 statistically stationary snapshots. Bandpass filtering of the pertinent variables was done using the sharp-spectral filter. Figure 2.5 indicates that velocity contributions from higher wavenumber ranges (regions D and above) are almost zero, and hence play virtually no part in the spectral transfer of scalar energy. We note that Fig. 2.5 has been discussed previously in Ref. [139], but is adapted for the current work in the context of studying filtering pertinent to LES.

We now take a closer look at the scalar mode contributions in Fig. 2.6(a). We observe that for scalar modes belonging to higher wavenumber ranges (e.g., regions D and above), the effective triadic interactions become extremely local, having a noticeable effect only on the immediately neighboring ranges. To be more specific, scalar modes belonging to lower wavenumber ranges contribute to transfer in non-neighboring ranges (for instance, scalar modes in range C affect transfer in ranges A, B, C, and D). However, scalar modes in range E affect transfer only in the immediately neighboring ranges (D, E, and F).

This locality of triadic interactions is not surprising, and is solely related to the faster decay of the velocity spectrum compared to the scalar spectrum (Fig. 1.5); it is not a consequence of bandpass filtering. For the sake of simplicity, let us assume that the velocity Fourier coefficients beyond $\kappa\eta = 2$ are exactly zero. Assuming $\widehat{\boldsymbol{u}}(\boldsymbol{\kappa}) = 0$ for $|\boldsymbol{\kappa}\eta| > 2$ helps us simplify the convolution integral in Eq. 2.21, which now reads

$$T(\kappa) = \left\langle 2\boldsymbol{\kappa} \cdot Im \left(\widehat{\phi}^*(\boldsymbol{\kappa}) \int_{|\boldsymbol{p}|<\frac{2}{\eta}} \widehat{\boldsymbol{u}}(\boldsymbol{p}) \widehat{\phi}(\boldsymbol{\kappa}-\boldsymbol{p}) d\boldsymbol{p} \right) \right\rangle \tag{2.25}$$

The only difference between Eqs. 2.21 and 2.25 is that the velocity modes are now restricted to those with non-zero amplitudes. Equation 2.25 communicates that among all mathematically possible triadic interactions between velocity and scalar modes, it is only the interactions within a relatively narrow band around $|\boldsymbol{\kappa}|$ (in this case, $\kappa \pm 2/\eta$) that result in a non-zero contribution to the transfer term at this wavenumber ($\boldsymbol{\kappa}$). This is depicted schematically in Fig. 2.7, and is a direct result of the large scale separation between η and η_B. The locality of the triadic interactions is indeed valid

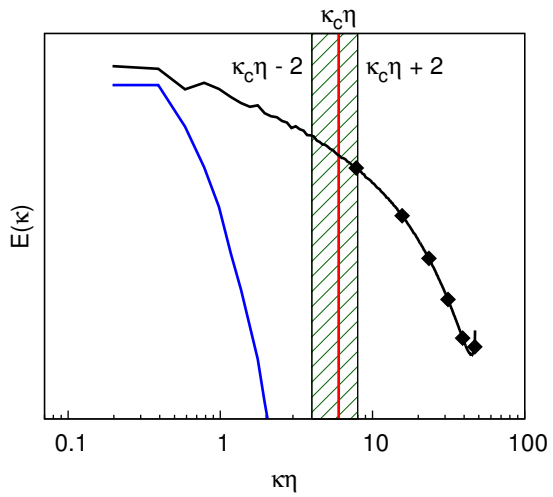

Figure 2.7: Locality of triadic interactions for high Schmidt number cases (as discussed in Eq. 2.25). The hatched region corresponds to all non-zero contributions from scalar-velocity triadic interactions to the transfer term at wavenumber κ_c.

only at high Schmidt numbers and in the viscous-convective subrange, as may be confirmed by the non-local behavior of decomposed transfer spectra ($S(\kappa|q)$) for low Schmidt number scalars [141].

2.3.2 Effect of filtering on spectral transfer

We now utilize the local nature of triadic interactions to analyze the cascade of scalar energy down to successively higher wavenumbers, and how it relates to filtering in the viscous-convective subrange. Scalar modes belonging to a particular wavenumber range, for instance, E (Fig. 2.6(a)), extract energy from the range to the immediate left (spike E$-$), and deposit energy at the end of the range in question (spike E+). At large wavenumbers, this deposition is balanced almost exactly by the extraction of energy by scalar modes belonging to the wavenumber range on the immediate right (spike F$-$). We clarify that this extraction is not analogous to molecular dissipation at the small scales (an assumption used in the Smagorinsky model [118]), and instead, is related to the convective (and not diffusive) 'turbulent cascade' responsible for breaking down large length scales into successively smaller ones. The near-perfect balance of energy transfer among neighboring wavenumber ranges indicates that triadic interactions originating from high wavenumber scalar modes cannot impact *directly* the transfer at intermediate (i.e., non-neighboring) wavenumbers.

Filtering the data with a low pass filter may still have an *indirect* effect on the scalar transfer

spectrum. For demonstration purposes, we suppose that the low-pass filter cutoff is placed at the boundary of regions E and F. The resulting transfer spectrum after filtering, shown in Fig. 2.6(b), is obtained by summing the scalar mode contributions from wavenumber ranges A through E. The excellent agreement between the full and filtered spectra at low and intermediate wavenumbers yet again emphasizes the minimal influence of high wavenumber modes. However, we note that there is no longer a cancellation of the E+ spike from an F− spike, since the F modes have been filtered out. The E+ spike, if left unchecked, can lead to a pile-up of scalar energy at the large wavenumbers. This could have an indirect effect on the scalar transfer, especially when using scalar energy conserving transport schemes. The high wavenumber modes involved in this pile-up cannot be represented on a given grid and are incorrectly represented at lower wavenumbers. Aliasing of this sort contaminates the energy content of the resolved Fourier modes in the simulation. These observations lead to the realization that the primary role of a subfilter model, when used with filtering in the viscous-convective subrange, is primarily to facilitate the dissipation of the equivalent of an E+ spike close to the cutoff wavenumber. Interaction of the subfilter model with low wavenumber scalar modes, for facilitating scalar transfer directly at the large length scales, is not essential for $Sc \gg 1$.

As a side note, we mention that the pile-up of energy discussed in this Section is often observed in scalar spectra obtained using spectral transport schemes. The pile-up manifests as an up-turned peak at the end of the spectrum (e.g., Fig. 1.5), since any spatial discretization removes higher wavenumber modes which would otherwise have led to energy cascading down to even smaller scales.

2.4 VR-SM simulations

We now discuss results from VR-SM runs of homogeneous isotropic turbulence, with no subfilter model implemented. The goal of these simulations is to analyze the impact of possible discretization errors on the scalar energy spectrum. The simulation parameters used for these VR-SM runs are listed in Table 2.2. The velocity field for the VR-SM runs, as well as for baseline Cases 1, 2, and 6, was forced spectrally by injecting energy in a low wavenumber shell [2]. The scalar was maintained statistically stationary using an imposed uniform mean scalar gradient (Eq. A.2 with

Table 2.2: VR-SM simulation parameters

Case	N	Re_λ	Sc	ν	η	$\kappa_c\eta$	$\kappa_c\eta_B$
A	128	8	1024	0.159	0.1290	8	0.250
B	256	8	1024	0.159	0.1283	16	0.500
C	512	48	1024	0.010	0.0272	7	0.218

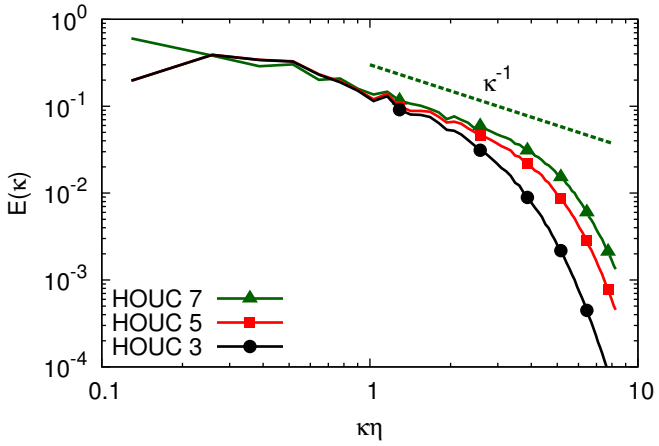

Figure 2.8: Scalar spectra comparison for Case A (VR-SM: Table 2.2) run with 3 different upwind convective schemes.

$G = 1$). High-Order Upwind Convective (HOUC) schemes [99, 41] were used for solving the scalar transport equation. A brief description of the implementation of these scalar transport schemes is provided in Appendix D.

Figure 2.8 shows results from simulations run with increasing order of scheme accuracy, namely HOUC 3, 5, and 7. These curves clearly indicate that numerical diffusion has a measurable impact on the results; higher-order schemes, characterized by lower artificial numerical diffusivity, exhibit higher energy content at large wavenumbers. The scalar energy spectrum in the viscous-convective subrange bears some semblance to a κ^{-1} scaling, especially for HOUC 7. It is important to note that the simulations are stable, even when high-order upwinded schemes (fifth- and seventh-order, as used in our VR-SM simulations) with supposedly low numerical diffusion are used. Thus, the numerical diffusion inherent in these schemes is sufficient to damp out the positive spike in the filtered transfer spectrum (akin to the E+ spike shown in Fig. 2.6(b)). This suggests that when using non-energy-conserving scalar schemes with $Sc \gg 1$, the numerical errors can remain larger than the magnitude of the SFF term.

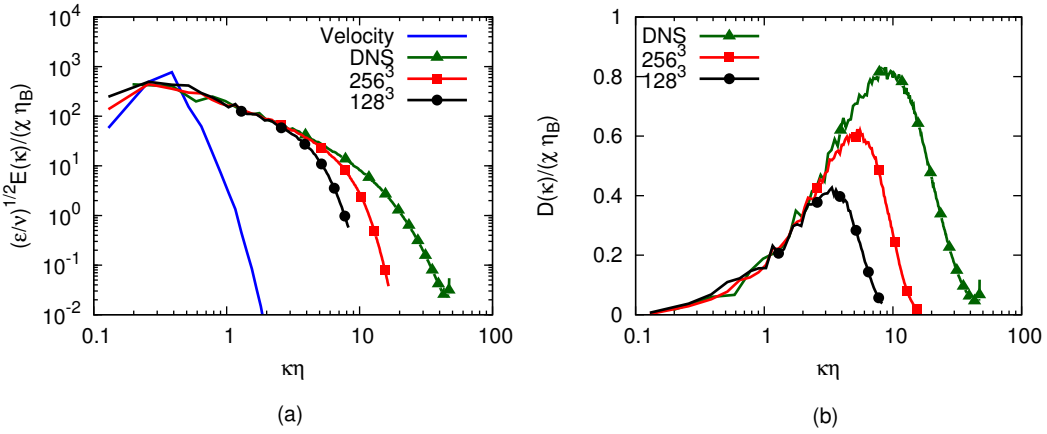

Figure 2.9: Scalar spectra comparison for Cases A, B (VR-SM: Table 2.2), and baseline Case 5 (DNS: Table 2.1). The mean scalar dissipation rate (χ) used for the filtered runs was estimated from an unfiltered run using the finite difference solver.

We now compare scalar spectra from VR-SM simulations, performed using the fifth-order HOUC scheme without an SFF term, to results obtained from the corresponding baseline DNS dataset. Figures 2.9(a) and 2.9(b) show the energy spectra and energy dissipation spectra ($D(\kappa) = \mathcal{D}\kappa^2 E(\kappa)$) of the filtered scalar fields for different filter cutoffs. We observe that, even for the coarsest grid simulation ($\kappa_c\eta = 8, N = 128$), the spectra shapes match the baseline data at the small wavenumbers (i.e., the large physical scales) quite well up to $\kappa\eta = 3$. This may be related to our observation in Sec. 2.3.1, regarding the limited role of subfilter terms in directly facilitating scalar transfer at the low wavenumbers. Nevertheless, differences in the dissipation spectra become more noticeable at higher wavenumbers, owing to an increased influence of numerical dissipation at the smallest length scales. A non-diffusive scalar transport scheme would show better agreement with the DNS result at large wavenumbers, but might require energy damping at the highest wavenumbers, as noted previously.

2.5 Summary

In this chapter, we have examined the dependence of the subfilter scalar-flux magnitude ($|SFF|$) on the filter-width (or equivalently, the filter cutoff wavenumber), the Schmidt number (Sc), and

the Reynolds number (Re_λ) in data obtained from direct numerical simulations. The results suggest that beyond a certain threshold cutoff ($\kappa_c\eta > 5$), there is an exponential drop in the $|SFF|$ with increasing κ_c. The $|SFF|$ curves were seen to vary systematically with the Schmidt number, however, appropriate rescaling led to a collapse of $|SFF|$ curves at different Reynolds numbers. This observation could be especially useful in anticipating $|SFF|$ behavior at very large Reynolds numbers, since moderate Re_λ DNS datasets (which can be used for extrapolating behavior at much larger Re_λ) can be generated with reasonable cost on currently available computational hardware. The concept of utilizing low Reynolds number data for model validation, and future application to high Reynolds number flows, is discussed in Chapter 5.

To understand the exact role of subfilter Fourier modes in the convective transfer of scalar variance, we have analyzed scalar-velocity triadic interactions in the viscous-convective subrange, by explicitly filtering DNS data. The results observed suggest that scalar modes originating in the far dissipation range ($\kappa\eta \gg 1$) have a limited range of influence on convective scalar transfer. The reason for this apparent decoupling is explained using mathematical arguments based on the observation that the velocity energy spectrum decays much faster than the energy spectrum of a high Schmidt number scalar. Filtered transfer spectra exhibit a distinctive pile-up of energy close to the cutoff wavenumber, which may be explained by a lack of energy extraction by smaller scales. Thus, simulations that do not resolve the physically dissipating scales (e.g., Large eddy simulations) require some form of energy damping to avoid solution instability caused by this pile-up. This damping is usually provided by appropriate subfilter models.

Finally, we note that velocity resolved - scalar modeled simulations of high Schmidt number scalar transport in homogeneous isotropic turbulence, run with no subfilter model implemented, gave rise to stable solutions. Discretization errors inherent in the scalar transport schemes used were large enough to damp out any possible energy pile-up. The results suggest that implementing a SFF model may not be justified, unless the numerical errors are controlled to be sufficiently smaller than the SFF magnitude. This provides strong incentive to explore the development of more effective numerical schemes, which is the subject of Chapter 3.

Chapter 3

An Improved Bounded Semi-Lagrangian Scheme for the Turbulent Transport of Passive Scalars[1]

The objective of this Chapter is to develop an improved scalar transport scheme, referred to as the Bounded Cubic Hermite polynomial (BCH) scheme, with the primary goal of achieving increased accuracy of turbulent simulations at lower computational cost than currently available schemes. The proposed scheme is based on the semi-Lagrangian treatment of the advection-diffusion equation [121], and uses a novel bounding algorithm designed specifically for cubic Hermite polynomials. Performance evaluation of certain existing semi-Lagrangian schemes [111, 17, 123] that make an effort to maintain scalar boundedness is also included, to assess the improvement that the proposed scheme offers.

Section 3.1 provides a brief overview of numerical methods, and the challenges encountered in scalar transport. The basic workings of semi-Lagrangian schemes are discussed in Section 3.2. The formulation of the proposed bounding algorithm is presented in Section 3.3. Section 3.4 presents an in-depth analysis of gain and phase error characteristics of the original cubic Hermite polynomial, for uniform one-dimensional (1D) advection of a passive scalar. Section 3.5 provides configuration

[1]The work in this chapter has been published in large part in Verma, S., Xuan, Y., Blanquart, G., Journal of Computational Physics (2014), doi:10.1016/j.jcp.2014.03.062

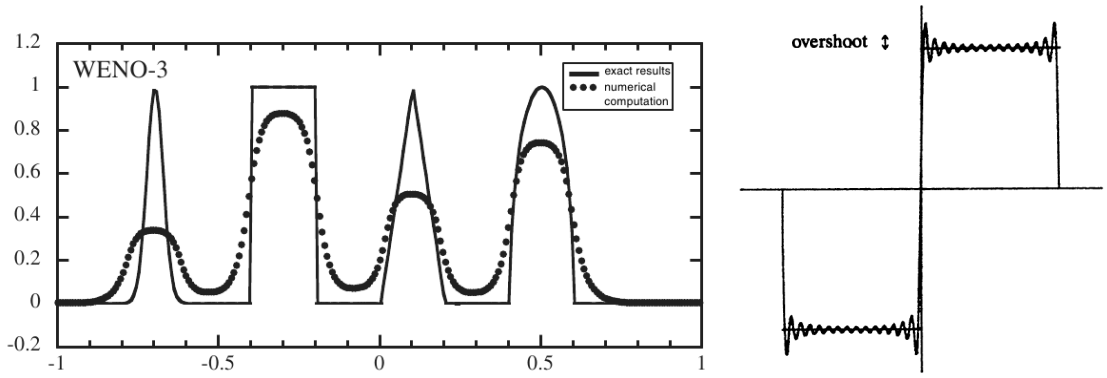

(a) Figure taken from Ref. [60]

(b) Figure taken from Ref. [50]

Figure 3.1: Figure showing (a) numerical diffusion inherent in FV/FD schemes for 1D uniform convection of a scalar profile; and (b) numerical oscillations in a square-wave discretized with a Fourier series.

description of the numerical tests used, which include three laminar cases and two turbulent cases. One of the turbulent test cases is used to assess numerical performance in comparison to spectral schemes, when working with large timesteps unconstrained by CFL number. Section 3.5 also involves discussion of scheme performance with regard to desirable scheme properties, in addition to comparison with several other commonly used Eulerian and semi-Lagrangian schemes.

3.1 Numerical methods: Background

Most numerical techniques employed for studying turbulent flows fall into two broad classifications, namely the Finite-volume (FV) or Finite-difference (FD) formulations, and pseudo-spectral methods. Each class offers a distinct set of advantages and drawbacks. For instance, when using FV/FD-based numerical transport schemes, numerical diffusion is known to be a pivotal issue of concern [82], since it can easily overwhelm the minuscule molecular diffusion associated with high Sc flows. The dissipative nature of these schemes is evident even in relatively simple flow configurations (Fig. 3.1(a)). Pseudo-spectral schemes [113, 63] offer some respite in this regard, but suffer from problems of their own. These schemes are notorious for the severity with which Gibbs phenomenon causes over/undershoots close to sharp gradients [50] (which are especially prevalent in high Sc flows), thereby raising the issue of breaching physical scalar bounds (Fig. 3.1(b)).

In general, spectral schemes are not as cost effective as FV/FD schemes in massively parallel implementations [55], given the need to take global transposes when computing discrete Fourier transforms. Additionally, even though spectral schemes find widespread use in academic studies of turbulence in simplified configurations, they are not particularly suited for turbulent simulations in complicated geometries, which may well be used for simulation-based optimization of machinery in the future. FV/FD schemes are much more versatile in this respect, and allow for efficient and fast parallel implementation when designed well, in addition to providing effective means of controlling unphysical over/undershoots. Given the flexibility that FV/FD schemes offer over pseudo-spectral formulations, we focus our discussion on issues specific to FV/FD schemes in the rest of the thesis.

As already discussed, turbulent transport of scalars is especially susceptible to numerical errors, and imposes stringent grid resolution requirements [144, 143, 47]. Thus, the need for high accuracy at small scales presents considerable challenges when using FV/FD schemes for practical simulations of important turbulent phenomena. Numerical performance of these transport schemes can be gauged by analyzing the following scheme properties:

- Boundedness
- Low numerical diffusion
- High accuracy
- Conservation

Of the four properties listed, scalar boundedness is a crucial property that must be respected when required by physical constraints. Almost all transported scalars, both passive and active, have physical bounds that must be maintained during transport. Violating boundedness in certain cases can lead to severe detrimental effects. Some examples include irreversible spurious precipitation in weather simulations [136], and the appearance of negative absolute temperature and unphysical species mass fractions (i.e., outside the bounds $[0, 1]$) in reacting flows.

Due to the critical nature of scalar boundedness in such simulations, there has been significant effort in the past to construct bounded finite-volume (e.g., WENO3 [85], MPWENO5 [10], OSMP7 [38],

BQUICK [60]) schemes based on the Eulerian treatment [82] of the scalar transport equation. Unfortunately, these transport schemes exhibit significant numerical diffusion, which leads to a decrease in simulation accuracy. Higher-order schemes coupled with a Flux Corrected Transport (FCT) algorithm [20, 145] can mitigate the issue of numerical diffusion. However, the resulting increase in accuracy comes at a significant increase in computational cost, owing to the need for a larger computational stencil. The use of high-order finite-volume schemes is also accompanied with increasingly restrictive stability criteria (i.e., a smaller limiting Courant- Friedrichs-Lewy (CFL) number) [121], which leads to further increase in computational cost. In addition, high-order schemes give rise to larger and more frequent oscillations (Runge's phenomenon), which makes ensuring boundedness difficult.

As an alternative to Eulerian schemes, semi-Lagrangian (SL) schemes are known to be stable at large CFL values, but suffer from the inability to conserve mass inherently [121]. This may not be an issue of major concern in certain scenarios [136]. The ability of SL schemes to maintain stability for CFL>1 makes them especially suitable for applications involving long integration times. This has led to widespread adoption of SL schemes in the atmospheric community, and a vast body of work exists in the literature [121, 136, 111, 17, 123, 140, 107, 78, 138]. An exhaustive review in this regard can be found in Ref. [121]. In addition to decreased restriction on timestep size, SL schemes can yield enhanced spatial accuracy, which makes them suitable for use in interface tracking in multiphase flows [140], and for turbulent simulations. Given the various advantageous attributes associated with semi-Lagrangian schemes, our goal in this Chapter is to develop an algorithm that is singularly suited for turbulent transport of passive scalars, while retaining the capability of preserving physical scalar bounds when necessary.

3.2 Semi-Lagrangian schemes

This section provides a brief outline of the numerical implementation of semi-Lagrangian schemes. Readers interested in the proposed bounding algorithm may proceed directly to Section 3.3.

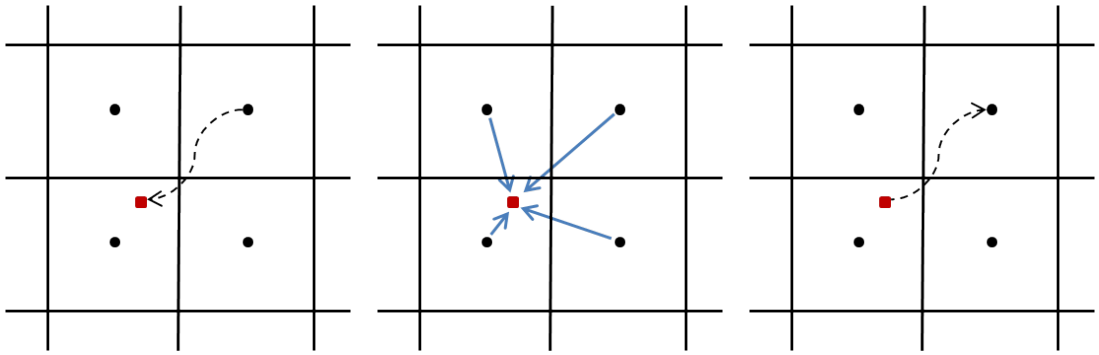

(a) Traceback (b) Interpolate (c) Advect to node

Figure 3.2: Basic steps involved in semi-Lagrangian transport. Location $\boldsymbol{x}^n$ in Eq. 3.4 corresponds to the red square shown.

3.2.1 Numerical implementation

The transport of passive scalars is governed by the advection-diffusion equation

$$\frac{D\phi}{Dt} = \frac{\partial \phi}{\partial t} + \boldsymbol{u} \cdot \nabla \phi \quad = \quad \mathcal{D} \nabla^2 \phi \tag{3.1}$$

where the transported scalar quantity is denoted by 'ϕ', $\mathcal{D}$ is the molecular diffusivity, and the $\frac{D}{Dt}$ operator represents the material derivative. All numerical tests used in this Chapter assume the incompressibility condition ($\nabla \cdot \boldsymbol{u} = 0$). To solve the discretized form of Eq. 3.1, we employ a fractional step method (Godunov splitting [82]), whereby the solution procedure is split into two steps: pure advection followed by diffusion. Using the superscript (*) to signify an intermediate solution associated with the advection step only, we get

$$\frac{D\phi^\star}{Dt} \quad = \quad 0 \tag{3.2}$$

Equation 3.2 implies that under pure advection, the scalar value associated with a Lagrangian particle remains unchanged. In the absence of source terms, and for non-negative molecular diffusivity, this prohibits the formation of new maxima and minima, as pointed out by Williamson & Rasch [136].

The advection step denoted by Eq. 3.2 is accomplished in semi-Lagrangian schemes via a sequence of three steps: traceback, interpolation, and advection to node (Fig. 3.2). Semi-Lagrangian schemes

are different from Eulerian and Lagrangian schemes in that they combine particle tracking (as done in Lagrangian schemes) with a static computational grid (generally used with Eulerian schemes). Tracking scalar particles in a fully Lagrangian fashion is not very efficient computationally, especially when using parallelized algorithms. The semi-Lagrangian framework adopts a workable compromise by employing a fixed grid, and tracking particles associated with the grid nodes.

The scalar value at any grid node 'i' is updated by first tracking the relevant material particle backward in time (Fig. 3.2(a)). Once this location, $\boldsymbol{x}^n$, has been determined, the scalar value at that location ($\phi_i^\star = \phi^n(\boldsymbol{x}^n)$) is computed using a suitable interpolation procedure (Fig. 3.2(b)). This intermediate scalar value is then assigned 'as-is' to the grid node in accordance with Eq. 3.2 (Fig. 3.2(c)). At this point, the advection step is complete. The diffusion term (as well as any other source terms present) may be accounted for as follows

$$\phi^{n+1} = \phi^\star + \Delta t \left(\mathcal{D}\nabla^2\phi^\star\right) \tag{3.3}$$

to obtain the final value ϕ_i^{n+1}. We now discuss each of the three basic steps of semi-Lagrangian transport in detail.

3.2.2 Traceback

For the traceback step depicted in Fig. 3.2(a), we track the location of a material particle that coincides with a grid node at time t^{n+1}, to its location $\boldsymbol{x}^n$ at the previous timestep t^n

$$\boldsymbol{x}^n = \boldsymbol{x}^{n+1} - \int_n^{n+1} \boldsymbol{u}\left(\boldsymbol{x}(t), t\right) dt \tag{3.4}$$

This step is equivalent to the computation of curved characteristic lines emanating from the grid nodes. An appropriate numerical integrator must be used for solving Eq. 3.4 since the velocity field $\boldsymbol{u}$ can vary temporally as well as spatially. For the current work, a second-order Runge-Kutta (RK2) integrator was used. Intermediate velocity values were computed using linear interpolation of cell face velocity components. We point out that the traceback step is completely independent of the

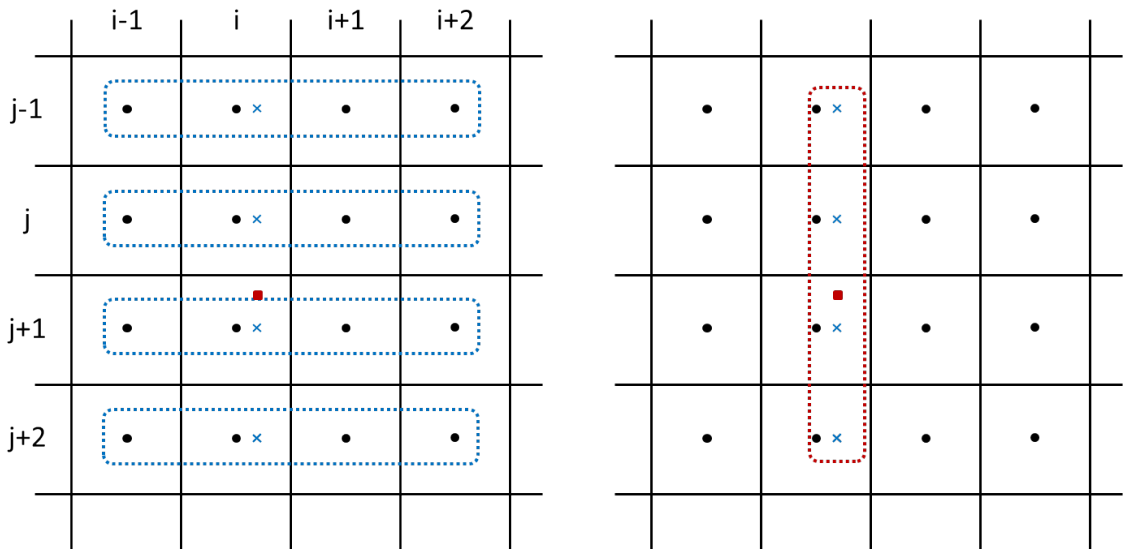

(a) Step 1–4 interpolations in x (b) Step 2–1 interpolation in y

Figure 3.3: Dimensional splitting to decompose 2D interpolation into a cascade of 1D interpolations.

passive scalar being transported. Thus, the $\boldsymbol{x}^n$ values need to be computed just once per timestep, even if transporting several distinct scalars simultaneously.

3.2.3 Interpolation

The interpolating polynomial used for the step shown in Fig. 3.2(b), along with any boundedness preserving corrections, forms the core of any semi-Lagrangian transport scheme. For comparison purposes, we will discuss three interpolation procedures, namely, the proposed Bounded Cubic Hermite polynomial (BCH), the fully Monotonic Cubic Hermite polynomial (MCH) [111], and a bounded cubic Lagrange polynomial (SL3) [17, 123]. 3D interpolation in all cases is done via a successive 'cascade' of 1D interpolations, based on the 'tensor product' approach [136]. Interpolation in this manner is much more efficient computationally when compared to constructing interpolating surfaces. The cascading procedure is illustrated for a 2D case in Fig. 3.3. One of the directions, for instance x, is selected for the first set of 1D interpolations. The scalar is interpolated at the locations marked by the blue '×'s for each of the four rows $j-1$ through $j+2$ (Fig. 3.3(a)). The second step uses these four interpolated values ($\phi_{\times_{j-1}}, \phi_{\times_j}, \phi_{\times_{j+1}}$, and $\phi_{\times_{j+2}}$) to compute $\phi_i^\star$ (Fig. 3.3(b)) by interpolating in the orthogonal direction (y).

One known issue of interpolating with polynomials of order greater than 1 is that these give rise to spurious oscillations (Godunov's theorem). Large over/undershoots are present close to sharp gradients due to the inability of the limited resolution grid to resolve high wavenumber modes (Gibbs phenomenon). This can be especially problematic in simulations that involve abrupt transitions or rapid fluctuations in the scalar field, for instance, at fuel-oxidizer interfaces in non-premixed combustion, and with passive transport of low-diffusivity scalars. The oscillations may cause the transported scalar to breach appropriate bounds, resulting in unphysical simulation data. High-order scalar-transport schemes must, therefore, encompass some means of detecting and correcting these unphysical oscillations. Details of such correction mechanisms in the bounded 1D interpolation algorithms for both SL3 and BCH are given in Section 3.3.

3.2.4 Incorporating the diffusive fluxes and other source terms

The algorithm discussed up until now accounts for just the advection step of Godunov splitting, i.e., determining $\phi^\star$ (Fig. 3.2(c)). The diffusive fluxes, in addition to any source or sink terms in the material transport equation (Eq. 3.1), are incorporated into the final update of the scalar value using Eq. 3.3. Although the diffusive term is implemented in a fully explicit fashion in this work, it is possible to use implicit formulations of Eq. 3.3 involving ϕ^{n+1}.

In the current implementation, a second-order-accurate finite-difference formula is used for the discretization of the Laplacian operator (∇^2) in Eq. 3.3. A fourth-order-accurate discretization was ruled out since it gave rise to unphysical oscillations close to velocity stagnation points and in regions with sharp scalar gradients. To maintain second-order accuracy on non-uniform grids, the discrete operator is implemented as a combination of the divergence operator acting on a gradient operator $\left(\nabla^2\phi = \nabla\cdot(\nabla\phi)\right)$.

$$\left(\nabla\phi_{i+\frac{1}{2}}\right)_x = \frac{\phi_{i+1}-\phi_i}{x_{i+1}-x_i} \tag{3.5}$$

$$\left(\nabla^2\phi_i\right)_x = \frac{\left(\nabla\phi_{i+\frac{1}{2}}\right)_x - \left(\nabla\phi_{i-\frac{1}{2}}\right)_x}{x_{i+\frac{1}{2}} - x_{i-\frac{1}{2}}} \tag{3.6}$$

$$\nabla^2\phi = (\nabla^2\phi_i)_x + (\nabla^2\phi_i)_y + (\nabla^2\phi_i)_z \tag{3.7}$$

Equation 3.6 reduces to the more familiar form $(\nabla^2\phi_i)_x = \dfrac{\phi_{i+1} - 2\phi_i + \phi_{i-1}}{\Delta x^2}$ when working with uniform grids. Incorporation of the source terms, as outlined here, completes the scalar transport step for semi-Lagrangian schemes.

3.3 Bounded interpolating polynomials

3.3.1 Bounded Cubic Hermite (BCH) polynomial

The BCH scheme makes use of Hermite polynomials, which differ from Lagrange polynomials in that they require knowledge of scalar derivatives (ϕ'_i, ϕ'_{i+1}) in addition to scalar values (ϕ_i, ϕ_{i+1}) at the interpolating nodes. The use of derivatives as constraints results in an enhanced ability to resolve sub-cell shape [136, 140], which in turn leads to a marked increase in interpolation accuracy. In the current formulation, scalar derivatives are computed using second-order central difference (CD2), which is equivalent to the 'arithmetic mean' derivative estimation mentioned in Ref. [111]. The appropriate interpolation coefficients are given below, using Fig. 3.3 as reference for the spatial indices. Subscript '$i+\frac{1}{2}$' indicates the cell face located in the middle of node locations 'i' and '$i+1$'.

$$w_i = 1 - 3\left(\frac{x_\times - x_i}{\Delta x}\right)^2 + 2\left(\frac{x_\times - x_i}{\Delta x}\right)^3 \tag{3.8}$$

$$w_{i+1} = 1 - w_i \tag{3.9}$$

$$w'_i = (x_\times - x_i)\left(1 - 2\frac{x_\times - x_i}{\Delta x} + \left(\frac{x_\times - x_i}{\Delta x}\right)^2\right) \tag{3.10}$$

$$w'_{i+1} = \frac{(x_\times - x_i)^2}{\Delta x}\left(-1 + \frac{x_\times - x_i}{\Delta x}\right) \tag{3.11}$$

$$\phi'_i = \frac{\phi_i - \phi_{i-1}}{x_i - x_{i-1}} \cdot \frac{x_{i+\frac{1}{2}} - x_i}{x_{i+\frac{1}{2}} - x_{i-\frac{1}{2}}} + \frac{\phi_{i+1} - \phi_i}{x_{i+1} - x_i} \cdot \frac{x_i - x_{i-\frac{1}{2}}}{x_{i+\frac{1}{2}} - x_{i-\frac{1}{2}}} \tag{3.12}$$

$$\phi'_{i+1} = \frac{\phi_{i+1} - \phi_i}{x_{i+1} - x_i} \cdot \frac{x_{i+\frac{3}{2}} - x_{i+1}}{x_{i+\frac{3}{2}} - x_{i+\frac{1}{2}}} + \frac{\phi_{i+2} - \phi_{i+1}}{x_{i+2} - x_{i+1}} \cdot \frac{x_{i+1} - x_{i+\frac{1}{2}}}{x_{i+\frac{3}{2}} - x_{i+\frac{1}{2}}} \tag{3.13}$$

$$\phi_\times = \phi_i \cdot w_i + \phi_{i+1} \cdot w_{i+1} + \phi'_i \cdot w'_i + \phi'_{i+1} \cdot w'_{i+1} \tag{3.14}$$

For uniform grids, the derivatives reduce to the familiar CD2 form $\phi'_i = \frac{\phi_{i+1} - \phi_{i-1}}{2\Delta x}$.

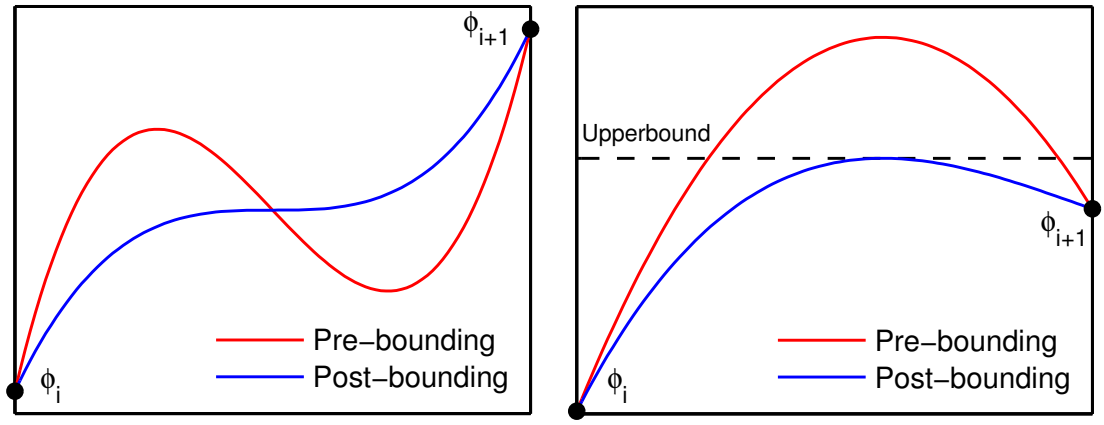

(a) Two sub-cell extrema

(b) Single sub-cell extremum

Figure 3.4: Initial and final profiles for bounding in (a) Case 1; (b) Case 2.

Boundedness (a term which we take to mean that the interpolated scalar value respects physical bounds, as opposed to requiring strict sub-cell *monotonicity*) is enforced in all of the cascading 1D interpolations by modifying the scalar derivatives at the interpolating nodes (ϕ'_i and ϕ'_{i+1}). For certain configurations (e.g., the laminar and turbulent simulations discussed in Secs. 3.5.3 and 3.5.4), the physical bounds are known with certainty, and lower and upper bounds can be specified accordingly. However, for other simulations, the concept of physical scalar bounds may not be applicable (e.g., the homogeneous isotropic turbulent simulations discussed in Sec. 3.5.5), in which case the bounding operation associated with the single-extremum cases (described below) is limited to the advection step, to prevent the generation of spurious mathematical extrema.

The cubic polynomial can give rise to two distinct scenarios, depending on the sign of the interpolating derivatives. Either a single extremum, or two extrema may exist within the interpolating cell (Fig. 3.4), and each case is treated differently as explained below.

Case 1: Two sub-cell extrema

If the two interpolating derivatives have the same sign ($\phi'_i\ \phi'_{i+1} > 0$), there may exist two sub-cell extrema in between nodes i and $i+1$ (Fig. 3.4(a)). The high wavenumber modes involved in this case cannot be resolved by the computational grid (Nyquist criterion), and their existence is caused

by the presence of artificial numerical oscillations. It could be argued that having scalar derivatives available in addition to scalar values makes it acceptable to accommodate multiple extrema in the interpolation. While true for an analytical interpolation profile, this argument is not valid if the multiple extrema in question occur within a single sub-cell of a discretized interpolation profile. Such a scenario would require that high wavenumber Fourier modes be represented on a grid that is incapable of resolving them. We reiterate that the derivatives are estimated from the scalar field itself, and any new high wavenumber modes generated can be attributed to the numerical approximation used, which in this case is CD2. As an alternative illustration, we consider that when using spectral schemes it is feasible to compute a large number of high order derivatives, to the extent allowed by the grid resolution. But the availability of these derivatives does not allow for the existence of more than a single extremum inside one cell, in accordance with the Nyquist criterion.

To avoid the formation of two extrema, the interpolating cubic polynomial is forced to be monotone in this case, irrespective of whether or not the interpolated value breaches physical bounds. To enforce monotonicity in the cubic Hermite polynomial, we use a derivative limiting procedure that is well-documented in the literature [39, 51, 64]. Constructing a monotonic cubic interpolant requires that both ϕ'_i and ϕ'_{i+1} have the same sign as the limiting derivative, ϕ'_{limit}, and be smaller in magnitude than the same.

$$\phi'_{limit} = 3\frac{(\phi_{i+1} - \phi_i)}{\Delta x} \tag{3.15}$$

The interpolating derivatives are modified to enforce compliance with these conditions using a 'minmod' limiter, so as to minimize the change engendered.

$$\phi'_i = \mathbf{minmod}\left(\phi'_i, \phi'_{limit}\right) \tag{3.16}$$

$$\phi'_{i+1} = \mathbf{minmod}\left(\phi'_{i+1}, \phi'_{limit}\right) \tag{3.17}$$

The minmod limiter is defined conventionally as follows [128, 112]

$$\textbf{minmod}\,(a,b) = \begin{cases} \textbf{sign}(a)\cdot\textbf{min}(\textbf{abs}(a,b)) & \text{if} \quad ab > 0 \\ \\ 0 & \text{if} \quad ab < 0 \end{cases} \tag{3.18}$$

The interpolation profiles before and after enforcing monotonicity for the case of two sub-cell extrema are shown in Fig. 3.4(a).

Case 2: Single sub-cell extremum

In case the two interpolating derivatives have opposite signs, there exists a single extremum in between nodes i and $i+1$ (Fig. 3.4(b)). Allowing sub-cell extrema to exist is not only *physically* plausible (they may have been missed by the grid upon discretization), but is *essential* for minimizing numerical dissipation, as will be shown in Sections 3.5.3 and 3.5.4. The treatment of these local extrema is also one of the major differences with the strictly monotonic formulation proposed in Ref. [136]. Sub-cell extrema are especially important in turbulent simulations of low molecular diffusivity scalars; extrema occur with relatively high frequency in such flows, due to reduced ability of the molecular diffusion to smooth them out. Schemes that enforce strict monotonicity in the interpolating polynomial [136, 17] destroy these extrema altogether, resulting in loss of accuracy and significant numerical dissipation. This observation becomes evident from the discussion in Section 3.5.4.2, even for turbulent flows with relatively high molecular diffusivity scalars.

With a single extremum, if the interpolated scalar value breaches physical bounds, the extremum of the interpolating polynomial is also guaranteed to be unbounded (Fig. 3.4(b)). The objective then is to modify both ϕ'_i and ϕ'_{i+1} such that the *location* of the extremum remains unchanged, and the extremum *value* itself is equal to the appropriate bound. The modified interpolation profile is constructed as follows:

$$\phi_\times(x) = \phi_i \cdot w_i(x) + \phi_{i+1} \cdot w_{i+1}(x) + a \cdot \phi'_i \cdot w'_i(x) + b \cdot \phi'_{i+1} \cdot w'_{i+1}(x) \tag{3.19}$$

The extremum location (x_{ext}) is computed as the appropriate root of the derivative of Eq. 3.14, and 'a' and 'b' are determined using the following constraints:

$$\phi_{\times}(x_{ext}) = bound \tag{3.20}$$

$$\left.\frac{d\phi_{\times}}{dx}\right|_{x_{ext}} = 0 \tag{3.21}$$

To ensure that the nature of the extremum (i.e., curvature sign) is not changed, both a and b are constrained to be positive. If either a or b is negative, strict monotonicity is enforced using the minmod limiter (Eqs. 3.15 through 3.18).

We now make three important observations regarding the bounding procedure. First, the procedure outlined here restores boundedness only in the case of the physical bounds being breached, i.e., if either the interpolated scalar is less than 0 or greater than 1 (as is appropriate when considering mole/mass/mixture fractions). In addition to these cases, spurious oscillations may occur without breaching the physically allowed minima and maxima (e.g., at the half step shown in Fig. 3.11). These instances are extremely difficult to detect numerically, and will not be ameliorated by the current scheme. Nevertheless, the procedure presented strikes a good balance between suppressing the formation of such spurious oscillations and minimizing numerical dissipation (see discussion relevant to Fig. 3.11). Second, it is evident from Fig. 3.4(b) that the bounding procedure alters the cell mass content. We recall that the initial, unbounded, semi-Lagrangian already suffers from the inability to conserve mass. The bounding procedure aggravates this problem even further. This is the case with all numerical schemes that re-condition the interpolating polynomial (e.g., Refs. [111, 17, 123]). Overall, this deficiency does not seem to deteriorate turbulent statistics predicted by the BCH scheme, as will become clear in Secs. 3.5.4 and 3.5.5. Third, the bounded reconstruction prioritizes restoring bounds, and the derivatives used for the reconstructed profile become inconsistent with the derivatives computed at the grid nodes from the scalar field.

3.3.2 Summary of the BCH scheme

Using the details of the bounding procedure for both Cases 1 and 2, the entire bounded interpolation algorithm for the BCH scheme can be summarized as follows:

1. Compute ϕ'_i and ϕ'_{i+1} using Eqs. 3.12 and 3.13.
2. If $\phi'_i \cdot \phi'_{i+1} \geq 0$, force monotonicity via Eqs. 3.15 through 3.18.
3. Compute $\phi_\times$ (Eq. 3.14).
4. If $\phi_\times \notin [lowerbound, upperbound]$ (which implies $\phi'_i \cdot \phi'_{i+1} < 0$), modify the profile using Eqs. 3.19 through 3.21. If either a or b < 0, force monotonicity via Eqs. 3.15 through 3.18.

The algorithm described in Sections 3.3.1 and 3.3.2, specifically as it pertains to a single sub-cell extremum, is a key contribution of this Chapter. An alternative to using the procedure described above is to enforce strict monotonicity (Eqs. 3.15 through 3.18) for *all* 1D polynomials in the interpolating cascade. Doing so gives us a scheme similar to one discussed by Rasch & Williamson in Ref. [111], which we will refer to as the MCH (Monotone Cubic Hermite) interpolation scheme for convenience. As will become evident from results presented in Section 3.5, using the BCH scheme leads to significant improvement over MCH in turbulent simulations, with regard to numerical dissipation.

3.3.3 Bounded Lagrange polynomial (SL3)

Bounded forms of the Lagrange polynomial are generally used by the climate modeling community for transporting moisture in air [136]. We use one such algorithm from Ref. [123] to compare performance of the BCH scheme with other bounded semi-Lagrangian schemes. The algorithm selected attempts to mirror, as closely as possible, the *modus operandi* of bounding in the BCH scheme.

Cubic Lagrange polynomials are constructed using a cascade (as shown for a 2D case in Fig. 3.3)

of 1D 4-point stencils:

$$w_i = \prod_{\substack{-1 \leq k \leq 2 \\ k \neq i}} \frac{(x_\times - x_k)}{(x_i - x_k)} \tag{3.22}$$

$$\phi_\times = \sum_{i=-1}^{2} w_i \phi_i \tag{3.23}$$

As discussed earlier, this cubic polynomial does not ensure scalar boundedness. Upon breaching bounds, the interpolating Lagrange polynomial can be modified to ensure boundedness either by switching locally to first-order linear interpolation, or by 'clipping' to the closest bound. For scheme comparison in this Chapter, we use the clipping procedure introduced by Bermejo et al. in [17], and improved upon by Sun et al. in [123]. This procedure subjects the interpolated scalar value to the following constraints:

$$f^- = min(\phi_i, \phi_{i+1}), \quad f^+ = max(\phi_i, \phi_{i+1}) \tag{3.24}$$

$$\phi_\times = \begin{cases} f^- & : \text{if } \phi_\times < f^- \\ \\ f^+ & : \text{if } \phi_\times > f^+ \end{cases} \tag{3.25}$$

To minimize numerical dissipation, clipping is turned off if a single sub-cell extremum is detected via the following condition

$$(\phi_{i+2} - \phi_{i+1}) \cdot (\phi_i - \phi_{i-1}) < 0 \tag{3.26}$$

If such single sub-cell extremum breaches physical bounds, the interpolated value is clipped to the global maximum or minimum, as might be appropriate. When Eq. 3.26 does not hold true, a single cell contains two extrema. As discussed in Section 3.3.1, such a profile cannot be resolved by the computational grid (Nyquist criterion). In this situation, the interpolated scalar is clipped using Eq. 3.25.

We note that one of the advantages of using Hermite polynomials in BCH over Lagrange polynomials is that we can detect and correct for *all* spurious high wavenumbers (two sub-cell extrema), which may not be the case when using Lagrange polynomials. For instance, clipping via Eq. 3.25 will not be triggered if the computed scalar value at the interpolating location lies within the interval $[f^-, f^+]$, even if there exist two sub-cell extrema.

3.3.4 Additional remarks

Inspiration

The formulation of the BCH scheme was inspired by attempts to use the 'Constrained Interpolation Profile' scheme (CIP) [140] for turbulent mixing simulations. CIP involves transporting the scalar derivative values (in all three directions) as passive scalars themselves. Unfortunately, the scalar and its derivatives rapidly become inconsistent with one another in turbulent tests. This makes it necessary to recompute the derivatives using the scalar field every few timesteps. The derivative transport process was eventually discarded altogether in favor of computing the derivatives at each timestep using CD2, as discussed in Section 3.3.1. This resulted in considerably lower memory requirement of the algorithm, as well as an appreciable decrease in numerical complexity of the scheme.

Derivative estimation

Of the several finite-difference formulae used for estimating the scalar derivatives during the formulation of the BCH scheme (e.g., fourth-order finite difference (FD4), high-order upwind differences, etc.), second-order central difference was seen to yield the best results. FD4 was observed to be too oscillatory, especially in regions close to velocity stagnation points and large scalar gradients, whereas the various upwind difference formulae introduced large dispersion errors.

$\mathcal{C}^0$ continuity

The bounding procedure in BCH makes the interpolating polynomial $\mathcal{C}^0$ continuous, since the value of the derivative used at a particular grid node may differ for interpolation in adjacent cells. $\mathcal{C}^1$ continuous forms of the monotone Hermite cubic polynomial were not examined since they are known to suffer from severe dispersion errors [136, 111]. Furthermore, using $\mathcal{C}^1$ forms of the interpolating polynomial can cause minor local corrections (necessary to restore boundedness) to 'ripple out' instantaneously throughout the domain. This sort of behavior is usually undesirable in hyperbolic systems.

Cascade interpolation

We close this discussion by pointing out that the cascade procedure discussed in Section 3.2.3 is not commutative, when used with the bounded form of SL3 or BCH (the unbounded form of SL3, however, does commute). Nevertheless, neither the laminar tests nor the turbulent tests exposed any discernible differences when the ordering of the cascading direction was altered (i.e., x-y-z, y-x-z, z-x-y, etc.).

3.4 Order of accuracy, gain, and phase error

Theoretical analysis of the BCH scheme involves determining the order of accuracy, and analyzing gain and phase error properties of the scheme. Analytical examination requires that we make certain simplifications, such as assuming uniform one-dimensional flow, and analyzing the reconstructed polynomial without bounding enforced. In general, there are relatively few instances of bounds being breached in the computational domain ($\lesssim 0.02\%$ in the turbulent mixing layer, Section 3.5.4), which makes the latter a reasonable simplification. Furthermore, we consider only the error associated with the interpolation step, and neglect any error inherent in the traceback step.

3.4.1 Order of accuracy

The order of accuracy of the cubic Hermite polynomial is determined by expressing $\phi^\star$ explicitly in terms of the grid node scalar values, using one of the 4-point 1D stencils shown in Fig. 3.3. A uniform grid with a constant 1D velocity field u is assumed, and all instances of $x_\times - x_i$ shown in Section 3.3.1 are replaced by their dependence on the constant CFL number σ ($\because\ x_\times - x_i = -u\Delta t = \sigma\Delta x,\ \sigma = |u|\Delta t/\Delta x$). With these simplifications, and the assumption of zero molecular diffusivity, the interpolating polynomial takes the following form:

$$\phi_i^{n+1} = \phi_i^\star = \phi_{i-1}^n w_{i-1} + \phi_i^n w_i + \phi_{i+1}^n w_{i+1} + \phi_{i+2}^n w_{i+2} \tag{3.27}$$

with

$$\begin{aligned} w_{i-1} &= \frac{-\sigma\left(\sigma-1\right)^2}{2} & w_i &= \frac{(\sigma-1)(3\sigma^2-2\sigma-2)}{2} \\ w_{i+1} &= \frac{\sigma\left(-3\sigma^2+4\sigma+1\right)}{2} & w_{i+2} &= \frac{\sigma^2(\sigma-1)}{2} \end{aligned} \tag{3.28}$$

and ϕ^* being the intermediate solution associated with the advection step as described in Section 3.2.1 (Eq. 3.2). The interpolation weights have been computed by making appropriate substitutions in Eqs. 3.8 through 3.14. The discretization error can be evaluated from Eq. 3.27 by expanding the scalar values at time step 'n' in their Taylor-series around $x_\times$ (e.g., $\phi_{i+1} = \phi_i^\star + \phi_i^{\star'}(1-\sigma)\Delta x + \phi_i^{\star''}(1-\sigma)^2\Delta x^2/2! + \cdots$). We must bear in mind that this type of analysis has limited range of applicability since a Taylor-series expansion assumes a sufficiently smooth function, which may not necessarily be valid for physically realistic cases [111]. Taking $\phi_i^\star$ to be the exact value at the interpolating location, the residual in Eq. 3.27 (after the relevant expansions) gives the discretization error at every time step:

$$\epsilon = \sigma\left(\sigma-1\right)\left(2\sigma-1\right)\frac{\Delta x^3}{3!}\phi_i^{\star'''} - 9\sigma^2\left(\sigma-1\right)^2\frac{\Delta x^4}{4!}\phi_i^{\star''''} + \cdots \tag{3.29}$$

The total error accumulated after simulation time 'T' is computed as follows:

$$\epsilon_{tot} = \frac{T}{\Delta t} \cdot \epsilon = \frac{T \cdot |u|}{\sigma \Delta x} \cdot \epsilon \tag{3.30}$$

$$= T \cdot |u| \left[(\sigma - 1)(2\sigma - 1) \frac{\Delta x^2}{3!} \phi_i^{\star\prime\prime\prime} - 9\sigma (\sigma - 1)^2 \frac{\Delta x^4}{4!} \phi_i^{\star\prime\prime\prime\prime} + \cdots \right] \tag{3.31}$$

The leading term in Eq. 3.31 is second-order accurate in space and determines the formal order of accuracy of the scheme. Second-order spatial accuracy is confirmed via grid convergence analysis in Section 3.5.2. Switching to the bounded form of the interpolant (Section 3.3.1) is expected to reduce the order of accuracy to first order locally in regions where bounds are enforced.

We emphasize the absence of a second-order derivative in both Eqs. 3.29 and 3.31, which is highly desirable, since it is the predominant source of interpolation-based dissipation when present. Even-order derivatives in the truncation error give rise to dissipation errors, whereas odd-order derivatives give rise to dispersion errors. The combined effect of these errors is termed "numerical diffusion" [82].

The dependence of the truncation error on σ suggests that the CFL number affects not only temporal accuracy, but also spatial accuracy for semi-Lagrangian schemes. This is unlike the behavior of Eulerian schemes, where the CFL number is related primarily to temporal accuracy. The variation of the coefficients for the first two terms in Eqs. 3.29 and 3.31 with σ is plotted in Fig. 3.5. Inspecting the single step error (Fig. 3.5(a)) is convenient for analytical examination, however, it is necessary to be mindful of the cumulative errors (Fig. 3.5(b)) that actually dictate the accuracy of the final solution. Both graphs indicate zero discretization error for $\sigma = 1$, which is not surprising since the interpolation becomes exact for this case. Unfortunately, when working with non-uniform (e.g., turbulent) velocity fields, the local CFL number fluctuates spatially, which makes it difficult to determine the discretization error with certainty. The coefficient of the third-order derivative in Fig. 3.5(a) (associated with numerical dispersion, or, phase error) vanishes for $\sigma = 0.5$, whereas the fourth-order derivative coefficient (associated with numerical dissipation, or gain error) attains its maximum at this point. It is interesting to note the change of sign of the K_3 coefficient at $\sigma = 0.5$.

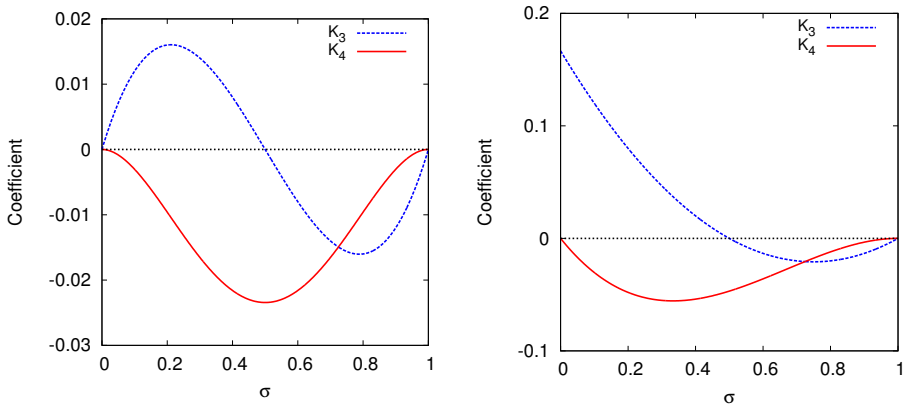

(a) Single step error (Eq. 3.29)

(b) Cumulative error (Eq. 3.31)

Figure 3.5: Dependence of truncation error terms on σ . (a) Single step coefficients: $K_3 = \sigma(\sigma-1)(2\sigma-1)/6$, $K_4 = -9\sigma^2(\sigma-1)^2/24$. (b) Cumulative error coefficients: $K_3 = (\sigma-1)(2\sigma-1)/6$, $K_4 = -9\sigma(\sigma-1)^2/24$

This will translate into phase speeds that are smaller (if $\sigma < 0.5$) and larger (if $\sigma > 0.5$) than the theoretical values. The combined effect of the third- and fourth-order derivatives can be minimized by keeping σ as close to 1 as possible. The observations discussed here are corroborated via Fourier analysis in the following section.

3.4.2 Gain and phase error

Gain and phase error analysis of Eulerian transport schemes is generally done via the commonly used von-Neumann and modified-equation methods [82]. Casting the transport equation in its Lagrangian form (Eq. 3.2) requires that we use a slightly different technique for the BCH scheme (without bounding enforced), such as the Fourier analysis method described by Utsumi et al. [126]. Assuming periodic boundary conditions, and using the relations given by Eqs. 3.2 and 3.27, the Fourier coefficients ($\widehat{\phi}^{n+1}(\kappa)$) of the scalar after the advection step are given as:

$$\widehat{\phi}^{n+1}(\kappa) = \frac{1}{L}\sum_{i=0}^{N-1} \phi_i^{\star} e^{-j\kappa i\Delta x}\Delta x \tag{3.32}$$

$$\Rightarrow \widehat{\phi}^{n+1}(\kappa,\sigma) = \frac{1}{L}\sum_{i=0}^{N-1}\big[\phi_{i-1}^{n}w_{i-1}(\sigma) + \phi_{i}^{n}w_{i}(\sigma) + \phi_{i+1}^{n}w_{i+1}(\sigma) + \phi_{i+2}^{n}w_{i+2}(\sigma)\,\big]\,e^{-j\kappa i\Delta x}\Delta x \tag{3.33}$$

where L is the domain size. We use the periodic boundary conditions to identify that

$$\frac{1}{L}\sum_{i=0}^{N-1}\phi_{i-1}^{n}e^{-j\kappa i\Delta x}\Delta x = e^{-j\kappa\Delta x}\widehat{\phi}^{n}(\kappa) \tag{3.34}$$

Equation 3.33 thus simplifies to

$$\widehat{\phi}^{n+1}(\kappa,\sigma) = \widehat{\phi}^{n}(\kappa)\left[e^{-j\kappa\Delta x}w_{i-1}(\sigma) + w_{i}(\sigma) + e^{j\kappa\Delta x}w_{i+1}(\sigma) + e^{2j\kappa\Delta x}w_{i+2}(\sigma)\,\right] \tag{3.35}$$

The complex gain factor can now be computed as follows:

$$g(\kappa,\sigma) = \frac{\widehat{\phi}^{n+1}}{\widehat{\phi}^{n}} \tag{3.36}$$

$$= e^{-j\kappa\Delta x}w_{i-1}(\sigma) + w_{i}(\sigma) + e^{j\kappa\Delta x}w_{i+1}(\sigma) + e^{2j\kappa\Delta x}w_{i+2}(\sigma) \tag{3.37}$$

The amplitude of $g(\kappa,\sigma)$ can be used to determine the gain error, and its argument to determine the numerical phase speed error.

For the analytical solution of the advection step ($\phi^{n+1}(x) = \phi^{n}(x - u\Delta t)$), the amplitude and phase angle of the gain factor are 1 and $\kappa\sigma\Delta x$, respectively:

$$\widehat{\phi}^{n+1}(\kappa) = \frac{1}{L}\int_{0}^{L}\phi^{n}(x - u\Delta t)e^{-j\kappa x}dx \tag{3.38}$$

$$= e^{j\kappa\sigma\Delta x}\cdot\widehat{\phi}^{n}(\kappa) \tag{3.39}$$

Using these values as reference, the dependence of the gain amplitude and the numerical phase speed on $\kappa\Delta x$ (the analytical phase speed) is plotted in Figs. 3.6 and 3.7. We can surmise that the BCH scheme is stable for $\sigma\epsilon\,[0,1]$ since the gain amplitude (Fig. 3.6) never gets larger than 1. In fact, the

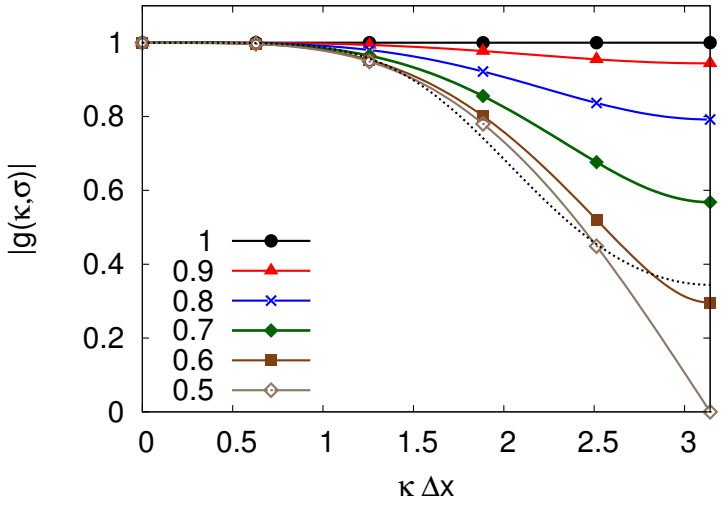

Figure 3.6: Amplitude of the gain factor (Eq. 3.37) for various CFL numbers. The gain is exact for $\sigma = 1$. Curves for $\sigma \epsilon [0, 0.5)$ are not shown since $|g(\kappa, \sigma)| = |g(\kappa, 1 - \sigma)|$. The broken line corresponds to the curve for HOUC5.

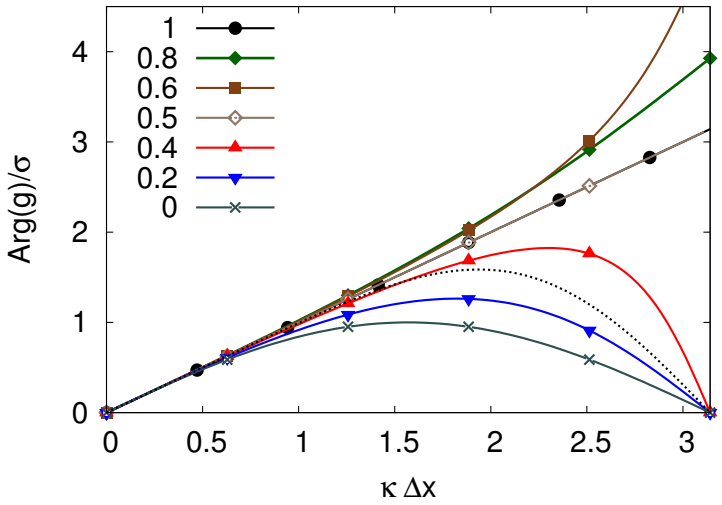

Figure 3.7: Numerical phase speed (Arg(g)/σ : Eq. 3.37) as a function of the true wave speed ($\kappa \Delta x$). The phase speed is exact for $\sigma = 0.5$ and 1. The broken line corresponds to the curve for HOUC5.

stability property can be extended to $\sigma > 1$, since the integer part of σ results only in a phase shift of $\widehat{\phi}^{n+1}$, leading to the same gain amplitude as for $\sigma - [\sigma]$:

$$|g(\sigma)| = |g(\sigma - [\sigma])| \tag{3.40}$$

Stability for $\sigma > 1$ was confirmed in numerical tests discussed in Section 3.5.3.3.

The gain error is worst for $\sigma = 0.5$, indicating large numerical dissipation for high wavenumber modes at this CFL number, and for $\sigma = 1$ we have no gain error at all. This result is consistent with curve K_4 shown in Fig. 3.5(a). The numerical phase speed (Arg(g)/σ) becomes exact for $\sigma = 0.5$ and 1, as shown in Fig. 3.7. Interestingly, the phase speed is lower than the theoretical value for $\sigma < 0.5$, and greater for $\sigma > 0.5$. These results are consistent with curve K_3 in Fig. 3.5(b). We note that the numerical phase speed matches the exact phase speed relatively well for $\sigma \geq 0.8$, but large lead and lag errors manifest at lower CFL values (except for $\sigma = 0.5$). Considering the need to minimize both gain and phase errors in the advection step, we infer that the CFL number must be kept as close to 1 as possible.

The gain and phase error curves for a fifth-order upwind convective Eulerian scheme (HOUC5) [99] are also included in Figs. 3.6 and 3.7 for comparison, and the relevant expressions have been derived in Appendix B. The curves suggest that the performance of BCH is similar to, or better than, that of the fifth-order accurate HOUC5 scheme. The gain error in the worst case scenario for BCH ($\sigma = 0.5$) is comparable to that of the HOUC5 scheme, which points to superior performance with respect to numerical dissipation, thereby allaying concerns regarding semi-Lagrangian schemes being overly dissipative. The phase error is considerably smaller for $\sigma \geq 0.4$, indicating improved numerical dispersion characteristics.

3.5 Numerical tests and results

We now examine results obtained from simulations using five bounded (WENO3 [85], BQUICK [60], SL3, BCH, MCH) and two unbounded (QUICK [81] and HOUC5 [99]) schemes. Of these, QUICK,

BQUICK, WENO3, and HOUC5 are Finite-Volume-based Eulerian schemes, which use the divergence form of the scalar transport equation (Eq. 3.41).

$$\frac{\partial \phi}{\partial t} + \nabla \cdot (\boldsymbol{u}\phi) = \mathcal{D}\nabla^2 \phi \tag{3.41}$$

The objective is to assess and compare scheme performance with regard to boundedness, numerical diffusion, accuracy, and conservation. Both laminar and turbulent test configurations are considered. Laminar tests are essential for examining certain qualitative as well as quantitative aspects of scalar schemes. These qualities are difficult to assess in turbulent cases owing to the non-deterministic nature of turbulent velocity fields. Results from the laminar tests are discussed first, followed by those from the turbulent tests.

3.5.1 Numerical solver

Numerical tests for both laminar and turbulent cases were carried out using an incompressible variable-density Navier-Stokes solver (NGA [41], description provided in Appendix C). The code uses a staggered variable arrangement, with scalar values stored at the cell centers, and velocity components stored at the appropriate cell faces. The velocity field was solved using a spatially second-order-accurate, energy conserving finite-difference scheme. Time integration for velocity was done using a second-order semi-implicit Crank-Nicolson method.

Whenever possible, multiple scalars were transported simultaneously in the test cases, with each scalar being assigned a distinct Eulerian or semi-Lagrangian scheme. The simultaneous transport was preferable for consistent comparison of results from the various scalar schemes, especially due to the non-deterministic nature of turbulent velocity fields. Time integration of the scalar transport equation was done using a second-order semi-implicit Crank-Nicolson method for the Eulerian schemes. The integration of the diffusive term in the semi-Lagrangian schemes was treated using the forward Euler method (Eq. 3.3).

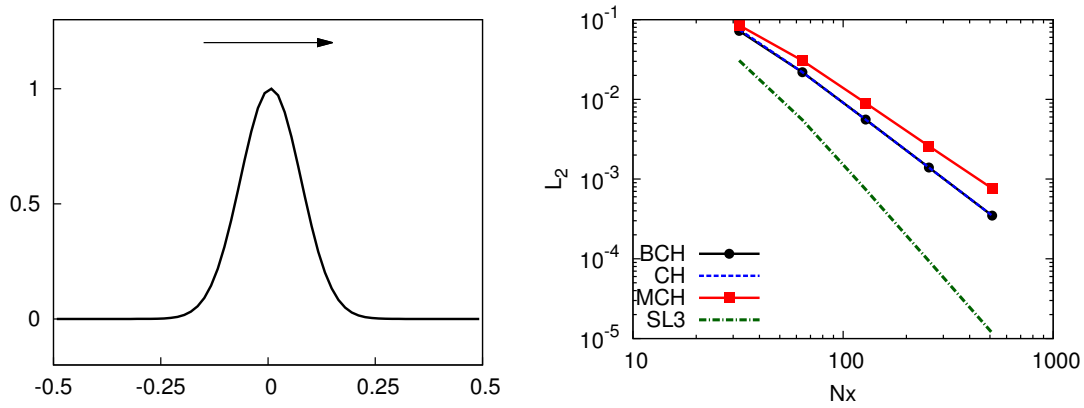

(a) Gaussian profile

(b) L_2 norm of the error

Figure 3.8: 1D advection of a Gaussian scalar profile, run for 5 rotations with CFL=0.9.

3.5.2 Formal order of accuracy

The formal order of accuracy for BCH without bounds enforced (or simply, CH) was determined analytically in Section 3.4.1. We now inspect numerically, the order of accuracy of all the semi-Lagrangian schemes discussed in this Chapter. Figure 3.8(b) shows the L_2 norm of the error for uniform advection of a 1D Gaussian scalar profile (Fig. 3.8(a)), run for 5 rotations with a CFL of 0.9. The curve suggests second-order spatial convergence ($O(\Delta x^2)$) for CH, which is consistent with the analytical results obtained in Section 3.4.1. We note that the results for both CH and BCH are virtually identical, which happens since the need to enforce bounding arises very rarely in the C^∞ continuous Gaussian profile. The result for MCH, however, is comparatively degraded, since MCH suppresses the extremum in the Gaussian profile even when physical bounds are not breached. SL3 exhibits $O(\Delta x^3)$ convergence, which is the best possible order of accuracy achievable using a cubic polynomial. The Hermite cubic polynomials are limited to $O(\Delta x^2)$ or lower, due to the fact that the relevant derivatives were computed using a 2^{nd} order accurate finite-difference formula (Section 3.3.4).

3.5.3 Laminar tests

Two laminar tests, consisting of a 1D case and a 2D case, were used for comparing scheme performance. For the 1D case, the composite profile shown in Fig. 3.9(a) was advected using a uniform

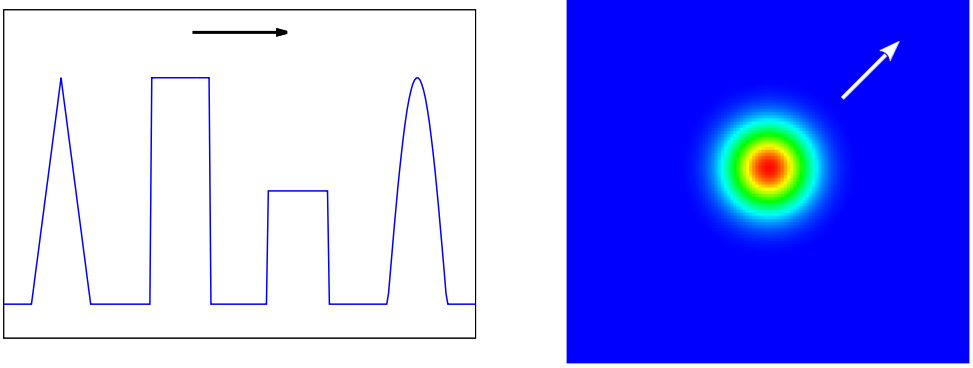

(a) 1D scalar advection (b) 2D scalar advection

Figure 3.9: 1D and 2D scalar advection in uniform velocity fields.

velocity field. The simulation was run for 5 complete rotations before comparing results from the various scalar transport schemes. The 1D profile shape introduces sharp gradients in the scalar field, which are generally the locations where maximum occurrences of numerical errors like dispersion and overshoot happen. The 2D laminar test (Fig. 3.9(b)) involves uniform advection of a 2D Gaussian scalar profile along the 45-degree diagonal. Results for this simulation were compared after ten rotations. Periodic boundary conditions and zero molecular diffusivity were used for both laminar tests.

3.5.3.1 Bounding vs. monotonicity

Laminar tests provide a good qualitative indication of boundedness. The effects of enforcing boundedness are best observed by comparing the same cubic Hermite interpolating polynomial with three different strategies: standard Cubic Hermite (CH), Bounded Cubic Hermite (BCH), and Monotone Cubic Hermite (MCH). Figure 3.10 indicates that the bounding operation is crucial for suppressing oscillations, and plays an important role in preventing the propagation of numerical errors (as found in the unbounded CH scheme). BCH is not as effective as MCH in preventing oscillations at the half-step in the 1D profile, since these oscillations are still within the specified physical bounds. Enforcing strict monotonicity using MCH, however, introduces significant numerical dissipation, as is evident from a marked decrease in scalar maxima in Fig. 3.10(c). The bounding procedure in BCH also introduces additional dissipation, albeit an insignificant amount, as can be surmised from good

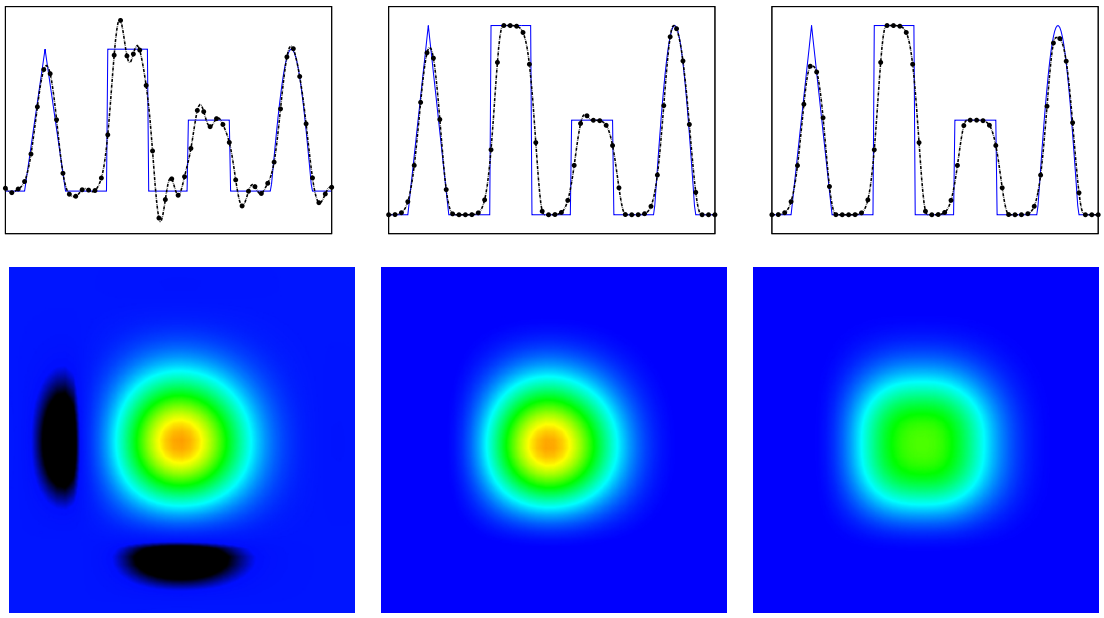

(a) CH (b) BCH (c) MCH

Figure 3.10: Comparison of unbounded, bounded, and monotone cubic Hermite interpolation. Results from 1D simulations are shown on top, and those from 2D simulations are shown on the bottom. Regions colored in black for the 2D case indicate scalar values outside the interval $[0, 1]$.

agreement between the physically viable extrema in results from CH and BCH. We stress that the laminar test cases discussed in this chapter do not involve any molecular dissipation (i.e., $\mathcal{D} = 0$).

Doing a qualitative comparison with the QUICK, BQUICK, HOUC5, WENO3, and SL3 schemes, we see the presence of large oscillations for the two unbounded schemes (QUICK and HOUC5) in Figs. 3.11 and 3.12. The four bounded schemes (BQUICK, WENO3, SL3, BCH), however, adhere strictly to the physical scalar bounds (0 and 1 in this case). Close inspection of the half-step in the 1D profile reveals that BQUICK (Fig. 3.11(c)) gives rise to oscillations similar to those caused by QUICK (Fig. 3.11(a)), if physical bounds are not breached. However, BCH (Fig. 3.10(b)) is able to suppress spurious oscillations at the half-step (which do manifest in CH, Fig. 3.10(a)) to a certain extent, even though the oscillations do not breach physical bounds.

3.5.3.2 Numerical dispersion and dissipation

The effects of numerical dispersion can be observed qualitatively through asymmetric deformation of the scalar profiles. We note that of all the results shown in Figs. 3.11 and 3.12, only SL3 preserves

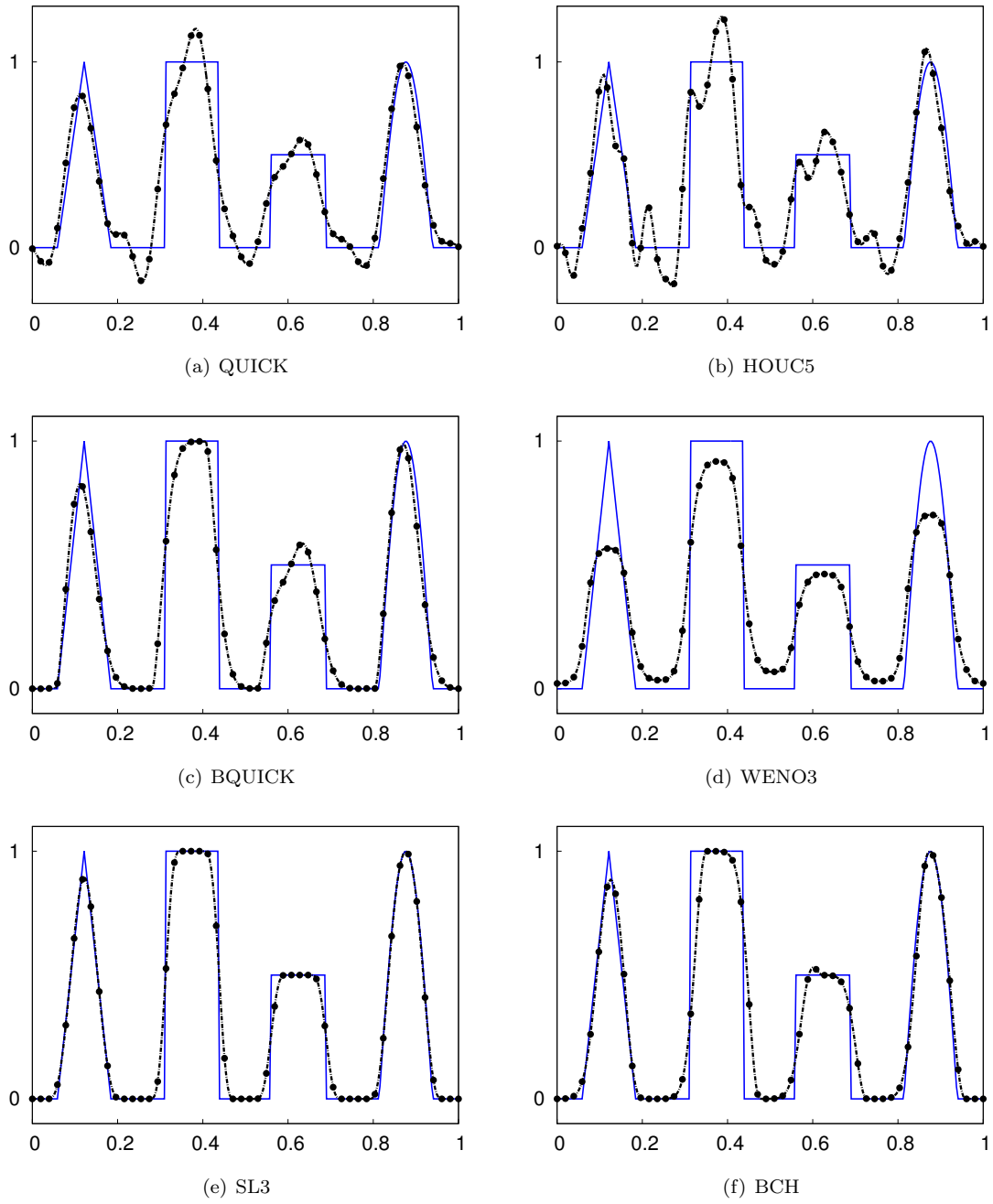

(a) QUICK

(b) HOUC5

(c) BQUICK

(d) WENO3

(e) SL3

(f) BCH

Figure 3.11: Comparison of scalar transport schemes for the 1D uniform advection case (5 rotations with CFL=0.8 on a 256 cell grid). Physical bounds of 0 and 1 were used in BCH, SL3, and BQUICK.

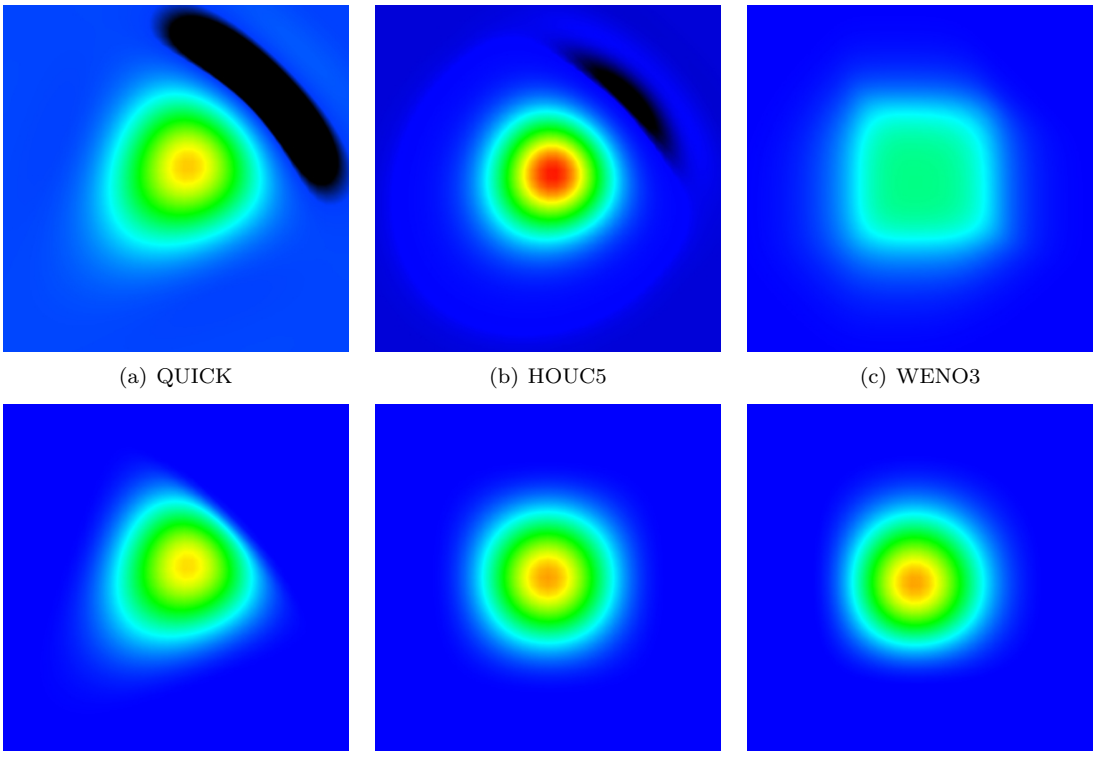

(a) QUICK (b) HOUC5 (c) WENO3

(d) BQUICK (e) SL3 (f) BCH

Figure 3.12: Uniform advection of a Gaussian profile along the 45° diagonal. Results shown after 5 rotations with CFL = 0.4 on a 64×64 grid. Red indicates maximum for the scalar ($z = 1$), and blue indicates minimum ($z = 0$). Regions colored in black depict scalar values less than 0 for QUICK and HOUC5. An explicit solver was used for all cases, and the HOUC5 case was run with CFL=0.2 due to stability issues.

Table 3.1: Comparison of scheme results for scalar maxima in the laminar tests, mean scalar dissipation rate in the turbulent mixing layer at the beginning of the self-similar regime (center plane only: $\chi = 2\mathcal{D}\langle(\partial\phi/\partial x)^2 + (\partial\phi/\partial z)^2\rangle$, partial derivatives of scalar 'ϕ' taken with respect to co-ordinate axes 'x' and 'z'), and relative computational cost with respect to BCH.

	max_ϕ—Laminar tests		χ—Turbulent tests		
Scheme	1D	2D	$\kappa_x\eta = 1.5$	$\kappa_x\eta = 3$	Cost
SL3	1.0000	0.8360	1.16e-3	1.56e-3	1.18
CH	1.2081	0.8398	1.76e-3	1.75e-3	0.83
BCH	1.0000	0.8399	1.48e-3	1.70e-3	1.00
MCH	0.9999	0.5712	9.54e-4	1.43e-3	0.92
WENO3	0.9179	0.3673	6.58e-4	1.16e-3	1.01
QUICK	1.1782	0.7872	1.14e-3	1.54e-3	0.45
BQUICK	0.9986	0.7834	1.13e-3	1.54e-3	1.02
HOUC5	1.2413	0.9804	1.43e-3	-	0.68

the symmetry of the initial profile. The upwinded schemes (QUICK, BQUICK, and HOUC5) show a great deal of asymmetric deformation, especially for the 2D advection case. BCH exhibits some dispersion, but these errors can be disposed of altogether by setting $\sigma = 0.5$ or $\sigma = 1$ in these laminar cases, as discussed in Section 3.4.

We emphasize that there are three distinct sources of dissipation in our simulations: 1) molecular dissipation, which is physical and expected; 2) numerical dissipation introduced by the interpolation operation, which we have discussed in Sec. 3.4.2 ; and 3) numerical dissipation from the bounding procedure (primarily from the single sub-cell extremum bounding), which we have seen impacts the MCH scheme quite severely (Sec. 3.5.3.1), but does not have a noticeable impact on the BCH scheme (Fig. 3.10). The term 'numerical dissipation' is taken to represent the combined effect of interpolation-based and bounding operation-based dissipation in the rest of the chapter. Numerical dissipation manifests as a smoothing of sharp edges in the 1D advection case and a drop in the maximum scalar value for the 2D case. Any dissipative effects noticeable in the laminar tests are purely numerical since they were run with zero molecular diffusivity. The maxima of the scalar profiles for the 1D and 2D cases are listed in Table 3.1. Both SL3 and BCH perform equally well with regard to numerical dissipation in uniform advection tests (Table 3.1, Figs. 3.11 and 3.12), and are superior to the other bounded schemes tested.

Before further discussion, we would like to emphasize that although the performance of SL3 may seem to be slightly better than that of BCH in the uniform advection cases, BCH performs

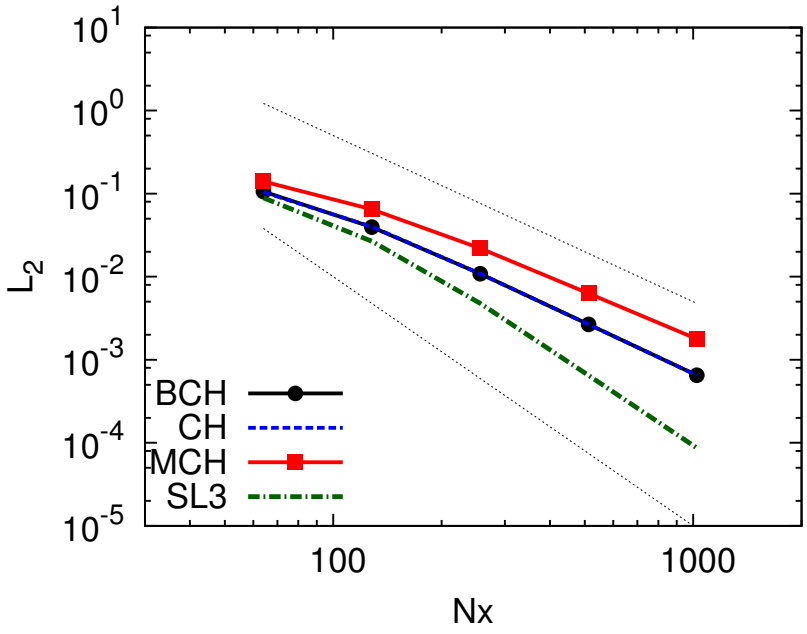

Figure 3.13: Grid convergence for Gaussian scalar profile advected for 5 rotations with CFL_{max}=1.9 in a non-uniform, divergence free velocity field: $u = 1 + 0.5\cos(2\pi x), v = 1 + \pi y \sin(2\pi x)$.

significantly better in the turbulent cases (as will be shown in Section 3.5.4). This observation should lead to the important realization that the suitability of numerical schemes for use in turbulent flows should not be judged based on performance in simple uniform advection cases. These idealized tests often fail to account for chaotic behavior that may affect scheme performance in unpredictable ways.

3.5.3.3 CFL>1, and non-uniform velocity field

Limitations on time step size for certain simulations (e.g., for weather prediction purposes) can often be imposed by numerical stability considerations, rather than by accuracy concerns [121]. Semi-Lagrangian schemes can reduce computational cost in such applications by permitting the use of much larger CFL values than would be allowable for Eulerian schemes.

We repeat some of the incompressible 1D tests discussed previously, with a spatially varying laminar velocity profile ($u = 1 + 0.5\cos(2\pi x), v = 1 + \pi y \sin(2\pi x)$) and a maximum CFL$>1$. Spatial variation in the velocity causes the CFL to fluctuate locally and span a range of values ($|u|_{min} \leq \text{CFL} \cdot \Delta x/\Delta t \leq |u|_{max}$). The same grid convergence results for the Gaussian profile from Fig. 3.8 are shown in Fig. 3.13 with non-uniform velocity. Both CH and BCH maintain second-order

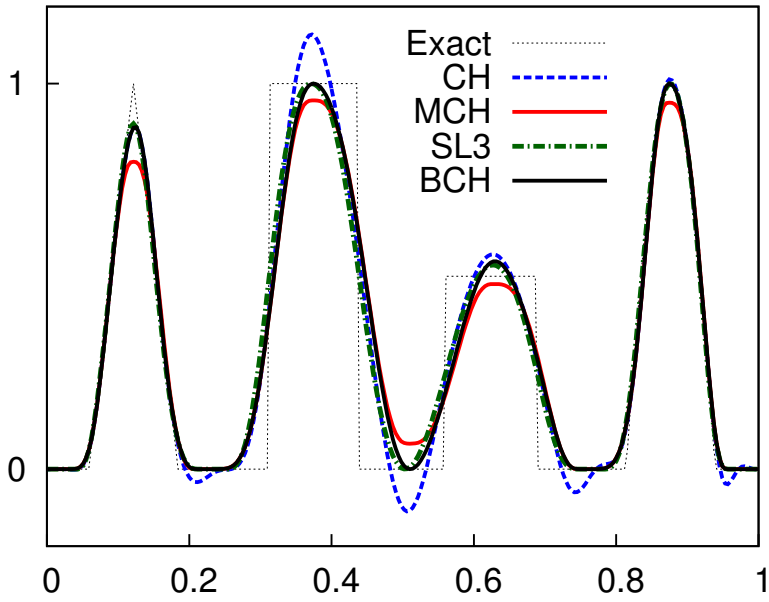

Figure 3.14: 1D profile advection with non-uniform velocity field. 5 rotations with $\text{CFL}_{max} = 1.8$ on a 256 cell grid.

accuracy, and SL3 maintains third-order accuracy. The 1D experiments shown in Fig. 3.11 were also repeated with the non-uniform velocity field for $\text{CFL}_{max} > 1$. The resulting profiles after 5 rotations are shown in Fig. 3.14. The proposed bounding algorithm (BCH) results in lower numerical dissipation than enforcing strict monotonicity (MCH), which reinforces similar observations from the uniform velocity test.

Although the proposed bounding algorithm appears to function well for the case when $\text{CFL}_{max} > 1$, maintaining sufficient accuracy in turbulent simulations often requires that the time step size be smaller than physical time scales [33]. Therefore, the capability to run at CFL > 1 plays a somewhat less crucial role, compared to the high spatial accuracy inherent in the bounded cubic Hermite polynomial. Nonetheless, results obtained by running turbulent simulations with $\text{CFL}_{max} > 1$ are discussed in Sec. 3.5.5. Additionally, it was observed that turbulent simulations with high-order-accurate Eulerian schemes required unnecessarily restrictive time step sizes even for CFL < 1, i.e., the largest useable time step size was restricted by numerical stability concerns. This reflects the well-known cost reducing potential of SL schemes in this regard, even when using CFL < 1.

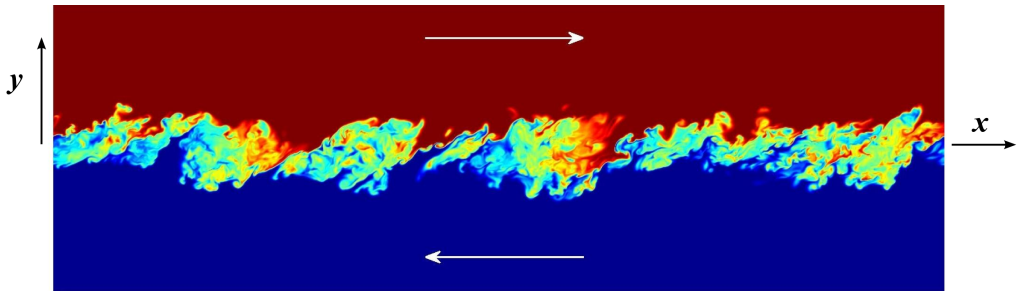

(a) Scalar profile obtained with the BCH scheme at normalized time $\tau = 127.5$

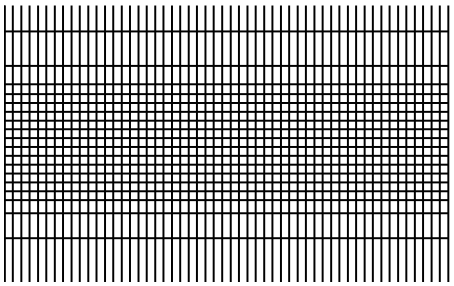

(b) Computational mesh

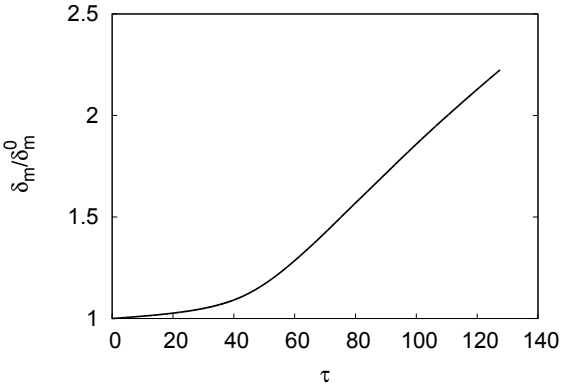

(c) Time evolution of momentum thickness

Figure 3.15: Turbulent mixing layer configuration.

3.5.4 Turbulent mixing layer

3.5.4.1 Configuration setup

In addition to the laminar tests described above, numerical tests were conducted in a 3D turbulent mixing layer configuration. This configuration follows very closely the work of Rogers & Moser [116]. It consists of two turbulent streams parallel to one another and going in opposite directions, separated by an initial interface at the mid-plane (Fig. 3.15(a)). The velocity field was initialized with two decorrelated velocity fields obtained from Direct numerical simulation (DNS) of a turbulent boundary layer [116]. The initial scalar distribution was represented by a Heaviside function, with the top half of the domain consisting of scalar values set to 1 (red region in Fig. 3.15(a)), and the bottom half set to 0 (blue). The scalar gradient in the y-direction acts as a source of scalar variance for the turbulent cascade of scalar energy, and obviates the need for forcing the scalar explicitly. The molecular diffusivity of the scalar was kept equal to the kinematic viscosity of the fluid (*i.e.*, $Sc = 1$).

Periodic boundary conditions were imposed in the streamwise (x) and spanwise (z) directions with periods $125\delta_m^0$ and $(125/4)\delta_m^0$, respectively [116], with δ_m^0 being the initial momentum thickness of the mixing layer as defined by Rogers & Moser [116]. Based on these values, the initial Reynolds number was computed to be $Re_m^0 = 960$ ($Re_m^0 = \delta_m^0 \Delta U/\nu$). A Neumann boundary condition was used for both the velocity and the scalar in the cross-stream (y) direction, which spans $81\delta_m^0$.

In order to reduce the computational cost of the turbulent test case, a stretched mesh (Fig. 3.15(b)) was used in the cross-stream direction, whereas the grid cells in the periodic directions were uniformly sized. The grid cells in the stretched direction were clustered close to the center plane so as to capture accurately the unsteady development of the core region (approximately $32\delta_m^0$ in height) of the mixing layer. A grid size of $1280 \times 444 \times 320$ cells was selected for adequate resolution of the velocity field by ensuring that $\kappa_{max}\eta \geq 1.5$. κ_{max} here is the largest wavenumber resolvable by the grid and η is the Kolmogorov scale on the center plane ($\eta = (\nu^3/\epsilon)^{1/4}$, where ν is the kinematic viscosity, and $\epsilon = \langle 2\nu S_{ij} S_{ij} \rangle$ is the average kinetic energy dissipation rate on the plane). The computational cells used were of unity aspect ratio in the core region, and were stretched in the y-direction outside the core (stretching factor $\approx 3\%$), as depicted in Fig. 3.15(b).

The simulation was run with a maximum CFL of 0.6, keeping the time step size for both the velocity and scalar solvers the same. We point out that in a turbulent case, the spatially and temporally varying local CFL value may span the entire range of [0,CFL$_{max}$]. Results from the various scalar transport schemes were compared once the core of the mixing layer attained a self-similar state, as indicated by the linear growth of the momentum thickness. The time evolution of the momentum thickness normalized by the initial momentum thickness is shown in Fig. 3.15(c). After a transient growth, the mixing layer enters a self-similar regime around $\tau = 60$. $\tau = t\Delta U/\delta_m^0$ (where t is the simulation time) represents the normalized time defined by Rogers and Moser [116]. The growth rate in the self-similar regime, i.e., the slope of the linear portion of the curve in Fig. 3.15(c) is similar to the value observed by Rogers and Moser.

3.5.4.2 Results

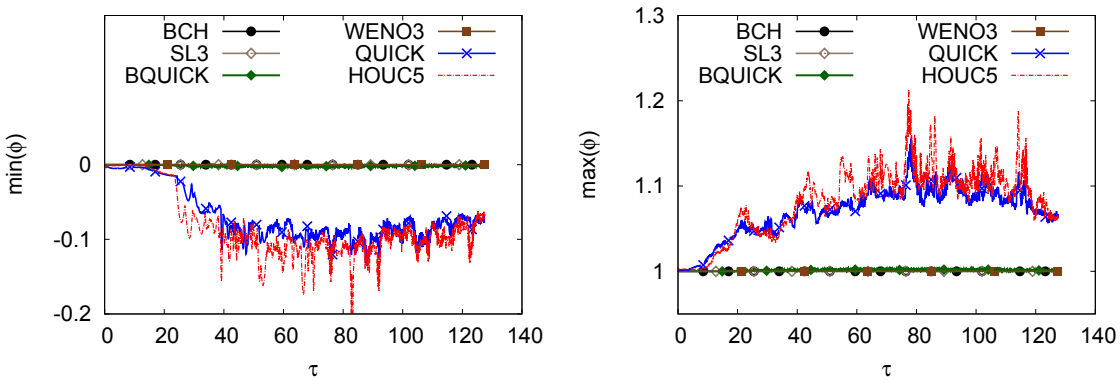

(a) Scalar minimum

(b) Scalar maximum

Figure 3.16: Time evolution of the scalar maximum and minimum in the turbulent mixing layer.

Turbulent flow fields are generally replete with occurrences of abrupt velocity changes, and the presence of irregular scalar structures with sharp gradients. Thus, turbulent simulations provide a more rigorous indication of the practical usability of numerical schemes in physically realistic scenarios, when compared to laminar simulations. The properties already discussed in Section 3.5.3 are, therefore, re-examined in the turbulent mixing layer.

Boundedness was inspected using the time evolution of the maximum and the minimum of the scalar in the computational domain (Fig. 3.16). It is evident that the unbounded schemes breach the global maximum and minimum, but the bounded schemes do not. In fact, both the QUICK and HOUC5 schemes can over/undershoot by more than 10%. Probability Density Functions (PDF) of scalar values breaching physical bounds for both these schemes are shown in Fig. 3.17(a), and confirm the occurrence of more severe oscillations for HOUC5 than for QUICK (Runge's phenomenon). The PDFs indicate that the majority of the breached values lie close to the bounds, and the distribution corresponding to relatively large deviations is small. This can be deduced from the Cumulative Distribution Function (CDF) shown in Fig. 3.17(b), which indicates that breaches with $-0.02 < \phi < 0$ or $1 < (1-\phi) < 1.02$ (as may be appropriate) account for close to 100% of the total breaches. We note that the distributions in Fig. 3.17 are slightly different, depending on whether we consider the upper or the lower bound being breached. This was observed as a persistent occurrence in our mixing layer datasets. One possible explanation for the observation may come from slight asymmetry

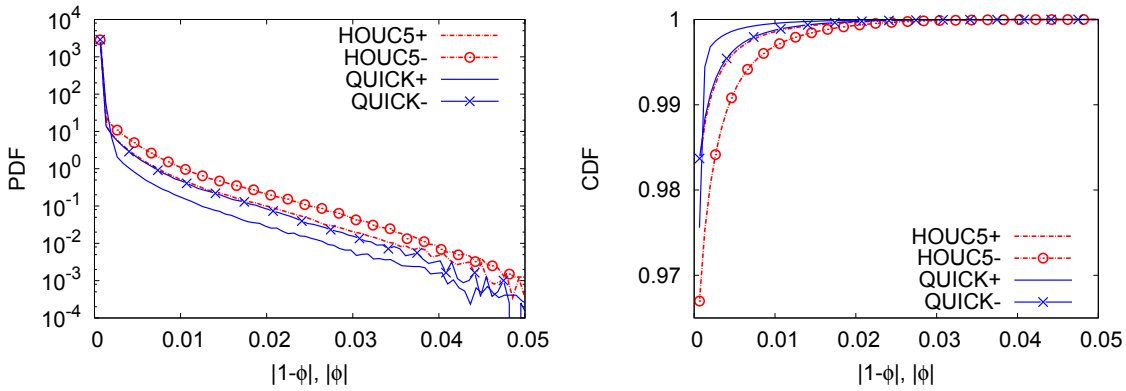

(a) PDF (b) CDF

Figure 3.17: Probability Density Function and Cumulative Distribution Function of the scalar value breaching bounds. Curve for upper bound breach ($1 < \phi < 1.05$) indicated with a '+', and that for lower bound breach ($-0.5 < \phi < 0$) indicated with a '−'.

present in the initial conditions, which gets exacerbated over time. The fact that the bias of the asymmetry observed (i.e., negative fluctuations being more severe than positive ones) is independent of whether the QUICK or HOUC5 scheme is used, lends support to this conjecture.

Numerical dispersion was not examined in the mixing layer as it is difficult to distinguish between deformation caused by numerically induced dispersion and that caused by straining from the non-uniform velocity field.

Numerical dissipation in turbulence computations poses one of the most significant hurdles, as it leads to degradation of accuracy at the dynamically important small length scales. This in turn can have a negative impact at the large scales. The effects of numerical dissipation are difficult to assess directly, and are instead evaluated by examining the one-dimensional scalar energy and dissipation spectra at the center plane of the mixing layer (Fig. 3.18). We note that in three-dimensions, the scalar energy spectrum is defined as $E(\kappa) = \langle |\widehat{\phi}(\boldsymbol{\kappa})|^2 \rangle_{sph}$, where $\widehat{\phi}(\boldsymbol{\kappa})$ are the Fourier coefficients of the scalar field, and $\langle \cdot \rangle_{sph}$ represents spherical averaging over wavenumber shells. The dissipation spectrum is defined as $D(\kappa) = 2\mathcal{D}\kappa^2 E(\kappa)$, and indicates the intensity of *molecular* dissipation as a function of wavenumber. The equivalent one-dimensional quantities are computed in the streamwise

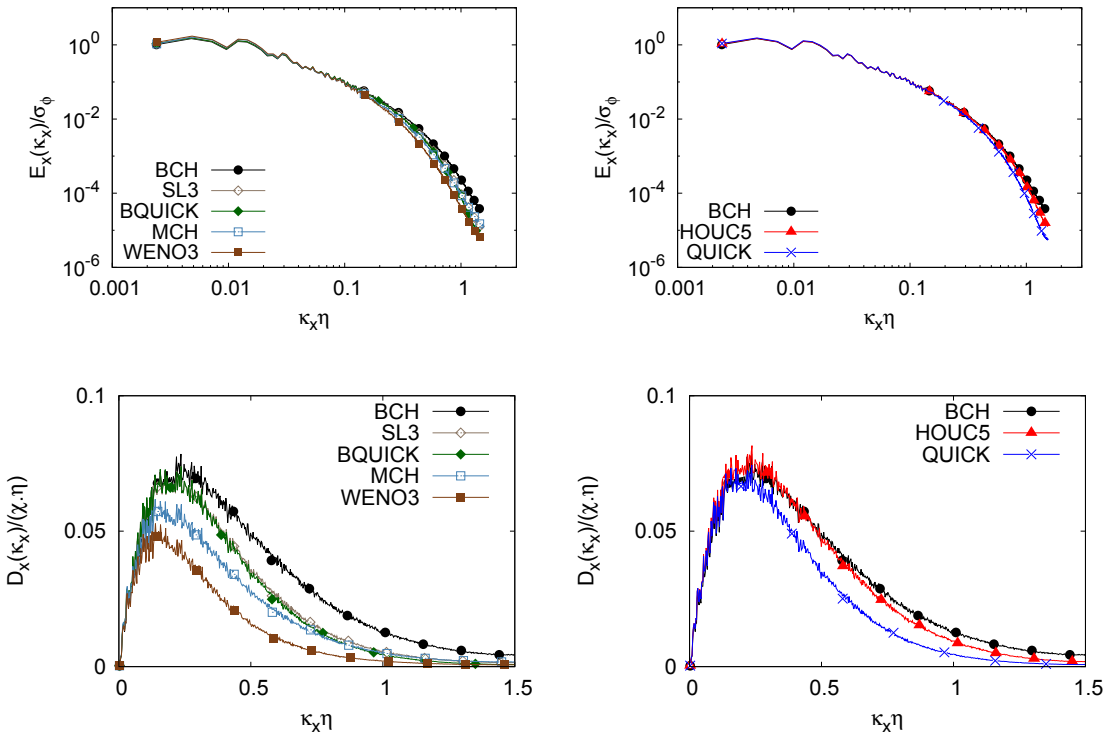

(a) BCH *vs.* bounded schemes

(b) BCH *vs.* unbounded schemes

Figure 3.18: 1D scalar energy (top) and dissipation (bottom) spectra in the streamwise direction, computed on the center plane of the mixing layer ($\kappa\eta = 1.5$). The dissipation spectra have been normalized by the instantaneous χ value for BCH at resolution $\kappa\eta = 3$, and then averaged over 11 separate snapshots in the self-similar state ($\tau = 106.25$ to 127.5, Fig. 3.15(c)). The scalar energy spectra have been averaged similarly, after normalization by the area under the individual curves (*i.e.*, the scalar variance σ_ϕ).

direction of the mixing layer as follows:

$$E_x(\kappa_x) = \int_{-\infty}^{\infty} R_{xx}(r) e^{-i\kappa_x r} dr \tag{3.42}$$

$$D_x(\kappa_x) = 2\mathcal{D}\kappa_x^2 E_x(\kappa_x), \tag{3.43}$$

where $R_{xx}(r) = \langle \phi(x+r)\phi(x) \rangle$ is the streamwise autocorrelation function, and $\langle \cdot \rangle$ represents ensemble averaging. E_x and R_{xx} are also referred to as E_{11} and R_{11} in some instances. The two quantities $E_x(\kappa_x)$ and $D_x(\kappa_x)$, which we refer to as the 1D scalar-energy and 1D scalar-dissipation spectra, respectively, are used for examining the wavenumber content of scalar energy and dissipation in the turbulent mixing layer. We note that while not being a true dissipation spectrum, $D_x(\kappa_x)$ shares many of the same features that $D(\kappa)$ exhibits.

Discriminating between 1D scalar energy spectra at large wavenumbers (i.e., the small length scales) becomes difficult (Fig. 3.18). For this reason, we will use the 1D scalar dissipation spectrum, which is more informative for comparing scheme performance. We observe that molecular dissipation peaks close to $\kappa_x \eta \approx 0.2$, and drops off to zero as $\kappa_x \eta$ approaches 1.5. There is reasonable agreement among the scheme results for low wavenumbers ($\kappa_x \eta \leq 0.1$), but large disparity can be observed at intermediate and high wavenumbers.

As is evident from Fig. 3.18, numerical dissipation results in a marked degradation of the dissipation spectra at high wavenumber modes for QUICK, BQUICK, WENO3, SL3, and MCH. The magnitudes of the dissipation spectra for BCH and HOUC5 are noticeably higher, which indicates comparatively smaller artificial dissipative damping. A more quantitative comparison is shown in Table 3.1, where higher values of the average scalar dissipation rate ($\chi = 2\mathcal{D}\langle(\partial\phi/\partial x)^2 + (\partial\phi/\partial z)^2\rangle$, averaged on the center plane) indicate lower numerical dissipation. The dissipation spectra as well as the mean scalar dissipation rates suggest that numerical dissipation in BCH is lower than in QUICK, and is comparable to that in HOUC5. This is especially remarkable since both QUICK and HOUC5 are unbounded schemes, and we expect numerical damping in bounded schemes to be slightly higher than that in unbounded schemes. The extremely well behaved nature of the BCH

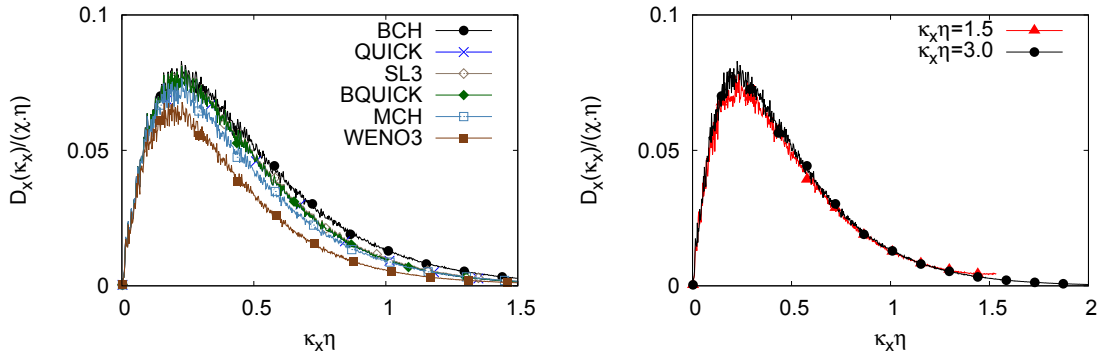

(a) Dissipation spectra at increased grid resolution (b) Coarse grid and fine grid spectra produced by BCH ($\kappa_x\eta = 3$)

Figure 3.19: 1D center plane dissipation spectra for the turbulent mixing layer with increased grid resolution ($\kappa_x\eta = 3$). All spectra normalized by the χ value for BCH, and then averaged over 11 separate snapshots.

scheme may be attributed to the sub-cell shape resolving capability of Hermite polynomials. Low numerical dissipation in BCH can be linked to the absence of a second-order derivative in Eqs. 3.29 and 3.31, which in turn implies that the excessive dissipation inherent in MCH results entirely from strict monotonicity enforcement.

Accuracy of the results furnished by BCH in the turbulent mixing layer is gauged by examining scalar dissipation spectra from a simulation run at twice the grid resolution (Fig. 3.19) of the base simulation. Upon grid refinement, spectra from all the schemes (barring WENO3) collapse onto a single curve (Fig. 3.19(a)), which is almost identical to the spectrum produced by BCH at the lower resolution (Fig. 3.19(b)). This collapse, in conjunction with the grid independent behavior of BCH, may be taken as evidence that the result furnished by the BCH scheme is indeed the 'true' solution of the simulation. Results for HOUC5 at the higher resolution could not be obtained owing to stability issues. We note that numerical dissipation in all of the schemes can be reduced greatly by increasing grid resolution (as indicated by the spectra, and the χ values listed in Table 3.1), but at a steep accompanying rise in computational cost.

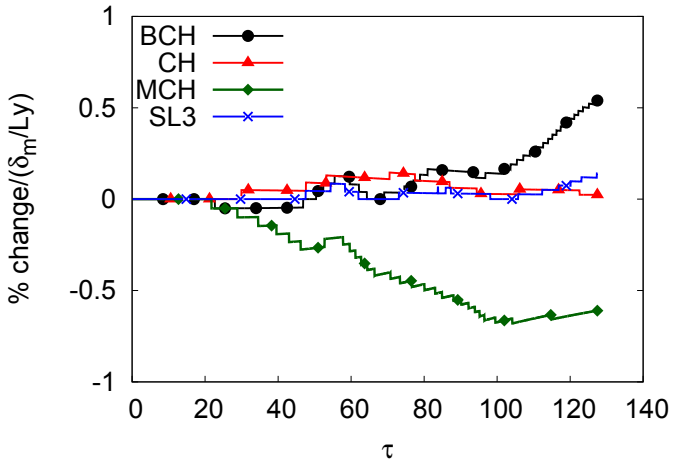

Figure 3.20: Time evolution of scalar mass change in the turbulent mixing layer. The y-axis has been normalized by δ_m/Ly, which is a measure of effective core thickness in time.

3.5.4.3 Mass conservation

Loss in conservation of the transported quantity is a central issue of concern when using semi-Lagrangian schemes. The interpolation procedure outlined in Section 3.2.3 is generally non-conservative, owing to the fact that the sum of all interpolation weights associated with a particular grid node (for a given time step) may not be equal to 1. This happens primarily in non-uniform velocity fields, where traceback causes certain grid nodes to be weighted more (or less) heavily than others. In addition to that, bounding corrections also introduce conservation errors into the scheme. There have been various efforts in the past to make semi-Lagrangian schemes conservative. However, these methods either introduce certain anomalous effects, such as failing to maintain physical bounds (as can happen with the use of so-called 'mass-fixers' [107, 78]), or are so prohibitively expensive that they are suitable for practical use only in 2D simulations (remapping techniques [77, 138]). As Williamson & Rasch [136] point out, conservation may only be important in a relative sense, especially when the conservation errors are small in comparison to source terms that may be present. That is to say, it may be possible to tolerate loss of conservation to a certain degree, in the similar manner that we tolerate discretization errors.

Turbulent simulations run using BCH show deviations in the total scalar mass amounting to approximately 0.5% in the mixing layer (Fig. 3.20). The curves shown in Fig. 3.20 were evaluated as

the total mass percentage deviation in the domain normalized by the effective core thickness. Both the mass deviation and the core thickness evolve in time. Normalization by the core thickness ratio δ_m/Ly (which varies from 0.012 to 0.027) was done to account for the fact that regions outside the core, where the scalar value is effectively constant, experience near perfect interpolation and do not suffer from mass deviation. Perfect interpolation occurs since all grid-node scalar values are either 0 or 1 in these regions.

It is important to note that minor mass fluctuations seem to have no measurable impact on the ability of the scheme to predict transport characteristics, as already confirmed in Section 3.5.2. On the contrary, results from the majority of the Eulerian schemes (Fig. 3.18), which do in fact conserve the transported scalar perfectly, were seen to be largely unusable if high accuracy is desired in turbulent cases. Loss in conservation could be cause for greater concern when considering active scalars, however, the scope of the work presented in this chapter is limited to the transport of passive scalars. Thus, depending on the demands of the physical problem, it might be preferable to tolerate a minute and inconsequential loss in conservation (as done in BCH), rather than to suffer from substantial numerical errors inherent in the transport scheme.

3.5.4.4 Cost

Apart from well-behaved numerics, computational efficiency plays a decisive role in determining the usability of numerical algorithms. Tests used to measure computational performance of the BCH scheme demonstrate that improved accuracy of the scheme is not necessarily associated with increased computational cost. In fact, turbulent runs indicate that the computational cost of the BCH scheme is comparable to that of BQUICK and WENO3 (Table 3.1).

Raw grind time, however, does not serve as a truly reliable measure of computational cost. For instance, scalar dissipation spectra in Fig. 3.19 establish that all bounded schemes require at least a twofold increase in grid resolution to be able to produce results of quality comparable to BCH. At a constant CFL number, this amounts to a 16$\times$ increase in computational cost. Needless to say, this is a prohibitively large increase, and makes the BCH scheme immediately attractive for use in

computationally intensive simulations.

3.5.5 Homogeneous isotropic turbulence

The turbulent mixing layer configuration discussed in Sec. 3.5.4 was selected specifically since it provides an ideal environment for testing scalar boundedness and assessing numerical diffusion. We now use an alternate turbulent configuration, namely, homogeneous isotropic turbulence, to compare the numerical performance of BCH against spectral schemes, which are used frequently in turbulence computations involving simple geometries. The configuration utilizes a uniform mesh on a cubic domain of length 2π, with periodic boundary conditions in all three directions. The velocity was forced spectrally in a low wavenumber shell [2].

Due to the absence of a natural means of sustaining scalar fluctuations in homogeneous isotropic turbulence, a mean scalar gradient ($\boldsymbol{G}$) was imposed as follows [101, 46]:

$$\frac{\partial \phi}{\partial t} + \boldsymbol{u} \cdot \nabla \phi = \mathcal{D} \nabla^2 \phi + \boldsymbol{G} \cdot \boldsymbol{u} \tag{3.44}$$

$$\boldsymbol{G} = (1, 0, 0) \tag{3.45}$$

The presence of the mean scalar gradient term implies that it is no longer appropriate to consider the scalar as being bounded by its initial maximum and minimum values. Under these conditions, the probability density function of scalar fluctuations is well represented by a Gaussian distribution [55].

The time steps for velocity and scalar transport were decoupled to enable multiple velocity iterations for a single scalar step. Since semi-Lagrangian schemes are stable for CFL > 1, this allows us to take larger timesteps for the scalar, constrained only by the physically relevant Kolmogorov time scale ($\Delta t_\phi < \tau_\eta = (\nu/\epsilon)^{1/2}$), instead of being constrained by the numerical stability of the velocity scheme. This can result in substantial computational savings, especially when using different grid resolutions for the velocity and scalar, determined by the Kolmogorov and Batchelor length scales ($\eta_B = \eta/\sqrt{Sc}$), respectively [55, 76].

The physical parameters for the homogeneous simulation were selected ($Re_\lambda = 140$, $Sc = 1$) to

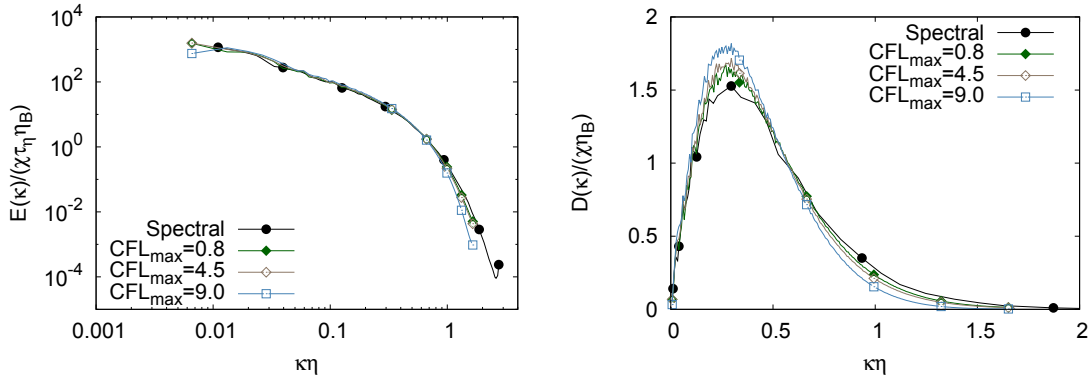

(a) (b)

Figure 3.21: 3D energy and dissipation spectra for homogeneous isotropic turbulence simulations. Results shown for spectral scheme (data taken from Ref [46]), and BCH with three different values of CFL_{max}.

allow for direct comparison with spectral scheme results available in Ref. [46]. A grid size of 512^3 was used to ensure that $\kappa_{max}\eta = 1.5$. At this grid resolution, the time step associated with stable velocity iterations was approximately $0.001\tau_\eta$. To assess the performance of BCH for $\mathrm{CFL}_{max} > 1$, Δt_ϕ was taken to be larger than the velocity timestep, and the simulations were run until the scalar statistics became stationary. The relevant scalar energy and dissipation spectra are plotted in Fig. 3.21, and indicate good agreement between results produced by BCH and the spectral scheme. Simulations run with CFL_{max} values much larger than 1 suffer from the presence of time-splitting errors, which may be related to the use of the forward Euler method in Eq. 3.3. The maximum deviation from mass conservation, defined as (total change in scalar mass in domain)/(initial mass), was observed to be approximately 0.1%, 0.2%, and 0.5%, for the CFL_{max} values of 0.8, 4.5, and 9, respectively. As in the mixing layer case, turbulent statistics in the homogeneous configuration remain unaffected by the minor loss in conservation.

To assess the comparison of BCH *vs.* Eulerian schemes at large Schmidt numbers, additional Direct numerical simulations of homogeneous turbulence were run with $Re_\lambda = 30$ and $Sc = 16$. Scalar dissipation spectra computed on grid resolutions of $\kappa_{max}\eta_B = 1.5$ and $\kappa_{max}\eta_B = 3$ (2× DNS resolution) are compared in Fig. 3.22. Once again, we confirm that the numerical dissipation inherent in BCH is much smaller than that in MCH, as is evident from Fig. 3.22(a). Furthermore, results produced by BCH in the homogeneous case are comparable in accuracy to HOUC5 (Fig. 3.22(b)),

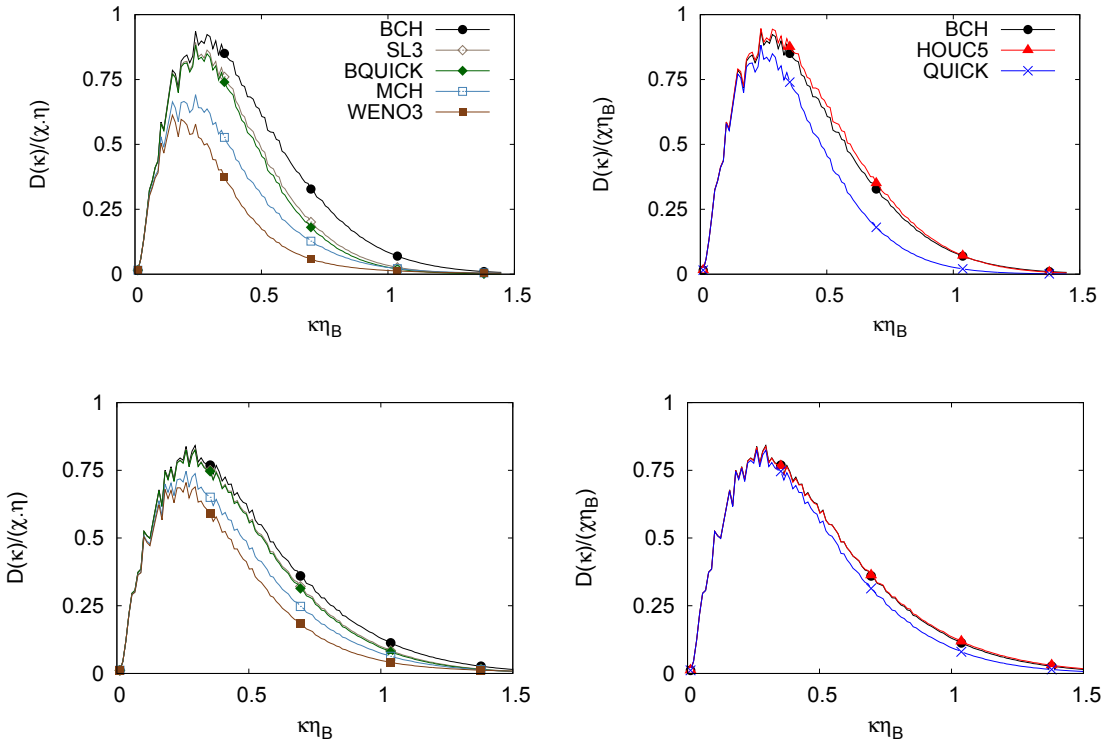

(a) BCH *vs.* bounded schemes

(b) BCH *vs.* unbounded schemes

Figure 3.22: 3D scalar dissipation for homogeneous isotropic turbulence, with $Re_\lambda = 30$, and $Sc = 16$. Top row shows results obtained with grid resolution $\kappa_{max}\eta_B = 1.5$, and bottom row shows results for $\kappa_{max}\eta_B = 3$. The dissipation spectra have been normalized by the χ value for BCH at the corresponding resolutions.

and are superior in quality to all the other schemes tested.

3.6 Summary

In this Chapter, an improved semi-Lagrangian transport scheme for passive scalar mixing is proposed, and tested in both laminar and turbulent flows. This scheme, named BCH, is designed specifically for the turbulent transport of scalars that must respect physical bounds. The scheme is based on the semi-Lagrangian treatment of the advection-diffusion equation, and makes use of cubic Hermite polynomials for interpolation. Boundedness of the scalar field is ensured by applying derivative limiting techniques to the Hermite polynomial. The novelty of the proposed algorithm lies in the way that sub-cell extrema are treated to restore boundedness. The approach is distinct from 'clipping' (which corresponds to a hard reset of the interpolated scalar to the nearest physical extremum), since it makes an effort to preserve the sub-cell shape of the interpolated profile. The shape-preserving ability of Hermite polynomials makes them especially useful for resolving fine scale scalar structures in turbulent simulations.

Performance of the proposed transport scheme, along with that of several other commonly used schemes (e.g., BQUICK, WENO3, HOUC5, etc.), is tested in two laminar cases, a three-dimensional turbulent mixing layer, and in homogeneous isotropic turbulence. The BCH scheme outperforms all other bounded schemes tested, with regard to the ability to resolve small scale turbulent structures. This is confirmed by examining scalar energy and dissipation spectra on the center plane of the mixing layer. Simulations run with the other bounded schemes require at least twice the spatial resolution to obtain spectra of comparable quality. In addition to cost savings on account of a coarser grid, comparatively lenient stability conditions for semi-Lagrangian schemes allow a further drop in computational cost for BCH, in comparison to Eulerian schemes. Additional simulations of homogeneous isotropic turbulence indicate that results produced by BCH are comparable to those produced by spectral schemes, with a slight loss of accuracy caused by time splitting errors, when using very large timesteps unconstrained by the CFL number. The superior performance of the BCH scheme, with respect to a majority of the other Eulerian schemes tested, persists even when using

relatively large Schmidt numbers in homogeneous turbulent simulations. Although semi-Lagrangian schemes are known to suffer from mass conservation issues (which the turbulent test cases confirm), the minimal loss in conservation had no measurable impact on predicting the correct turbulent characteristics.

Overall, the BCH scheme offers an attractive alternative to Eulerian schemes for turbulent simulations of passive scalar mixing, on account of reduced numerical errors and computational cost, and relative ease of implementation. With excellent performance in both shear dominated and homogeneous turbulent cases, the BCH scheme is ideal for generating reference DNS as well as LES datasets aimed at investigating subfilter scalar-flux behavior, unhampered by the presence of numerical errors. Having reduced the numerical errors associated with the transport of a scalar field, the next step is to identify the best subfilter scale model for use in LES.

Chapter 4

Subfilter Scalar-Flux Vector Orientation in Homogeneous Isotropic Turbulence[1]

In this chapter, we investigate the alignment behavior of the subfilter scalar-flux vector in homogeneous isotropic turbulence, given the critical role of the vector's orientation in regulating subfilter dissipation. The primary objectives of the work presented are threefold: 1) to relate the predicted vector's orientation to known velocity-dependent quantities (such as vorticity); 2) to identify the influence (if any) of the Schmidt number of the transported scalar, and the influence of width and shape of the filtering kernel used; and 3) to assess the ability of an existing model in describing this orientation. In the scope of reducing the computational cost of LES of high Schmidt number scalar transport, the present analysis focuses on filtering in the viscous-convective subrange.

Details of the simulations used for *a priori* analysis are provided in Sec. 4.1. Section 4.2 examines the preferential alignment of the vorticity vector ($\boldsymbol{\omega}$), the scalar gradient vector ($\nabla\phi$), and the numerically computed SFF vector ($\boldsymbol{\tau}_\phi$) in the strain-rate eigenframe. The accuracy with which the tensor-diffusivity model describes the orientation of $\boldsymbol{\tau}_\phi$ is discussed in Sec. 4.3. Section 4.4 details the mathematical analysis of the tensor-diffusivity model, which is used to explain the preferential alignment observed in Sec. 4.2. Finally, the effects of filter-shape and scalar-forcing method on $\boldsymbol{\tau}_\phi$ orientation, and the ensuing implications of using implicit filtering in LES, are discussed in Sec. 4.5.

[1] The work in this chapter has been published in large part in Verma, S., Blanquart, G., Physical Review E (2014).

Table 4.1: DNS datasets used for analyzing $\boldsymbol{\tau}_\phi$ behavior ($Re_\lambda = 30$).

Case	N	Sc	$\kappa_{max}\eta$	$\kappa_{max}\eta_B$
A	1024	256	23.2	1.4
B	512	16	11.6	2.9
C	512	4	11.6	5.8

4.1 Simulation details

To investigate *a priori* the behavior of the orientation of the computed SFF vector, Direct numerical simulations of homogeneous isotropic turbulence are used. The simulations were performed using a second-order energy conserving Finite-Difference velocity scheme [41], and a fifth-order accurate upwind Finite-Volume scheme for the scalar [99]. The velocity field was forced by injecting energy in a low wavenumber shell [2]. Two distinct scalar-forcing techniques were used, one characterized by the presence of a Mean Scalar Gradient (MSG) [101], and the other simulating the decay of scalar fluctuations (Linear Scalar forcing—LS) [31]. The use of the two scalar-forcing methods allows us to investigate differences in $\boldsymbol{\tau}_\phi$ alignment that might be related to distinct scalar variance cascade mechanisms (forced vs. decaying) at the small length scales. Simulations using both MSG and LS forcings were run simultaneously; two independent scalars were transported using the same velocity field, each being forced using one of the forcing methods.

Details of the physical parameters used in the simulations are given in Table 4.1. The Taylor-scale Reynolds number for all the simulations was kept constant at a value of $Re_\lambda = 30$, and the Schmidt number was varied from $Sc = 4$ to $Sc = 256$. It was necessary to restrict Re_λ to a relatively low value, since resolving the Batchelor scale at high Sc incurs considerable computational cost. Nonetheless, scalar transport in the viscous-convective subrange is governed largely by the velocity scales in the dissipative range [13], which show universal behavior to some extent even at low Reynolds numbers [143]. $Re_\lambda = 30$ yields a sufficiently turbulent flow-field for our purpose, and most of the results discussed in this Chapter may be extended to larger Reynolds numbers with appropriate consideration.

For post-processing purposes, scalar and velocity modes corresponding to the highest $2/3^{rd}$ of the wavenumbers were deleted using a sharp-spectral filter to prevent aliasing caused by multiplication

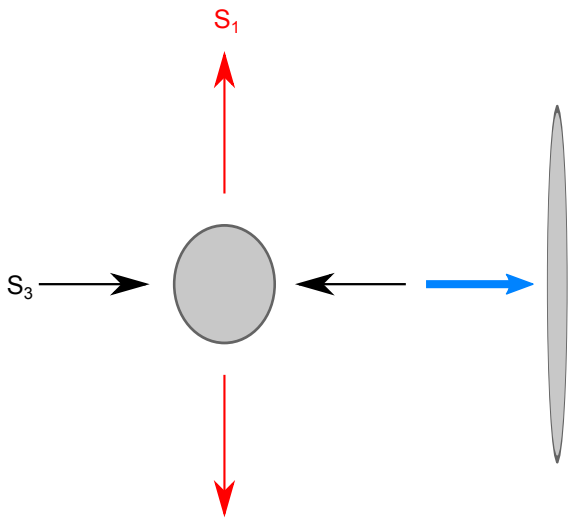

Figure 4.1: Schematic of scalar material element undergoing straining.

of variables (Orszag's '$2/3^{rd}$' truncation rule [100]).

4.2 Vector alignment in the local strain-rate eigenframe

4.2.1 Choice of reference frame

Inspecting the orientation of the various vectors of interest (e.g., $\boldsymbol{\omega}$, $\nabla\phi$, $\boldsymbol{\tau}_\phi$) requires the selection of an appropriate reference frame. The lab-fixed frame is not an ideal choice for this purpose, since the homogeneous and isotropic nature of the turbulent fluctuations results in random orientation of the vectors with respect to the lab-based orthonormal axes. Instead, the orthonormal reference frame formed by the eigenvectors of the local strain-rate tensor ($S_{ij} = \frac{1}{2}(u_{i,j} + u_{j,i})$) presents a more suitable choice [4, 62]. This is due to the fact that the dynamics of passive scalar transport (as well as those of the velocity field itself) are governed largely by straining from the velocity field. Additionally, the tensor-diffusivity model depends closely on vorticity and the velocity strain-rate (as will become apparent in Sec. 4.4), which provides further motivation for using the eigenframe as a basis for determining vector orientation.

Figure 4.1 shows the schematic of a scalar material element undergoing deformation in a straining flow field. S_1 represents the direction of the most extensive eigenvector of S_{ij} (positive eigenvalue:

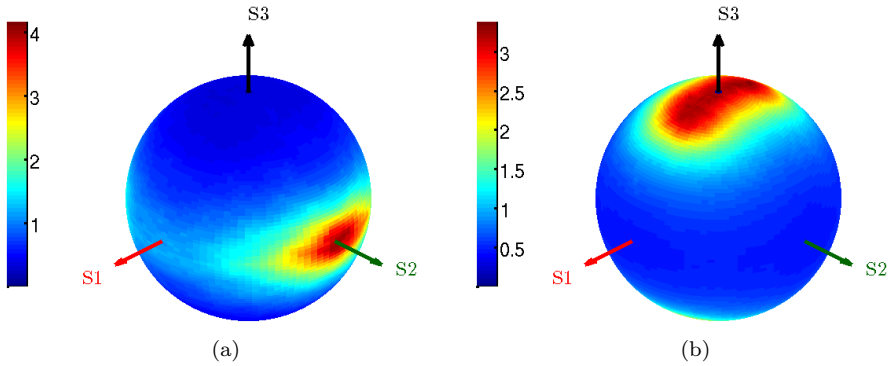

Figure 4.2: Alignment of (a) $\boldsymbol{\omega}$ and (b) $\nabla\phi$ in the S_{ij} eigenframe. (Case A: $Re_\lambda = 30$, $Sc = 256$).

$\lambda_1 > 0$), and S_3 represents the direction of the most compressive one ($\lambda_3 < 0$). The intermediate eigenvalue (corresponding to the eigenvector S_2) is known to be close to zero (and slightly positive) from experimental [125] and numerical studies [4] of incompressible homogeneous isotropic turbulence. Thus, the S_2 direction experiences comparatively little material element deformation.

4.2.2 Alignment of $\boldsymbol{\omega}$ and $\nabla\phi$ in the eigenframe

To examine the preferential alignment of the various quantities of interest, we make use of three-Dimensional (3D) joint Probability Density Functions (PDF), hereafter referred to as 'sphere-PDFs'. Such illustrations, e.g., the ones shown in Fig. 4.2 for the vorticity vector ($\boldsymbol{\omega} = \nabla \times \boldsymbol{u}$) and the scalar gradient vector ($\nabla\phi$), provide a powerful means of visualizing vector orientation in the strain-rate eigenframe [61, 62]. The color levels denote the probability density function of vector orientation, normalized by the PDF value for uniform random orientation ($\text{PDF}_{random} = 1/(4\pi) = 0.0796$). In other words, a value of 1 on the color axis denotes probability equal to that of random orientation, a value lower than 1 indicates aversion to alignment at the corresponding locations, and a value greater than 1 suggests preferred orientation.

Both $\boldsymbol{\omega}$ and $\nabla\phi$ are known to exhibit strong preferential orientation in the S_{ij} eigenframe, with the vorticity vector aligning along the intermediate eigenvector S_2 [4, 125, 59, 58, 61] (Fig. 4.2(a)), and the scalar gradient vector aligning with the most compressive eigenvector S_3 [4] (Fig. 4.2(b)). It is evident from Fig. 4.2(a) that the probability of alignment of $\boldsymbol{\omega}$ along the S_2 axis is approximately

4 times higher than would be expected for random orientation, and falls quickly to values close to 0 in regions far away from the axis. The scalar gradient (Fig. 4.2(b)) tends to align along the S_3 axis with a normalized PDF value slightly greater than 3. The alignment of $\nabla\phi$ with S_3 is an expected physical outcome, and may be explained using Fig. 4.1. Contraction of the material element in the S_3 direction gives rise to the highest scalar gradient magnitude in this direction.

4.2.3 Alignment of $\boldsymbol{\tau}_\phi$ in the eigenframe

One of the important metrics that can be used to gauge model effectiveness in *a priori* studies is the models' ability to describe the orientation of the $\boldsymbol{\tau}_\phi$ vector. Accurate knowledge of this orientation is crucial for correctly determining the amount of subfilter scalar variance dissipation given by:

$$\chi_{\boldsymbol{\tau}_\phi} = -2\nabla\phi \cdot \boldsymbol{\tau}_\phi, \tag{4.1}$$

which originates from the filtered scalar-variance equation:

$$\frac{\partial\widetilde{\phi}^2}{\partial t} + \nabla\cdot\left(\widetilde{\boldsymbol{u}}\widetilde{\phi}^2\right) = \mathcal{D}\nabla^2\widetilde{\phi}^2 - 2\mathcal{D}|\nabla\widetilde{\phi}|^2 - 2\nabla\cdot\left(\widetilde{\phi}\boldsymbol{\tau}_\phi\right) + 2\nabla\widetilde{\phi}\cdot\boldsymbol{\tau}_\phi \tag{4.2}$$

To inspect the alignment of $\boldsymbol{\tau}_\phi$, the appropriate terms in Eq. 1.3 are obtained by filtering the DNS datasets spatially. This operation corresponds to a convolution with a filtering kernel in physical space, or equivalently, multiplication in Fourier space. Three different filtering kernels, namely the Gaussian filter, the box (or top-hat) filter, and the sharp-spectral filter are used here. The respective kernel representations in physical space are given below [79]:

$$Gaussian \quad : \quad G(x) = \left(\frac{6}{\pi\Delta^2}\right)^{\frac{1}{2}} exp\left(-\frac{6x^2}{\Delta^2}\right) \tag{4.3}$$

$$Box \quad : \quad G(x) = \frac{1}{\Delta}H\left(\frac{\Delta}{2} - |x|\right) \tag{4.4}$$

$$Sharp \quad : \quad G(x) = \frac{sin(\pi x/\Delta)}{\pi x} \tag{4.5}$$

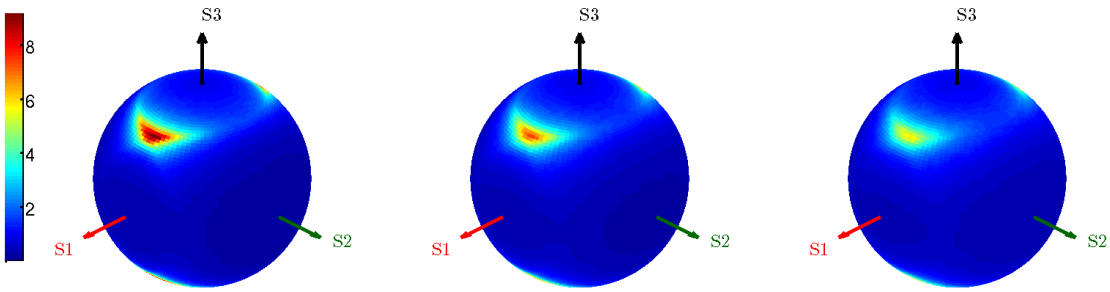

(a) $\kappa_c\eta = 10,\ \kappa_c\eta_B = 0.625$ (b) $\kappa_c\eta = 1.6,\ \kappa_c\eta_B = 0.1$ (c) $\kappa_c\eta = 0.8,\ \kappa_c\eta_B = 0.05$

Figure 4.3: Alignment of the subfilter flux vector ($\boldsymbol{\tau}_\phi$) in the filtered strain-rate ($\widetilde{S}_{ij}$) eigenframe, computed from Case A using the Gaussian filtering kernel. Figures shown correspond to three different filter cutoffs.

Here, Δ is referred to as the filter-width. The forms of the Gaussian and top-hat filters in Eqs. 4.3 and 4.4 ensure that their second moments ($\int_{-\infty}^{\infty} x^2 G(x)dx$) match [79]. The width (in physical space) for the sharp filter is defined through the filter cutoff wavenumber ($\kappa_c = \pi/\Delta$) in Fourier space. In most of the analysis shown in this Chapter, Δ has been chosen such that the effective filter cutoff wavenumber lies in the viscous-convective subrange; in other words, $\kappa_c\eta > 1.5$.

Figure 4.3 shows the sphere-PDF for $\boldsymbol{\tau}_\phi$ in the eigenframe, computed pointwise for Case A ($Re_\lambda = 30,\ Sc = 256$) using the Gaussian filter. The panels show the alignment behavior for three different effective filter-widths, corresponding to a scenario when approximately 60% ($\kappa_c\eta_B = 0.625$), 93% ($\kappa_c\eta_B = 0.1$), and 97% ($\kappa_c\eta_B = 0.05$) of the scalar modes have been filtered out. At these cutoff widths, $\boldsymbol{\tau}_\phi$ exhibits strong preference for alignment at a particular angle in the $S_1 - S_3$ plane, specifically, at a polar angle of $41.4° \pm 1.8°$ from the S_3 axis. The normalized PDF maxima are 9.14, 7.32, and 5.77 times the value expected for random orientation, respectively. It is surprising to observe such large values of PDF_{max}, especially in cases where more than 90% of the scalar modes present originally have been filtered out (Figs. 4.3(b) and 4.3(c)). Nonetheless, there is a noticeable drop in the value of PDF_{max} with increasing filter-width size.

We note that the velocity field (and hence $\widetilde{S}_{ij}$) is fully resolved for the first two panels ($\kappa_c\eta = 10$ and 1.6), and only marginally filtered for the last one ($\kappa_c\eta = 0.8$). This happens since filtering in the viscous-convective subrange (feasible only for $Sc \gg 1$: Table 4.1) does not impact the velocity field, as long as $\kappa_c\eta \geq 1.5$. The same argument would not hold for $Sc \leq 1$, since cutoffs with $\kappa_c\eta \leq 1.5$

Table 4.2: PDFs of SFF vector alignment for different Schmidt numbers, using the Gaussian filtering kernel. The range of accuracy for θ_P and θ_A is $\pm 0.9°$ and $\pm 1.8°$, respectively, since 100 bins were used for discretizing both of these angles when constructing the sphere-PDFs.

	Case A ($Sc = 256$)		
PDF	$\kappa_c\eta = 10$	$\kappa_c\eta = 1.6$	$\kappa\eta = 0.8$
min	0.15	0.17	0.18
max	9.14	7.32	5.77
θ_P	42.3°	42.3°	42.3°
θ_A	5.4°	1.8°	5.4°
	Case B ($Sc = 16$)		
	$\kappa_c\eta = 3.2$	$\kappa_c\eta = 1.6$	$\kappa_c\eta = 0.8$
min	0.14	0.14	0.15
max	9.57	8.57	7.09
θ_P	40.5°	40.5°	40.5°
θ_A	-1.8°	-1.8°	-1.8°
	Case C ($Sc = 4$)		
	$\kappa_c\eta = 1.8$	$\kappa_c\eta = 1.6$	$\kappa_c\eta = 0.8$
min	0.14	0.14	0.13
max	8.91	8.75	7.10
θ_P	40.5°	40.5°	40.5°
θ_A	1.8°	1.8°	1.8°

would result in both scalar and velocity modes being filtered.

Sphere-PDFs for all the datasets listed in Table 4.1 were computed in a similar manner, and the relevant quantitative data is listed in Table 4.2. We use θ_P to denote the polar angle measured from axis S_3 to the location of PDF_{max} on the sphere-PDFs, and θ_A to represent the corresponding azimuthal angle measured from axis S_1. For enhanced readability, all angles have been confined using symmetry to the quadrant that is prominently visible in Fig. 4.3, i.e., we set $\theta_P = 180° - \theta_P$ if $\theta_P > 90°$, $\theta_A = \theta_A - 180°$ if $90° < \theta_A \leq 270°$, and $\theta_A = \theta_A - 360°$ if $\theta_A > 270°$. θ_P values for all three cases (A through C in Table 4.2) are observed to be $41.4° \pm 1.8°$, and θ_A values fall within the range $1.8 \pm 5.4°$. The angles, as well as the PDF max/min data show little variation among the three cases, which points to possible Schmidt number independence of the SFF vector orientation. This observation, as well as the weak influence of the filter- width discussed earlier, are related to the fact that the orientation of the SFF vector in the eigenframe can be shown to be completely independent of the scalar field when using the Gaussian filter. In addition, sphere-PDFs computed using the box filter (Fig. 4.4) are virtually identical to those computed using the Gaussian filter

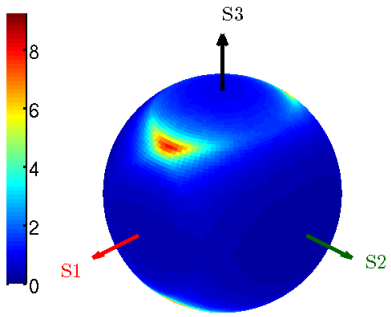

Figure 4.4: Alignment of $\boldsymbol{\tau}_\phi$ computed from Case A using the box filter with $\kappa_c\eta = 1.6$ ($\kappa_c\eta_B = 0.1$).

(Fig. 4.3(b)), both qualitatively and quantitatively. The reason for this behavior of $\boldsymbol{\tau}_\phi$ orientation, as well as that for its apparent independence from the filtered scalar field, is discussed in Sec. 4.4.1.

4.3 $\boldsymbol{\tau}_\phi$ orientation and the tensor-diffusivity model

In this section, we compare the accuracy with which the tensor-diffusivity model [79, 35, 80, 16], describes $\boldsymbol{\tau}_\phi$ orientation when using a Gaussian filter. Other SFF models, namely, the Smagorinsky model [118] and the stretched vortex model [110], were not examined since they are designed primarily for use with the filter-width located in the inertial subrange. For instance, the model constant for the stretched vortex model is zero with the filter-width located in the viscous-convective subrange, since it involves the use of subfilter velocity energy (which is zero if $\widetilde{\boldsymbol{u}} \equiv \boldsymbol{u}$).

4.3.1 The tensor-diffusivity model

In this section, we will evaluate the tensor-diffusivity model, which seems to be a good candidate for representing the subfilter scalar-flux when the filter-width is located in the viscous-convective subrange. For sufficiently smooth velocity ($\boldsymbol{u}$) and scalar (ϕ) fields, and for a small filter-width Δ, the tensor-diffusivity model is evaluated from the leading order term in the Taylor-series expansion of Eq. 1.3. More precisely, the expansion takes the following form for a variety of filtering kernels,

including the Gaussian and box filters [16, 30, 109]:

$$\begin{aligned} \boldsymbol{\tau}_\phi &= \widetilde{\boldsymbol{u}\phi} - \widetilde{\boldsymbol{u}}\widetilde{\phi} \\ &= C\ \nabla\widetilde{\boldsymbol{u}} \cdot \nabla\widetilde{\phi} + O(\Delta^4) \end{aligned} \tag{4.6}$$

The leading order term in Eq. 4.6 constitutes the tensor-diffusivity model. With the filter cutoff located in the viscous-convective subrange, $\nabla\widetilde{\boldsymbol{u}} = \nabla\boldsymbol{u}$, and Eq. 4.6 simplifies to:

$$\boldsymbol{\tau}_\phi \approx C\ \nabla\boldsymbol{u} \cdot \nabla\widetilde{\phi}. \tag{4.7}$$

The higher-order terms ($\mathrm{O}(\Delta^4)$), which were neglected in the expression above, involve higher-order velocity and scalar derivatives. In the viscous-convective subrange, scalar material elements have been speculated to experience effectively linear straining [13]. Under these conditions, it is appropriate to keep only the leading order term in Eq. 4.7. Given the dependence of the model on $\nabla\widetilde{\phi}$, an interesting approach may be to consider the evolution of the filtered scalar gradient equation in the turbulent field. However, we did not pursue this line of thought in the current work.

The coefficient C in Eq. 4.7 depends on the second moment ($\int_{-\infty}^{\infty} x^2 G(x)dx$) of the filtering kernel, and is identical for the forms of the Gaussian and box filtering kernels shown in Eqs. 4.3 and 4.4 ($C = \Delta^2/12$). This implies that, to leading order, $\boldsymbol{\tau}_\phi$ is virtually identical for both the Gaussian and box filters, which can be confirmed from Figs. 4.3(b) and 4.4. We note that moment integrals of the sharp-spectral kernel do not converge to finite values for order greater than 0. To demonstrate the importance of having a finite second moment integral, we show sphere-PDFs of $\boldsymbol{\tau}_\phi$ computed using the sharp filter in Fig. 4.5. We observe a drastic change in the behavior of the SFF orientation, when compared with equivalent results from the Gaussian and box filters (Figs. 4.3 and 4.4). The SFF vector distribution in the eigenframe is close to being completely random (i.e., PDF value $\approx$ 1) with the sharp filter, an observation which persists for more than an order of magnitude variation in the filter cutoff (Fig. 4.5). PDF values obtained using the three different filtering kernels are provided in Table 4.3, along with data relevant for comparing MSG and LS

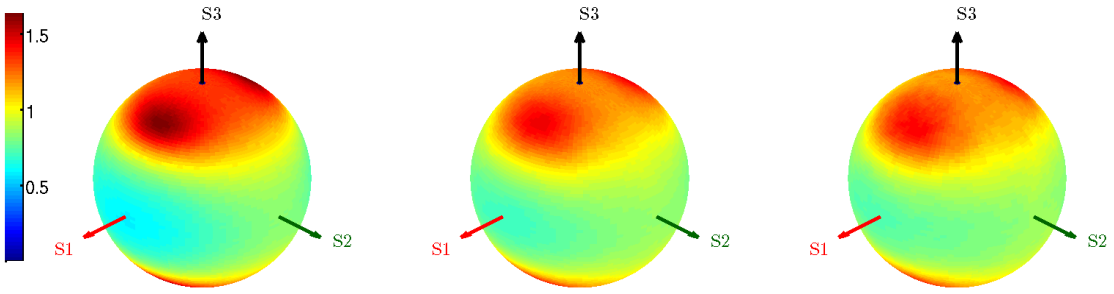

(a) $\kappa_c\eta = 10,\ \kappa_c\eta_B = 0.625$ (b) $\kappa_c\eta = 1.6,\ \kappa_c\eta_B = 0.1$ (c) $\kappa_c\eta = 0.8,\ \kappa_c\eta_B = 0.05$

Figure 4.5: Similar to Fig. 4.3, but computed using the sharp-spectral filter.

Table 4.3: Case A ($Re_\lambda = 30$, $Sc = 256$). Comparison of alignment data for different filtering kernels, and for MSG and LS forcing. The range of accuracy for θ_P and θ_A is $\pm 0.9°$ and $\pm 1.8°$, respectively.

		MSG			LS		
Filter	PDF	$\kappa_c\eta = 10$	$\kappa_c\eta = 1.6$	$\kappa_c\eta = 0.8$	$\kappa_c\eta = 10$	$\kappa_c\eta = 1.6$	$\kappa_c\eta = 0.8$
Gaussian	min	0.15	0.17	0.18	0.15	0.18	0.20
	max	9.14	7.32	5.77	9.03	7.09	5.48
	θ_P	42.3°	42.3°	42.3°	42.3°	42.3°	42.3°
	θ_A	5.4°	1.8°	5.4°	5.4°	5.4°	1.8°
Box	min	0.15	0.17	0.17	0.15	0.18	0.20
	max	9.23	7.88	6.42	9.10	7.64	6.03
	θ_P	42.3°	42.3°	40.5°	42.3°	42.3°	42.3°
	θ_A	5.4°	5.4°	1.8°	5.4°	5.4°	1.8°
Sharp-spectral	min	0.29	0.35	0.36	0.29	0.36	0.37
	max	1.63	1.46	1.44	1.63	1.43	1.42
	θ_P	35.1°	36.9°	35.1°	35.1°	35.1°	33.3°
	θ_A	1.8°	1.8°	9°	1.8°	5.4°	9°

forced scalar fields [31] (to be discussed in Sec. 4.5.1). The quantitative data confirms significant differences that arise when using the Gaussian/box filters vs. the sharp-spectral filter. These results suggest that the observed alignment of $\boldsymbol{\tau}_\phi$ does not have a physical significance independently of the filtering operation.

Severe filter dependence of the correlation between model described and exact subfilter stress tensor ($\boldsymbol{\tau}_{\boldsymbol{u}}$) has been observed in previous numerical [104, 40] and experimental [84] studies. Thus, the current observations, combined with those available in the literature, provide strong support for the viewpoint that in order to get accurate results, filtering and modeling must be treated as a unified process [104, 108, 137, 40] , irrespective of whether the velocity or the scalar is being modeled.

In spite of very different orientation of $\boldsymbol{\tau}_\phi$ when using the sharp-spectral filter, the results discussed in Sec. 4.2.3, and those to be discussed in Sec. 4.4, remain broadly applicable, since the expansion in Eq. 4.6 is valid for a wide class of continuous and discrete filters [30, 109] with finite second moments [30, 109]. We reiterate that Eq. 4.6 is not valid when using the sharp-spectral filtering kernel, since the second moment of the sharp filter does not converge to a finite value. Thus, the tensor-diffusivity model may not perform well in describing $\boldsymbol{\tau}_\phi$ orientation when coupled with the sharp filter.

In addition to the original tensor-diffusivity model shown in Eq. 4.7, we use a 'regularized' form of the model [9], which removes the λ_1 and λ_2 components from the model definition:

$$\boldsymbol{\tau}_\phi = \frac{\Delta^2}{12}\left(\lambda_3 \widehat{\boldsymbol{e}}_3 \cdot |\nabla\widetilde{\phi}|\widehat{\boldsymbol{e}}_\phi + \frac{1}{2}\boldsymbol{\omega} \times \nabla\widetilde{\phi}\right) \tag{4.8}$$

This form of the model is consistent with assumptions that will be used later on to arrive at a simplified version of the equation (Eq. 4.15 in Sec. 4.4.1).

4.3.2 Orientation described by the two subfilter models

To compare the effectiveness of the tensor-diffusivity model in describing $\boldsymbol{\tau}_\phi$ orientation, we compute PDFs of the angles that the vectors defined by the two model terms in Eqs. 4.7, and 4.8 subtend

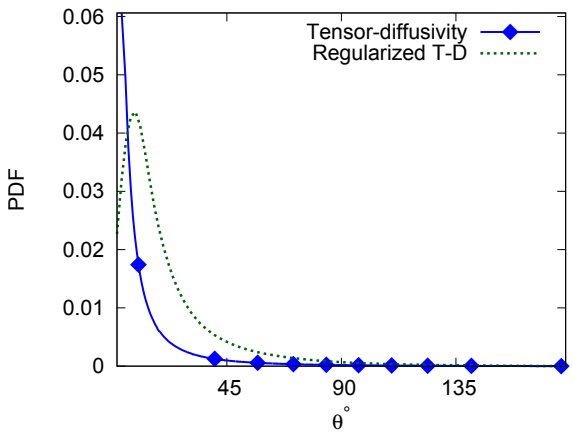

Figure 4.6: PDFs of the angle between the true SFF vector and the model descriptions. Computed *a priori* from dataset B by filtering with the Gaussian filter at $\kappa_c\eta = 1.6$.

with the vector defined by Eq. 1.3. The results shown in Fig. 4.6 indicate that the tensor-diffusivity model-described vector is co-aligned with the exact $\boldsymbol{\tau}_\phi$, whereas the regularized form of the model leads to a slight deterioration in alignment. Similar results were found for all three models when using the box filter. Given the strong directional correlation between the exact $\boldsymbol{\tau}_\phi$ and the tensor-diffusivity model prediction, we conduct a detailed examination of the tensor-diffusivity model with regard to the strain-rate eigenframe.

4.4 Strain-rate eigenframe-based analysis of the tensor-diffusivity model

The SFF vector computed from filtered DNS data (Eq. 1.3) shows a very strong preference for alignment at a particular angle in the $S_1 - S_3$ plane, when using the Gaussian or box filtering kernels (Figs. 4.3 and 4.4). This dependence can be explained by analyzing the tensor-diffusivity model [79, 35, 80, 16] for scalar transport. A similar analysis was carried out by Higgins et al. [62] regarding subfilter heat flux orientation in atmospheric measurement data. The authors found $\boldsymbol{\tau}_\phi$ to lie in the plane spanned by the 'mixed model', i.e., the tensor-diffusivity model combined with the Smagorinsky model. However, we'll show that the orientation of $\boldsymbol{\tau}_\phi$ in simulation data can be

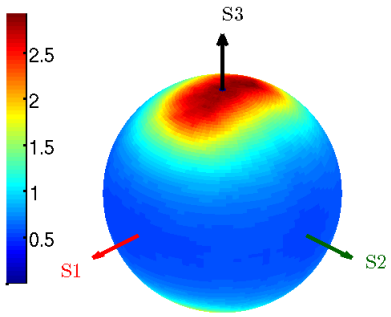

Figure 4.7: Alignment of $\nabla\widetilde{\phi}$ in the S_{ij} eigenframe. Computed from Case A using the Gaussian filter with $\kappa_c\eta = 1.6$ ($\kappa_c\eta_B = 0.1$).

described exactly by the tensor-diffusivity model alone.

4.4.1 Explanation for orientation

To examine the reason for $S_1 - S_3$ orientation of $\boldsymbol{\tau}_\phi$, the velocity gradient tensor ($\nabla\boldsymbol{u}$) in Eq. 4.7 is decomposed [62] into its symmetric and anti-symmetric parts, i.e., the strain-rate tensor $S_{ij} = 1/2(u_{i,j} + u_{j,i})$ and the rotation tensor $\Omega_{ij} = 1/2(u_{i,j} - u_{j,i})$:

$$\boldsymbol{\tau}_\phi = \frac{\Delta^2}{12}(\boldsymbol{S} + \boldsymbol{\Omega}) \cdot \nabla\widetilde{\phi} \tag{4.9}$$

$$= \frac{\Delta^2}{12}\boldsymbol{S} \cdot \nabla\widetilde{\phi} + \frac{\Delta^2}{24}\boldsymbol{\omega} \times \nabla\widetilde{\phi} \tag{4.10}$$

Furthermore, from the Taylor-series expansion [137] of $\nabla\widetilde{\phi}$ (for the Gaussian and box filters):

$$\nabla\widetilde{\phi} = \nabla\phi + \frac{\Delta^2}{24}\nabla^2(\nabla\phi) + \cdots, \tag{4.11}$$

the filtered scalar gradient orientation resembles that of the unfiltered gradient, which is the leading order term. We can confirm that the orientation of $\nabla\widetilde{\phi}$ is virtually identical to that of the unfiltered $\nabla\phi$, albeit with a slight drop in the maximum normalized PDF value, by comparing Figs. 4.7 and 4.2(b).

Using the observed alignment of $\boldsymbol{\omega}$ (Fig. 4.2(a)) and $\nabla\widetilde{\phi}$ in the eigenframe (Fig. 4.7), we make

the following simplifications:

$$\boldsymbol{\omega} = \pm|\boldsymbol{\omega}|\ \widehat{e}_2 \tag{4.12}$$

$$\nabla\widetilde{\phi} = \pm|\nabla\widetilde{\phi}|\ \widehat{e}_3, \tag{4.13}$$

where $\widehat{e}_2$ is the unit vector in the direction of axis S_2, and $\widehat{e}_3$ is the unit vector for S_3. Equation 4.10 can then be interpreted as follows:

$$\boldsymbol{\tau}_\phi \approx \frac{\Delta^2}{12}\left(\pm\boldsymbol{S}\cdot|\nabla\widetilde{\phi}|\ \widehat{\boldsymbol{e}}_3 \pm \frac{1}{2}|\boldsymbol{\omega}|\ \widehat{\boldsymbol{e}}_2 \times |\nabla\widetilde{\phi}|\ \widehat{\boldsymbol{e}}_3\right) \tag{4.14}$$

$$\approx \pm\frac{\Delta^2}{12}|\nabla\widetilde{\phi}|\left(\lambda_3\ \widehat{\boldsymbol{e}}_3 \pm \frac{1}{2}|\boldsymbol{\omega}|\ \widehat{\boldsymbol{e}}_1\right) \tag{4.15}$$

As is evident from Eq. 4.15, $\boldsymbol{\tau}_\phi$ has measurable components only in the S_1 and S_3 directions. This explains the strong aversion to alignment in the S_2 direction (Figs. 4.3 and 4.4). Equation 4.15 also explains the enstrophy dependence of $\boldsymbol{\tau}_\phi$ orientation observed in Ref. [34]. In regions of low enstrophy ($|\boldsymbol{\omega}|^2/2$), the $\widehat{\boldsymbol{e}}_3$ component of Eq. 4.15 is dominant, which results in $\boldsymbol{\tau}_\phi$ aligning with the S_3 eigenvector.

Equation 4.15 can further be used to extract deterministic information about $\boldsymbol{\tau}_\phi$ orientation in the $S_1 - S_3$ plane. The tensor-diffusivity model described SFF vector (Eq. 4.15) makes an angle of

$$\theta_{S_3} = \arctan\left(\pm\frac{|\boldsymbol{\omega}|}{2\lambda_3}\right) \tag{4.16}$$

with the S_3 axis, whereas the exact $\boldsymbol{\tau}_\phi$ (Eq. 1.3) subtends the following angle:

$$\alpha_{S_3} = \arccos\left(\frac{\boldsymbol{\tau}_\phi\cdot\widehat{\boldsymbol{e}}_3}{|\boldsymbol{\tau}_\phi|\ |\widehat{\boldsymbol{e}}_3|}\right). \tag{4.17}$$

The PDFs of θ_{S_3} and α_{S_3} computed from dataset B are plotted in Fig. 4.8. The distribution described by the tensor-diffusivity model, i.e., the PDF of θ_{S_3}, matches that of α_{S_3} quite well. The peaks in the PDFs occur at approximately 40° and 140°, which compares well with the θ_P values shown in

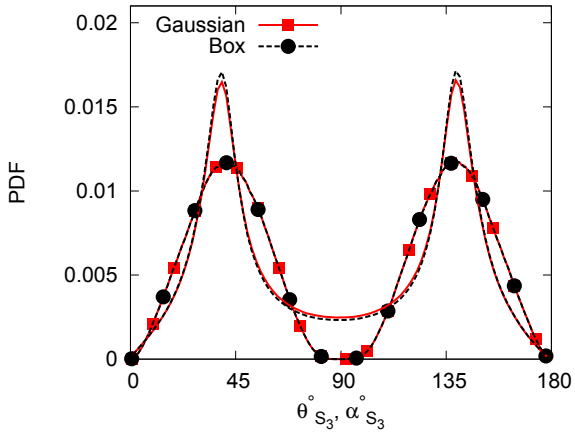

Figure 4.8: PDFs of θ_{S_3} (lines with symbols) and α_{S_3} (lines without symbols), computed pointwise from dataset B. Results shown for both Gaussian (solid lines) and box (broken lines) filters at $\kappa_c\eta = 1.6$.

Table 4.2. Thus, the four symmetric orientation angles resulting from Eq. 4.16, specifically, $\pm|\theta_{S_3}|$ and $\pi \pm |\theta_{S_3}|$, are in excellent agreement with the sphere-PDFs shown in Figs. 4.3 and 4.4. Overall, the numerical results support the analytical form of $\boldsymbol{\tau}_\phi$ given by Eq. 4.15, when using the Gaussian and box filters.

The complete independence of the angle in Eq. 4.16 from any scalar field related variable explains the Schmidt number and filter-width independence of the orientation of $\boldsymbol{\tau}_\phi$ observed in Sec. 4.2. The orientation only depends on velocity dependent variables, $\boldsymbol{\omega}$ and λ_3, which are largely unaffected by filtering for $\kappa_c\eta \geq 1.5$. However, the magnitude of $\boldsymbol{\tau}_\phi$ *will* depend on the filtered scalar field, as is clearly evident from the presence of $|\nabla\widetilde{\phi}|$ in Eq. 4.15. We remark that it is conceivable that θ_{S_3} may depend on the Taylor-scale Reynolds number, contingent on how Re_λ affects the ratio $|\boldsymbol{\omega}|/\lambda_3$. The observations in this section confirm that the tensor-diffusivity model provides an excellent means of representing the subfilter-scale scalar flux vector orientation analytically, when using the Gaussian or box filters.

4.4.2 Numerical stability of the tensor-diffusivity model

Although the tensor-diffusivity model provides close to an exact analytical form for the subfilter term, *a posteriori* implementation for velocity modeling in LES has been known to give rise to stability

issues [132, 133, 137]. More precisely, insufficient subfilter dissipation caused by the presence of negative viscosity in the model can result in the solution going unstable [80]. A common approach is to restore stability by augmenting the tensor-diffusivity model with a Smagorinsky term [132, 133, 137], which provides additional subfilter dissipation to compensate for the occurrence of negative viscosity. Other attempts to restore stability rely on either clipping negative viscosity [84], or incorporating regularization specific to the numerical method used [93]. In contrast to these issues, certain studies have noted that the tensor-diffusivity model by itself can lead to stable solutions, without augmentation with an additional dissipative term [137]. However, the subfilter dissipation was found to be insufficient in those cases, giving rise to inaccurate results. It is important to note that most of the *a posteriori* studies that observed solution instability were concerned with modeling the subfilter velocity stress tensor ($\boldsymbol{\tau_u}$), and not the subfilter scalar flux vector ($\boldsymbol{\tau}_\phi$). One exception is reference [93] which discusses *a posteriori* implementation for scalar transport, albeit in laminar 1D and 2D test cases.

Fortunately, the occurrence of negative diffusivity may not be a dominant issue when using the tensor-diffusivity model for scalar transport in homogeneous isotropic turbulence. More specifically, the tensor-diffusivity model may lead to stable results when used in the viscous-convective subrange. We can arrive at this conclusion by inspecting the subfilter dissipation ($\chi_{\boldsymbol{\tau}_\phi}$) of the filtered scalar variance. The filtered scalar transport equation, Eq. 1.2, is multiplied by the filtered scalar ($\widetilde{\phi}$), and in conjunction with the incompressibility condition ($\nabla \cdot \boldsymbol{u} = 0$) yields:

$$\frac{\partial \widetilde{\phi}^2}{\partial t} + \nabla \cdot \left(\widetilde{\boldsymbol{u}} \widetilde{\phi}^2 \right) = \mathcal{D} \nabla^2 \widetilde{\phi}^2 - 2\mathcal{D} |\nabla \widetilde{\phi}|^2 - 2\nabla \cdot \left(\widetilde{\phi} \boldsymbol{\tau}_\phi \right) + 2 \nabla \widetilde{\phi} \cdot \boldsymbol{\tau}_\phi \tag{4.18}$$

Here, $\chi_R = 2\mathcal{D}|\nabla \widetilde{\phi}|^2$ and $\chi_{\boldsymbol{\tau}_\phi} = -2\nabla \widetilde{\phi} \cdot \boldsymbol{\tau}_\phi$ are the resolved and unresolved scalar dissipation rates, respectively. $\chi_{\boldsymbol{\tau}_\phi}$ is responsible for scalar variance dissipation by the subfilter terms. Recalling that the scalar gradient vector shows strong preference for alignment with the $\widehat{\boldsymbol{e}}_3$ vector, and using

Eq. 4.10, the subfilter scalar dissipation takes the following form:

$$\chi_{\boldsymbol{\tau}_\phi} \approx -\frac{\Delta^2}{6}\nabla\widetilde{\phi}\cdot\left(\widetilde{\boldsymbol{S}}\cdot\nabla\widetilde{\phi}+\frac{1}{2}\widetilde{\boldsymbol{\omega}}\times\nabla\widetilde{\phi}\right) \tag{4.19}$$

$$\approx -\lambda_3|\nabla\widetilde{\phi}|^2\frac{\Delta^2}{6} \tag{4.20}$$

Using the fact that λ_3 is negative, Eqs. 4.18 and 4.20 indicate that the tensor-diffusivity model should always act as a sink for the resolved scalar variance. The absence of a positive λ_1 term, which would act as a positive source for scalar variance, negates the issue of negative diffusivity contributing to scalar variance increase.

We note however, that Eq. 4.13 is a simplification since, in addition to the $\widehat{\boldsymbol{e}}_3$ component of $\nabla\widetilde{\phi}$, there is a minimal spread in the $\widehat{\boldsymbol{e}}_1$ direction (Fig. 4.7). Nevertheless, dissipation cause by the λ_3 term (Eq. 4.20) should dominate the minimal backscatter related to the minuscule $\widehat{\boldsymbol{e}}_1$ component of $\nabla\widetilde{\phi}$. Thus, it should be possible to use the tensor-diffusivity model for scalar transport in homogeneous turbulence, without implementing extraneous means of restoring stability. We remark that the negative components of $\chi_{\boldsymbol{\tau}_\phi}$ may also result in breach of physical scalar bounds, which is not a pressing issue for forced homogeneous isotropic turbulence cases, but may pose problems in turbulent mixing layer simulations (Chapter 6).

We close the discussion on solution stability by noting that backscatter is a physically appropriate phenomenon associated with the stretching of material elements (Fig. 4.1), and is one of the several ways in which the small scales affect the large scales in turbulent flows [45]. In terms of scalar energy-transfer in spectral-space [130], backscatter represents an increase in variance at large scales due to deposition of energy by the small scales. Thus, solution stability permitting, subfilter models should try to account for backscatter whenever possible. This is another advantage that the tensor-diffusivity model offers over eddy-diffusivity-based models, which are unable to account for backscatter inherently.

4.5 Discussion

4.5.1 Effect of scalar-forcing

The $\boldsymbol{\tau}_\phi$ distributions discussed in Secs. 4.2.3 and 4.4 were computed for a scalar field forced by imposing a Mean Scalar Gradient (MSG) [101]. Identical computations were carried out for a scalar field mimicking the dynamics of decaying scalar fluctuations (Linear Scalar forcing [31]). The alignment trends observed were identical in both cases (Table 4.3), even though the means of sustaining small scale fluctuations, and consequently, the scalar variance spectra, have been seen to differ at high Schmidt numbers [31]. The indifference of $\boldsymbol{\tau}_\phi$ orientation to the forcing method is reminiscent of the Schmidt number and filter-width independence observed in Sec. 4.2.3, and may yet again be explained using the absence of a $\widetilde{\phi}$ dependent term in Eq. 4.16.

4.5.2 Implications for practical LES and VR-SM simulations

The present results indicate that model selection for practical LES/VR-SM simulations must be strongly contingent on the filtered DNS solution desired, i.e., by keeping in mind the effective filtering kernel that a particular subfilter model represents. This raises a few crucial questions, particularly: 1) Is it appropriate to use implicit filtering in LES?; and 2) Is it appropriate to think of subfilter terms as being entirely physical in nature, rather than to consider their combined physical and mathematical role? The first question is related to the fact that the sharp-spectral filter does not give rise to any particular subfilter flux orientation; this lack of a definitive orientation makes it difficult to pick a suitable model representation. Both these questions are of critical relevance to practical LES, where implicit filtering (not to be confused with Implicit LES [88]) and filter-independent model selection are common approaches.

Implicit filtering removes high wavenumber spatial fluctuations by projecting the solution on to a coarse grid such that $\Delta = \Delta x$, which contrasts with explicit filtering where the solution is convolved with a filtering kernel (and $\Delta > \Delta x$). Projection on a coarse grid, when using spectral methods in LES, is equivalent to filtering with a sharp-spectral filter. The use of Finite-Volume and

Finite-Difference schemes may introduce yet another level of filtering, which may not be well-defined mathematically [114, 129, 40, 86, 21], i.e., a simple representation for an equivalent filtering kernel may not exist. Thus, relying on implicit filtering can result in very poor correlation of the model described and exact SFF terms, which can be detrimental to solution accuracy. In this regard, explicit filtering has been considered in the literature as a means of introducing some measure of predictability into the behavior of subfilter terms, in addition to providing control over discretization errors. More specifically Refs. [30, 137] use explicit filtering to ensure strong correlation between the subfilter terms and the models used, and Refs. [129, 86, 21] note a reduction in numerical error (along with a tendency to obtain grid-independent results) when using explicit filtering.

The second question posed is concerned with the fact that there is a prevalent tendency to view the subfilter term as being physical in nature, and the choice of a particular model for LES is often made independently of the implicit/explicit filter used [104]. The filter dependence of subfilter terms suggests that there is a dominant mathematical aspect involved in modeling, which must not be ignored. Thus, modeling and filtering must be treated as a unified process by using appropriate model-filter combinations in LES.

4.6 Summary

In this Chapter, we have examined the alignment behavior of the subfilter-scale scalar flux vector in the eigenframe of the strain-rate tensor. Once again, the focus is placed on filtering in the viscous-convective subrange. Results obtained from filtered DNS datasets indicate strong preferential alignment of the SFF vector ($\boldsymbol{\tau}_\phi$) in a particular direction, when using both the Gaussian and box filters. The alignment direction is explained by analyzing the tensor-diffusivity model, based on the observed preferential orientation of the vorticity ($\boldsymbol{\omega}$) and scalar gradient ($\nabla\widetilde{\phi}$) vectors. The independence of the SFF vector orientation from the filter-width, the flow Schmidt number, and the scalar-forcing method, is explained by extracting the orientation angle from the tensor-diffusivity model. The relevant orientation angle, θ_{S_3}, is shown to depend only on velocity related variables, $\boldsymbol{\omega}$ and λ_3. The remarkable agreement between numerical results and those predicted by the tensor-

diffusivity model confirms that it provides close to an exact analytical form for the subfilter term, when using the Gaussian or box filtering kernels.

Using the orientation of $\nabla\widetilde{\phi}$ in the strain-rate eigenframe, it is shown that the subfilter dissipation term for the tensor-diffusivity model acts predominantly as a sink for the scalar variance. Thus, the issue of solution instability induced by the occurrence of negative diffusivity may not arise when using the model for scalar transport. This result should remain valid, at least, as long as the filter-width is located in the viscous-convective subrange.

Analyzing the effect of filter-shape indicates close to random orientation of the SFF vector when using the sharp-spectral filter. Such strong dependence of the subfilter term on filter-shape raises concern regarding the suitability of using implicit filtering in LES/VR-SM simulations, which is often the preferred method of choice for such simulations. The results reinforce the viewpoint that filtering and modeling must be tackled as a unified issue in LES/VR-SM simulations, and an appropriate subfilter model must be used depending on the filtered DNS solution desired. The observed filter dependence also suggests that it may not be appropriate to ascribe a solely physical role to subfilter models, and that it is more pertinent to examine their combined physical and mathematical role in such simulations. Having identified the most suitable SFF model via *a priori* analysis in this Chapter, we assess its performance in *a posteriori* tests in Chapter 5.

Chapter 5

Validation of the Tensor-diffusivity Model for VR-SM Simulations of Homogeneous Isotropic Turbulence

In addition to analyzing DNS datasets to assess the capability of subfilter models, it is usually recommended [106] that models be tested in actual Large Eddy/VR-SM Simulations. Occasionally, *a priori* analyses of models are known to yield observations that may not agree well with results obtained in *a posteriori* tests. In order to verify the validity of the *a priori* observations made in Chapter 4, and to assess whether the tensor-diffusivity model causes a significant deviation from the speculated behavior, we perform *a posteriori* Velocity Resolved - Scalar Modeled (VR-SM) simulations of homogeneous isotropic turbulence.

The implementation of the relevant equations in the simulations is explained in Sec. 5.1. Section 5.2 provides theoretical background linking various filter-dependent scalar-variance and scalar-dissipation rates via the governing scalar transport equations. Section 5.3 compares VR-SM results of the homogeneous simulations to both filtered and unfiltered DNS data, when using highly resolved grids. The high resolution grid serves to eliminate any effects of numerical errors on the result. The behavior of the model, when using large filter-widths is also analyzed in this section, along with a discussion regarding the need for model regularization in certain situations (Sec. 5.3.3). Finally, results obtained from Velocity Resolved - Scalar Modeled simulations on truncated grids, a concept which is more aligned with the practical use of VR-SM simulations, are scrutinized in Sec. 5.4.

5.1 Implementation

All *a posteriori* tests used in this Chapter are performed by solving the following modeled scalar transport equation:

$$\frac{\partial \bar{\phi}}{\partial t} + \nabla \cdot \left(\boldsymbol{u} \bar{\phi} \right) \quad = \quad \mathcal{D} \nabla^2 \bar{\phi} - \nabla \cdot \left(\frac{\Delta^2}{12} \nabla \boldsymbol{u} \cdot \nabla \bar{\phi} \right) \tag{5.1}$$

Theoretically, in the equation above, the filtered velocity $\widetilde{\boldsymbol{u}}$ should be used. However, since the filter-width is placed in the viscous-convective subrange, this filtered velocity can be replaced by the actual velocity, i.e., $\widetilde{\boldsymbol{u}} = \boldsymbol{u}$. We reiterate the distinction between $\widetilde{\phi}$ used in the other chapters, and $\bar{\phi}$ used in Eq. 5.1. $\widetilde{\phi}$ represents the solution obtained by filtering a DNS dataset with a particular filtering kernel, whereas $\bar{\phi}$ represents the resolved scalar field obtained as the solution of the modeled equation (Eq. 5.1). As discussed in Chapter 2, the objective of the model term in Eq. 5.1 ($\Delta^2 \nabla \boldsymbol{u} \cdot \nabla \bar{\phi}/12$) is to ensure that $\bar{\phi}$ resembles $\widetilde{\phi}$ as closely as possible.

We have already noted in Chapter 4 that the model term used in Eq. 5.1 ($\Delta^2 \nabla \boldsymbol{u} \cdot \nabla \bar{\phi}/12$) corresponds to filtering the DNS solution with a Gaussian or box filter. Thus, we expect the stationary solution of Eq. 5.1 to resemble DNS data filtered with a Gaussian kernel. The extent of resemblance is a useful indicator of the accuracy with which the model represents subfilter terms in *a posteriori* tests. All simulations discussed in this Chapter use the BCH scheme for scalar transport, unless noted otherwise. The Reynolds and Schmidt numbers are kept constant at $Re_\lambda = 30$ and $Sc = 256$, respectively.

Velocity Resolved - Scalar Modeled (VR-SM) simulations, a term which signifies that the velocity field is fully resolved but the scalar field is modeled, are performed using two distinct grid resolutions to determine whether discretization errors degrade the solutions excessively: using very fine grids (with resolution equal to that of a DNS, i.e., $\Delta x = \Delta x_{DNS}$) to minimize the effect of numerical errors; and using truncated grids (i.e., $\Delta x > \Delta x_{DNS}$), as is the norm in practical applications of VR-SM simulations. The relevant interpretation in wavenumber space may be understood from the schematic shown in Fig. 5.1. In the figure, $\kappa_T = \pi/\Delta x$ and $\kappa_c = \pi/\Delta$ correspond to grid

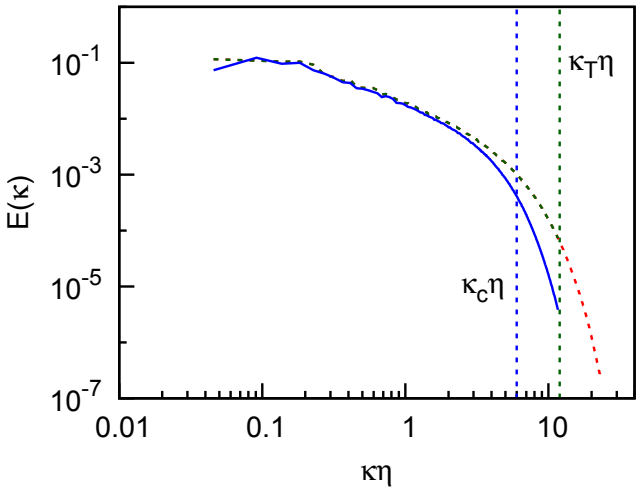

Figure 5.1: Depiction of grid truncation wavenumber κ_T, and filter cutoff wavenumber κ_c, and their respective effects on the scalar energy spectrum.

truncation wavenumber, and filter cutoff wavenumber, respectively. In fully resolved 'control' VR-SM simulations, Δx (and hence, κ_T) is selected such that $\kappa_T \eta_B = 1.5$ (or equivalently, $\kappa_T \eta = 24$), which corresponds to a grid size of 1024^3 for the given Reynolds and Schmidt numbers. Grid resolution for 'grid-truncated' VR-SM simulations is selected such that $\kappa_T \eta_B < 1.5$. κ_c may be selected independently of κ_T in either case, as long as $\kappa_T > \kappa_c$.

5.2 Scalar-variance and scalar-dissipation rate

To compare performance of VR-SM to DNS, we make extensive use of the scalar variance and scalar-dissipation rates. Thus, a brief description of the relevant quantities and the governing equations is provided here. When imposing a mean gradient in the scalar field [101], the scalar transport equation takes the following form:

$$\frac{\partial \phi}{\partial t} + \nabla \cdot (\boldsymbol{u}\phi) = \mathcal{D}\nabla^2 \phi - \boldsymbol{G} \cdot \boldsymbol{u} \tag{5.2}$$

Here, $G = (-1, 0, 0)$ is the mean gradient imposed in the simulations. Upon filtering this equation, we get:

$$\frac{\partial \widetilde{\phi}}{\partial t} + \nabla \cdot (\widetilde{\boldsymbol{u}}\widetilde{\phi}) = \mathcal{D}\nabla^2 \widetilde{\phi} - \boldsymbol{G} \cdot \widetilde{\boldsymbol{u}} - \nabla \cdot \boldsymbol{\tau}_\phi \tag{5.3}$$

We reiterate that filtering in the viscous-convective subrange implies that $\widetilde{\boldsymbol{u}} = \boldsymbol{u}$. We can now define a variety of scalar-variances that will be useful for comparisons in the sections that follow:

$$\sigma_\phi = \langle (\phi - \langle \phi \rangle)^2 \rangle = \langle \phi^2 \rangle - \langle \phi \rangle^2 \tag{5.4a}$$

$$\sigma_\phi^R = \langle (\widetilde{\phi} - \langle \widetilde{\phi} \rangle)^2 \rangle = \langle \widetilde{\phi}^2 \rangle - \langle \widetilde{\phi} \rangle^2 = \langle \widetilde{\phi}^2 \rangle - \langle \phi \rangle^2 \tag{5.4b}$$

$$\sigma_\phi^{SF} = \langle \phi^2 \rangle - \langle \widetilde{\phi}^2 \rangle \tag{5.4c}$$

The brackets $\langle \cdot \rangle$ refer to an ensemble average. σ_ϕ is the scalar-variance associated with the raw DNS field, σ_ϕ^R is the variance resolved up until the grid truncation wavenumber κ_T, and σ_ϕ^{SF} is the subfilter variance. We note that for homogeneous simulations $\langle \widetilde{\phi} \rangle = \widetilde{\langle \phi \rangle} = \langle \phi \rangle$, which implies that $\sigma_\phi^{SF} = \sigma_\phi - \sigma_\phi^R$.

To scrutinize the temporal variation of the scalar-variances defined in Eqs. 5.4a through 5.4c, we obtain the appropriate variance-transport equations by multiplying Eq. 5.2 by ϕ, and Eq. 5.3 by $\widetilde{\phi}$:

$$\frac{\partial \phi^2}{\partial t} + \nabla \cdot \left(\boldsymbol{u}\phi^2 \right) = \mathcal{D}\nabla^2 \phi^2 - 2\mathcal{D}|\nabla \phi|^2 - 2\phi \boldsymbol{G} \cdot \boldsymbol{u} \tag{5.5}$$

$$\frac{\partial \widetilde{\phi}^2}{\partial t} + \nabla \cdot \left(\widetilde{\boldsymbol{u}}\widetilde{\phi}^2 \right) = \mathcal{D}\nabla^2 \widetilde{\phi}^2 - 2\mathcal{D}|\nabla \widetilde{\phi}|^2 - 2\widetilde{\phi}\boldsymbol{G} \cdot \boldsymbol{u} - 2\nabla \cdot \left(\widetilde{\phi}\boldsymbol{\tau}_\phi \right) + 2\nabla \widetilde{\phi} \cdot \boldsymbol{\tau}_\phi \tag{5.6}$$

Ensemble averaging of these equations, under the condition of homogeneous, isotropic turbulence (i.e., $\langle \nabla \cdot \alpha \rangle = \nabla \cdot \langle \alpha \rangle = 0$, where α is any turbulent quantity) leads to:

$$\frac{d\sigma_\phi}{dt} = -\langle 2\mathcal{D}|\nabla \phi|^2 \rangle - \langle 2\phi \boldsymbol{G} \cdot \boldsymbol{u} \rangle \tag{5.7}$$

$$\frac{d\sigma_\phi^R}{dt} = -\langle 2\mathcal{D}|\nabla \widetilde{\phi}|^2 \rangle - \langle 2\widetilde{\phi}\boldsymbol{G} \cdot \widetilde{\boldsymbol{u}} \rangle - \langle -2\nabla \widetilde{\phi} \cdot \boldsymbol{\tau}_\phi \rangle \tag{5.8}$$

and consequently,

$$\frac{\partial \sigma_\phi^{SF}}{\partial t} = \frac{\partial \sigma_\phi}{\partial t} - \frac{\partial \sigma_\phi^{R}}{\partial t} = -\langle 2\mathcal{D}|\nabla\phi|^2\rangle - \langle 2\phi \boldsymbol{G}\cdot\boldsymbol{u}\rangle + \langle 2\mathcal{D}|\nabla\widetilde{\phi}|^2\rangle + \langle 2\widetilde{\phi}\boldsymbol{G}\cdot\widetilde{\boldsymbol{u}}\rangle + \langle -2\nabla\widetilde{\phi}\cdot\boldsymbol{\tau}_\phi\rangle \quad (5.9)$$

The imposed mean gradient ($\boldsymbol{G}$) acts as a source of scalar-variance [31], whereas molecular dissipation (χ for DNS, and χ_R for VR-SM) and subfilter dissipation ($\chi_{\boldsymbol{\tau}_\phi}$ for VR-SM) act to remove scalar-variance from the field. These quantities are defined below:

$$\chi = 2\mathcal{D}|\nabla\phi|^2 \quad (5.10a)$$

$$\chi_R = 2\mathcal{D}|\nabla\widetilde{\phi}|^2 \quad (5.10b)$$

$$\chi_{\boldsymbol{\tau}_\phi} = -2\nabla\widetilde{\phi}\cdot\boldsymbol{\tau}_\phi = -\frac{\Delta^2}{6}\nabla\widetilde{\phi}\cdot\nabla\widetilde{\boldsymbol{u}}\cdot\nabla\widetilde{\phi} \quad (5.10c)$$

In addition, the total mean scalar-dissipation rate for σ_ϕ^R in a VR-SM simulation is defined as follows:

$$\langle\chi_{Tot}\rangle \quad = \quad \langle\chi_R\rangle + \langle\chi_{\boldsymbol{\tau}_\phi}\rangle \quad (5.11)$$

In a statistically stationary state, the scalar-variance is constant and production is balanced exactly by dissipation. In other words:

$$2\boldsymbol{G}\cdot\langle\boldsymbol{u}\phi\rangle \quad = \quad \langle\chi\rangle \quad (5.12)$$

$$2\boldsymbol{G}\cdot\langle\widetilde{\boldsymbol{u}}\widetilde{\phi}\rangle \quad = \quad \langle\chi_R\rangle + \langle\chi_{\boldsymbol{\tau}_\phi}\rangle \quad (5.13)$$

It is important to note that the magnitude of the scalar-variance in homogeneous isotropic turbulence with mean scalar gradient (MSG) forcing [101] is not known *a priori*, as it is controlled entirely by the expressions given above. In other words, scalar-variance production may vary slightly between DNS and VR-SM ($\langle\boldsymbol{u}\phi\rangle \neq \langle\widetilde{\boldsymbol{u}}\widetilde{\phi}\rangle$), which in turn will affect the magnitude of the scalar-variance and the different scalar-dissipation rates. For this reason, most of the relevant quantities to be compared

Table 5.1: Table showing scalar statistics computed from filtered DNS.

	Filtered DNS			
$\kappa_c\eta$	σ_ϕ^R	$\langle\chi_R\rangle$	$\langle\chi_{Tot}\rangle$	$\sigma_\phi^R/\langle\chi_{Tot}\rangle$
Raw	1.848	1.159	1.159	1.59
24	1.842	1.078	1.207	1.53
12	1.826	0.898	1.300	1.40
6	1.779	0.562	1.427	1.25
3	1.680	0.241	1.474	1.14
1.5	1.526	0.076	1.433	1.06

will need to be normalized appropriately, as indicated later in Sec. 5.3.1.

As a preliminary step before running the VR-SM simulation, the raw DNS data are filtered explicitly (with a Gaussian filter) and the quantities discussed above are computed. Table 5.2 shows the effect of filtering on the resolved scalar-variance σ_ϕ^R and the mean scalar dissipation rates for filtered DNS data. The distinction between ensemble-averaging and volume/time-averaging should be made here. The proposed configuration reaches a state of statistical stationarity. Under this condition, ensemble averages are (theoretically) equivalent to averages over an infinite time. Similarly, since the configuration is homogeneous in space, ensemble averages are equivalent also to averages over an infinite volume. Thus, ensemble averages are represented as volume averages over the triply periodic domain, and as temporal averages over multiple uncorrelated snapshots.

For the filtered DNS data, we first observe that with increasing filter-width (i.e., with decreasing $\kappa_c\eta$), both σ_ϕ^R and $\langle\chi_R\rangle$ decrease. This is an expected trend, since an increase in filter-width results in a lower contribution to these two terms from the large wavenumber Fourier modes. We remark that changes in $\langle\chi_R\rangle$ with $\kappa_c\eta$ are quite pronounced (when compared to the initial unfiltered DNS data), in comparison to analogous changes in σ_ϕ^R. This is related to the variance being controlled mostly by the energy producing scales (low κ), and the scalar dissipation rate being dependent largely on high κ modes. More precisely, χ_R is dependent on the resolved scalar gradient $\nabla\widetilde{\phi}$, which is quite sensitive to fluctuations at the smallest scales.

Even for $\kappa_c\eta = 12$ and 6, there is measurable contribution from subfilter dissipation, which accounts for a ratio of approximately 0.3 and 0.6 of the total dissipation rate, respectively. This indicates that the subfilter model is required to play a substantial role in controlling the net scalar

dissipation-rate, even when using relatively small filter-widths. At $\kappa_c\eta = 1.5$ the total scalar dissipation rate, $\langle\chi_{Tot}\rangle$, is dominated almost entirely by the contribution from the subfilter model, $\langle\chi_{\boldsymbol{\tau}_\phi}\rangle = \langle\chi_{Tot}\rangle - \langle\chi_R\rangle$, and the resolved molecular dissipation term is negligible (around 5%). The implication is that with increasing Schmidt number (i.e., with decreasing absolute value of $\langle\chi_R\rangle$, since $\mathcal{D}$ decreases), the scalar statistics should become independent of the Sc. This is indeed the case as will be shown explicitly in Chapter 6 for simulations of the turbulent mixing layer. We will now compare results obtained from Velocity Resolved - Scalar Modeled simulations to the filtered DNS data presented in Table 5.1.

5.3 VR-SM simulations on fine grid

5.3.1 Comparison to DNS

For comparing results to DNS data, VR-SM simulations of homogeneous isotropic turbulence were run first using two different explicit cutoff wavenumbers: $\kappa_c\eta = 12$ and 6. The grid resolution used corresponds to that of a fully resolved DNS ($\kappa_T\eta = 24$), which allows for scrutiny of subfilter model accuracy without contamination from numerical errors. To assess the ability of VR-SM simulations to recreate the large-scale transport characteristics, we compare scalar spectra and scalar-variance obtained from these simulations to their filtered and unfiltered DNS counterparts. The relevant quantities may be obtained by replacing $\widetilde{\phi}$ with $\bar{\phi}$ in Eqs. 5.4 and 5.10. The 3D scalar-energy spectra in Fig. 5.2 show good agreement between the VR-SM simulations and DNS data (both filtered and unfiltered) at low wavenumbers (up to $\kappa\eta = 2$). This observation can be attributed to the occurrence of spectral decoupling discussed in Chapter 2, where we deduced that scalar-energy transfer at the low wavenumbers remains largely unaffected by the subfilter scales. As a result, we do not expect significant differences in the three simulations with respect to scalar statistics at low wavenumbers, which is indeed the case in Fig. 5.2. The disparity at large wavenumbers is solely the result of attenuation from the filtering operation, and the VR-SM simulations data matches filtered DNS quite well in this regard. We reiterate that the purpose of the VR-SM simulations is not to

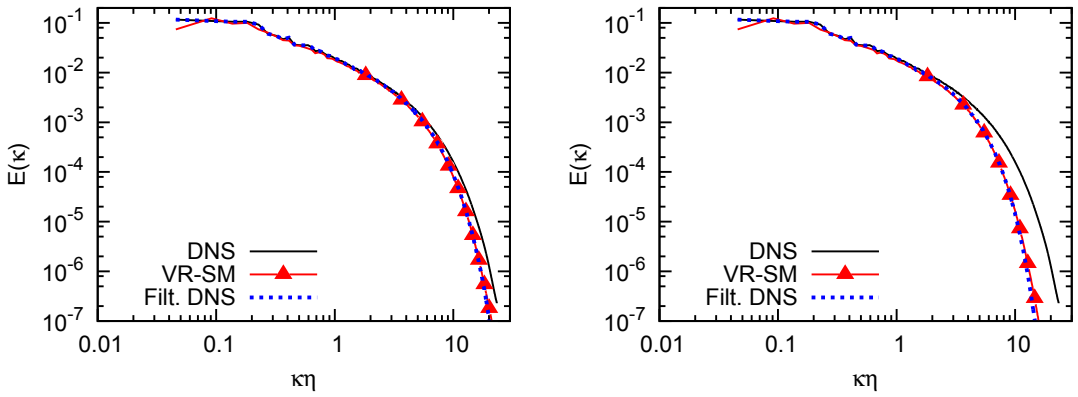

(a) $\kappa_c\eta = 12$ (b) $\kappa_c\eta = 6$

Figure 5.2: 3D Raw scalar-energy spectra from VR-SM simulations compared to corresponding spectra from filtered and unfiltered DNS ($Re_\lambda = 30,\ Sc = 256$).

Table 5.2: Table showing scalar statistics computed from VR-SM simulations using the tensor-diffusivity (T-D) model. $\kappa_T\eta = 24$ for all simulations. Data listed for the original tensor-diffusivity model have been obtained from simulations discussed in Sec. 5.3.1, and those for the regularized model have been obtained from simulations described in Sec. 5.3.4.

T-D model	$\kappa_c\eta$	VR-SM				Filtered DNS
		σ_ϕ^R	$\langle\chi_R\rangle$	$\langle\chi_{Tot}\rangle$	$\sigma_\phi^R/\langle\chi_{Tot}\rangle$	$\sigma_\phi^R/\langle\chi_{Tot}\rangle$
Original	12	1.752	0.843	1.233	1.42	1.40
	6	1.708	0.540	1.406	1.21	1.25
Regularized	12	1.747	0.801	1.173	1.49	1.40
	6	1.688	0.473	1.259	1.34	1.25
	3	1.574	0.174	1.214	1.30	1.14
	1.5	1.395	0.049	1.186	1.18	1.06

solve directly the exact scalar transport equation (Eq. 2.1), but instead, to solve the model equation (Eq. 2.3a) which tries to recreate filtered DNS data (Eq. 2.2).

The resolved scalar-variances (σ_ϕ^R) for the data shown in Fig. 5.2, and computed using Eq. 5.4b (after replacing $\widetilde{\phi}$ with $\bar{\phi}$), are listed in Table 5.2. We observe that σ_ϕ^R from VR-SM simulations compare well with the values computed from filtered DNS. However, these values are consistently lower than those obtained from the filtered DNS result by approximately 10%. As mentioned in the previous section, the variance of the simulated scalar field is not imposed *a priori*, and instead results from Eq. 5.13. As the production terms might be slightly different, the more appropriate quantities to compare are the variances normalized by their respective production rate (or equivalently, total dissipation rate), i.e., $\sigma_\phi^R/\langle\chi_{Tot}\rangle$. Data from Table 5.2 also suggests that the tensor-diffusivity model is extremely effective in accounting for differences between the resolved and filtered DNS

mean dissipation rates, since $\langle \chi_{Tot} \rangle$ from VR-SM simulations exhibit values quite close to those listed for $\langle \chi_{Tot} \rangle$ from the filtered DNS (Table 5.1). The consistently lower values in VR-SM *vs.* filtered DNS may yet again be attributed to a smaller production term in VR-SM simulations. Lower variance production requires a correspondingly smaller balancing $\langle \chi_{Tot} \rangle$ in order to maintain statistical stationarity.

To examine scalar fluctuations at the smaller resolved scales, we turn our attention to molecular dissipation spectra of the resolved/filtered scalar field ($D(\kappa) = 2\mathcal{D}\kappa^2 E(\kappa)$), and Probability Density Functions (PDF) of the resolved scalar dissipation rate (χ_R) shown in Fig. 5.3. Both these quantities are associated with molecular dissipation in Eq. 5.5, and are used frequently in investigations of the small-scale statistical nature of the scalar field [135, 55]. Heavy tails of the PDF of χ, for instance, indicate frequent occurrence of extreme fluctuations in the scalar field. These fluctuations, associated with large values of the scalar gradient, correspond to physical locations where rapid mixing takes place at the molecular level. To account for differences arising from slightly different production/dissipation in VR-SM data, and from slight variation in scalar statistics among different data snapshots, appropriate normalization was used for the curves shown in Fig. 5.3. Differences between the VR-SM result and the filtered DNS are barely discernible in Fig. 5.3(a) and 5.3(b). Good agreement between VR-SM and filtered DNS indicates that differences between VR-SM/filtered DNS and unfiltered DNS arise primarily as a result of the filtering operation, and not because of any detrimental effects inherent in the modeling or numerics.

5.3.2 Filtering with large Δ, and the occurrence solution instability

We now examine what effect using larger values of the filter-width (Δ) has on the performance of the tensor-diffusivity model. Figure 5.4 shows the scalar variance spectrum computed from a VR-SM simulation run with $\kappa_c\eta = 1.5$ ($\kappa_c = \pi/\Delta$), while still maintaining $\kappa_T\eta = 24$ ($\kappa_T = \pi/\Delta x$). An accumulation of energy at large wavenumbers may be observed which would suggest that using too small a value of $\kappa_c\eta$ can lead to solution instability, as postulated by Leonard [80]. One of the interesting outcomes of the blowup is that the peak for BCH is considerably higher (approximately

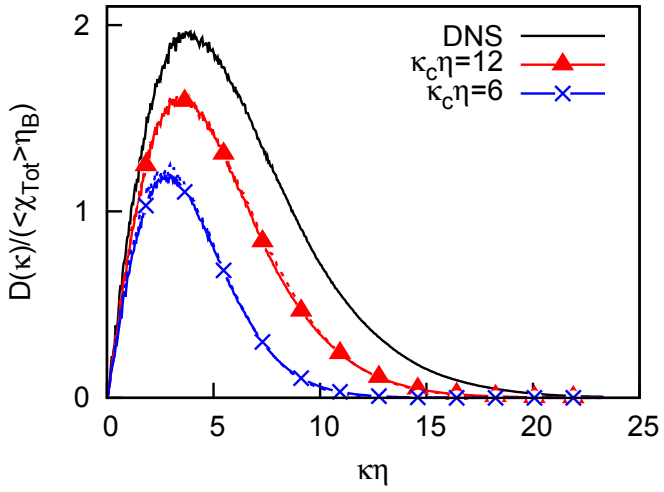

(a) Scalar dissipation spectra

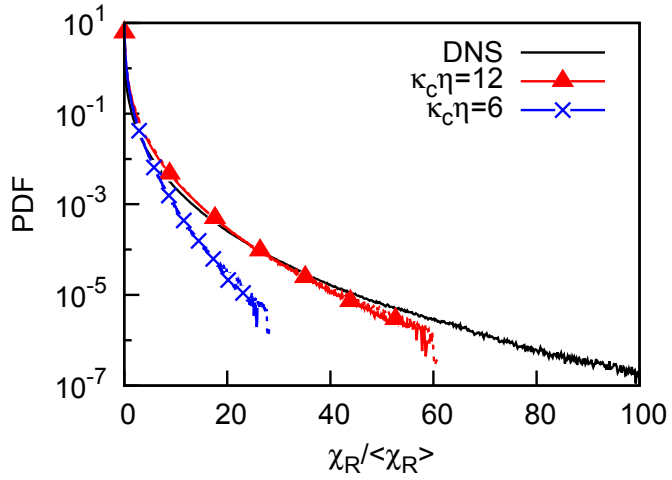

(b) PDFs of χ_R

Figure 5.3: Normalized spectra and PDFs shown for $\kappa_c\eta = 6$ and 12, at $\kappa_T\eta = 24$ (DNS resolution). Solid lines with symbols correspond to VR-SM results, whereas broken lines correspond to filtered DNS.

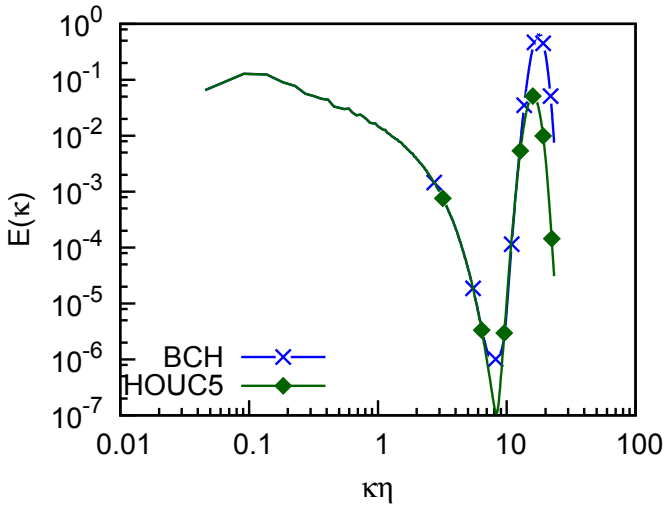

Figure 5.4: Solution instability induced at large wavenumbers with $\kappa_c\eta = 1.5$ at $\kappa_T\eta = 24$ (DNS resolution).

an order of magnitude in $E(\kappa)$) than the corresponding peak for HOUC5. This is indicative of lower numerical diffusion in BCH than in HOUC5, and is a remarkable occurrence, given that BCH still experiences some numerical diffusion caused by bounds-enforcement (Sec. 3.3.1).

The manifestation of solution instability at low values of $\kappa_c\eta$, and its absence at sufficiently large values, can be understood by analyzing the filter-width dependence of the total scalar dissipation rate:

$$\chi_R + \chi_{\tau_\phi} = 2\mathcal{D}|\nabla\bar{\phi}|^2 - \frac{\Delta^2}{6}\nabla\bar{\phi}\cdot\nabla\boldsymbol{u}\cdot\nabla\bar{\phi} \tag{5.14}$$

Figure 5.5 shows PDFs of $\chi_R + \chi_{\tau_\phi}$ computed from filtered DNS data, for various values of $\kappa_c\eta$. On the PDF curves, the negative leg ($\chi_R + \chi_{\boldsymbol{\tau}_\phi} < 0$) tends to become increasingly dominant with decreasing $\kappa_c\eta$. On the other hand, the positive leg shows only a slight increase with Δ. Below a threshold value of $\kappa_c\eta$, the increasing negative leg, although still weak in comparison to the positive one (which confirms the *a priori* conjecture made in Sec. 4.4.2), seems to be sufficient to trigger the instability observed in Fig. 5.4. In this scenario, model regularization (Sec. 5.3.3) may be used to suppress the growth of solution instability. However, we reiterate that the solution remains stable on its own when $\kappa_c\eta$ is located sufficiently far within the viscous-convective subrange, as determined in Sec. 5.3.1. Although seemingly limited in utility, this approach can be extremely useful when

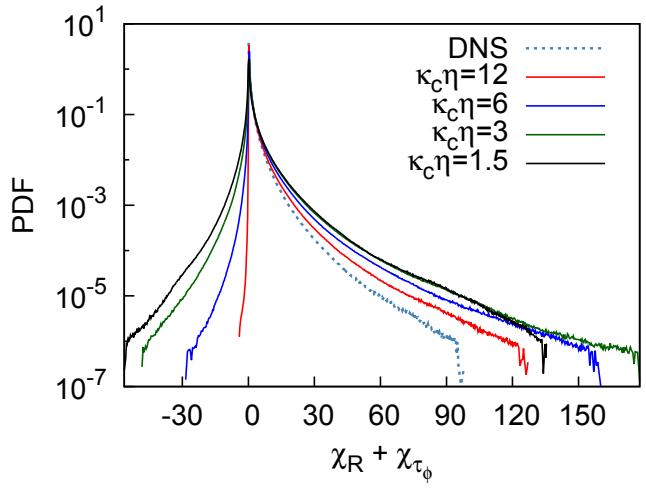

Figure 5.5: Variation of the PDF of total scalar dissipation rate with $\kappa_c\eta$ (or equivalently, Δ), as measured by filtering DNS dataset.

VR-SM simulations are run with the intention of studying small-scale behavior, which necessitates that $\kappa_c\eta$ be sufficiently large.

We observe that the majority of the scalar dissipation originates from the subfilter model, as can be confirmed by comparing the total scalar dissipation rate to the model contribution in Fig. 5.6, as well as from data provided in Table 5.2. The positive contribution of χ_R results in only a marginal decrease in the negative leg and increase in the positive leg, when going from $\chi_{\boldsymbol{\tau}_\phi}$ to $\chi_R + \chi_{\boldsymbol{\tau}_\phi}$.

5.3.3 Model regularization

The observations in Sec. 5.3.2 suggest that if the tensor-diffusivity is intended to be used with large Δ, some sort of model regularization may need to be implemented. In order to deduce the best approach of doing so, we expand the tensor-diffusivity model in terms of the strain-rate eigenvectors and eigenvalues [80]:

$$\boldsymbol{\tau}_\phi = \frac{\Delta^2}{12}\left(\boldsymbol{S}\cdot\nabla\bar{\phi} + \frac{1}{2}\boldsymbol{\omega}\times\nabla\bar{\phi}\right) \tag{5.15}$$

$$= \frac{\Delta^2}{12}\left(|\nabla\bar{\phi}|(\lambda_1\widehat{\boldsymbol{e}}_1\otimes\widehat{\boldsymbol{e}}_1 + \lambda_2\widehat{\boldsymbol{e}}_2\otimes\widehat{\boldsymbol{e}}_2 + \lambda_3\widehat{\boldsymbol{e}}_3\otimes\widehat{\boldsymbol{e}}_3)\cdot\widehat{\boldsymbol{e}}_\phi + \frac{1}{2}\boldsymbol{\omega}\times\nabla\bar{\phi}\right), \tag{5.16}$$

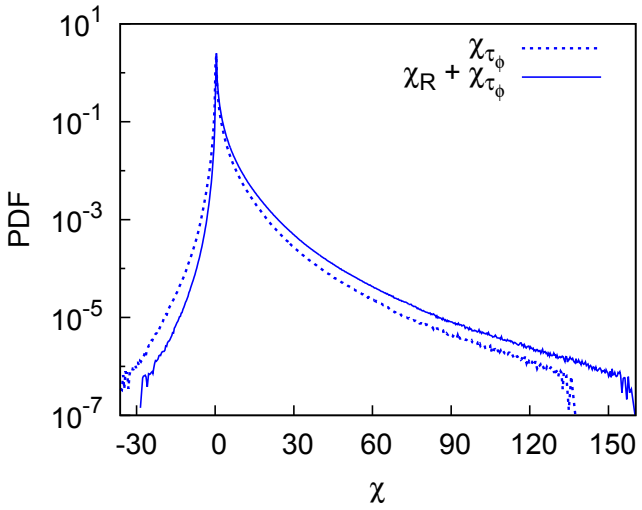

Figure 5.6: Total scalar dissipation rate ($\chi_R + \chi_{\boldsymbol{\tau}_\phi}$) *vs.* the contribution from the subfilter model ($\chi_{\boldsymbol{\tau}_\phi}$). Curves computed by filtering DNS dataset with $\kappa_c\eta = 6$.

The subfilter dissipation-rate contribution of the tensor-diffusivity model can be decomposed in a similar manner:

$$\chi_{\boldsymbol{\tau}_\phi} = -\frac{\Delta^2}{6}\nabla\bar{\phi}\cdot\left(\boldsymbol{S}\cdot\nabla\bar{\phi} + \frac{1}{2}\boldsymbol{\omega}\times\nabla\bar{\phi}\right) \tag{5.17}$$

$$= -\frac{\Delta^2}{6}|\nabla\bar{\phi}|^2\left(\lambda_1(\widehat{\boldsymbol{e}}_1\cdot\widehat{\boldsymbol{e}}_\phi)^2 + \lambda_2(\widehat{\boldsymbol{e}}_2\cdot\widehat{\boldsymbol{e}}_\phi)^2 + \lambda_3(\widehat{\boldsymbol{e}}_3\cdot\widehat{\boldsymbol{e}}_\phi)^2\right) \tag{5.18}$$

We have confirmed in Sec. 5.3.2, that large values of Δ give rise to increasing occurrence of negative $\chi_R + \chi_{\boldsymbol{\tau}_\phi}$. This negative component originates from the λ_1 and λ_2 (i.e., positive eigenvalue) terms in Eq. 5.18. Thus, one feasible approach of suppressing solution instability is to remove the λ_1 and λ_2 components in Eq. 5.16. This sort of regularization to prevent the occurrence of negative diffusivity can be found in other approaches as well, for instance, when clipping negative eddy diffusivity in the dynamic Smagorinsky model [84], when implementing numerical method-specific regularization [93], or when including bacskscatter limiters in multifractal models [27]. Upon regularization, the modified tensor-diffusivity model takes the following form:

$$\boldsymbol{\tau}_\phi = \frac{\Delta^2}{12}\left(\left(\lambda_3\widehat{\boldsymbol{e}}_3\cdot\nabla\bar{\phi}\right)\widehat{\boldsymbol{e}}_3 + \frac{1}{2}\boldsymbol{\omega}\times\nabla\bar{\phi}\right) \tag{5.19}$$

This form was discussed in a recent paper by Balarac et al. [9]. However, the accompanying Large eddy simulations (with $Sc \leq 4$) of homogeneous turbulence and a temporal turbulent plane jet, used just the first term in Eq. 5.19 as the scalar-flux model. Furthermore, these authors preferred a rather involved dynamic procedure over a static model-coefficient, which might not be essential for determining the model coefficient accurately. The analytically determined $\Delta^2/12$ coefficient performs extremely well (Fig. 5.3), when used in the viscous-convective subrange. The need for dynamic filtering might be related to the fact that Balarac et al. used the sharp-spectral filter for computing $\widetilde{\boldsymbol{u}}$ (instead of the more appropriate Gaussian or box filter with the tensor-diffusivity model), and it is unclear whether they employed $\kappa_T\eta > \kappa_c\eta$ for the model implemented with the static $\Delta^2/12$ coefficient. These observations reinforce the need for using correct model-filter combination in VR-SM simulations, as discussed in Chapter 4.

5.3.4 Impact of regularization on results

We now provide arguments to support the use of the regularized form in Eq. 5.19, and theorize (and later, show) that regularization has limited detrimental impact on model performance. Figure 5.5 substantiates our *a priori* conjecture from Sec. 4.4.2, that the non-regularized model's contribution to negative subfilter dissipation is indeed small in comparison to the positive contribution. The overall effect of regularization is the suppression of this comparatively small negative component of $\chi_{\boldsymbol{\tau}_\phi}$, as depicted in Fig. 5.7. The differences between the two curves are simply related to the fact that PDFs, by definition, require the area under the curve to be unity, which necessitates a vertical upward shift for the regularized curve upon curtailing the negative segment. Furthermore, we recall that the analysis in Chapter 4 was associated with the regularized form of the model, since Eqs. 4.15 and 4.16, neglect the presence of the λ_1 and λ_2 components. The excellent agreement between θ_{S_3} and α_{S_3} in Fig. 4.8 indicates that the regularized model retains most of the alignment characteristics of the 'true' SFF vector.

In addition to these observations, limiting backscatter by implementing model regularization may also be justified from a spectral viewpoint. Our analysis in Sec. 2.3 suggests that backscatter

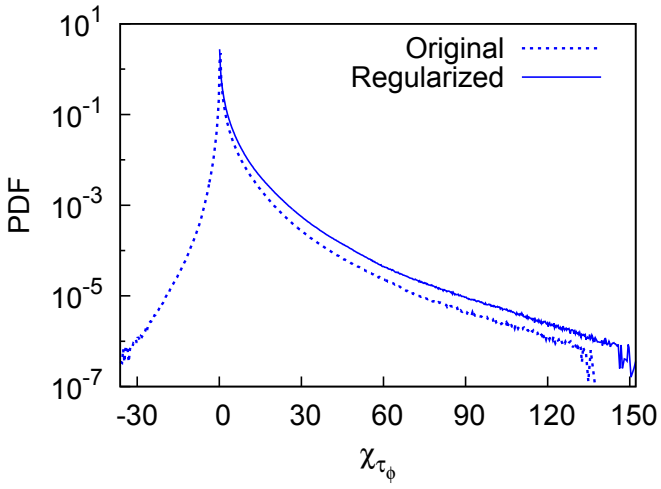

Figure 5.7: Illustration showing the effect of model regularization on the subfilter scalar dissipation rate. Curves computed by filtering DNS dataset with $\kappa_c\eta = 6$.

originating from scalar modes in the far-dissipation range may not impact the resolved scales directly (Fig. 2.7). Thus, suppressing the negative component of χ_{τ_ϕ}, when filtering in the viscous-convective subrange, might not affect the VR-SM results adversely at the large scales.

A posteriori simulations with the regularized model (Eq. 5.19) implemented confirm that the VR-SM results do not differ significantly from filtered DNS data. Moreover, the regularization is able to restore stability when using larger values of Δ. The pertinent scalar dissipation spectra in Fig. 5.8 show excellent agreement with filtered DNS data, and are similar to the results obtained with the non-regularized model (Fig. 5.3(a)). The spectra obtained for simulations with $\kappa_c\eta = 1.5$ and 3, both of which are unstable when using the non-regularized model with $\Delta x = \Delta x_{DNS}$, compare relatively well to the filtered DNS data.

5.4 VR-SM simulations on truncated grid

5.4.1 Further *a priori* considerations

Results from Velocity Resolved - Scalar Modeled simulations in the previous sections indicate that the tensor-diffusivity model is ideal for replicating the subfilter scalar-flux term. However, all *a posteriori* tests discussed until now have been run with $\Delta x = \Delta x_{DNS}$. Although using these highly

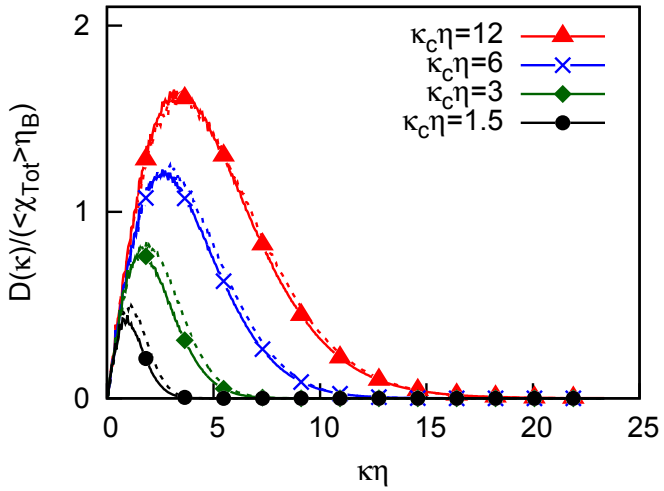

Figure 5.8: Scalar dissipation spectra from VR-SM with the regularized model. Curves shown for $\kappa_c\eta$= 1.5, 3, 6 and 12, at $\kappa_T\eta = 24$ (DNS resolution). Solid lines with symbols correspond to VR-SM results, and broken lines correspond to filtered DNS.

refined grids is convenient for keeping numerical errors to a minimum, doing so defeats the primary purpose of VR-SM simulations: to provide us with the capability to run accurate simulations on coarse grids. The question remains as to whether the model will perform well in situations that more closely reflect conditions encountered in practical Velocity Resolved - Scalar Modeled simulations, for instance, on truncated grids that do not resolve the smallest subfilter scales.

To determine the extent to which small scale fluctuations are important in Velocity Resolved - Scalar Modeled simulations, we first define the subfilter-model dissipation spectrum, $(D_{\boldsymbol{\tau}_\phi}(\kappa))$, which is evaluated in a manner analogous to the transfer spectrum shown in Eq. 2.21:

$$D_{\boldsymbol{\tau}_\phi}(\kappa) = \left\langle -2Re\left(\widehat{\tilde{\phi}}^*(\boldsymbol{\kappa})\ \widehat{\nabla\cdot\boldsymbol{\tau}_\phi}(\boldsymbol{\kappa})\right)\right\rangle \tag{5.20}$$

As shown in Eq. 5.11, the energy dissipation in the VR-SM simulations may come either from molecular dissipation of the filtered scalar field (χ_R), or from subfilter scale transport ($\chi_{\boldsymbol{\tau}_\phi}$). Figure 5.9 shows plots of the total scalar-dissipation spectrum, which is the sum of the molecular and subfilter dissipation spectra $(D(\kappa) + D_{\boldsymbol{\tau}_\phi}(\kappa))$, for the four different κ_c values used in VR-SM simulations in the previous sections. Comparing Fig. 5.9 to Figs. 5.3(a) and 5.8, we notice that adding on the sub-

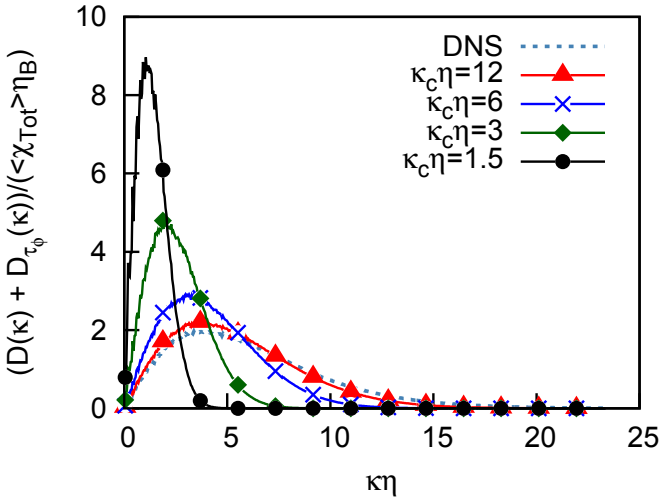

Figure 5.9: Normalized total scalar-dissipation spectra, computed from filtered DNS for several values of $\kappa_c\eta$.

filter contribution causes the dissipation spectrum to overshoot the spectrum expected from DNS. This observation is consistent with the data listed in Table 5.2, where $\langle\chi_{Tot}\rangle$ for VR-SM simulations are larger than $\langle\chi\rangle$ for the DNS. This is the reason why the variance of any VR-SM scalar field is smaller than that of the unfiltered DNS field. All the curves in Fig. 5.9 decay rapidly beyond their respective explicit filter cutoff wavenumbers, which is an expected occurrence, given the high attenuation inherent in the Gaussian filter beyond κ_c. This raises the possibility that beyond a certain wavenumber, no useful information, with regard to transport of the filtered scalar, is retained on the grid.

To explore this possibility in detail, we consider some of the data shown in Fig. 5.9, but now we evaluate the cumulative total-dissipation rate as the ratio of the area under the dissipation spectra (Fig. 5.10). The mathematical definition is given as follows:

$$\text{Cumulative dissipation} = \frac{\int_0^{\kappa}\left(D(\kappa)+D_{\boldsymbol{\tau}_\phi}(\kappa)\right)d\kappa}{\int_0^{\kappa_T}\left(D(\kappa)+D_{\boldsymbol{\tau}_\phi}(\kappa)\right)d\kappa} \tag{5.21}$$

The cumulative total-dissipation quickly ascend to a value of 1.0 close to approximately $2\kappa_c\eta$, for both $\kappa_c\eta = 1.5$ and 3. Quantitative values from the curves, listed in Table 5.3, confirm that more than 95% (and in fact close to 99%) of the filtered dissipation spectrum is resolved by the time we

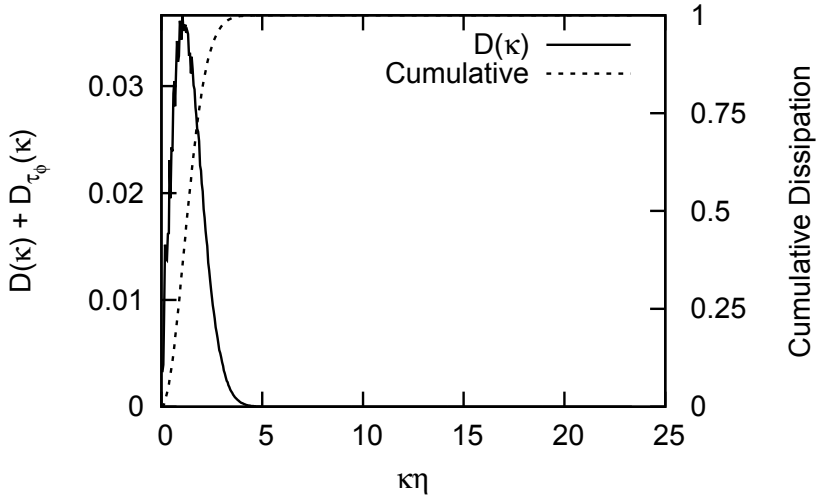

(a) $\kappa_c\eta = 1.5$

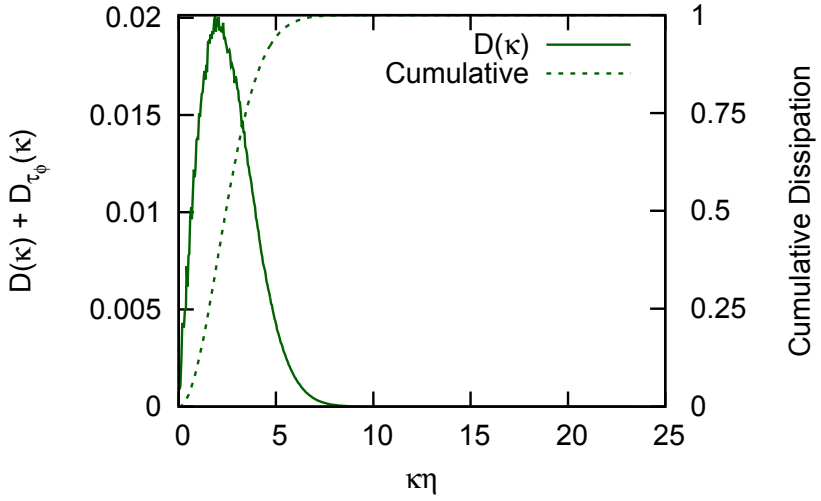

(b) $\kappa_c\eta = 3$

Figure 5.10: Total scalar-dissipation spectra computed from filtered DNS, and the ratio of the area under the curve as a function of $\kappa\eta$.

Table 5.3: Table showing $\kappa\eta$ values when approximately 95% and 99% of the total-dissipation rate is resolved, for the curves shown in Fig. 5.9.

% Resolved	$\kappa_c\eta = 1.5$	$\kappa_c\eta = 3$	$\kappa_c\eta = 6$	$\kappa_c\eta = 12$
95%	2.7	5.1	8.4	11.3
99%	3.4	6.3	10.6	14.6

reach $2\kappa_c\eta$. These observations suggest that keeping $\kappa_T\eta$ larger than $2\kappa_c\eta$ may not be an effective use of computational resources, as the entire total-dissipation spectrum is resolved at $2\kappa_c\eta$. To test the accuracy with which truncated grids with $\kappa_T\eta = 2\kappa_c\eta$ are able to support VR-SM simulations, we conduct additional *a posteriori* simulations using both the original and regularized forms of the tensor-diffusivity model in the following Section.

5.4.2 *A posteriori* testing with $\kappa_T\eta = 2\kappa_c\eta$

In this section, we repeat the *a posteriori* simulations discussed in Sec. 5.3, using both the original and the regularized tensor-diffusivity models, for model-validation on truncated grids (Sec. 5.1). These VR-SM tests are conducted in spirit of 'true LES', i.e., for predicting large-scale behavior when the smallest dynamical scales are unresolved on the simulation grid. For the first test, a grid size of 512^3 is used ($\kappa_T\eta = 12$), Δ is set such that $\kappa_c\eta = 6$, and both the HOUC5 and BCH scalar transport schemes are used. The relevant scalar dissipation spectra and PDFs of χ_R are shown in Fig. 5.11. The spectra indicate that results from BCH agree very well with the filtered DNS, but there is a slight discrepancy for results computed using the HOUC5 scheme. The differences noticeable may be attributed to slightly higher numerical diffusion in HOUC5 than in BCH, which justifies the effort put into formulating the improved numerical scheme in Chapter 3. The PDF curves show good agreement with the filtered DNS data, and are similar to results shown in Fig. 5.3(b). The use of model regularization does not induce any unwarranted effects on the result, as can be inferred from the dissipation and PDF curves shown in Figs. 5.11(c) and 5.11(d). These observations confirm that the tensor-diffusivity model is capable of reproducing filtered DNS data quite well, when using truncated grids with $\kappa_T\eta = 2\kappa_c\eta$.

To determine model accuracy on truncated grids, additional Velocity Resolved - Scalar Modeled simulations with $\kappa_c\eta = 3$ and $\kappa_c\eta = 1.5$ (the test used for generating Fig. 5.4) are conducted on grids corresponding to $\kappa_T\eta = 3$, 6 and 12. Barring the combination of $\kappa_c\eta = 1.5$ with $\kappa_T\eta = 12$, the simulations using the non-regularized model (i.e., the original tensor-diffusivity formulation) on these coarse grids do not suffer the instability that manifests when using extremely refined grids.

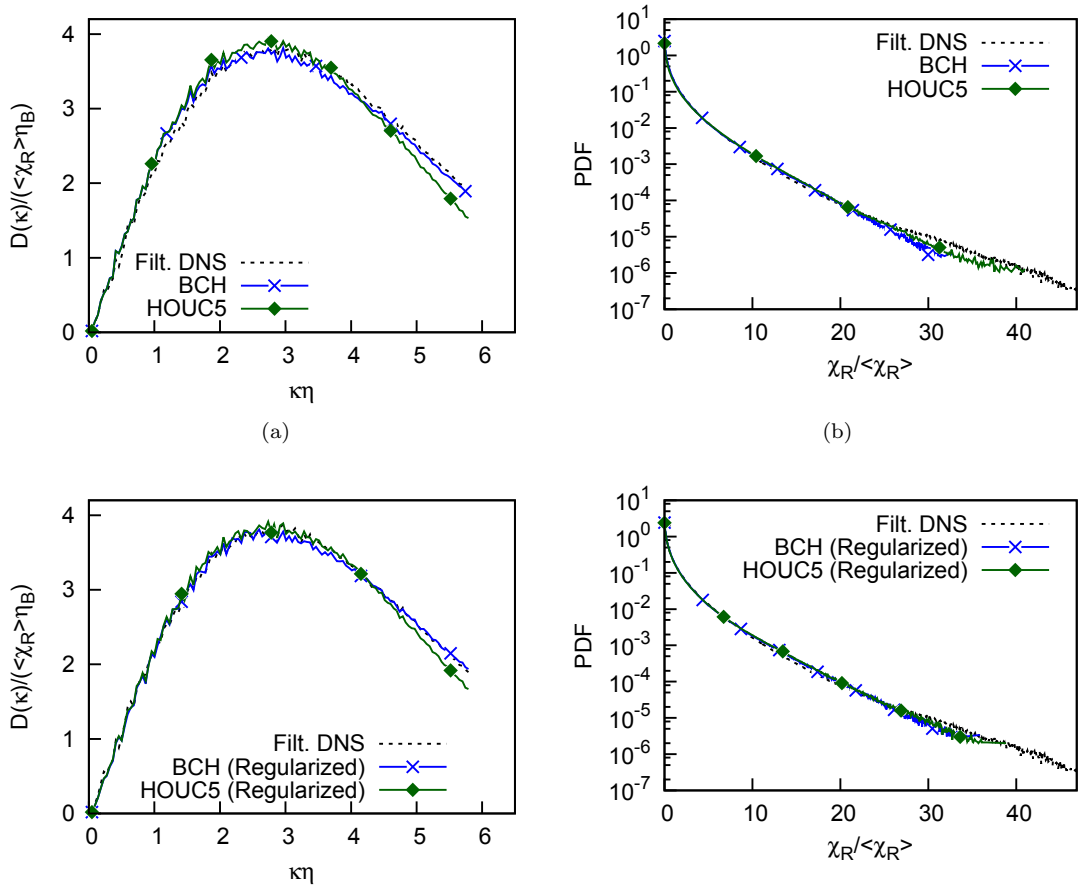

(a)

(b)

(c) Scalar dissipation spectra

(d) PDFs of χ_R

Figure 5.11: Results for $\kappa_c\eta = 6$ at $\kappa_T\eta = 12$ (truncated grid). Curves shown for filtered DNS, and data obtained using the BCH and HOUC5 schemes on truncated grid with the original tensor-diffusivity model (top row), and the regularized model (bottom row).

The implication of this observation is that numerical dissipation in BCH, although less severe than that for all other transport schemes considered in this thesis (Chapter 3), becomes large enough on coarse grids to suppress the modestly sized negative component of $\chi_{\boldsymbol{\tau}_\phi}$.

Figure 5.12 shows the scalar dissipation spectra obtained for the stable cases, with all the $\kappa_c\eta - \kappa_T\eta$ combinations used. The dissipation spectra are considered for comparison of the various cases as they put greater emphasis on the smallest resolved scales. We observe that at $\kappa_T\eta = 12$ and 6, the original tensor-diffusivity model shows better agreement with the filtered DNS than the regularized form, for both filter-cutoff locations $\kappa_c\eta = 1.5$ and 3 (Figs. 5.12(a) through (d)). The regularized model is marginally over-dissipative (which may be explained by the absence of backscatter in the model, i.e., missing λ_1 and λ_2 terms), leading to a slight mismatch with filtered DNS spectra. At $\kappa_T\eta = 3$ (Figs. 5.12(e)), we begin to see the effects of negative $\chi_{\boldsymbol{\tau}_\phi}$ manifest as a surplus in large wavenumber energy content in the non-regularized $\kappa_c\eta = 1.5$ spectrum. Comparatively better agreement of the regularized form with filtered DNS data for $\kappa_c\eta = 1.5$ (Figs. 5.12(f)) is merely due to the increased model-dissipation compensating the surplus close to the cutoff.

One of the important realizations that the $\kappa_c\eta = 3$, $\kappa_T\eta = 3$ (or in other words, $\Delta = \Delta x$, i.e., implicit filtering) spectra shown in Fig. 5.12(e) and (f) lead to, is that when used in conjunction with implicit filtering, neither the original, nor the regularized forms of the tensor-diffusivity model perform very well in reproducing filtered DNS data. There is a distinct pile-up of energy at large wavenumbers (the reason for the pile-up is explained in Sec. 2.3.2), which is reminiscent of remarks in the literature [132, 133, 137] concerning the insufficiently dissipative nature of the tensor-diffusivity model.

The results in this section suggest that in a majority of situations, it may be preferable to use low-dissipation FV/FD numerical schemes (e.g., BCH) in combination with the original form of the tensor-diffusivity model. Model regularization on truncated grids should be considered only if necessary, for instance, when considering pseudo-spectral schemes (without any numerical dissipation), or when regularization assists in maintaining physical scalar bounds (Chapter 6, and Ref. [9]). We note that with an adequately large $\Delta/\Delta x$ ratio (e.g., $\Delta/\Delta x \geq 2$, for the cases tested), the presence

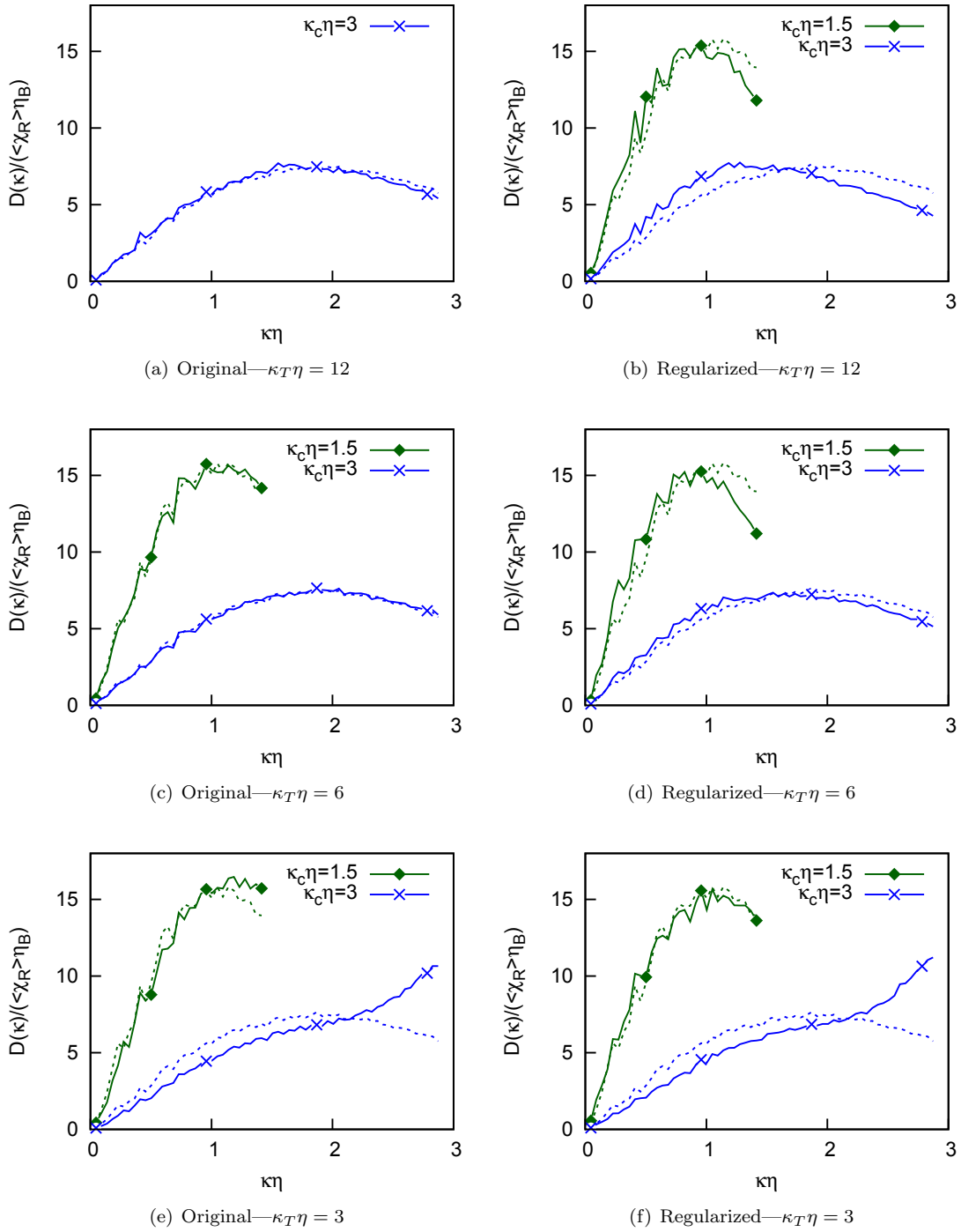

(a) Original—$\kappa_T\eta = 12$

(b) Regularized—$\kappa_T\eta = 12$

(c) Original—$\kappa_T\eta = 6$

(d) Regularized—$\kappa_T\eta = 6$

(e) Original—$\kappa_T\eta = 3$

(f) Regularized—$\kappa_T\eta = 3$

Figure 5.12: Effect of varying $\kappa_T\eta$ on scalar dissipation spectra. Top row—$\kappa_T\eta = 12$, middle row—$\kappa_T\eta = 6$, bottom row—$\kappa_T\eta = 3$. Solid lines with symbols correspond to VR-SM simulations, and broken lines correspond to filtered DNS.

of relatively minor numerical dissipation does not degrade the VR-SM result at the resolved scales, since numerical errors are mainly dominant at the subfilter scales.

5.5 Summary

In this Chapter, we have verified the *a priori* observations from Chapter 4, by performing Velocity Resolved - Scalar Modeled simulations of homogeneous isotropic turbulence using the tensor-diffusivity model. The results indicate that the model is stable for sufficiently large κ_c, and is capable of reproducing filtered DNS data with remarkable accuracy. Comparison to unfiltered DNS data indicates good agreement at the small wavenumbers, i.e., at the large physical length scales. The differences observed with unfiltered DNS at large wavenumbers are the result of the effective Gaussian filtering kernel inherent in the modeled equation. Solution instability manifests at smaller values of κ_c (i.e., large Δ), which is explained by analyzing the κ_c dependence of the negative component of subfilter dissipation. To address the issue of instability, model regularization is implemented by suppressing the negative dissipation, and yields stable simulations even with larger Δ. The results produced by the regularized model compare well with those obtained using the original non-regularized model, as well as with results from filtered DNS.

Velocity Resolved - Scalar Modeled simulations conducted on truncated grids also yield extremely accurate results, suggesting that the tensor-diffusivity model may be exceptionally well-suited for simulation of practical scenarios. Solution instability is not observed on truncated grids with sufficiently small $\kappa_T\eta$, since numerical diffusion damps the negative component of subfilter dissipation at the smallest scales. These small numerical errors do not seem to have an adverse effect on the resolved scales in the VR-SM simulations, as long as a ratio of $\Delta/\Delta x \geq 2$ is used. Filter-width ratios much larger than 2 may not be ideal, since very little information is retained at the subfilter scales beyond $2\kappa_c\eta$.

We surmise that in order to avoid solution instability, it may be preferable to use low-dissipation FV/FD numerical schemes in combination with the original form of the tensor-diffusivity model, rather than relying on model regularization. The effect of using implicit filtering is also examined,

and these simulations result in a pile-up of energy close to the grid truncation wavenumber, which is reminiscent of observations noted in the literature. The results provide support for the argument that Velocity Resolved - Scalar Modeled simulations of turbulent scalar transport must be performed by using an appropriate combination of subfilter model and $\kappa_T\eta/\kappa_c\eta$ ratio. For the $Re_\lambda = 30$, $Sc = 256$ test case used in this chapter, accurate results are obtained when using the tensor-diffusivity model on truncated grids with ($\kappa_c\eta$, $\kappa_T\eta$) values of (6, 12) and (3, 6).

Chapter 6

Application of the Tensor-Diffusivity Model for VR-SM Simulations of the Turbulent Mixing Layer

In the previous chapters, we have developed a new scalar transport scheme (Chapter 3), identified *a priori* the best SFF model to use when modeling in the viscous-convective subrange (Chapter 4), and validated this model *a posteriori* in homogeneous isotropic turbulence (Chapter 5). We now present results from Velocity Resolved - Scalar Modeled simulations of the turbulent mixing layer, with the tensor-diffusivity model implemented as the subfilter scalar-flux model. Once again, the filter-width is placed in the viscous-convective subrange. The goal is to assess the effectiveness of the model in simulating shear-dominated scenarios with large Schmidt numbers.

The simulation setup is described in Sec. 6.1, along with details regarding the simulation Reynolds number and the need for using the regularized form of the model. Scalars differing in Schmidt number by three orders of magnitude are transported simultaneously, and the corresponding mixing characteristics are analyzed, before and after entering the self-similar mixing regime, in Sec. 6.2. Relevant discussions involve examination of the scalar-variance, scalar autocorrelation functions, scalar-energy spectra, and planar averages of the resolved and subfilter scalar dissipation rates.

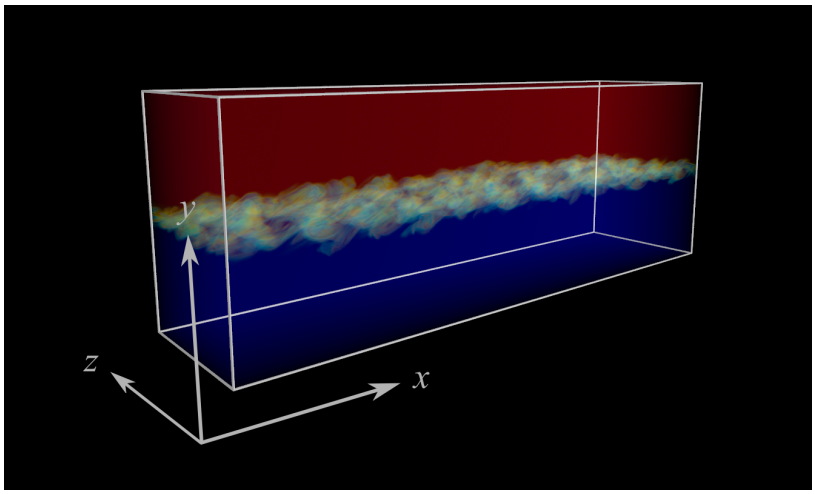

Figure 6.1: The 3D turbulent mixing layer configuration, with the streamwise, cross-stream, and spanwise axes depicted as x, y, and z, respectively. Color indicates scalar value, with blue corresponding to $\phi = 0$, and red corresponding to $\phi = 1$.

6.1 Simulation details

The initial conditions used in the simulations discussed in this Chapter are identical to the mixing layer case discussed in Chapter 3. The velocity field is initialized with two uncorrelated boundary layers flipped horizontally and vertically, and the scalar distribution is a Heaviside function with transition from 0 to 1 at the center plane. The 3D configuration setup is shown in Fig. 6.1, and a corresponding 2D $x - y$ plane cut was shown in Fig. 3.15(a).

The time evolution of the simulation Taylor-scale Reynolds number ($Re_\lambda = u'\lambda/\nu$) on the center plane of the mixing layer is shown in Fig. 6.2. As defined in Chapter 3, $\tau = t\Delta U/\delta_m^0$ is the non-dimensional simulation time associated with the mixing layer. The two Reynolds numbers shown, namely Re_{λ_x} and Re_{λ_z}, were computed using λ evaluated in the streamwise and spanwise directions, respectively. λ is a geometrically defined quantity, dependent on the osculating parabola of the longitudinal velocity autocorrelation function (see Fig. 6.7 in Ref. [106]). Using appropriate geometrical relations, the dependence of λ on r.m.s velocity and velocity derivatives is expressed as

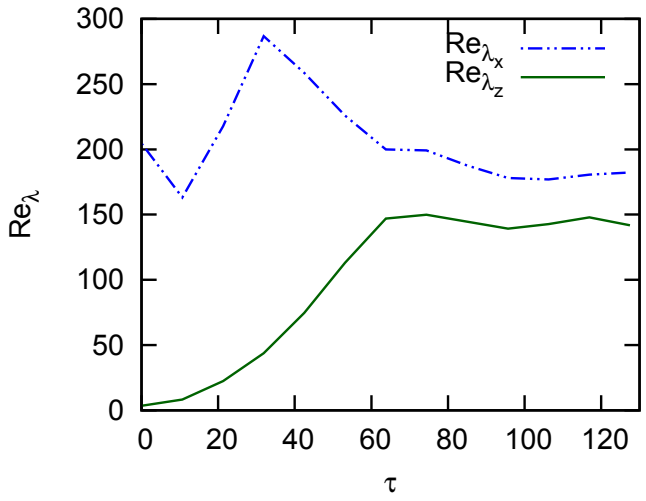

Figure 6.2: Time variation of the Taylor-scale Reynolds numbers computed using the streamwise (λ_x) and spanwise (λ_z) Taylor-microscales.

follows [106]:

$$\left\langle \left(\frac{\partial u}{\partial x} \right)^2 \right\rangle = \frac{2u'^2}{\lambda_x^2} \tag{6.1}$$

$$\left\langle \left(\frac{\partial w}{\partial z} \right)^2 \right\rangle = \frac{2w'^2}{\lambda_z^2} \tag{6.2}$$

Computation of both the velocity derivative and the velocity r.m.s. values was restricted to the central plane of the mixing layer. With λ_x and λ_z obtained from these definitions, we define $Re_{\lambda_x} = u'\lambda_x/\nu$ and $Re_{\lambda_z} = w'\lambda_z/\nu$. In Fig. 6.2, we observe some fluctuation in Re_{λ_x} in the early stages of the simulation, while Re_{λ_z} increases as turbulent flow develops in the spanwise direction. Both the Reynolds numbers attain a stationary value in the self-similar mixing regime (which starts at approximately $\tau = 60$: see Fig. 3.15(c)), with $Re_{\lambda_x} \approx 180$ and $Re_{\lambda_z} \approx 140$. These are relatively large values, and indicate the establishment of a well-developed turbulent velocity field.

As done in the previous chapters, we aim to keep the velocity field fully resolved in Velocity Resolved - Scalar Modeled simulations for scalar transport. Thus, we use truncated grids for the mixing layer simulations with $\kappa_T\eta = 3$, and Δ selected such that $\kappa_c\eta = 1.5$. The grid truncation wavenumber has been selected in accordance with observations in Sec. 5.4.2, which indicate that a

majority of the dissipation spectrum is resolved for $\kappa_T \eta = 2\kappa_c \eta$. Four different scalars are transported simultaneously, each with a different Schmidt number: 1, 10, 100, and 1000. We note that of these four, the scalar corresponding to $Sc = 1$ is unlikely to deviate much from the expected DNS results since it satisfies the fully resolved DNS criterion of $\kappa \eta_B \geq 1.5$, barring some attenuation from the effective explicit filter.

The regularized tensor-diffusivity model is used for SFF modeling, since backscatter in the original form of the model gave rise to significant breach of physical scalar bounds. The maximum breach observed with the original model, i.e., ϕ values outside the physical bounds $[0, 1]$, were 1.0007 for $Sc = 1$, 1.051 for $Sc = 10$, 1.14 for $Sc = 100$, and 1.174 for $Sc = 1000$. For $Sc = 1000$, which presents the worst case scenario in terms of bounds being breached, less than 0.05% of the total number of points in the simulation domain experienced such a breach. We clarify that these excursions are not a result of interpolation errors associated with the advection step (when using the BCH scheme), but instead arise due to negative diffusion from the λ_1 and λ_2 components in the model source term (Eq. 5.18). The scalar excursions resulting from negative diffusivity become progressively severe with increasing Sc due to the dependence of $\chi_{\ bm\tau_\phi}$ on $|\nabla\widetilde{\phi}|$, which is larger for higher Sc.

Using the regularized model led to noticeable improvement in terms of preserving scalar bounds, but minor fluctuations were observed nonetheless (maximum ϕ: 1.000 for $Sc = 1$, 1.0007 for $Sc = 10$, 1.019 for $Sc = 100$, and 1.028 for $Sc = 1000$, with less than 0.02% of the total number of points in the domain experiencing such a breach for $Sc = 1000$). It may be possible to eliminate these fluctuations by using an implicit treatment for time integration of the model source term, or by implementing 'clipping' after accounting for the SFF term, however, these possibilities were not explored in the current implementation.

Since these excursions happen outside of the advection step (Eq. 3.3), a single additional directive was included in the BCH algorithm to bypass bounding and enforce monotonicity, if either of the interpolating-node scalar values themselves were outside the range $[0, 1]$ (Fig. 6.3). Less than 25% of all the interpolations that breached physical bounds (for $Sc = 1000$) were observed to trigger this bypass; the rest followed the normal bounding procedure established in Chapter 3.

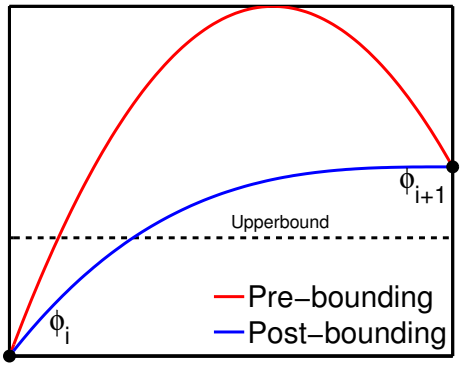

Figure 6.3: Bounding relevant to single sub-cell extremum bypassed to enforce monotonicity (contrast with Fig. 3.4(b)). ϕ_{i+1} is outside physical bounds due to contribution from the SFF model.

6.2 Scalar statistics in the mixing layer

6.2.1 Resolved cross-stream scalar-variance

We now discuss large-scale statistical results obtained from the simulations at various time instances, and for the four different Schmidt numbers involved. We begin our assessment by examining the time-varying cross-stream profile of the resolved scalar-variance, σ_ϕ^R, computed on $x-z$ planes and plotted in Fig. 6.4. The domain in the cross-stream direction extends from $y/\delta_m^0 = -37.24$ to $+37.24$, however we limit our attention to the region close to the central core. For both $Sc = 1$ and 1000, we observe a distinct change in scalar distribution before and after entering the self-similar mixing regime, which occurs at approximately $\tau = 60$. Initially, there is a sharp build-up of scalar-variance in the core, with minimal spread in the y direction, as large patches of unmixed scalar with ϕ=0 and 1 form. Rapid mixing in the self-similar state results in a drop in these sharp variance peaks, as the scalar field becomes more homogenized. The increasing spread of the curves that ensues is associated with expansion of the core in the y direction. The flattening of the variance profile in the core region has been observed previously in experimental studies [95], as well as in DNS studies [6]. We remark that the flattening occurs only after the self- similar mixing regime has been reached, and is not evident in the transient regime at all. It may be related to the turbulence in the core having reached a state of homogeneous turbulent shear flow [124, 115, 106], which is expected once self-similar mixing is attained.

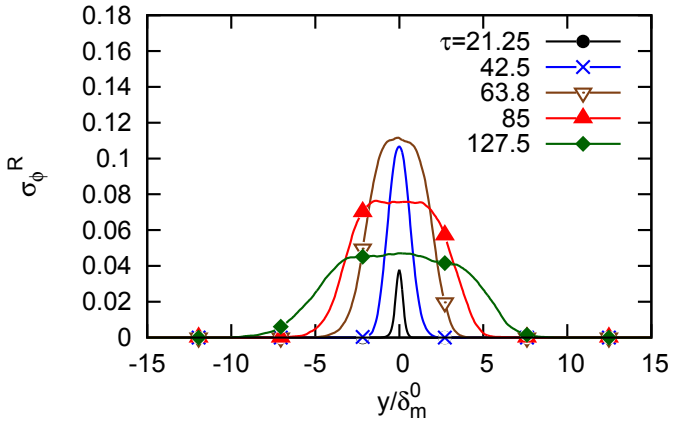

(a) $Sc = 1$

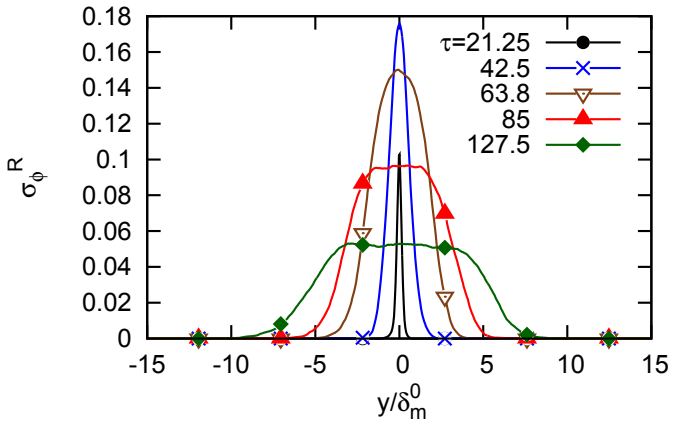

(b) $Sc = 1000$

Figure 6.4: Time evolution of the resolved scalar variance, for $Sc = 1$ and $Sc = 1000$, plotted as a function of distance from the center plane in the cross-stream direction.

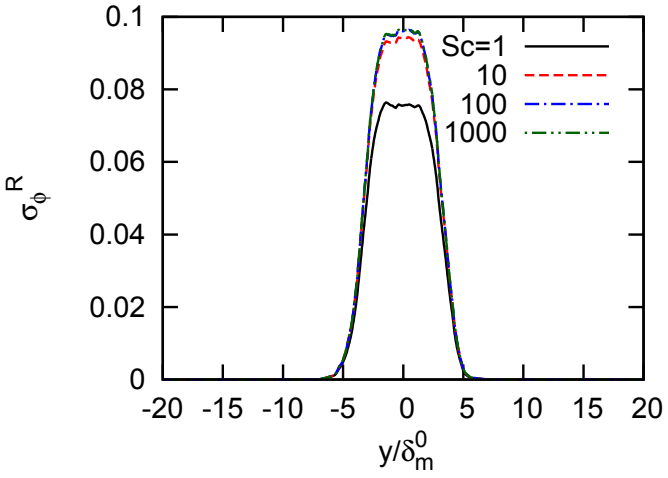

Figure 6.5: Schmidt number dependence of the resolved scalar variance at $\tau = 85$.

A larger Schmidt number results in a corresponding rise in the scalar-variance (Figs. 6.4 and 6.5), since molecular dissipation gets weaker with increasing Sc. From Fig. 6.5, we observe that the increase in resolved scalar-variance stagnates at large Sc, and the curve for $Sc = 100$ is virtually identical to that for $Sc = 1000$. Similar weakening of Schmidt number dependence of large-scale scalar statistics has been observed in experimental studies of gas-phase and liquid-phase mixing [73, 22, 23, 95]. The Schmidt number independence observed in our simulations is expected, if we consider that the resolved scalar-variance is related to the area under the resolved scalar-energy spectrum curve (Parseval's theorem). As will be shown later, the scalar-energy spectra for $Sc = 100$ and $Sc = 1000$ are virtually identical up until the grid truncation wavenumber, $\kappa_T\eta = 3$ (Fig. 6.11). Theoretically, Schmidt number dependent differences appear in scalar spectra at large wavenumbers, however, our simulations do not capture these high $\kappa\eta$ modes since they lie at subfilter scales. Further discussion regarding contribution from subfilter scales is provided in Sec. 6.3.

The temporal evolution of the maximum of σ_ϕ^R shown in Fig. 6.6 also suggests that the scalar fields for $Sc = 100$ and 1000 evolve in a similar manner over time. As with previous observations, we note a continuous increase in the maximum of the variance in the transient regime marked by $\tau < 60$, and a subsequent drop in the self-similar regime. An interesting occurrence on the figure is the leftward shift of the peak with increasing Sc. This is probably related to the fact that with

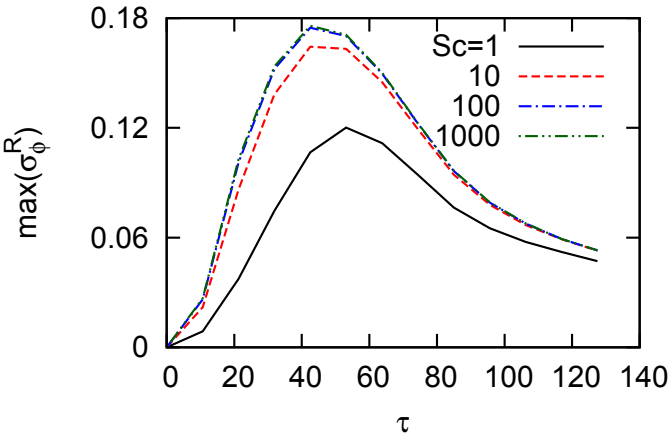

Figure 6.6: Temporal evolution of the maximum of σ_ϕ^R on the center plane.

a sharp build-up in the magnitude of $\nabla\widetilde{\phi}$ for higher Sc, the model-contributed subfilter dissipation kicks in earlier, thereby giving rise to the trend observed.

To determine whether we can identify differences between the transient and self-similar regimes, Fig. 6.4 is replotted in Fig. 6.7 after appropriate normalization. The vertical axis has been normalized with the value of σ_ϕ^R at the center plane, and the horizontal axis has been normalized using a 'scalar thickness' (δ_ϕ), defined as the distance between the two planes where the scalar variance is 5% of the value at the center plane. The two curves in the self-similar regime ($\tau > 60$) collapse quite well for both $Sc = 1$ and 1000, and are distinctly different from the normalized curves in the transient regime ($\tau < 60$).

6.2.2 Scalar autocorrelation function

We now examine scalar autocorrelation functions, which are defined as follows:

$$R_{xx}(r) = \frac{\left\langle \widetilde{\phi}(x+r)\widetilde{\phi}(x) \right\rangle}{\sigma_\phi^R} \tag{6.3}$$

$$R_{zz}(r) = \frac{\left\langle \widetilde{\phi}(z+r)\widetilde{\phi}(z) \right\rangle}{\sigma_\phi^R} \tag{6.4}$$

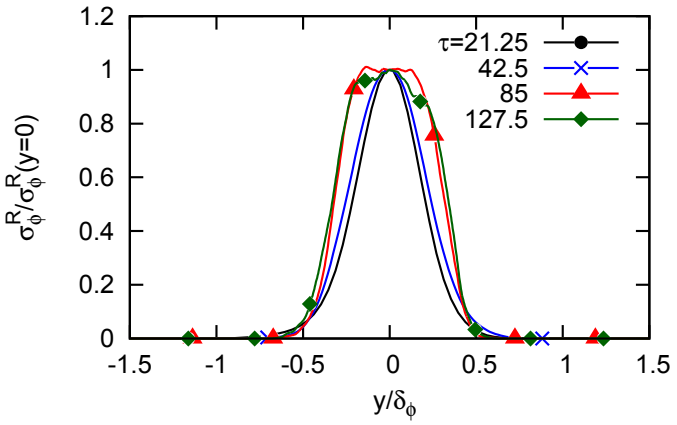

(a) $Sc = 1$

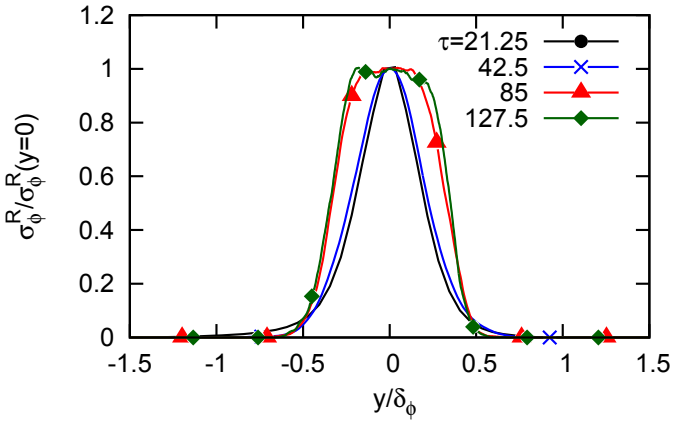

(b) $Sc = 1000$

Figure 6.7: Same as Fig. 6.4, but normalized to show collapse in the self-similar regime.

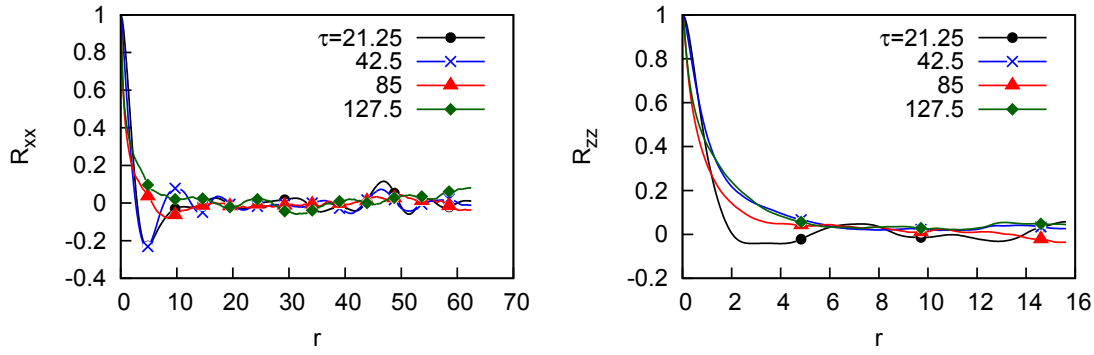

(a) Streamwise autocorrelation function

(b) Spanwise autocorrelation function

Figure 6.8: Time evolution of the streamwise and spanwise scalar autocorrelation functions for $Sc = 1000$.

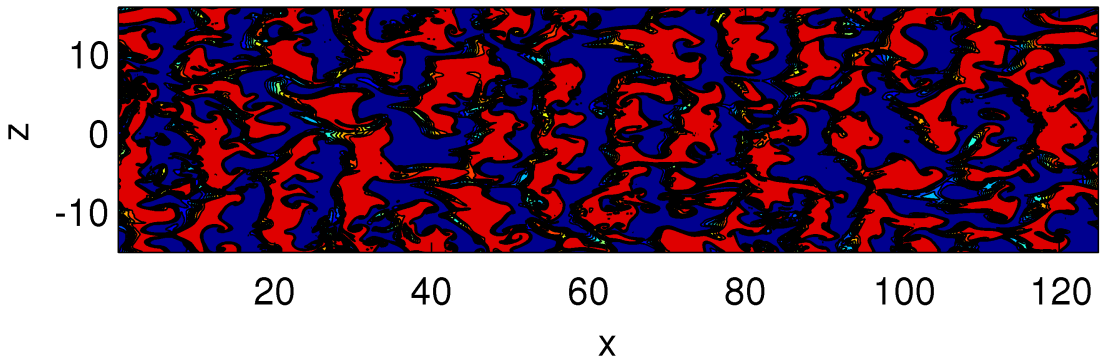

Figure 6.9: Center plane cut showing the roll-up caused by Kelvin-Helmholtz instability in the turbulent mixing layer ($\tau = 42.5$). Color axis corresponds to scalar value, with $\phi = 1$ shown in red, and $\phi = 0$ shown in blue.

These autocorrelation functions are related to the 1D scalar-energy spectra via the Fourier transform:

$$E_x(\kappa) = \int_{-\infty}^{\infty} R_{xx}(r) e^{-i\kappa r} dr \tag{6.5}$$

$E_x(\kappa)$ is referred to simply as $E(\kappa)$ in most places throughout this chapter. Both the streamwise and spanwise autocorrelation functions, computed for the scalar with $Sc = 1000$, are shown for different time instances in Fig. 6.8. We notice a strong negative dip in R_{xx} at approximately $r = 5$ for time instances $\tau \leq 42.5$, which is most likely associated with roll-up induced by Kelvin-Helmholtz instability in the early stages. The phenomenon is visualized using a top-view cut of the scalar field at the central plane in Fig. 6.9. As expected, R_{zz} does not show a similar indication of roll-up

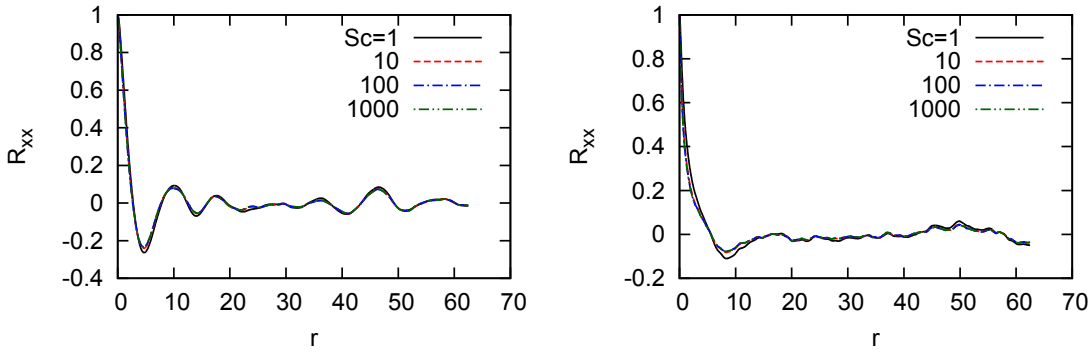

(a) $\tau = 42.5$ (b) $\tau = 85$

Figure 6.10: Comparison of streamwise autocorrelation functions for the four different Schmidt numbers.

(Fig. 6.8(b)), since distinct vortical structures are not likely to form in the streamwise direction. As time passes, mixing on the center-plane reaches a more homogenized state, and the strong negative dip in R_{xx} curves disappears for $\tau = 85$ and 127.5 (Fig. 6.8(a)), i.e., after entering the self-similar mixing regime.

To assess the Schmidt number dependence of autocorrelation functions, we compare R_{xx} computed from two separate snapshots in Fig 6.10. The first snapshot was taken before entering the self-similar mixing regime ($\tau = 42.5$), and the second after entering it ($\tau = 85$). Schmidt number induced differences in the autocorrelation functions are barely discernible, which is expected, since diffusion-based effects are dominant at the smallest length-scales, and autocorrelation functions focus primarily on the large scales. To examine Sc dependent effects that may indicate distinct scalar-transport behavior at the small scales, we take a closer look at 1D scalar-energy spectra.

6.2.3 1D scalar-energy spectra

While autocorrelation functions give us a good idea of the large-scale structure of the scalar field, 1D scalar-energy spectra provide us with a much more extensive view of scalar transport dynamics, specifically by depicting the energy content of scalar Fourier modes in wavenumber-space. The relevant spectra computed for the four different Schmidt numbers at the end of the simulation ($\tau = 127.5$) are provided in Fig 6.11. The spectrum for $Sc = 1$ exhibits a well-developed viscous-

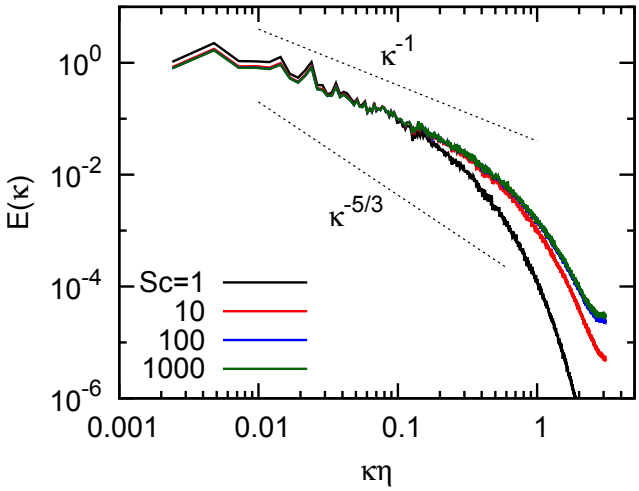

Figure 6.11: Non-normalized 1D scalar-energy spectra computed in the streamwise direction at $\tau = 127.5$, on the center plane of the mixing layer.

diffusive subrange, and resembles the form expected for a fully resolved DNS. For $Sc = 10$, the onset of roll-off (i.e., faster decay than a power-law behavior) is noticeable in the spectrum at approximately $\kappa\eta = 0.3$, which is associated with the beginning of the viscous-diffusive subrange ($\kappa\eta_B \approx 0.1$). The implication of this observation is that VR-SM simulations are able to recreate the expected transition from non-diffusive to diffusive scales.

The energy spectra in Fig. 6.11 seem to approach a power law scaling with a slope that lies between $-5/3$ and -1. Compensated spectra shown in Fig. 6.12. indicate that the scaling is quite close to being -1 for large Schmidt numbers. The spectra for $Sc = 100$ and 1000 are virtually identical all the way up to the grid truncation wavenumber. This, again, is an expected occurrence, as can be confirmed from Fig. 1.5; scalar spectra for high Sc scalars are virtually identical until the beginning of roll-off associated with the viscous-diffusive subrange. Additionally, scalar transport outside the viscous-diffusive subrange is expected to be largely independent of the Schmidt number (for $Sc \gg 1$), owing to the phenomenon of spectral decoupling discussed in Chapter 2. Finally, we recall from Fig. 6.5 that the resolved variance is relatively constant across planes in the core region ($-2 < y/\delta_m^0 < 2$), which suggests that planar scalar-energy spectra computed across the core most likely resemble those shown in Fig 6.11.

To follow the temporal evolution of scalar Fourier mode energy content, we plot the relevant

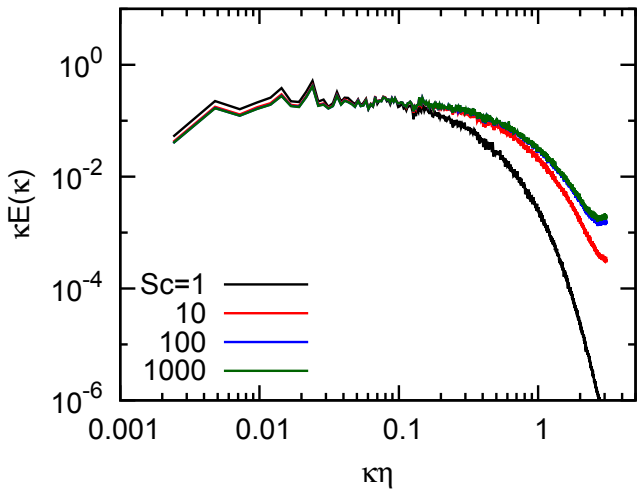

Figure 6.12: Same as Fig. 6.11, but compensated to depict -1 scaling.

spectra in Fig. 6.13. Before entering the self-similar mixing regime (i.e., for $\tau \leq 42.5$), we notice a slight 'bump' in all the spectra at approximately $\kappa\eta = 0.03$. Once again, this is related to the Kelvin-Helmholtz instability-induced roll-up, which manifests as the dip in R_{xx} in Fig. 6.8(a). Once self-similar mixing is attained, the shapes of the spectra do not change noticeably from $\tau = 85$ to 127.5, which is an expected outcome in this regime.

We also note a slight up-turn in the scalar spectra for $Sc = 100$ and 1000, close to the grid truncation wavenumber. This occurrence is usually observed in DNS with spectral codes, and results from scalar-energy being aliased from the unresolved modes to the smallest resolved modes. The existence of the up-turned tail is indicative of extremely low numerical diffusion inherent in the transport scheme, and is yet another confirmation that the BCH scheme performs quite well for Velocity Resolved - Scalar Modeled simulations of scalar transport.

6.2.4 Scalar dissipation rate

We now investigate the cross-stream variation of the resolved and total mean scalar-dissipation rates. As discussed in Sec. 5.2 these quantities play a pivotal role in regulating the net scalar variance available in the domain. The total mean scalar-dissipation rate, $\langle\chi_{Tot}\rangle = \langle\chi_R\rangle + \langle\chi_{\boldsymbol{\tau}_\phi}\rangle$, includes contribution from both the resolved molecular dissipation, as well as subfilter model-contributed dis-

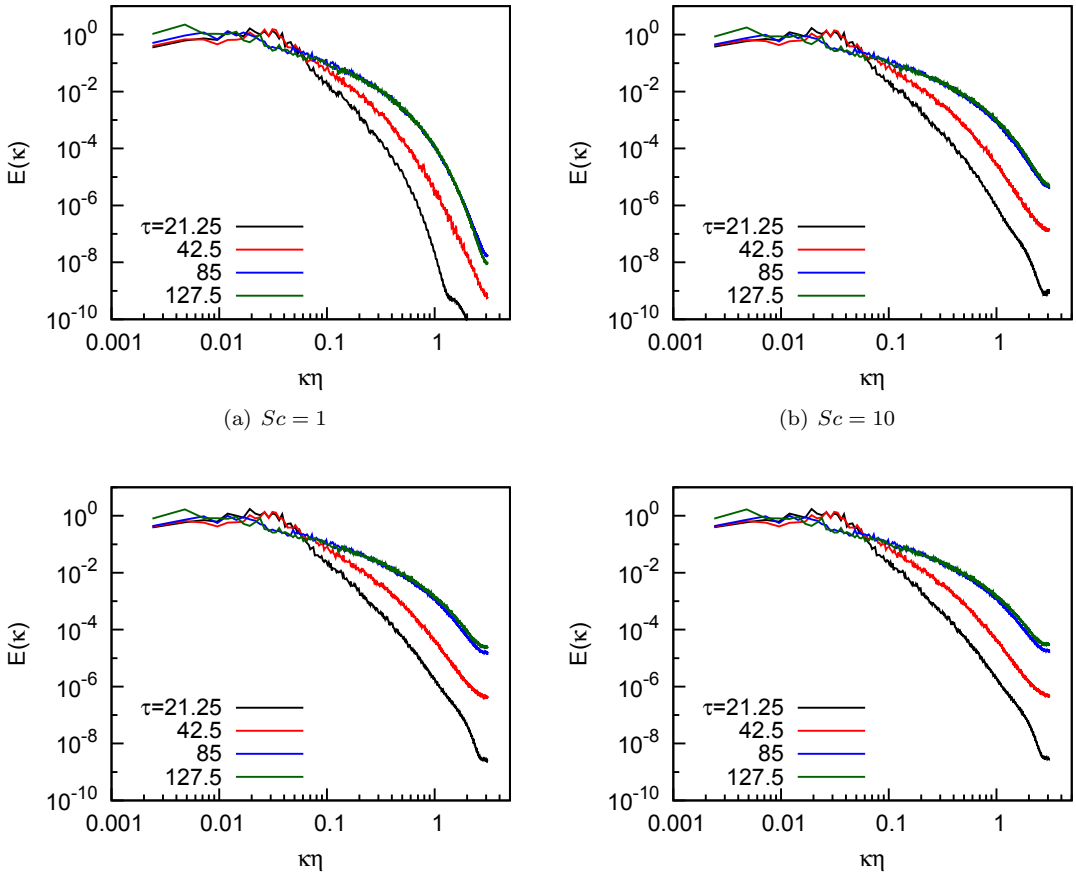

(a) $Sc = 1$ (b) $Sc = 10$

(c) $Sc = 100$ (d) $Sc = 1000$

Figure 6.13: Temporal evolution of the 1D scalar-energy spectra for the four different Schmidt numbers.

sipation. Figure 6.14(a) indicates that the resolved mean scalar dissipation rate, $\langle \chi_R \rangle = 2\mathcal{D}|\nabla\widetilde{\phi}|^2$, decreases significantly with increasing Sc, which may be attributed to the decreasing molecular diffusivity and the relatively constant value of the resolved scalar gradient ($|\nabla\widetilde{\phi}|$). $\langle \chi_{Tot} \rangle$, on the other hand, reaches a plateau (Fig. 6.14(b)), which points to a trend of it becoming Schmidt number independent for $Sc \gg 1$. This suggests that at large Sc, the majority of scalar-dissipation is contributed by the subfilter model, and molecular dissipation is close to being negligible in comparison. The present results confirm the observations made in Sec. 5.2 for homogeneous turbulence. The consequence of the existence of similar total dissipation rates is that the time-evolution of the scalar field occurs in a similar manner as well. This explains the apparent saturation of the scalar-variance and scalar-energy spectra with increasing Sc, observed in Fig. 6.5, 6.6, and 6.11.

We remark that the curves for $Sc = 1$ show barely any difference between the planar distribution of $\langle \chi_R \rangle$ and $\langle \chi_{Tot} \rangle$. This is expected, since the scalar is close to being fully resolved for $Sc = 1$ ($\kappa_c \eta_B \geq 1.5$), and subfilter model contribution to scalar transport should be negligible.

6.3 Discussion

The results in this chapter, as well as those in Chapter 5 (Fig. 5.2), suggest that the VR-SM simulation framework combined with the tensor-diffusivity model is capable of predicting large-scale scalar statistics (the so-called 'large scale observables') with reasonable accuracy. Simulation results mirror trends observed in experimental studies [73, 22, 23, 95], indicating that the observed molecular mixing becomes less dependent on increasing Schmidt number when the Reynolds number is sufficiently large. The simulations are able to recreate the expected behavior of the resolved small-scale statistics as well, as indicated by the dissipative roll-off for $Sc = 10$ in Fig. 6.11. However, the extent of this capability is limited ultimately by the effective filter cutoff wavenumber used for the simulation. If small-scale quantities at the unresolved scales (i.e., subfilter scales, for instance to be used in reacting flow simulations) are of interest, additional modeling of subfilter quantities may be incorporated into the VR-SM framework. Such modeling can involve estimating the subfilter quantities (such as the subfilter scalar-variance or scalar-dissipation rate) as a function of the mod-

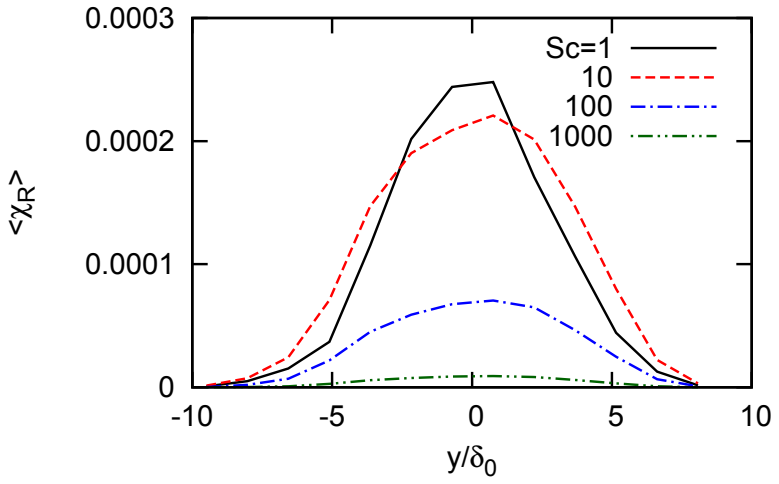

(a) Resolved mean scalar dissipation rate

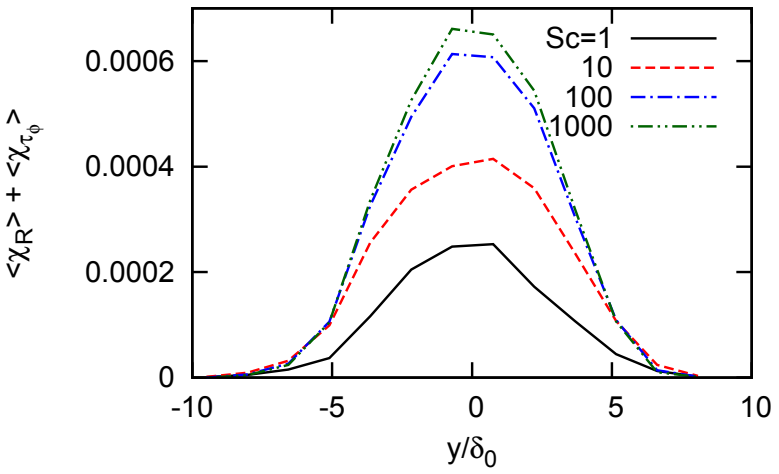

(b) Total mean scalar dissipation rate

Figure 6.14: Resolved, and total mean scalar dissipation rates for the four different Schmidt numbers, computed at $\tau = 127.5$ on the center plane of the mixing layer.

eled scalar quantity [67, 8], or can involve solving additional transport equations for the subfilter quantities in the same spirit as discussed in [97, 70].

6.4 Summary

In this Chapter, Velocity Resolved - Scalar Modeled simulations have been performed in the turbulent mixing layer, to assess the effectiveness of the tensor-diffusivity model in simulating shear-dominated flows with large Schmidt numbers. The regularized form of the model is used in these simulations to minimize breach of physical bounds. The effect of the Schmidt number on a variety of scalar statistics is examined, specifically, by analyzing scalar autocorrelation functions, 1D energy spectra, cross-stream scalar-variance, and planar averages of the resolved and subfilter scalar dissipation rates. The quantities analyzed show distinctively different behavior in the regimes before and after attaining self-similar mixing. The two regimes are characterized by a sharp build-up of scalar-variance/energy in the initial transient stage, and a switch to rapid mixing in the self-similar state.

Further examination of the resolved and subfilter scalar-dissipation rates suggests that with increasing Sc, subfilter dissipation dominates the resolved molecular dissipation, and attains a plateau as the Schmidt number is increased. This explains why resolved large-scale statistics become relatively independent of the Schmidt number for $Sc \gg 1$. The results in this chapter indicate that the simulation framework established is capable of providing reasonable estimates of large-scale scalar statistics, at much lower computational cost than would be required for fully resolved DNS.

We remark that modeling of subfilter quantities, i.e., recreating quantities that have been filtered out, is outside the scope of the work presented in this thesis, but this could be included in future extensions of the work presented. Furthermore, additional future work in advancing modeling capability for high Re, high Sc flows may entail analyzing VR-SM datasets in the same manner as has been done for DNS datasets in Chapter 4. In that case, the objective would be to assess and validate the best approach of conducting Large Eddy Simulations at large Reynolds and Schmidt numbers, when filtering in the inertial subrange. This will become necessary since modeling in the viscous-convective subrange for application to atmospheric and oceanic flows would not be computationally

feasible in the foreseeable future. The relevant analysis could be done in two stages, as has been the approach pursued in this thesis; *a priori* evaluation of model suitability would involve filtering VR-SM data in the inertial subrange to identify a suitable LES model, which could be followed by *a posteriori* tests to assess model performance in actual Large Eddy Simulations.

Chapter 7

Summary of the Thesis

The objective of this thesis was to develop a framework to conduct velocity resolved - scalar modeled (VR-SM) simulations, which will enable accurate simulations at higher Reynolds and Schmidt (Sc) numbers than are currently feasible. The framework established in this thesis serves as a first step to enable future simulation studies for practical applications. To achieve this goal, in-depth analyses of the physical, numerical, and modeling aspects related to $Sc \gg 1$ were presented, specifically when modeling in the viscous-convective subrange. Transport characteristics specific to the viscous-convective subrange were scrutinized by examining scalar-velocity Fourier mode interactions, via *a priori* analysis of high resolution DNS datasets. Special attention was paid to the combined physical/mathematical behavior of the subfilter scalar-flux vector orientation, which led to the identification of an optimal subfilter model for scalar transport. Velocity resolved - scalar modeled simulations of homogeneous isotropic turbulence were conducted to confirm the behavior theorized in these *a priori* analyses. VR-SM simulation of a turbulent mixing layer was also discussed, with the intent of analyzing Schmidt number dependence of a variety of scalar statistics. In addition to physical and modeling considerations, the impact of numerical errors on simulations was also discussed. To lower numerical dissipation while maintaining scalar bounds during the convective step of scalar transport, a novel method of enforcing physically and mathematically appropriate bounds was formulated, specifically for use with cubic Hermite polynomials.

7.1 Analyzing subfilter scalar-flux behavior and scalar-velocity triadic interactions in the viscous-convective subrange

In Chapter 2, we examined the dependence of the subfilter scalar-flux magnitude ($|SFF|$) on the filter-width (or equivalently, the filter cutoff wavenumber), the Schmidt number (Sc), and the Reynolds number (Re_λ) used in simulations. This was done to identify the role that subfilter models must play, specifically in the viscous-convective subrange, when trying to recreate filtered DNS data. The results suggest that beyond a certain threshold cutoff ($\kappa_c\eta > 5$), there is an exponential drop in the $|SFF|$ with increasing κ_c. The $|SFF|$ curves were seen to vary systematically with the Schmidt number, however, appropriate rescaling led to a collapse of $|SFF|$ curves at different Reynolds numbers. This observation could be especially useful in anticipating $|SFF|$ behavior at very large Reynolds numbers, since moderate Re_λ DNS datasets (which can be used for extrapolating behavior at much larger Re_λ) can be generated with reasonable cost on currently available computational hardware.

To understand the exact role of subfilter Fourier modes in the convective transfer of scalar variance, we analyzed scalar-velocity triadic interactions in the viscous-convective subrange, by explicitly filtering DNS data. The results observed suggest that scalar modes originating in the far dissipation range ($\kappa\eta \gg 1$) have a limited range of influence on convective scalar transfer. This apparent decoupling is explained using mathematical arguments based on the observation that the velocity energy spectrum decays much faster than the energy spectrum of a high Schmidt number scalar. Filtered transfer spectra exhibit a distinctive pile-up of energy close to the cutoff wavenumber, which may be explained by a lack of energy extraction by smaller scales. Thus, simulations that do not resolve the physically dissipating scales (e.g., velocity resolved - scalar modeled simulations) require some form of energy damping to avoid solution instability caused by this pile-up. This damping is usually provided by appropriate subfilter models.

Finally, we note that velocity-resolved, scalar-filtered simulations of high Schmidt number scalar transport in homogeneous isotropic turbulence, run with no subfilter model implemented, give rise

to stable solutions. Discretization errors inherent in the scalar transport schemes used are large enough to damp out any possible energy pile-up. The results suggest that implementing an SFF model may not be justified, unless the numerical errors are controlled to be sufficiently smaller than the SFF magnitude. This provides strong incentive to explore the development of more effective numerical schemes.

7.2 Developing an improved, bounded semi-Lagrangian scalar transport scheme for turbulent flows

In Chapter 3, an improved semi-Lagrangian transport scheme for passive scalar mixing was proposed, and tested in both laminar and turbulent flows. This scheme, named BCH, was designed specifically for the turbulent transport of scalars that must respect physical bounds. The scheme is based on the semi-Lagrangian treatment of the advection-diffusion equation, and makes use of cubic Hermite polynomials for interpolation. Boundedness of the scalar field is ensured by applying derivative limiting techniques to the Hermite polynomial. The novelty of the proposed algorithm lies in the way that sub-cell extrema are treated to restore boundedness. The shape-preserving ability of Hermite polynomials makes them especially useful for resolving fine scale scalar structures in turbulent simulations.

Performance of the proposed transport scheme, along with that of several other commonly used schemes (e.g., BQUICK, WENO3, HOUC5, etc.), was tested in two laminar cases, a three dimensional turbulent mixing layer, and in homogeneous isotropic turbulence. Three separate sources of dissipation were identified in these simulations, namely, dissipation associated with molecular diffusion, dissipation inherent in the interpolation procedure, and dissipation introduced by the bounding algorithm. The BCH scheme outperforms all other bounded schemes tested, with regard to the ability to resolve small scale turbulent structures. This was confirmed by examining scalar energy and dissipation spectra on the center plane of the mixing layer. Simulations run with the other bounded schemes required at least twice the spatial resolution to obtain spectra of comparable quality. In

addition to cost savings on account of a coarser grid, comparatively lenient stability conditions for semi-Lagrangian schemes allow a further drop in computational cost for BCH, in comparison to Eulerian schemes. Additional simulations of homogeneous isotropic turbulence indicated that results produced by BCH are comparable to those produced by spectral schemes, with a slight loss of accuracy caused by time splitting errors, when using very large timesteps unconstrained by the CFL number. The superior performance of the BCH scheme, with respect to a majority of the other Eulerian schemes tested, persists even for relatively large Schmidt numbers. Although semi-Lagrangian schemes are known to suffer from mass conservation issues, the turbulent test cases indicate minimal deviation in total scalar mass for the BCH scheme. The minimal loss in conservation had no measurable impact on predicting the correct turbulent characteristics.

Overall, the BCH scheme offers an attractive alternative to Eulerian schemes for turbulent simulations of passive scalar mixing, on account of reduced numerical errors and computational cost, and relative ease of implementation.

7.3 Examining subfilter scalar-flux vector orientation in homogeneous isotropic turbulence, and identifying an optimal subfilter model

In Chapter 4, we examined the alignment behavior of the subfilter-scale scalar flux vector in the eigenframe of the strain rate tensor. Results obtained from filtered DNS datasets indicated strong preferential alignment of the SFF vector ($\boldsymbol{\tau}_\phi$) in a particular direction, when using both the Gaussian and box filters. The alignment direction was explained by analyzing the tensor-diffusivity model, based on the observed preferential orientation of the vorticity ($\boldsymbol{\omega}$) and scalar gradient ($\nabla\widetilde{\phi}$) vectors. The independence of the SFF vector orientation from the filter-width, the flow Schmidt number, and the scalar-forcing method, was explained by extracting the orientation angle from the tensor-diffusivity model. The relevant orientation angle, θ_{S_3}, was shown to depend only on velocity related variables, $\boldsymbol{\omega}$ and λ_3. The remarkable agreement between numerical results and those predicted

by the tensor-diffusivity model confirms that it provides close to an exact analytical form for the subfilter term, when using the Gaussian or box filtering kernels.

Using the orientation of $\nabla\widetilde{\phi}$ in the strain rate eigenframe, it was shown that the subfilter dissipation term for the tensor-diffusivity model acts predominantly as a sink for the scalar variance. Thus, the issue of solution instability induced by the occurrence of negative diffusivity may not arise when using the model for scalar transport. This result should remain valid, at least, as long as the filter-width is located in the viscous-convective subrange.

Analyzing the effect of filter-shape indicated close to random orientation of the SFF vector when using the sharp-spectral filter. Such strong dependence of the subfilter term on filter-shape raises concern regarding the suitability of using implicit filtering in LES/VR-SM simulations, which is often the preferred method of choice for such simulations. The results reinforce the viewpoint that filtering and modeling must be tackled as a unified issue in LES/VR-SM simulations, and an appropriate subfilter model must be used depending on the filtered DNS solution desired. The observed filter dependence also suggests that it may not be appropriate to ascribe a solely physical role to subfilter models, and that it is more pertinent to examine their combined physical and mathematical role in such simulations.

7.4 Validation of the tensor-diffusivity model in homogeneous isotropic turbulence

In Chapter 5, we verified the *a priori* observations from Chapter 4, by performing velocity resolved - scalar modeled simulations of homogeneous isotropic turbulence using the tensor-diffusivity model. The results indicated that the model was stable for sufficiently large κ_c, and was capable of reproducing filtered DNS data with remarkable accuracy. Comparison to unfiltered DNS data indicates good agreement at the small wavenumbers, i.e., at the large physical length scales. The differences observed with unfiltered DNS at large wavenumbers are the result of the effective Gaussian filtering kernel inherent in the modeled equation. Solution instability manifested at smaller values of κ_c

(i.e., large Δ), which was explained by analyzing the κ_c dependence of the negative component of subfilter dissipation. To address the issue of instability, model-regularization was implemented by suppressing the negative dissipation, and yielded stable simulations even with very large Δ. The results produced by the regularized model compared well with those obtained using the original non-regularized model, as well as with results from filtered DNS.

Velocity resolved - scalar modeled simulations conducted on truncated grids combined with explicit filtering also yielded extremely accurate results, suggesting that the tensor-diffusivity model may be exceptionally well-suited for simulation of practical scenarios. Solution instability was not observed on truncated grids with sufficiently small $\kappa_T\eta$, since numerical diffusion damps the negative component of subfilter dissipation at the smallest scales. These numerical errors do not seem to have an adverse effect on the resolved scales in the VR-SM simulations, as long as a ratio of $\Delta/\Delta x = 2$ is used. Filter-width ratios much larger than 2 may not be ideal, since very little information is retained at the subfilter scales beyond $2\kappa_c\eta$.

Tests conducted at a fixed $\kappa_c\eta$ but by varying the grid resolution (i.e., varying $\kappa_T\eta$) indicated that for small $\kappa_c\eta$, the regularized tensor-diffusivity model suffers slightly in terms of accuracy, when compared to the original form of the model. We surmise that in order to avoid solution instability, it may be preferable to use low-dissipation FV/FD numerical schemes in combination with the original form of the tensor-diffusivity model, rather than relying on model-regularization. The effect of using implicit filtering is also examined, and these simulations result in a pile-up of energy close to the cutoff wavenumber, which is reminiscent of observations noted in the literature. The results provide further support for the argument that velocity resolved - scalar modeled simulations of turbulent scalar transport must be performed by using an appropriate combination of subfilter model and explicit filtering.

7.5 Application of the tensor-diffusivity model in the turbulent mixing layer

In Chapter 6, we applied the tensor-diffusivity model to perform velocity resolved - scalar modeled simulations of the turbulent mixing layer. The goal was to assess the effectiveness of the model in supporting shear-dominated flows with large Schmidt number scalars. The regularized form of the model was used in these simulations to minimize breach of physical bounds. The effect of the Schmidt number on a variety of scalar statistics was examined, specifically, by analyzing scalar autocorrelation functions, 1D energy spectra, cross-stream scalar-variance, and planar averages of the resolved and subfilter scalar dissipation rates. The quantities analyzed show distinctively different behavior in the regimes before and after attaining self-similar mixing. The two regimes are characterized by a sharp build-up of scalar-variance/energy in the initial transient stage, and a switch to rapid mixing in the self-similar state. Further examination of the resolved and subfilter scalar-dissipation rates suggests that with increasing Sc, subfilter dissipation dominates the resolved molecular dissipation, and attains a plateau. This explains why resolved large-scale statistics become relatively independent of the Schmidt number for $Sc \gg 1$. The results from this chapter indicate that the simulation framework established is capable of providing reasonable estimates of large-scale scalar statistics, at much lower computational cost than would be required for fully resolved DNS.

7.6 Outlook

Future work in advancing modeling capability for high Re, high Sc flows may entail incorporating modeling of subfilter quantities in the VR-SM framework, and analyzing VR-SM datasets in the same manner as has been done for DNS datasets in this thesis. In that case, the objective would be to assess and validate the best approach of conducting Large Eddy Simulations at large Reynolds and Schmidt numbers, when filtering in the inertial subrange. This will become necessary since modeling in the viscous-convective subrange for application to atmospheric and oceanic flows would not be computationally feasible in the foreseeable future. The relevant analysis could be done in two stages, as has been the approach pursued in this thesis; *a priori* evaluation of model suitability would involve filtering VR-SM data in the inertial subrange to identify a suitable LES model, which could be followed by *a posteriori* tests to assess model performance in actual Large Eddy Simulations.

Appendix A

Anisotropy Due to the Imposed Mean Scalar Gradient

In order to mimic the mixing of scalars in experimental setups, the baseline datasets use an imposed mean scalar gradient in the transport equation. This maintains statistical stationarity and stops the spectrum from decaying. The modified transport equation is shown in Eq. A.2, and is obtained by decomposing the scalar into its mean and spatially fluctuating parts as follows:

$$\Phi = \phi + G \cdot x \tag{A.1}$$

G represents the imposed mean scalar gradient in the x-direction, and scalar fluctuation is given by ϕ. The transport equation shown in Eq. 3.1, under the assumption of incompressibility ($\nabla \cdot \boldsymbol{u} = 0$) now becomes

$$\frac{\partial \phi}{\partial t} + \boldsymbol{u} \cdot \nabla \phi \quad = \quad \mathcal{D}\nabla^2 \phi - uG \tag{A.2}$$

The additional source term (uG) is responsible for maintaining the variance at a constant level, but introduces anisotropy in the scalar field in the x-direction [144, 24]. Upon inspection of the scalar fluxes (Fig. A.1(a) and A.1(b)) in the baseline data, it was found that the x-component ($u\phi$) has a non-negligible negative mean value and its PDF is skewed. In order to avoid unforeseen complications that this large anisotropy in the baseline dataset might give rise to in the *a priori* analysis, we chose to use a combination of only the y and z components of the scalar flux. Fig. A.1(b) confirms that

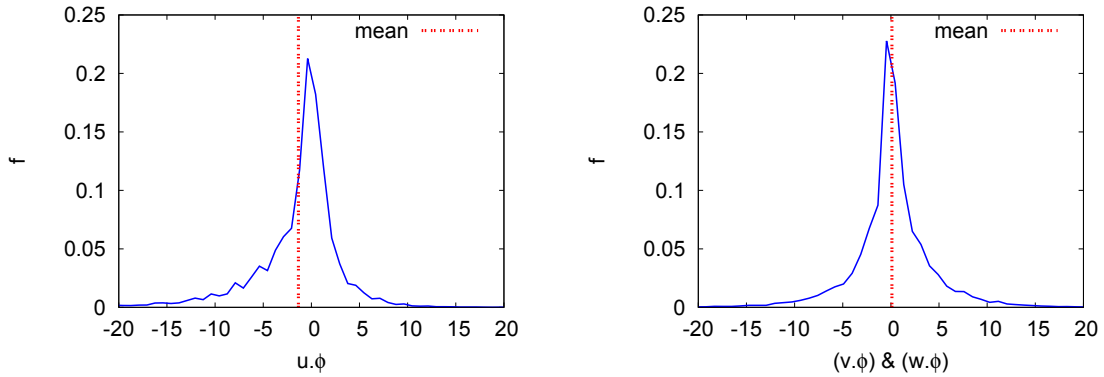

(a) PDF of scalar flux in the x-direction. Mean value = -1.34.

(b) Combined PDF of scalar flux in the y and z directions. Mean value = 0.11

Figure A.1: Probability Density Function (PDF) of scalar flux components. Baseline Case 5, averaged over 4 stationary snapshots.

the combined PDF for the y and z fluxes ($v\phi$ and $w\phi$) is indeed centered at zero.

Appendix B

Gain and Phase Error for the HOUC5 Scheme

The curves for HOUC5 shown in Figs. 3.6 and 3.7 were derived using the procedure described in Ref. [98]. Beginning with Eq. 3.2, we can write the analytical solution for a 1D periodic problem with uniform advection as follows:

$$\phi(x,t) = f(t)e^{j\kappa x} \tag{B.1}$$

Denoting volume averages stored at the cell centers with an overbar ($\bar{\cdot}$), we have

$$\overline{\phi}_i = \frac{1}{\Delta x}\int_{x_{i-\frac{1}{2}}}^{x_{i+\frac{1}{2}}} \phi(x)dx \tag{B.2}$$

$$= \frac{f(t)}{j\kappa\Delta x}\left(e^{j\kappa x_{i+\frac{1}{2}}} - e^{j\kappa x_{i-\frac{1}{2}}}\right) \tag{B.3}$$

This expression can be generalized to the following form

$$\overline{\phi}_{i+m} = \frac{f(t)e^{j\kappa x_{i+\frac{1}{2}}}}{j\kappa\Delta x}\left(e^{j\kappa m\Delta x} - e^{j\kappa(m-1)\Delta x}\right) \tag{B.4}$$

In the finite-volume formulation, cell-face scalar flux values are used to discretize Eq. 3.2

$$\frac{\partial\overline{\phi}_i}{\partial t} = -\frac{u}{\Delta x}\left(\overline{\phi}_{i+\frac{1}{2}} - \overline{\phi}_{i-\frac{1}{2}}\right) \tag{B.5}$$

For HOUC5, the cell-face scalar values are computed as follows

$$\overline{\phi}_{i+\frac{1}{2}} = -\frac{6}{120}\overline{\phi}_{i-1} + \frac{54}{120}\overline{\phi}_{i} + \frac{94}{120}\overline{\phi}_{i+1} - \frac{26}{120}\overline{\phi}_{i+2} + \frac{4}{120}\overline{\phi}_{i+3} \tag{B.6}$$

$$\overline{\phi}_{i-\frac{1}{2}} = -\frac{6}{120}\overline{\phi}_{i-2} + \frac{54}{120}\overline{\phi}_{i-i} + \frac{94}{120}\overline{\phi}_{i} - \frac{26}{120}\overline{\phi}_{i+1} + \frac{4}{120}\overline{\phi}_{i+2} \tag{B.7}$$

Expanding the right hand sides of these two expressions using Eq. B.4, and substituting into Eq. B.5 we have

$$\begin{aligned}\frac{\partial\overline{\phi}_i}{\partial t} = -\frac{uf(t)e^{j\kappa x_{i+\frac{1}{2}}}}{60j\kappa\Delta x^2}\big[&-3e^{-j\kappa 3\Delta x} + 33e^{-j\kappa 2\Delta x} \\ &-10e^{-j\kappa\Delta x} - 80 + 75e^{j\kappa\Delta x} - 17e^{j\kappa 2\Delta x} + 2e^{j\kappa 3\Delta x}\big]\end{aligned} \tag{B.8}$$

To compare this expression to the analytical solution, we differentiate Eq. B.3 with respect to time, and use the fact that $df/dt = -uj\kappa f(t)$ (from Eqs. 3.2 and B.1) to get

$$\frac{\partial\overline{\phi}_i}{\partial t} = -\frac{uf(t)e^{j\kappa x_{i+\frac{1}{2}}}}{\Delta x}\left(1 - e^{-j\kappa\Delta x}\right) \tag{B.9}$$

Comparing Eq. B.8 and Eq. B.9, we get the expression for the effective wavenumber (κ_{eff})

$$\begin{aligned}\kappa_{eff}\Delta x = \big[&-3e^{-j\kappa 3\Delta x} + 33e^{-j\kappa 2\Delta x} - 10e^{-j\kappa\Delta x} - 80 \\ &+75e^{j\kappa\Delta x} - 17e^{j\kappa 2\Delta x} + 2e^{j\kappa 3\Delta x}\big]/60j\left(1 - e^{-j\kappa\Delta x}\right)\end{aligned} \tag{B.10}$$

The numerical phase speed for HOUC5 is equal to $\Re(\kappa_{eff}\Delta x)$ (Fig. 3.7), and the gain amplitude is equal to $e^{-\Im(\kappa_{eff}\Delta x)}$ (Fig. 3.6).

Appendix C

Description of Navier-Stokes Solver (NGA)[1]

NGA (Next Generation ARTS) is an extension of the high order conservative finite difference scheme initially developed by Morinishi et. al [94]. It allows for three-dimensional, variable density turbulent flows to be simulated in complex geometries, which can be either cylindrical or Cartesian, on uniform or non-uniform meshes [41]. The code discretely conserves mass, momentum, and kinetic energy, and can provide arbitrarily high order of accuracy. NGA makes use of staggered variable arrangement on the computational mesh to improve convergence and stability of the pressure solution, which is coupled to the velocity field for incompressible simulations. All scalar quantities, such as the density (ρ) and the scalar (ϕ), are stored at the cell-centers; the velocity components (u, v, and w) are stored at the cell-faces. An overview of NGA, including the governing equations being solved and the schemes by which they are solved, is provided in this Appendix.

I am grateful to Phares L. Carroll for having provided the bulk of the material discussed in this Appendix, as well as in Appendix D.

C.1 Governing equations

NGA solves the variable density, incompressible Navier-Stokes equations [41]. These include expressions of mass conservation,

$$\frac{\partial \rho}{\partial t} + \frac{\partial}{\partial x_j}\left(\rho u_j\right) = 0, \tag{C.1}$$

and momentum conservation,

$$\frac{\partial \rho u_i}{\partial t} + \frac{\partial}{\partial x_j}\left(\rho u_i u_j\right) = -\frac{\partial p}{\partial x_i} + \frac{\partial \sigma_{ij}}{\partial x_j}. \tag{C.2}$$

Here, p is the pressure, u_i is one of the three-components of the velocity field, ρ is the density, and σ_{ij} is the deviatoric stress tensor. The deviatoric stress tensor is defined as,

$$\sigma_{ij} = \mu\left(\frac{\partial u_i}{\partial x_j} + \frac{\partial u_j}{\partial x_i}\right) - \frac{2}{3}\mu\frac{\partial u_k}{\partial x_k}\delta_{ij}, \tag{C.3}$$

where δ_{ij} is the Kronecker delta and μ is the dynamic viscosity. The conserved scalar quantity is calculated from the transport equation,

$$\frac{\partial \rho\phi}{\partial t} + \frac{\partial}{\partial x_j}\left(\rho u_j \phi\right) = \frac{\partial}{\partial x_j}\left(\rho\mathcal{D}\frac{\partial \phi}{\partial x_j}\right), \tag{C.4}$$

where $\mathcal{D}$ is the molecular diffusivity of the scalar. The iterative procedure to solve this equation system is described with the implemented second-order semi-implicit Crank-Nicolson (a time-advancement) scheme in Sec. C.4, which is both stable and accurate [41, 103].

C.2 Variable-density conservative finite-difference scheme

The coordinate system with which the current work is concerned is a standard Cartesian one. Accordingly, physical space can be represented as $\boldsymbol{x} = (x, y, z)$. In NGA, physical space is mapped

to a uniform computational grid of unity spacing. The grid spacing is written as $\boldsymbol{\xi} = (\xi_1, \xi_2, \xi_3)$. Here, ξ_1 is the spacing increment in the x-direction, ξ_2 is the spacing increment in the y-direction, and ξ_3 is the spacing increment in the z-direction. After applying this mapping, scaling factors associated with this transformation from a physical space representation to a computational space representation can be expressed as:

$$h_1 = \frac{dx}{d\xi_1} \qquad h_2 = \frac{dy}{d\xi_2} \qquad h_3 = \frac{dz}{d\xi_3}. \tag{C.5}$$

The Jacobian of this transformation can be written, correspondingly, as

$$J = h_1 h_2 h_3. \tag{C.6}$$

C.3 Convective treatment

With the coordinate system defined, (discrete) operators representative of those implemented in the code can be introduced. A second-order interpolation operator of stencil size n in the ξ_i direction acting on variable ϕ is expressed as $\bar{\phi}^{n,\xi_i}(\boldsymbol{\xi})$. The interpolation operator in the ξ_1 direction,

$$\bar{\phi}^{n,\xi_1}(\xi_1, \xi_2, \xi_3) = \frac{\phi(\xi_1 + n/2, \xi_2, \xi_3) + \phi(\xi_1 - n/2, \xi_2, \xi_3)}{2}, \tag{C.7}$$

is provided as an example. Operators in the ξ_2 and ξ_3 directions are analogous. A second-order (discrete) differentiation operator of stencil size n in the ξ_i direction acting on variable ϕ is represented as $\frac{\delta_n \phi}{\delta_n \xi_i}(\boldsymbol{\xi})$. As an example, the differentiation operator in the ξ_1 direction is written as,

$$\frac{\delta_n \phi}{\delta_n \xi_1}(\xi_1, \xi_2, \xi_3) = \frac{\phi(\xi_1 + n/2, \xi_2, \xi_3) - \phi(\xi_1 - n/2, \xi_2, \xi_3)}{n}. \tag{C.8}$$

Differentiation operators in the ξ_2 and ξ_3 directions are analogous. NGA is capable of providing an arbitrarily high order of accuracy since it employs discrete operators of arbitrarily high order. To

construct n^{th} order accurate discrete operators, interpolation weights, α_l, are calculated via:

$$\sum_{l=1}^{n/2} (2l-1)^{2(i-1)} \alpha_l = \delta_{il} \qquad \text{for } i \in [1, n/2]. \tag{C.9}$$

Following this, the n^{th} order interpolation operator in the ξ_i direction can be expressed as,

$$\bar{\phi}^{nth,\xi_i} = \sum_{l=1}^{n/2} \alpha_l \bar{\phi}^{(2l-1)\xi_i}, \tag{C.10}$$

and the n^{th} order differentiation operator in the ξ_i direction can be expressed as,

$$\frac{\delta_{nth}\phi}{\delta_{nth}\xi_i} = \sum_{l=1}^{n/2} \alpha_l \frac{\delta_{2l-1}\phi}{\delta_{2l-1}\xi_i}. \tag{C.11}$$

By using these staggered operators, superior effective wavenumber behavior is attained. The effect of dissipative errors is reduced [41] by using centered or staggered operators.

Using the operators defined, the governing equations can be discretized. In the momentum equation, Eq. C.2, the divergence terms are represented by,

$$\frac{\partial}{\partial x}(\rho u_i u) \longrightarrow \sum_{i=1}^{3} \left\{ \frac{1}{\bar{J}^{1,\xi_1}} \sum_{l=1}^{n/2} \alpha_l \frac{\delta_{2l-1}}{\delta_{2l-1}\xi_i} \left(\overline{\frac{J\rho u_i}{h_i}} \right)^{nth,\xi_1} \bar{u}^{(2l-1),\xi_i} \right\}, \tag{C.12}$$

$$\frac{\partial}{\partial y}(\rho u_i v) \longrightarrow \sum_{i=1}^{3} \left\{ \frac{1}{\bar{J}^{1,\xi_2}} \sum_{l=1}^{n/2} \alpha_l \frac{\delta_{2l-1}}{\delta_{2l-1}\xi_i} \left(\overline{\frac{J\rho u_i}{h_i}} \right)^{nth,\xi_2} \bar{v}^{(2l-1),\xi_i} \right\}, \tag{C.13}$$

$$\frac{\partial}{\partial z}(\rho u_i w) \longrightarrow \sum_{i=1}^{3} \left\{ \frac{1}{\bar{J}^{1,\xi_3}} \sum_{l=1}^{n/2} \alpha_l \frac{\delta_{2l-1}}{\delta_{2l-1}\xi_i} \left(\overline{\frac{J\rho u_i}{h_i}} \right)^{nth,\xi_3} \bar{w}^{(2l-1),\xi_i} \right\}, \tag{C.14}$$

where the appropriate operators have been applied. The pressure gradient term is also expressed according to,

$$\frac{\partial p}{\partial x_i} \longrightarrow \frac{J}{\bar{J}^{1,\xi_i}} \frac{1}{h_i} \left(\frac{\delta_{nth} p}{\delta_{nth}\xi_i} \right). \tag{C.15}$$

In the mass conservation equation, Eq. C.1, the divergence term is written as,

$$\frac{\partial}{\partial x_j}\left(\rho u_j\right) \longrightarrow \sum_{i=1}^{3}\left\{\frac{1}{J}\frac{\delta_{nth}}{\delta_{nth}\xi_i}\left(\frac{J\rho u_i}{h_i}\right)\right\}. \tag{C.16}$$

The inverse of the Jacobian in the previous relations, $1/\bar{J}^{1,\xi_i}$, is expressed via second-order interpolation, as initially suggested by Morinishi et al. [94]. Numerical solution of the scalar transport equation, Eq. C.4, is accomplished via the finite-volume upwind schemes discussed in Appendix D.

A comment needs to be made here about the relationship between the three components of the velocity field, u_i, and the momentum vector, $g_i = \rho u_i$. As NGA staggers the variables in space, the velocity components are located at a different position from the density values. To account for this, the i^{th} component of the momentum vector is expressed as,

$$g_i = \bar{\rho}^{2nd,x_i} u_i, \tag{C.17}$$

where the operator acting on the density field is a second-order linear interpolation in physical space. The density field is limited to second-order interpolation such that it is total variation diminishing (TVD). Imposing the TVD property prevents the density field from becoming unbounded, and ensures the simulations remain realizable. It should be stated that the density interpolation is limited to second-order irrespective of the order of the rest of the scheme. It was found that such a limitation had little effect on the quality of the results obtained [41]. We note that for all of the simulations discussed in this thesis, the fluid density ρ was kept constant.

C.3.1 The pressure field

In an incompressible formulation of the Navier-Stokes equations, the pressure field, p, is solved for via a Poisson's equation. To ensure that the Poisson's equation solved for p (analytically expressed as $\nabla^2 p = 0$) has a solution, mass must be conserved in a global sense such that,

$$\Delta\left(\delta p\right) = \frac{1}{\Delta t}\left(\sum_{i=1}^{3}\frac{1}{J}\frac{\delta_{nth}}{\delta_{nth}\xi_i}\left(\frac{Jg_i}{h_i}\right)\right) = 0. \tag{C.18}$$

Here, the middle term represents continuity and the left most term represents the discrete version of the Poisson's equation for pressure. Therefore, the following must be satisfied,

$$\sum_{x,y,z} J \sum_{i=1}^{3} \frac{1}{J} \frac{\delta_{nth}}{\delta_{nth}\xi_i} \left(\frac{Jg_i}{h_i} \right) = 0. \tag{C.19}$$

As long as Eq. C.19 is satisfied, then the pressure field can be obtained from Eq. C.18.

C.3.2 Viscous treatment

As viscous terms are dissipative by nature, they are inherently more stable than the convective terms that were addressed previously. The operators that are necessary to discretize the viscous terms are different than those presented for the discretization of the convective terms, and these new operators are based on a local Lagrange polynomial representation of the quantity to which they are applied.

To develop an n^{th} order accurate interpolation and differentiation operator for a quantity ϕ at a location x in the direction of x_i, an $(n-1)^{th}$ order Lagrange polynomial is needed. This $(n-1)^{th}$ order Lagrange polynomial is fit through the n data points that are present in the stencil. As this fitting operation is centered about the point being evaluated, the interpolation or differentiation of the quantity ϕ is calculated from an equal number of points on either side of the point being evaluated. The new interpolation operator can be written as,

$$\bar{\phi}^{nth,x_i} = P(x), \tag{C.20}$$

while the new differentiation operator can be written as,

$$\frac{\delta_{nth}\phi}{\delta_{nth}x_i} = P'(x), \tag{C.21}$$

where $P(x)$ and $P'(x)$ are the Lagrange polynomial expression and the derivative of the Lagrange polynomial expression. Using this approach, the viscous terms in the Navier-Stokes equations can be written in terms of these viscous operators. First, the divergence of the velocity field vector

becomes,

$$\frac{\partial u_i}{\partial x_i} \longrightarrow \frac{\delta_{nth}u}{\delta_{nth}x} + \frac{\delta_{nth}v}{\delta_{nth}y} + \frac{\delta_{nth}w}{\delta_{nth}z}, \tag{C.22}$$

which is termed A_{div} in the deviatoric stress tensor relations to follow. The deviatoric stress tensor is expressed as,

$$\frac{\partial \sigma_{i1}}{\partial x} \longrightarrow \frac{\delta_{nth}}{\delta_{nth}x}\left\{2\mu\left(\frac{\delta_{nth}u}{\delta_{nth}x} - \frac{1}{3}A_{div}\right)\right\} + \frac{\delta_{nth}}{\delta_{nth}y}\left\{\overline{\bar{\mu}^{2nd,x}}^{2nd,y}\left(\frac{\delta_{nth}u}{\delta_{nth}y} + \frac{\delta_{nth}v}{\delta_{nth}x}\right)\right\} + \frac{\delta_{nth}}{\delta_{nth}z}\left\{\overline{\bar{\mu}^{2nd,x}}^{2nd,z}\left(\frac{\delta_{nth}u}{\delta_{nth}z} + \frac{\delta_{nth}w}{\delta_{nth}x}\right)\right\}, \tag{C.23}$$

$$\frac{\partial \sigma_{i2}}{\partial y} \longrightarrow \frac{\delta_{nth}}{\delta_{nth}x}\left\{\overline{\bar{\mu}^{2nd,x}}^{2nd,y}\left(\frac{\delta_{nth}v}{\delta_{nth}x} + \frac{\delta_{nth}u}{\delta_{nth}y}\right)\right\} + \frac{\delta_{nth}}{\delta_{nth}y}\left\{2\mu\left(\frac{\delta_{nth}v}{\delta_{nth}y} - \frac{1}{3}A_{div}\right)\right\} + \frac{\delta_{nth}}{\delta_{nth}z}\left\{\overline{\bar{\mu}^{2nd,y}}^{2nd,z}\left(\frac{\delta_{nth}v}{\delta_{nth}z} + \frac{\delta_{nth}w}{\delta_{nth}y}\right)\right\}, \tag{C.24}$$

and

$$\frac{\partial \sigma_{i3}}{\partial z} \longrightarrow \frac{\delta_{nth}}{\delta_{nth}x}\left\{\overline{\bar{\mu}^{2nd,x}}^{2nd,z}\left(\frac{\delta_{nth}w}{\delta_{nth}x} + \frac{\delta_{nth}u}{\delta_{nth}z}\right)\right\} + \frac{\delta_{nth}}{\delta_{nth}y}\left\{\overline{\bar{\mu}^{2nd,y}}^{2nd,z}\left(\frac{\delta_{nth}w}{\delta_{nth}y} + \frac{\delta_{nth}v}{\delta_{nth}z}\right)\right\} + \frac{\delta_{nth}}{\delta_{nth}z}\left\{2\mu\left(\frac{\delta_{nth}w}{\delta_{nth}z} - \frac{1}{3}A_{div}\right)\right\}. \tag{C.25}$$

C.3.3 Scalar treatment

Similar to the momentum equation (Eq. C.2), differential operators for the terms in the scalar transport equation (Eq. C.4) can be obtained. The differential operator for the advection term is defined to be,

$$\frac{\partial}{\partial x_j}\left(\rho u_j \phi\right) \longrightarrow \sum_{i=1}^{3}\left\{\frac{1}{J}\frac{\delta_{nth}}{\delta_{nth}\xi_i}\left(\frac{J}{h_i}\rho u_i \overline{\phi}^{\xi_i}\right)\right\}. \tag{C.26}$$

Here, $\overline{\phi}^{\xi_i}$ represents the interpolation of a scalar quantity, ϕ, from its position of storage at the cell center to the cell-face in the ξ_i direction. The diffusion term can be discretized similarly according to,

$$\frac{\partial}{\partial x_j}\left(\rho\mathcal{D}\frac{\partial\phi}{\partial x_i}\right) \longrightarrow \sum_{i=1}^{3}\left\{\frac{1}{J}\frac{\delta_{nth}}{\delta_{nth}\xi_i}\left(\frac{J}{h_i}\overline{\rho}^{\xi_i}\overline{\mathcal{D}}^{\xi_i}\phi'\right)\right\}, \tag{C.27}$$

where the primed variable, ϕ', denotes the gradient of the scalar quantity, ϕ, at the cell-face, and $\overline{\rho}^{\xi_i}$ and $\overline{\mathcal{D}}^{\xi_i}$ denote the interpolation of the density and scalar diffusivity to the cell-faces. The means by which these quantities are interpolated to the cell-face depends on the transport scheme employed. The operator varies with the method implemented. The specific form that this interpolation operator takes is described in Appendix D for the the generalized High-Order Upwind Convective (HOUC) schemes [99].

C.4 Time integration

Lastly, with the convective and viscous operators expressed, the time integration can be performed. The Navier-Stokes equations are time-advanced via a second-order, semi-implicit Crank-Nicolson method [103]. This method makes use of a fractional step approach [69], and it uses staggering in time between the momentum, scalar, and density fields. The scalar field is solved first, followed by advancement of the momentum equations in time. Finally, the pressure field is addressed by solving a Poisson's equation for the pressure to enforce continuity, as discussed previously [41]. This six-part iterative, time integration process is described below, where a uniform time step, Δt, is employed. There are a total of M sub-iterations assumed. The scalar quantities are first adressed in the algorithm; the density, scalar, and pressure fields are advanced from time $t^{n+1/2}$ to time $t^{n+3/2}$. Then, the velocity field is advanced from time t^n to time t^{n+1}.

First, assuming the previous time step has converged, these converged solutions are $\rho^{n+1/2}$ for the density field, $p^{n+1/2}$ for the pressure field, $\boldsymbol{u}^n$ for the velocity component fields, and $\phi^{n+1/2}$ for

the scalar fields. These values are used as the initial values in the iterative steps to come,

$$\rho_0^{n+3/2} = \rho^{n+1/2} \qquad p_0^{n+3/2} = p^{n+1/2} \qquad \boldsymbol{u}_0^{n+1} = \boldsymbol{u}^n \qquad \phi_0^{n+3/2} = \phi^{n+1/2}, \tag{C.28}$$

where the superscript denotes the time and the subscript denotes the sub-iteration level, $k \in [0, M]$. Second, the scalar field is treated. When the semi-implicit Crank-Nicolson scheme is applied to the scalar transport equation (Eq. C.4), we get:

$$\phi_k^* = \frac{\phi^{n+1/2} + \phi_{k-1}^{n+3/2}}{2},$$

$$\rho_{k-1}^{n+3/2}\phi_k^{n+3/2} = \rho^{n+1/2}\phi^{n+1/2} + \Delta t \cdot \left([C_k^{n+1} + D_k^{n+1}] \cdot \phi_k^*\right) + \frac{\Delta t}{2}\left(\frac{\partial C}{\partial \phi} + \frac{\partial D}{\partial \phi}\right)_k^{n+1} \cdot \left(\phi_k^{n+3/2} - \phi_{k-1}^{n+3/2}\right). \tag{C.29}$$

In this notation, and for compactness, the differentiation/interpolation operators in the convective and diffusive terms are denoted $\partial C/\partial \phi$ and $\partial D/\partial \phi$. Then, the momentum equation is advanced according to:

$$\boldsymbol{u}_k^* = \frac{\boldsymbol{u}^n + \boldsymbol{u}_{k-1}^{n+1}}{2}, \tag{C.30}$$

$$\frac{\rho^{n+1/2} + \rho_k^{n+3/2}}{2}\boldsymbol{u}_k^\dagger = \frac{\rho^{n-1/2} + \rho^{n+1/2}}{2}\boldsymbol{u}^n + \Delta t \cdot \left([C_k^{n+1/2} + D_k^{n+1/2}] \cdot \boldsymbol{u}_k^* + \nabla p_{k-1}^{n+3/2}\right) + \frac{\Delta t}{2}\left(\frac{\partial C}{\partial \boldsymbol{u}} + \frac{\partial D}{\partial \boldsymbol{u}}\right)_k^{n+1/2} \cdot \left(\boldsymbol{u}_k^\dagger - \boldsymbol{u}_{k-1}^{n+1}\right), \tag{C.31}$$

where $\boldsymbol{u}_k^\dagger$ is an intermediate velocity that is the solution to the above momentum equation. Again, for compactness, the differentiation/interpolation operators in the convective and diffusive terms are denoted $\partial C/\partial \boldsymbol{u}$ and $\partial D/\partial \boldsymbol{u}$. After that, the Poisson's equation for the pressure field is solved. This

calculates the hydrodynamic pressure to be,

$$\nabla^2\left(\delta p_k^{n+3/2}\right) = \frac{1}{\Delta t}\left(\nabla\cdot\left\{\frac{\rho^{n+1/2}+\rho_k^{n+3/2}}{2}\boldsymbol{u}_k^{\dagger}\right\} + \frac{\rho_k^{n+3/2}-\rho^{n+1/2}}{\Delta t}\right). \tag{C.32}$$

The velocity field is then updated accordingly by projecting it onto a divergence free field,

$$\boldsymbol{u}_k^{n+1} = \boldsymbol{u}_k^{\dagger} - \frac{2\Delta t}{\rho^{n+1/2}+\rho_k^{n+3/2}}\cdot\nabla\left(\delta p_k^{n+3/2}\right). \tag{C.33}$$

A converged solution is obtained following M sub-iterations. Once the sub-iterations are converged, then, lastly, the calculated (time-advanced) field values are updated and stored,

$$\rho^{n+3/2} = \rho_M^{n+3/2} \qquad p^{n+3/2} = p_M^{n+3/2} \qquad \boldsymbol{u}^{n+1} = \boldsymbol{u}_M^{n+1} \qquad \phi^{n+3/2} = \phi_M^{n+3/2}. \tag{C.34}$$

Following this process, the next time step is addressed, and the process begins again.

Appendix D

Implementation of the High-Order Upwind Convective (HOUC) Scalar Transport Schemes

For illustrative purposes, the scalar transport schemes to be presented are applied in only one dimension (the x-direction). Here, the subscripts denote the scalar field variable value to the right $(i+1)$ or to the left $(i-1)$ of the central node. The central node has index i. Recall that the grid is staggered, so the momentum fluxes, ρu, are stored at the cell-faces; the cell-faces have indices $i+1/2$ and $i-1/2$. From this it follows that the finite-volume algorithm implemented by NGA can be written as:

$$\frac{\partial\left(\rho\phi\right)_{i,j,k}}{\partial t}+\frac{\left(\rho u\phi\right)_{i+1/2,j,k}-\left(\rho u\phi\right)_{i-1/2,j,k}}{\Delta x}=\frac{\left(\rho\mathcal{D}\frac{\partial\phi}{\partial x}\right)_{i+1/2,j,k}-\left(\rho\mathcal{D}\frac{\partial\phi}{\partial x}\right)_{i-1/2,j,k}}{\Delta x}. \tag{D.1}$$

The values of the momentum fluxes at the cell-faces are known ($(\rho u)_{i+1/2}$ and $(\rho u)_{i-1/2}$), but the scalar field values are known only at the cell centers. To determine the value of the scalar at the cell-face, the cell-centered value is interpolated from its storage position at i, $i+1$, or $i-1$ to the cell-face at $i+1/2$ or $i-1/2$,

$$\begin{aligned}\left(\rho u\phi\right)_{i-1/2,j,k}&=\left(\rho u\right)_{i-1/2,j,k}\overline{\overline{\phi}}_{i-1/2,j,k}\\ \left(\rho u\phi\right)_{i+1/2,j,k}&=\left(\rho u\right)_{i+1/2,j,k}\overline{\overline{\phi}}_{i+1/2,j,k},\end{aligned} \tag{D.2}$$

where the operation $\overline{\overline{\phi}}_{i+1/2,j,k}$ determines the value of the scalar at the cell-face from the value at the cell center by use of polynomial fitting. The form of this interpolation operation (polynomial expression) is specific to the scalar transport scheme. The following subsections detail the interpolating coefficients associated with the third- and fifth-order HOUC schemes.

D.1 Third-order HOUC scheme

The third-order HOUC scheme, more commonly known as the Quadratic Upstream Interpolation for Convective Kinematics (QUICK) scheme [81], uses upwinded quadratic interpolation for determining cell-face scalar values. The finite-volume form of the QUICK scheme is third-order accurate in space ($O(\Delta x^3)$). The upwinding inherent in the scheme reduces the severity with which spurious oscillations manifest in polynomials with a centered interpolating stencil. The relevant interpolation coefficients are given below:

$$\begin{aligned}
\overline{\overline{\phi}}_{i-1/2,j,k} &= -\frac{1}{6}\phi_{i-2} + \frac{5}{6}\phi_{i-1} + \frac{1}{3}\phi_i \\
\overline{\overline{\phi}}_{i+1/2,j,k} &= \frac{1}{3}\phi_{i-1} + \frac{5}{6}\phi_i - \frac{1}{6}\phi_{i+1},
\end{aligned} \tag{D.3}$$

which allows for the convective flux terms,

$$\begin{aligned}
(\rho u\phi)_{i-1/2,j,k} &= (\rho u)_{i-1/2,j,k}\,\overline{\overline{\phi}}_{i-1/2,j,k} \\
(\rho u\phi)_{i+1/2,j,k} &= (\rho u)_{i+1/2,j,k}\,\overline{\overline{\phi}}_{i+1/2,j,k},
\end{aligned} \tag{D.4}$$

to be calculated.

For constant density and constant molecular diffusivity flow, the diffusive flux in Eq. D.1 is computed using second-order centered-difference:

$$\begin{aligned}
\left(\frac{\partial\phi}{\partial z}\right)_{i+1/2,j,k} &= \frac{\phi_{i+1,j,k} - \phi_{i,j,k}}{\Delta x} \\
\left(\frac{\partial\phi}{\partial z}\right)_{i-1/2,j,k} &= \frac{\phi_{i,j,k} - \phi_{i-1,j,k}}{\Delta x}.
\end{aligned} \tag{D.5}$$

Once the relevant components of the diffusive term have been calculated at the cell-faces, then the scalar equation (Eq. D.1) can be advanced in time.

D.2 Fifth-order HOUC scheme

The fifth-order HOUC scheme [99] follows the same general solution procedure as that outlined for the QUICK scheme in Sec. D.1. The main difference lies in the interpolating polynomial and stencil size used. HOUC5 uses a 5-point stencil for interpolation, with three points located in the upwind direction from the interpolating face, and two points located downwind. The interpolating polynomial takes the following form:

$$\begin{aligned}
\bar{\bar{\phi}}_{i+1/2,j,k} &= -\frac{6}{120}\phi_{i-1,j,k} + \frac{54}{120}\phi_{i,j,k} + \frac{94}{120}\phi_{i+1,j,k} - \frac{26}{120}\phi_{i+2,j,k} + \frac{4}{120}\phi_{i+3,j,k} \\
\bar{\bar{\phi}}_{i-1/2,j,k} &= -\frac{6}{120}\phi_{i-2,j,k} + \frac{54}{120}\phi_{i-1,j,k} + \frac{94}{120}\phi_{i,j,k} - \frac{26}{120}\phi_{i+1,j,k} + \frac{4}{120}\phi_{i+2,j,k}.
\end{aligned} \tag{D.6}$$

Note that these polynomial coefficients assume a uniform grid mesh. Following the interpolation, the convective fluxes are computed, followed by the diffusive fluxes for use in Eq. D.1, and the solution is advanced in time.

Bibliography

[1] Burden of disease from the joint effects of household and ambient air pollution for 2012. Technical report, World Health Organization, 2014.

[2] K. Alvelius. Random forcing of three-dimensional homogeneous turbulence. *Phys. Fluids*, 11(7):1880–1889, 1999.

[3] R. A. Antonia and P. Orlandi. Effect of Schmidt number on small-scale passive scalar turbulence. *Appl. Mech. Rev.*, 56(6):615–632, 2003.

[4] Wm. T. Ashurst, A. R. Kerstein, R. M. Kerr, and C. H. Gibson. Alignment of vorticity and scalar gradient with strain rate in simulated Navier-Stokes turbulence. *Phys. Fluids*, 30(8):2343–2353, 1987.

[5] A. Attili and F. Bisetti. Application of a robust and efficient Lagrangian particle scheme to soot transport in turbulent flames. *Comput. Fluids*, 84:164 – 175, 2013.

[6] A. Attili and F. Bisetti. Fluctuations of a passive scalar in a turbulent mixing layer. *Phys. Rev. E*, 88(3):033013, 2013.

[7] A. Attili, F. Bisetti, M. E. Mueller, and H. Pitsch. Formation, growth, and transport of soot in a three-dimensional turbulent non-premixed jet flame. *Combust. Flame*, 2014.

[8] G. Balarac, H. Pitsch, and V. Raman. Development of a dynamic model for the subfilter scalar variance using the concept of optimal estimators. *Phys. Fluids*, 20(3):035114, 2008.

[9] G. Balarac, J. Le Sommer, X. Meunier, and A. Vollant. A dynamic regularized gradient model of the subgrid-scale scalar flux for large eddy simulations. *Phys. Fluids*, 25(7):075107, 2013.

[10] D. S. Balsara and C.-W. Shu. Monotonicity preserving weighted essentially non-oscillatory schemes with increasingly high order of accuracy. *J. Comput. Phys.*, 160(2):405–452, 2000.

[11] J. Bardina, J. H. Ferziger, and W. C. Reynolds. Improved subgrid-scale models for large-eddy simulation. *Am. Inst. Aeronaut. Astronaut. Pap.*, 80-1357, 1980.

[12] J. Bardina, J. H. Ferziger, and W. C. Reynolds. Improved turbulence models based on large eddy simulation of homogeneous, incompressible turbulent flows. *Stanford Univ. Report*, (May 1983), 1983.

[13] G. K. Batchelor. Small-scale variation of convected quantities like temperature in turbulent fluid: Part 1. General discussion and the case of small conductivity. *J. Fluid Mech.*, 5(01):113–133, 1959.

[14] G. K. Batchelor, I. D. Howells, and A. A. Townsend. Small-scale variation of convected quantities like temperature in turbulent fluid: Part 2. The case of large conductivity. *J. Fluid Mech.*, 5(01):134–139, 1959.

[15] H. A. Becker, H. C. Hottel, and G. C. Williams. The nozzle-fluid concentration field of the round, turbulent, free jet. *J. Fluid Mech.*, 30(2):285–303, 1967.

[16] K. W. Bedford and W. K. Yeo. Conjunctive filtering procedures in surface water flow and transport. In B. Galperin and S. A. Orszag, editors, *Large Eddy Simulation of Complex Engineering and Geophysical flows*, pages 513–537, 1993.

[17] R. Bermejo and A. Staniforth. The conversion of semi-Lagrangian advection schemes to quasi-monotone schemes. *Mon. Wea. Rev.*, 120:2622–2632, 1992.

[18] F. Bisetti, G. Blanquart, M. E. Mueller, and H. Pitsch. On the formation and early evolution of soot in turbulent nonpremixed flames. *Combust. Flame*, 159(1):317 – 335, 2012.

[19] D. Bogucki, J. A. Domaradzki, and P. K. Yeung. Direct numerical simulations of passive scalars with Pr>1 advected by turbulent flow. *J. Fluid Mech.*, 343:111, 1997.

[20] J. P. Boris and D. L. Book. Flux-corrected transport. I. SHASTA, a fluid transport algorithm that works. *J. Comput. Phys.*, 11(1):38 – 69, 1973.

[21] S. T. Bose, P. Moin, and D. You. Grid-independent large-eddy simulation using explicit filtering. *Phys. Fluids*, 22(10):105103, 2010.

[22] R. Breidenthal. *A chemically reacting, turbulent shear layer.* PhD thesis, California Institute of Technology, 1979.

[23] R. Breidenthal. Structure in turbulent mixing layers and wakes using a chemical reaction. *J. Fluid Mech.*, 109:1–24, 1981.

[24] G. Brethouwer, J. C. R. Hunt, and F. T. M. Nieuwstadt. Micro-structure and Lagrangian statistics of the scalar field with a mean gradient in isotropic turbulence. *J. Fluid Mech.*, 474:193–225, 2003.

[25] G. C. Burton. Scalar-energy spectra in simulations of Sc≫1 mixing by turbulent jets using the nonlinear large-eddy simulation method. *Phys. Fluids*, 20(7):071701, 2008.

[26] G. C. Burton. The nonlinear large-eddy simulation method applied to Sc ≈ 1 and Sc≫1 passive-scalar mixing. *Phys. Fluids*, 20(3):035103, 2008.

[27] G. C. Burton and W. J. A. Dahm. Multifractal subgrid-scale modeling for large-eddy simulation. II. Backscatter limiting and a posteriori evaluation. *Phys. Fluids*, 17(7):075112, 2005.

[28] I. Calmet and J. Magnaudet. Large-eddy simulation of high-Schmidt number mass transfer in a turbulent channel flow. *Phys. Fluids*, 9(2):438, 1997.

[29] I. Calmet and J. Magnaudet. High-Schmidt number mass transfer through turbulent gas-liquid interfaces. *International journal of heat and fluid flow*, 19:522, 1998.

[30] D. Carati, G. S. Winckelmans, and H. Jeanmart. On the modelling of the subgrid-scale and filtered-scale stress tensors in large-eddy simulation. *J. Fluid Mech.*, 441:119–138, 2001.

[31] P. L. Carroll, S. Verma, and G. Blanquart. A novel forcing technique to simulate turbulent mixing in a decaying scalar field. *Phys. Fluids*, 25(9):095102, 2013.

[32] S. Chen, G. Doolen, J. R. Herring, R. H. Kraichnan, S. A. Orszag, and Z. S. She. Far-dissipation range of turbulence. *Phys. Rev. Lett.*, 70(20):3051–3054, 1993.

[33] H. Choi and P. Moin. Effects of the computational time step on numerical solutions of turbulent flow. *J. Comput. Phys.*, 113:1–4, 1994.

[34] S. G. Chumakov. A priori study of subgrid-scale flux of a passive scalar in isotropic homogeneous turbulence. *Phys. Rev. E*, 78(3):036313, 2008.

[35] R. A. Clark, J. H. Ferziger, and W. C. Reynolds. Evaluation of subgrid-scale models using an accurately simulated turbulent flow. *J. Fluid Mech.*, 91(1):1–16, 1979.

[36] S. Corrsin. On the spectrum of isotropic temperature fluctuations in an isotropic turbulence. *J. Appl. Phys.*, 22(4):469–473, 1951.

[37] W. J. A. Dahm. *Experiments on entrainment, mixing and chemical reactions in turbulent jets at large Schmidt number*. PhD thesis, California Institute of Technology, 1985.

[38] V. Daru and C. Tenaud. High order one-step monotonicity-preserving schemes for unsteady compressible flow calculations. *J. Comput. Phys.*, 193(2):563 – 594, 2004.

[39] C. de Boor and B. Swartz. Piecewise monotone interpolation. *J. Approx. Theory*, 21(4):411–416, 1977.

[40] G. De Stefano and O. V. Vasilyev. Sharp cutoff versus smooth filtering in large eddy simulation. *Phys. Fluids*, 14(1):362, 2002.

[41] O. Desjardins, G. Blanquart, G. Balarac, and H. Pitsch. High order conservative finite difference scheme for variable density low Mach number turbulent flows. *J. Comput. Phys.*, 227(15):7125, 2008.

[42] P. E. Dimotakis. The mixing transition in turbulent flows. *J. Fluid Mech.*, 409:69, 2000.

[43] P. E. Dimotakis. Turbulent mixing. *Ann. Rev. Fluid Mech.*, 37(1):329–356, 2005.

[44] P. E. Dimotakis and P. L. Miller. Some consequences of the boundedness of scalar fluctuations. *Phys. Fluids A: Fluid Dyn*, 2:1919, 1990.

[45] J. A. Domaradzki and E. M. Saiki. Backscatter models for large-eddy simulations. *Theor. Comp. Fluid Dyn.*, 9(2):75–83, 1997.

[46] D. A. Donzis, K. R. Sreenivasan, and P. K. Yeung. The Batchelor spectrum for mixing of passive scalars in isotropic turbulence. *Flow Turbul. Combust.*, 85:549–566, 2010.

[47] D. A. Donzis and P. K. Yeung. Resolution effects and scaling in numerical simulations of passive scalar mixing in turbulence. *Physica D*, 239:1278, 2010.

[48] D. R. Dowling and P. E. Dimotakis. Similarity of the concentration field of gas-phase turbulent jets. *J. Fluid Mech.*, 218(1):109, 1990.

[49] H. Feng, M. G. Olsen, J. C. Hill, and R. O. Fox. Simultaneous velocity and concentration field measurements of passive-scalar mixing in a confined rectangular jet. *Exp. Fluids*, 42(6):847, 2007.

[50] J. Foster and F. B. Richards. The Gibbs phenomenon for piecewise-linear approximation. *Amer. Math. Monthly*, 98(1):47–49, 1991.

[51] F. N. Fritsch and R. E. Carlson. Monotone piecewise cubic interpolation. *SIAM J. Numer. Anal.*, 17(2):238–246, 1980.

[52] A. E. Gargett. Evolution of scalar spectra with the decay of turbulence in a stratified fluid. *J. Fluid Mech.*, 159:379–407, 1985.

[53] M. Germano, U. Piomelli, P. Moin, and W. H. Cabot. A dynamic subgrid-scale eddy viscosity model. *Phys. Fluids A*, 3(7):1760, 1991.

[54] C. H. Gibson and W. H. Schwarz. The universal equilibrium spectra of turbulent velocity and scalar fields. *J. Fluid Mech.*, 16(3):365–384, 1963.

[55] T. Gotoh, S. Hatanaka, and H. Miura. Spectral compact difference hybrid computation of passive scalar in isotropic turbulence. *J. Comput. Phys.*, 231:7398, 2012.

[56] H. L. Grant, B. A. Hughes, W. M. Vogel, and A. Moilliet. The spectrum of temperature fluctuations in turbulent flow. *J. Fluid Mech.*, 34(3):423–442, 1968.

[57] Tennekes H. and Lumley J. L. *A first course in turbulence*. MIT Press, Cambridge, MA, 1972.

[58] P. E. Hamlington, J. Schumacher, and W. J. A. Dahm. Direct assessment of vorticity alignment with local and nonlocal strain rates in turbulent flows. *Phys. Fluids*, 20(11):111703, 2008.

[59] P. E. Hamlington, J. Schumacher, and W. J. A. Dahm. Local and nonlocal strain rate fields and vorticity alignment in turbulent flows. *Phys. Rev. E*, 77(2):1–8, 2008.

[60] M. Herrmann, G. Blanquart, and V. Raman. Flux corrected finite volume scheme for preserving scalar boundedness in reacting large-eddy simulations. *AIAA J.*, 44(12):2879–2886, 2006.

[61] C. W. Higgins, M. B. Parlange, and C. Meneveau. Alignment trends of velocity gradients and subgrid-scale fluxes in the turbulent atmospheric boundary layer. *Bound.-Lay. Meteorol.*, 109:59–83, 2003.

[62] C. W. Higgins, M. B. Parlange, and C. Meneveau. The heat flux and the temperature gradient in the lower atmosphere. *Geophys. Res. Lett.*, 31(22), 2004.

[63] M. Y. Hussaini and T.A. Zang. Spectral methods in fluid dynamics. *Ann. Rev. Fluid Mech.*, 19:339–367, 1987.

[64] H. T. Huynh. Accurate monotone cubic interpolation. *SIAM J. Numer. Anal.*, 30(1):57–100, 1993.

[65] ESA Envisat image. Algal bloom in the Baltic sea. `http://eoimages.gsfc.nasa.gov/images/imagerecords/81000/81919/california_amo_2013234_lrg.jpg`, 2005. Accessed: 2014-03-23.

[66] NASA MODIS image. Yosemite Rim Fire. `http://eoimages.gsfc.nasa.gov/images/imagerecords/81000/81919/california_amo_2013234_lrg.jpg`, 2013. Accessed: 2014-03-23.

[67] W. P. Jones and P. Musonge. Closure of the Reynolds stress and scalar flux equations. *Phys. Fluids*, 31:3589–3604, 1988.

[68] M. C. Jullien, P. Castiglione, and P. Tabeling. Experimental observation of Batchelor dispersion of passive tracers. *Phys. Rev. Lett.*, 85(17):3636, 2000.

[69] J. Kim and P. Moin. Application of a fractional-step method to incompressible Navier-Stokes equations. *J Comput. Phys.*, 59(2):308–323, 1985.

[70] E. Knudsen, E. S. Richardson, E. M. Doran, H. Pitsch, and J. H. Chen. Modeling scalar dissipation and scalar variance in large eddy simulation: Algebraic and transport equation closures. *Phys. Fluids*, 24(5):055103, 2012.

[71] S. Komori, T. Kanzaki, Y. Murakami, and H. Ueda. Simultaneous measurements of instantaneous concentrations of two species being mixed in a turbulent flow by using a combined laser-induced fluorescence and laser-scattering technique. *Phys. Fluids A*, 1:349, 1989.

[72] S. Komori and H. Ueda. Turbulent effects on the chemical reaction for a jet in a nonturbulent stream and for a plume in a gridgenerated turbulence. *Phys. Fluids*, 27:77–86, 1984.

[73] J. H. Konrad. *An experimental investigation of mixing in two-dimensional turbulent shear flows with applications to diffusion-limited chemical reactions.* PhD thesis, California Institute of Technology, 1977.

[74] R. H. Kraichnan. The structure of isotropic turbulence at very high Reynolds numbers. *J. Fluid Mech.*, 5(4):497–543, 1959.

[75] R. H. Kraichnan. Small-scale structure of a scalar field convected by turbulence. *Phys. Fluids*, 11(5):945–953, 1968.

[76] J.-B. Lagaert, G. Balarac, and G.-H. Cottet. Hybrid spectral-particle method for the turbulent transport of a passive scalar. *J. Comput. Phys.*, 260:127–142, 2014.

[77] P. H. Lauritzen. A stability analysis of finite-volume advection schemes permitting long time steps. *Mon. Wea. Rev.*, 135(7):2658–2673, 2007.

[78] M. Lentine, J. T. Grétarsson, and R. Fedkiw. An unconditionally stable fully conservative semi-Lagrangian method. *J. Comput. Phys.*, 230(8):2857–2879, 2011.

[79] A. Leonard. Energy cascade in large-eddy simulations of turbulent fluid flows. In *Adv. Geophys.*, volume 18 A, pages 237–248, 1974.

[80] A. Leonard. Large-eddy simulation of chaotic convection and beyond. *Am. Inst. Aeronaut. Astronaut. Pap.*, 97-0204:1–8, 1997.

[81] B. P. Leonard. A stable and accurate convective modelling procedure based on quadratic upstream interpolation. *Comput. Method. Appl. M.*, 19:59–98, 1979.

[82] R. J. Leveque. *Finite volume methods for hyperbolic problems*. Cambridge University Press, 2002.

[83] D. K. Lilly. A proposed modification of the Germano subgrid-scale closure method. *Phys. Fluids A*, 4(3):633, 1992.

[84] S. Liu, C. Meneveau, and J. Katz. On the properties of similarity subgrid-scale models as deduced from measurements in a turbulent jet. *J. Fluid Mech.*, 275:83–119, 1994.

[85] X.-D. Liu, S. Osher, and T. Chan. Weighted essentially non-oscillatory schemes. *J. Comput. Phys.*, 115(1):200–212, 1994.

[86] T. S. Lund. The use of explicit filters in large eddy simulation. *Comput. Math. Appl.*, 46:603–616, 2003.

[87] J. Magnaudet and I. Calmet. Turbulent mass transfer through a flat shear-free surface. *J. Fluid Mech.*, 553:155, 2006.

[88] L. G. Margolin and W. J. Rider. A rationale for implicit turbulence modelling. *Int. J. Numer. Meth. Fluids.*, 39:821–841, 2002.

[89] P. L. Miller and P. E. Dimotakis. Reynolds number dependence of scalar fluctuations in a high Schmidt number turbulent jet. *Phys. Fluids A*, 3(5):1156, 1991.

[90] P. L. Miller and P. E. Dimotakis. Stochastic geometric properties of scalar interfaces in turbulent jets. *Phys. Fluids A*, 3(1):168, 1991.

[91] P. L. Miller and P. E. Dimotakis. Measurements of scalar power spectra in high Schmidt number turbulent jets. *J. Fluid Mech.*, 308:129, 1996.

[92] A. Misra and D. I. Pullin. A vortex-based subgrid stress model for large-eddy simulation. *Phys. Fluids*, 9(8):2443–2454, 1997.

[93] P. Moeleker and A. Leonard. Lagrangian methods for the tensor-diffusivity subgrid model. *J. Comput. Phys.*, 167:1–21, 2001.

[94] Y. Morinishi, O. V. Vasilyev, and T. Ogi. Fully conservative finite difference scheme in cylindrical coordinates for incompressible flow simulations. *J. Comput. Phys.*, 197(2):686–710, 2004.

[95] N. J. Mueschke, O. Schilling, D. L. Youngs, and M. J. Andrews. Measurements of molecular mixing in a high-Schmidt-number Rayleigh-Taylor mixing layer. *J. Fluid Mech.*, 632:17–48, 2009.

[96] I. Nakamura, Y. Sakai, and M. Miyata. Diffusion of matter by a non-buoyant plume in grid-generated turbulence. *J. Fluid Mech.*, 178:379, 1987.

[97] G. R. Newman, B. E. Launder, and J. L. Lumley. Modelling the behaviour of homogeneous scalar turbulence. *J. Fluid Mech.*, 111:217–232, 1981.

[98] X. Nogueira, I. Colominas, L. Cueto-Felgueroso, and S. Khelladi. On the simulation of wave propagation with a higher-order finite volume scheme based on reproducing kernel methods. *Comput. Methods Appl. Mech. Engrg.*, 199(23–24):1471–1490, 2010.

[99] R. R. Nourgaliev and T. G. Theofanous. High-fidelity interface tracking in compressible flows: Unlimited anchored adaptive level set. *J. Comput. Phys.*, 224(2):836, 2007.

[100] S. A. Orszag. On the elimination of aliasing in finite-difference schemes by filtering high-wavenumber components. *J. Atmos. Sci.*, 28:1074, 1971.

[101] M. R. Overholt and S. B. Pope. Direct numerical simulation of a passive scalar with imposed mean gradient in isotropic turbulence. *Phys. Fluids*, 8(11):3128–3148, 1996.

[102] P. N. Papanicolaou and E. J. List. Investigations of round vertical turbulent buoyant jets. *J. Fluid Mech.*, 195:341, 1988.

[103] C. D. Pierce. *Progress-variable approach for large-eddy simulation of turbulent combustion.* PhD thesis, Stanford University, 2001.

[104] U. Piomelli, P. Moin, and J. H. Ferziger. Model consistency in large eddy simulation of turbulent channel flows. *Phys. Fluids*, 31(7):1884, 1988.

[105] H. Pitsch, O. Desjardins, G. Balarac, and M. Ihme. Large-eddy simulation of turbulent reacting flows. *Prog. Aerospace Sci.*, 44(6):466, 2008.

[106] S. B. Pope. *Turbulent flows.* Cambridge University Press, 2000.

[107] A. Priestley. A quasi-conservative version of the semi-Lagrangian advection scheme. *Mon. Wea. Rev.*, 121:621–629, 1993.

[108] C. D. Pruett and N. A. Adams. A priori analyses of three subgrid-scale models for one-parameter families of filters. *Phys. Fluids*, 12(5):1133, 2000.

[109] C. D. Pruett, J. S. Sochacki, and N. A. Adams. On Taylor-series expansions of residual stress. *Phys. Fluids*, 13(9):2578, 2001.

[110] D. I. Pullin. A vortex-based model for the subgrid flux of a passive scalar. *Phys. Fluids*, 12(9):2311, 2000.

[111] P. J. Rasch and David L. Williamson. On shape-preserving interpolation and semi-Lagrangian transport. *SIAM J. Sci. Stat. Comput.*, 11(4):656–687, 1990.

[112] P. L. Roe. Characteristic-based schemes for the euler equations. *Ann. Rev. Fluid Mech.*, 18:337–365, 1986.

[113] R. S. Rogallo. Numerical experiments in homogeneous turbulence. *NASA Technical Memorandum*, 81315, 1981.

[114] R. S. Rogallo and P. Moin. Numerical simulation of turbulent flows. *Ann. Rev. Fluid Mech.*, 16:99–137, 1984.

[115] M. M. Rogers and P. Moin. The structure of the vorticity field in homogeneous turbulent flows. *J. Fluid Mech.*, 176:33–66, 1987.

[116] M. M. Rogers and R. D. Moser. Direct simulation of a self-similar turbulent mixing layer. *Phys. Fluids*, 6(2):903–923, 1994.

[117] B. I. Shraiman and E. D. Siggia. Scalar turbulence. *Nature*, 405(6787):639–646, 2000.

[118] J. Smagorinsky. General circulation experiments with the primitive equations, I. The basic experiment. *Mon. Wea. Rev*, 91:99–163, 1963.

[119] K. R. Sreenivasan. The passive scalar spectrum and the Obukhov-Corrsin constant. *Phys. Fluids*, 8:189–196, 1996.

[120] K. R. Sreenivasan and R. A. Antonia. The phenomenology of small-scale turbulence. *Ann. Rev. Fluid Mech.*, 29:435–472, 1997.

[121] A. Staniforth and J. Côté. Semi-Lagrangian integration schemes for atmospheric models—A review. *Mon. Wea. Rev.*, 119(9):2206–2223, 1991.

[122] R. W. Stewart. Turbulence, 16mm sound film and accompanying text. In *Illustrated Experiments in Fluid Mechanics*, pages 82–88. MIT Press, Cambridge, 1972.

[123] W.-Y. Sun, K.-S. Yeh, and R.-Y. Sun. A simple semi-Lagrangian scheme for advection equations. *Q.J.R. Meteorol. Soc.*, 122:1211–1226, 1996.

[124] S. Tavoularis and S. Corrsin. Experiments in nearly homogenous turbulent shear flow with a uniform mean temperature gradient. Part 1. *J. Fluid Mech.*, 104:311–347, 1981.

[125] A. Tsinober, E. Kit, and T. Dracos. Experimental investigation of the field of velocity gradients in turbulent flows. *J. Fluid Mech.*, 242:169–192, 1992.

[126] T. Utsumi, T. Kunugi, and T. Aoki. Stability and accuracy of the cubic interpolated propagation scheme. *Computer physics communications*, 101:9–20, 1997.

[127] C. W. Van Atta and T. T. Yeh. Evidence for scale similarity of internal intermittency in turbulent flows at large Reynolds numbers. *J. Fluid Mech.*, 71:417–440, 1975.

[128] B. van Leer. Towards the ultimate conservative difference scheme. V. A second-order sequel to Godunov's method. *J. Comput. Phys.*, 32:101–136, 1979.

[129] O. V. Vasilyev, T. S. Lund, and P. Moin. A general class of commutative filters for LES in complex geometries. *J. Comput. Phys.*, 146(1):82–104, 1998.

[130] S. Verma and G. Blanquart. On filtering in the viscous-convective subrange for turbulent mixing of high Schmidt number passive scalars. *Phys. Fluids*, 25(5):055104, 2013.

[131] T. Voelkl, D. I. Pullin, and D. C. Chan. A physical-space version of the stretched-vortex subgrid-stress model for large-eddy simulation. *Phys. Fluids*, 12(7):1810, 2000.

[132] B. Vreman, B. Geurts, and H. Kuerten. Large-eddy simulation of the temporal mixing layer using the Clark model. *Theor. Comp. Fluid Dyn.*, 8:309–324, 1996.

[133] B. Vreman, B. Geurts, and H. Kuerten. Large-eddy simulation of the turbulent mixing layer. *J. Fluid Mech.*, 339:357–390, 1997.

[134] Z. Warhaft. Passive scalars in turbulent flows. *Ann. Rev. Fluid Mech.*, 32:203–240, 2000.

[135] T. Watanabe and T. Gotoh. Statistics of a passive scalar in homogeneous turbulence. *New J. Phys.*, 6:40–40, 2004.

[136] D. L. Williamson and P. J. Rasch. Two-dimensional semi-Lagrangian transport with shape-preserving interpolation. *Mon. Wea. Rev.*, 117:102–129, 1989.

[137] G. S. Winckelmans, A. A. Wray, O. V. Vasilyev, and H. Jeanmart. Explicit-filtering large-eddy simulation using the tensor-diffusivity model supplemented by a dynamic Smagorinsky term. *Phys. Fluids*, 13:1385–1403, 2001.

[138] F. Xiao, T. Yabe, X. Peng, and H. Kobayashi. Conservative and oscillation-less atmospheric transport schemes based on rational functions. *J. Geophys. Res.*, 107(D22):1–11, 2002.

[139] S. Xu. *Turbulent mixing of passive scalars at high Schmidt number.* PhD thesis, Georgia Institute of Technology, 2005.

[140] T. Yabe, F. Xiao, and T. Utsumi. The constrained interpolation profile method for multiphase analysis. *J. Comput. Phys.*, 169(2):556–593, 2001.

[141] P. K. Yeung. Multi-scalar triadic interactions in differential diffusion with and without mean scalar gradients. *J. Fluid Mech.*, 321:235, 1996.

[142] P. K. Yeung, D. A. Donzis, and K. R. Sreenivasan. High-Reynolds-number simulation of turbulent mixing. *Phys. Fluids*, 17(8):081703, 2005.

[143] P. K. Yeung, S. Xu, D. A. Donzis, and K. R. Sreenivasan. Simulations of three-dimensional turbulent mixing for Schmidt numbers of the order 1000. *Flow Turbul. Combust.*, 72:333, 2004.

[144] P. K. Yeung, S. Xu, and K. R. Sreenivasan. Schmidt number effects on turbulent transport with uniform mean scalar gradient. *Phys. Fluids*, 14(12):4178, 2002.

[145] S. T. Zalesak. Fully multidimensional flux-corrected transport algorithms for fluids. *J. Comput. Phys.*, 31:335–362, 1979.

[146] Y. Zang, R. L. Street, and J. R. Koseff. A dynamic mixed subgrid-scale model and its application to turbulent recirculating flows. *Phys. Fluids A*, 5(12):3186, 1993.

[147] K. Zhou, A. Antonio, and F. Bisetti. Direct numerical simulation of aerosol growth processes in a turbulent mixing layer. In *Seventh International Conference on Computational Fluid Dynamics, Big Island, Hawaii*, 2012.